PETROLEUM RESEARCH JOURNAL

TECHNICAL PAPERS

ENGINEERING

Borehole Stability Control .....
Nehad Elhemali, Jim Somerville and Brain Smart 1

The Enhancement of Wear Resistance of AISI-316 Austenitic Stainless Steel by Gas Nitriding: Response Surface Analysis and Optimization .....
Tarek M. Belgasam, Farag M. Shuaeib and A. AL-Khatib 15

Development of Low and High Chromium Alloyed Creep Resistance Steels forPower Plants and Related Applications .....
Yousef Elarbi and Bela Palotas 25

Role of Magnetic Field at High PH on Scaling Tendency .....
Mabrouk Hassan and Noureddine Boucif 39

A Study of the Predictive Thermodynamic Models for the Wax Deposition of Synthetic Fuels .....
Layla Alghanduri, Abdulghani A. Nhaesi, Mohamed M. Elgarni 49

EXPLORATION

A Stratigraphic Review of the Al Bayda Formation, NE Libya: Calcareous Nannofossils versus Foraminifera .....
Esam O. Abdulsamad and Ahmed F.A.Tmalla 57

Analysis of Fault Zone Characteristics Using Potential Field and Seismic Data, Al Hagfa Trough, Sirt Basin - Libya .....
Hussein Ghanoush and Milad Elmaradi 67

Petrography, Diagenetic Aspects and Isotopes of the An Nagaza Member of the Al Khums Formation, NW Libya .....
Mahmoud T. Elbakai; Aisha, K. Shalghum and Lila I. Hafez 81

CHEMISTRY

Basic Nitrogen Compounds Identification in Rasco Crude Oil Blend and in its Distillates and Residue .....
Youssef A. Al Mestiri and Abeer A. Al Shiki 99

Distribution of and Identification of Some Sulfur Compounds in Rasco Light Gas Oil (Diesel Oil) .....
Abeer A. ALShiki 107

VOLUME 21 - (2008/2009)

Libyan Petroleum Institute
P.O. Box 6431, Tripoli
Great Socialist People's Libyan Arab Jamahiriya

Petroleum Res. J. Vol. 21 (2008/2009); P. 1–14, 10 Figs.

Borehole Stability Control

Nehad Elhemali*, Jim Somerville** and Brain Smart**

Abstract: Wellbore stability is one of the biggest challenges for drilling engineers. The main question is how to keep the wellbore stable to assure a safe drilling operation. Optimizing borehole pressure, hence the equivalent circulating density (ECD) within the limit between collapse pressure and fracture pressure is important to avoid borehole failure.

In this study, the drilling induced wellbore failure in two wells in one of the North Sea fields was examined. Four-arm caliper log was used for observation of wellbore failure where density log, sonic log and leak-off test were used to estimate elastic parameters and the magnitude of the three principal in-situ stresses. The typical problems encountered in both wells have included washout and breakout sections. Due to lack of data such as: laboratory test measurements and shear wave in one of the wells, empirical formulas were used.

An analytical model was constructed in order to optimize the mud weight requirements to drill through instable zones, and mud weight ranges were identified to minimize wellbore instability. The key parameters were imported from Excel sheet including elastic properties, in-situ stresses and rock strength.

The collapse pressure, fracture pressure and mud weight, which can be used safely while drilling, were calculated. As the appropriate mud weight range was estimated ECD has been predicted for different assumed pressure losses.

INTRODUCTION

Wellbore stability is one of the most serious problems in the oil industry. It can lead to delays in the drilling

Process, increases in drilling cost, and in some cases even to abandonment of the well[1],[2]. It is estimated that this problem costs the oil industry one billion U.S. dollars per year[3].

Wellbore instability is an important factor that should be considered while drilling and maintance of boreholes. Drilling problems frequently occur due to severe mechanical instabilities at the borehole wall where stress amplification has exceeded the strength of the rock [4]. This is because the rock surrounding the hole must support the stress previously supported by material removed in the drilling process. To prevent wellbore failure the stresses around the wellbore should be minimized.

In order to achieve a successful drilling operation, the drilling fluid pressure should be maintained to stay within a tight mud weight window defined by the pressure limits for wellbore stability [5].

Pore pressure or collapse pressure is the lower pressure limit of drilling fluid and the upper limit is the fracture pressure. If the drilling fluid pressure is less than the pore pressure then formation fluids could flow into the borehole, with the subsequent risk of a blowout [5]. An increase in drilling fluid pressure more than the upper limit pressure, there will be a risk of fracturing the formation.

The Equivalent Circulating Density (ECD)

The equivalent circulating density (ECD) is defined as the effective mud weight at a given depth created by the total hydrostatic pressure (including the cutting pressure) and dynamic pressure (hydrostatic pressure plus friction pressure)[6],[7]. ECD can be represents by the following equation:

$$ECD = \frac{P_{hyd} + \Delta P_{fric}}{D}$$

High ECD is responsible for many problems while drilling that have direct relation with wellbore pressure.

*Libyan Petroleum Institute.
** Heriot –Watt University, UK

Management of borehole pressure is a critical part in the drilling operation, in which static and dynamic fluid pressure are the main key in containing formation pressures and assuring wellbore stability. For successful drilling operation, drilling fluid should be well selected and optimized, which will affect the equivalent ECD. When circulation is established, the equivalent mud weight slowly builds up to the ECD as a result of friction pressure losses. Measurement of ECD while drilling will give an indication of possible cuttings/carvings build up in the wellbore [8].

ROCK MECHANICAL PROPERTIES AND STRENGTH

Definitions of Rock Mechanics Parameters

Stress

Stress is an applied external force on solid body that causes internal resulting forces to exist within the body whose resultant force will be equal in magnitude but opposite in direction to the applied force. A stress could be tension if it tends to elongate the subjected body or compression if it tends to contact the subjected body.

$$\sigma = \frac{F}{A}$$

Stress is measured in Pascal (N/sq.m), atm, bar, psi and/or dyne/sq.cm.

Strain

Strain is the resultant deformation of a body, as a function of its original dimension; caused by an applied force (stress).

$$Tensile\ \ strain = \frac{L_O - L}{L_O} = \frac{\Delta L}{L_O}$$

$$Shearing\ strain = \tan\phi = \phi$$

Where:

ϕ : Deformation angle.

$$Volume\ \ strain = \frac{\Delta V}{V_O}$$

Elasticity Modulus

When a body is subjected to a specific stress, it will undergo a specific strain. If the body returns to its original dimension upon removal of the stress, the action is said to be elastic. However, if upon the removal of the stress the body does not return to its original dimensions, and there is a residual strain, the action is said to be inelastic.

Poisson's Ratio

It is the ratio of the absolute value of stain in the lateral direction to the strain in the axial direction. The Poisson's ratio is defined as:

$$\upsilon = -\frac{\varepsilon_X}{\varepsilon_Z} = \frac{Lateral\ strain}{Axial\ strain}$$

Young's Modulus

A measurement of the opposition of a substance to extensional stress is determined by:

$$E = \left[2G(1+\upsilon)\right]$$

Poisson's ratio and Young's modulus are function of rock's hardness and elasticity.

Shear Modulus

The opposition of a substance to shear stresses, is determined by

$$G = C\left[\frac{\rho_b}{\left(\Delta t_s\right)^2}\right]$$

FAR FIELD STRESSES

The stresses that exist in the rock mass are related to the weight of the overburden and also to its geological history. Knowledge of the in-situ stress in rocks is important in drilling stable borehole. The magnitudes of stresses in the rock generally increase with depth. Rock stress can be divided into virgin or in-situ stress and induced stress. The in-situ stresses are existing as the rock is stable, at which the rocks are supporting each other, without any disturbance that created by induced stresses such as drilling [8].

The In-situ Principal

Stresses. Total stress components are defined

vertically and horizontally. A simple linear coordinate system requires a vertical stress component ($ó_z$), and two horizontal components $ó_x$ and $ó_y$ as shown in Fig.1.

Vertical Stress $ó_v$

It is normally the maximum principal stress, and fundamentally due to the weight of overlaying rocks (overburden) and often called lithostatic stress. In geologically relaxed areas having little tectonic activity, the overburden gradient is taken as 1.0 psi/ft. In tectonically active areas, as in sedimentary basins which are still undergoing compaction or in highly faulted areas, the overburden gradient varies with depth, and an average value of 0.8 psi/ft is normally taken as representative of the overburden gradient.

For elastic solid:

$$\sigma_v = \rho g z$$

Where: ñ: is the density of the overlaying rock
g : acceleration of gravity.
z : is the depth

Horizontal Stress

This is a summation of tectonic and nontectonic stresses, the first related to plate motions and the second related to lateral expansion due to overburden load. Two mutually perpendicular horizontal stresses ($ó_H$ and $ó_h$) can be calculated, and it is therefore necessary to determine the orientations and magnitude of the two principal horizontal stresses.

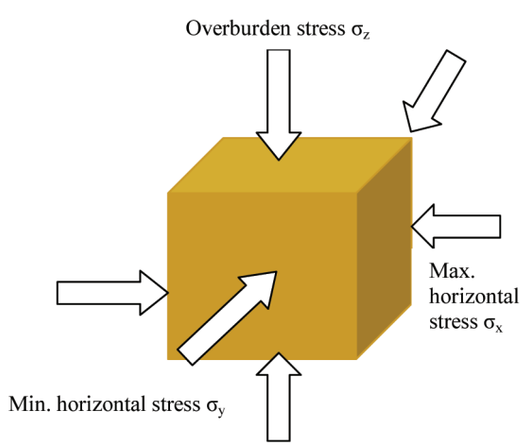


Fig. 1. The principal stresses.

Pore Pressure

Pore pressure plays a crucial role in wellbore stability exerted by the formation fluids on the walls of the rock pores. Pore pressure supports part of the weight of the overburden, while the other part is supported by the grains of the rock. The terms pore pressure; formation pressure and fluid pressure are synonymous, referring to formation pressure. Hydrostatic pressure due to weight of a column of water

$$P_p = \rho_w g z$$

FAILURE CRITERIA

Borehole walls may fail when the surrounding stress exceeds the tensile, the compressive, or the shear strengths of the rock formation, whichever is reached first. To analyse the initiation of failure, the effective stress concentration near the wellbore due to the far-field stresses and the specific borehole orientation should be taken into consideration.

Tensile Failure

Tensile failure occurs if the minimum principal stress becomes sufficiently negative; ó3d≤-To

Shear Failure

This type of failure is most often described by Mohr-Coulomb criterion:

$$\tau = S_o + \sigma \tan\phi$$

WELLBORE INSTABILITY PROBLEMS

The wellbore instability caused by imbalance between the near wellbore stresses and the rock strength can be classified into [9], [10]:

Washout

Washout while drilling can be observed from LWD calliper (Four-arm calliper) and some other states such as: excess of cuttings return to surface, excessive hole fill after tripping and an increase in mud volume. Washout occurred by either collapse of borehole due to insufficient mud weight and/or

erosion of the borehole wall due to inappropriate mud chemical design.

Hole Collapse (Breakout)

Hole collapse or breakout occurs when the stress around the borehole exceeds that required to cause compressive failure of the borehole wall. Breakout can be observed from four-arm calliper log data. Breakouts are zones of spalling and fracture on opposite sides of the wellbore, which elongate it in cross section from circular to approximately elliptical.

Hole Tight

Hole tight or undergauge hole occurs when there is a reduction in the annular clearance, and this causes an increase in torque and drag, stuck pipe, an increase in swab and surge pressure and overpull.

Mud Losses

Mud losses or lost circulation caused by the initiation of hydraulic fracturing due to high mud weight which causes a tensile failure. Propagation of fracture may occur depending on the maximum pressure in the borehole.

STRESSES AROUND BOREHOLES

Before a well is drilled, the rocks are pressed by overburden and horizontal stresses as well as formation pore pressure. After the well is drilled, the drilling fluid in the borehole will provide the support for the borehole stability instead of the rock that drilled off, causing an alteration in the stress state of the rock around the wellbore [11]. When a vertical well is drilled in a formation subjected to maximum and minimum horizontal stresses, the state of local principal stresses around the borehole wall are expressed by the following equations:

$$\sigma r = \Delta P$$

$$\sigma\theta = \sigma_H + \sigma_h - 2(\sigma_H - \sigma_h)\cos 2\theta - 2\,p_p - \Delta P$$

$$\sigma_z = \sigma_v - 2\nu(\sigma_H - \sigma_h)\cos 2\theta - P_p$$

Where: ÄP: is the pressure difference between the borehole pressure and pore pressure.

When the local stresses exceeds the rock strength the rocks around borehole will undergoes failure.

WELLBORE INSTABILITY ANALYSES

Case History

Two deviated wells were drilled in the North Sea with KCl polymer mud (C64 and C80).

Well C64, the $12^1/_4$in hole was drilled smoothly with no problems at angle degree of 45^0. An $8^1/_2$ in hole drilled smoothly to 10760 ft (MD) without problems using static mud weight of 9.3ppg, at this point hole failure continued throughout drilling operation until 10880 ft (MD) causing a enlargement in the original designed borehole size.

Well C80, the well was drilled without any drilling problems until reaching a depth of 15565 ft (MD) in a hole size of $8^1/_2$ in. Another hole failure problem while drilling $8^1/_2$ in hole was encountered from 16060ft (MD).

Area Geology

Based on the formation evaluation (Gamma ray log and SP log) a general description of the lithology could be discerned. The formation interval from 10760 to 10820 ft in well C64 is characterized by dipping beds of about 32^0, and interval from 15565 ft to 15660 ft with dipping bed of about 28^0 and from 16230 ft and 16350 ft with bedding dip of 20^0 in well C80 can be described as shale or mudstone with shale beds interspersed in a few layers.

Detection of Wellbore Failure

Four-arm caliper log is the only tool used to detect the wellbore failure in both wells. Two caliper measurements (C1 and C2) were available as recorded by dipmeter tool and the caliper analysis focused on data in the shale unit above the reservoir.

Figure 2 shows that caliper reading versus depth for well C64. From the caliper data, it is clear that the borehole has undergone significant failure below 10760ft, MD (7747ft, tvd). A large washout zone is encountered in the intervals from 10760 to 10806ft, MD (7747 to 7780ft, tvd) and caliper two (C2) gives the large reading. A peak value in washout reaches up to 18.85in for caliper C2 which is almost the double of the bit size (8.5 in) and caliper C1 has a similar

peak value distribution to the C2, and is generally about 16.88 in.

Below 10806 to 10824ft, MD (7780 to 7793ft, tvd) caliper one C1 has approximately constant value which is close to the bit size (8.5in) with an increase in the reading of caliper C2 to 10.65in this interval can be considered as breakout zone.

Below 10824ft, MD (7793ft, tvd) both C1 and C2 have similar values (8.6-8.8in). In this well a good breakout is hard to find because none of the two calipers are constant while the other is increased.

Figure 2 shows that the hole deviation increases along the hole from 17.7^0 to 73^0 and the hole azimth ranges from 255^0 to 340^0.

Figure 3, represents the reading of C1 and C2 for well C80, Both caliper readings show a washout zone from 15569 to 15604ft, MD (8423 to 8441ft, tvd) where the large caliper peak reading value is about 16.5in while the smaller one is 12.86in. From 15604 to 15637ft, MD (8442 to 8460ft, tvd) the calliper C1 becomes constant at 8.5in and calliper C2 reading ranges between 8.7 and 9.4in.

Below 16174ft, MD (8750ft, tvd) repeated breakout zones are encountered with a large a breakout intervals from 16246.5 to 16413.5ft, MD (8789 to 8880ft, tvd) and the tool rotated 90^0 causing caliper C1 to become larger and give a reading of 15.46 in.

From Figure 3, the hole deviation increases from 17.5^0 to 31^0 and the hole azmith ranges from 91^0 to 209^0.

CONSTRUCTION OF ANALYTICAL MODEL

In order to understand, control the wellbore instability (breakout) and mud weight window for conducting safe drilling operation, an analytical model has been derived. The key parameters for evaluating stability and those needed to construct an analytical model are the three principal in-situ stresses and rock strength parameters defining the two common failure criterions (tensile and compressional failure). Once these parameters were calculated the three principal stresses at the wellbore wall and predictions of failure can be obtained (Fig. 4).

The model is derived from conventional Leak-off test and logging (density log and, Acoustic waves) from which variables can be calculated such as: Young's moduls, Poisson's ratio, unconfined compressive strength and the in-situ stresses.

Determination of Elastic Properties

Due to the absence of laboratory data, Poisson's ratio and Young's modulus were derived using density log and acoustic velocities of compressional velocity (Vp) and shear velocity (Vs) which recorded in monople data [12]

$$\nu = \frac{v_p^2 - 2v_s^2}{2\left(v_p^2 - v_s^2\right)}$$

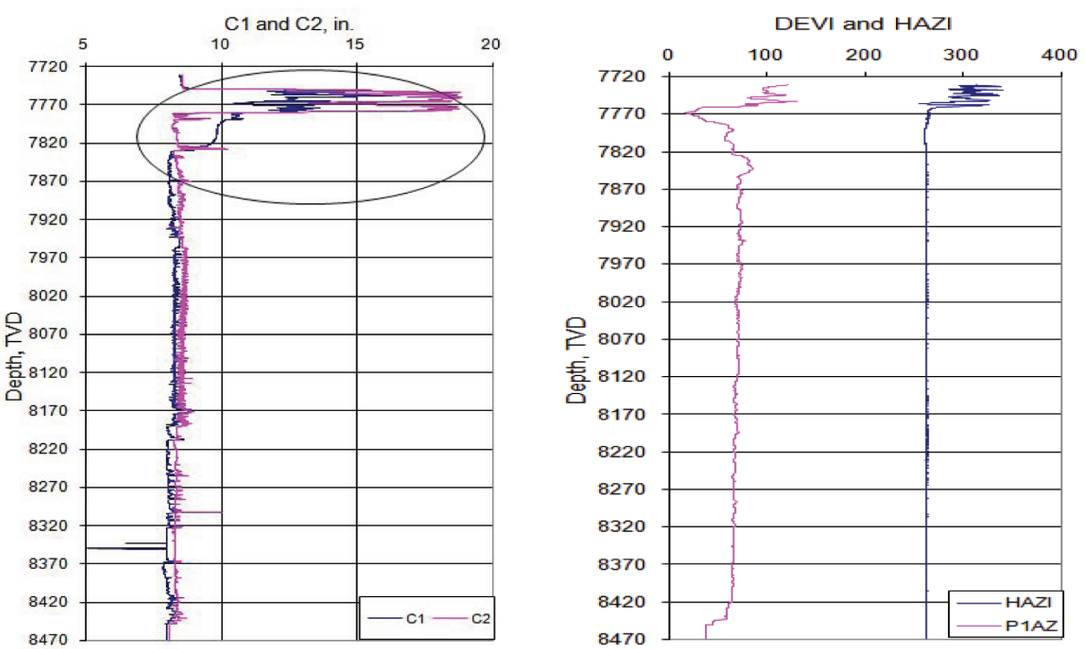


Fig. 2. Four-arm caliper log, hole azmith HAZI and Deviation DEVI from hole C64.

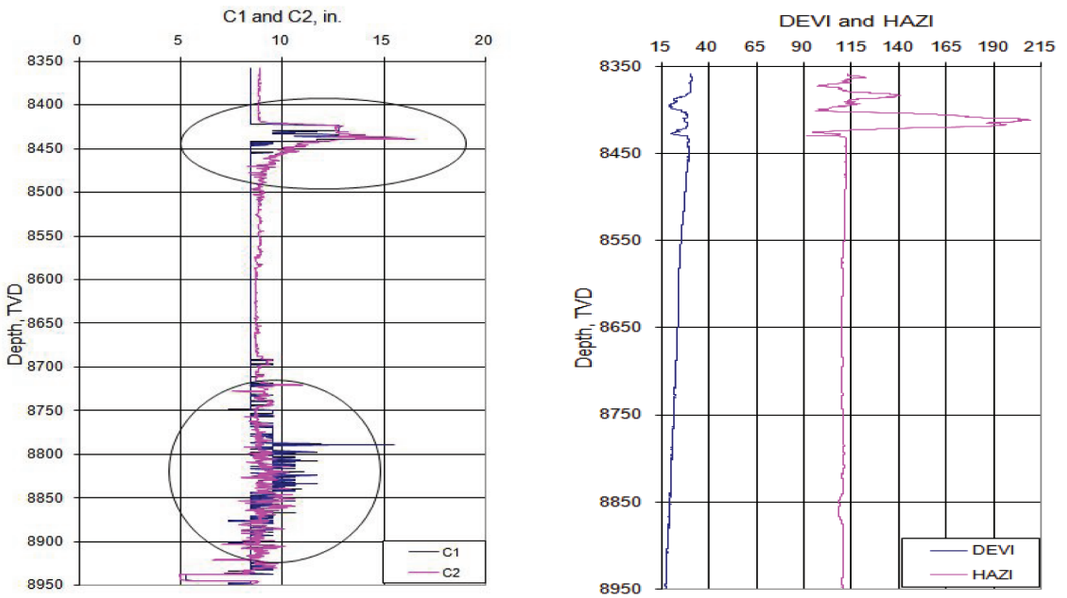


Fig. 3. Four-arm caliper log, hole azmith HAZI and Deviation DEVI for hole C80.

and

$$E = \rho v_s^2 \frac{3v_p^2 - 4v_s^2}{v_p^2 - v_s^2}$$

In well C64, only monopole sonic was used in the hole which measured the compressional velocity and there is no direct measurement of the shear waves. In order to estimate Vs in this well, two methods were tested for Vs prediction, and the result from the two methods was checked using the available Vs from well C80.

The most common method of shear velocity prediction is Castagna's relationship, which is known as mudrock equation (ARCO mudrock line) has been used[13]

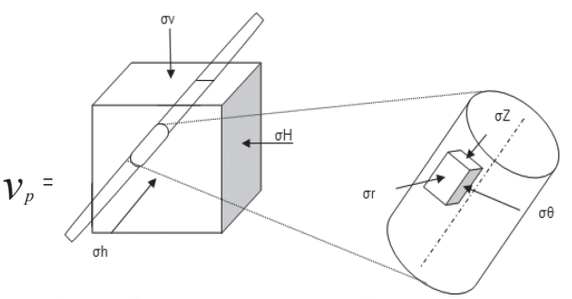


Fig. 4. Stresses acting on the wellbore.

The second method gave a better match with the measured Vs than the Castagna's relationship and gives the same results when used to determine the elastic properties (Fig.5).

$$v_s = 0.73 v_p - 767$$

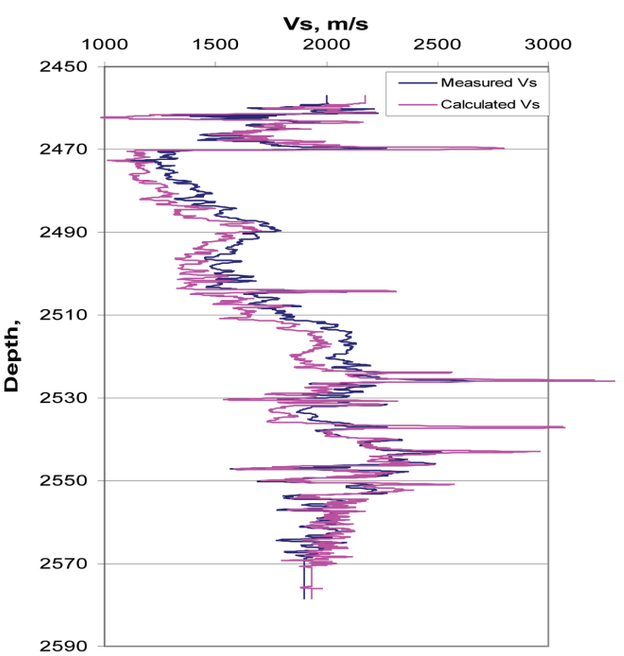


Fig. 5. The measured and calculated shear wave versus depth relationship for well C80.

Determination of Rock Mechanics

In order to predict the wellbore stability, the mechanical properties of the rock, in particular the unconfined compressive strength (UCS) should be known. Due to the unavailability of laboratory

measurements an alternative approach for deriving UCS is used based on well log data. The following relationship was developed in North Sea for high porosity (Ø>0.27) shale [13]:

$$UCS[MPa] = 0.286\,\phi^{-1.762}$$

Figure 6 shows the plots of bulk density, sonic transit time, calculated dynamic elastic properties and unconfining compressive strength. From these plots, the trends are strongly correlated between the rock stiffness and rock strength.

IN-SITU STRESS

Determination of Vertical Stress

Vertical stress was derived for both wells from integration of density log data taken into account the hydrostatic pressure due to water depth:

$$\sigma_v = \int \rho_b g\, D_s + \int \rho_w g\, D_w$$

A linear trend was established for the upper several meters up to the seafloor.

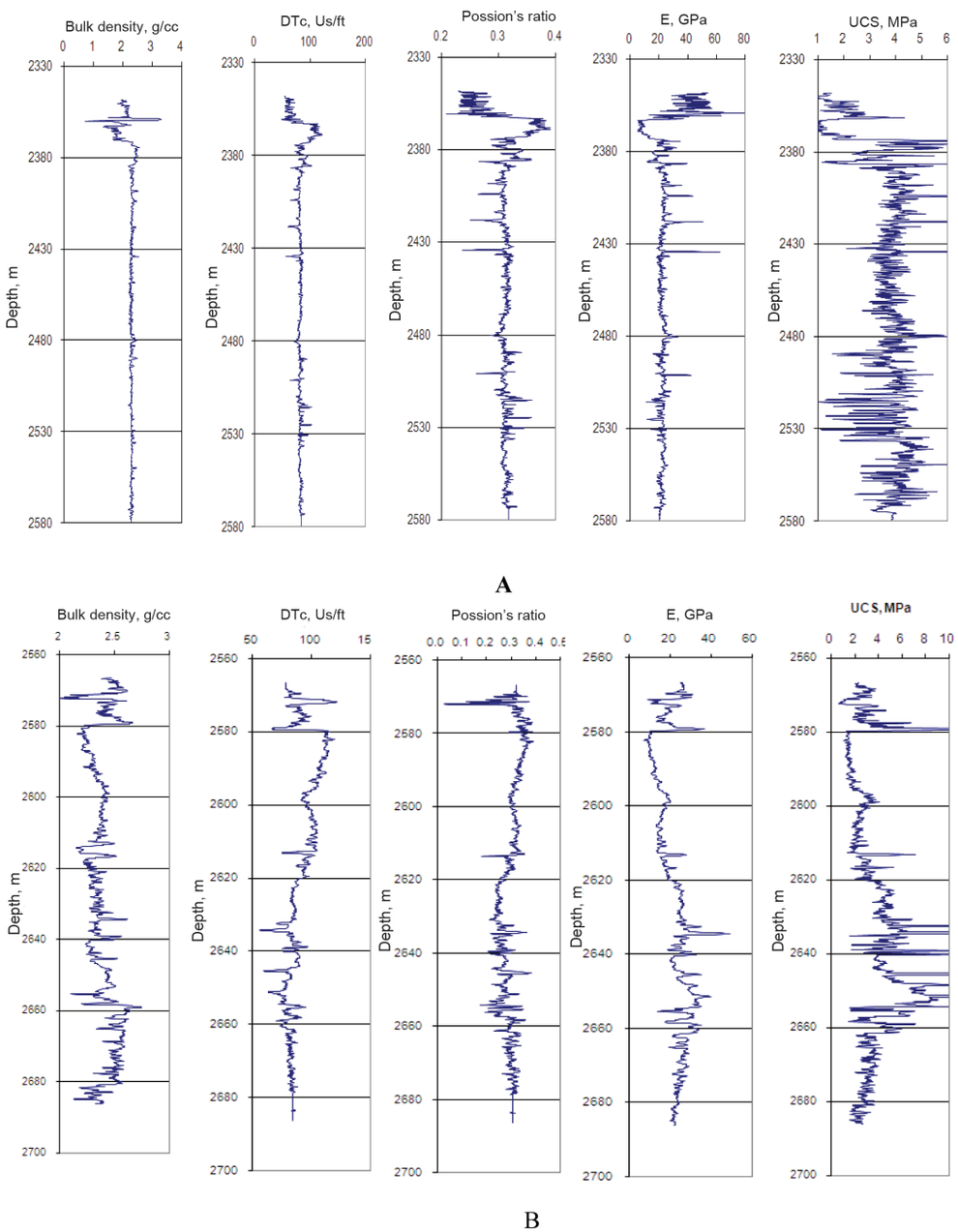


Fig. 6. Bulk density, transit time, calculated elastic properties and calculated UCS, A for well C64 and B for well C80.

The magnitude of Horizontal Stresses

Full LOTs and XLOTs are rarely conducted, and pressure decline following leak-off test is not universally monitored [14]. In our case there are no extended leak-off tests conducted in both wells, therefore the determination of the minimum horizontal stress in both wells was based on conventional leak-off tests.

In both wells the leak-off tests were conducted in depths above the depths of the interest. In order to overcome the lack of LOTs in the regions of interest, a linear stress gradient was assumed and the linear stress gradient to the depth of interest was extrapolated.

Determination of Minimum Horizontal Stress

The minimum horizontal stress was derived from the conventional LOTs in both wells using Leak-off pressure:

$$\sigma_h = p_{lot} + p_{hyd}$$

Determination of Maximum Horizontal Stress

With only conventional Leak-off tests available, the only method of determination of the maximum horizontal stress is to use the leak off pressure P_{lot}

$$\sigma_H = 2P_{lot} + T_o - P_p$$

The tensile strength is ignored since the rock is assumed to be as a weak rock.

DISCUSSION

In order to optimize mud weight and to predict mud weight window, some parameters such as: elastic properties, in-situ stresses, pore pressure and rock strength have to be determined.

This study is mainly based on density log, sonic log, leak-off test and four arm caliper to derive formation mechanical properties, magnitude of in situ stresses and identification of wellbore instability. No laboratory test measurements were used in this study.

The results of four arm caliper analysis show that both holes C64 and C80 undergo mechanical induced borehole enlargement and elongation. Both washout and breakout are observed in the two wells. Breakout candidate that fulfilled the breakout condition which encountered in well C64, is shown in Table 1. In well C80, four breakout candidates, where one calliper increases while the other is constant, are found in this well and these breakout sections are shown in Table 2. Since that four-arm calliper is the only tool used in this study the orientation of the maximum horizontal stress can not be made.

Figures 7 and 8 show the relationship of depth versus in-situ stresses and pore pressure data for both wells. The pore pressure gradient determined from the RFT is 0.28psi/ft for oil and 0.49psi/ft for water column. The vertical stress of each well was derived by the integration of bulk density log data taken after drilling.

In order to assess wellbore stability, the minimum and maximum horizontal principal stress should be measured. Extended leak-off test and minifrac tests are the common and more reliable tests used to constrain minimum and maximum horizontal stress. Due to the unavailability of XLOT and/or minifrac testes in this field, two conventional leak-off tests (a single test in each well) were used to constrain the least principal stress. The two leak-off tests were conducted at depths above the depth of interest. To overcome this, a linear gradient trend was assumed between the LOT and area of interest as mentioned before.

The magnitude of the maximum horizontal stress is the most difficult stress to be determined. As a result of lack of tests which are commonly used to constrain the magnitude of maximum horizontal stress, conventional leak-off tests were used by equalizing the least principal stress with the leak-off

Table 1. Summary of borehole breakout sections in well C64.

Depth, MD	Breakout depth	Hole angle
10806 to 10824, ft	2.24 in.	34˚

Table 2. Summary of boeakout sections in well C80.

Depth, MD	Breakout depth, in.	Hole angle
15565 to 15568.5, ft	1.93 in.	27.7˚
15585.5 to 15588, ft	4.184 in.	28.98˚
15604.5 to 15637, ft	3.3 in.	29˚
16246.5 to 16413.5, ft	1.1 – 9.95 in.	20.5˚

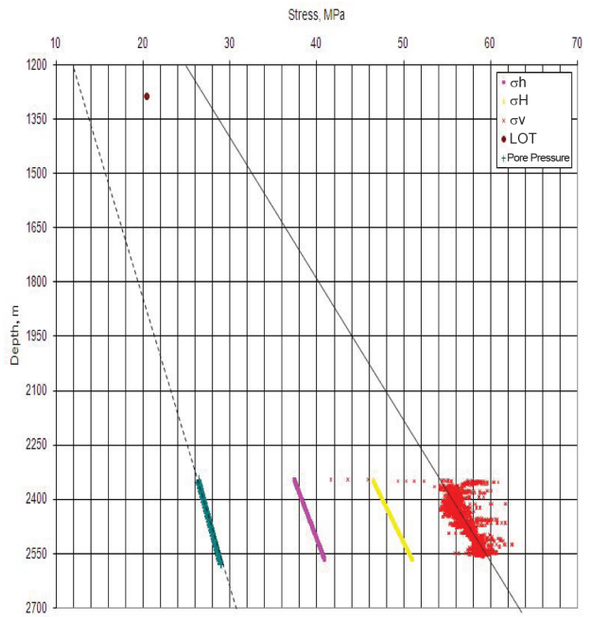


Fig. 7. Stress and pore pressure versus depth, well C64.

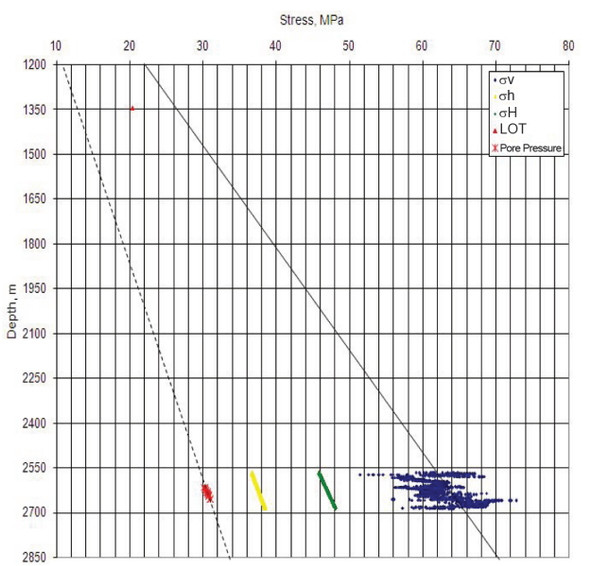


Fig. 8. Stress and pore pressure versus depth, well C80.

pressure. Tables 3 and 4 show the calculated rock mechanical parameters and Tables 5 and 6 show the stresses and pressure form both wells.

The data in these Tables such as in-situ stresses pore pressure gradients, elastic properties and rock strength are taken from the prepared Excel sheets for the depth where borehole breakout starts.

Prevention of wellbore failure requires that the stresses around the wellbore be minimized. An example of the calculations and equations for determining the borehole pressure limits and minimum and maximum mud weight for well C80 are illustrated in Appendix A.

Tables 7and 8 show the minimum, median and maximum mud weight for wells C64 and C80. These tables show that the actual mud weight used in drilling the instable zones in both wells is less than the minimum mud weight (collapse mud weight). Figures 9 and 10 display the profile of predicted minimum and maximum mud weight, the in-situ stresses and pore pressure (expressed in pound per gallon) with depth for both wells.

Table 3. Rock mechanical properties and strength for well C64.

Depth,MD	υ	E, MPa	UCS MPa	T_o	Φ, degree	β
10806 ft,MD 7780 ft, tvd	0.3	13.6	2.5	-	30	60

Table 4. Rock mechanical properties and strength for well C80.

Depth,MD	υ	E, MPa	UCS, MPa	T_o	Φ, degree	β
15565 ft,MD 8421 ft, tvd	0.3	26.1	2.4	-	30	60
15585.5 ft,MD 8432 ft, tvd	0.3	30.1	2.6	-	30	60
15604.5 ft,MD 8442 ft, tvd	0.3	24.1	3.9	-	30	60
16246.5 ft,MD 8789 ft, tvd	0.3	23.2	2.4	-	30	60

Table 5. The principal stresses and pore pressure for well C64.

Depth, MD	σ_v, MPa	σ_H,MPa	σ_h, MPa	Pore pressure gradient, psi/ft
10806 ft,MD 7780 ft, tvd	53.9	46.7	37.6	0.49

Table 6. The principal stresses and pore pressure for well C80.

Depth, MD	σ_v, MPa	σ_H, MPa	σ_h,MPa	Pore pressure gradient, psi/ft
15565 ft,MD 8421 ft, tvd	61.6	45.8	36.7	0.49
15585.5 ft 8432 ft, tvd	66.4	45.9	36.8	0.49
15604.5 ft 8442 ft,tvd	66.9	46	36.8	0.49
16246.5 ft 8789 ft, tvd	65.5	48	38.4	0.49

Table 7. Predicted and actual mud weight for well C64.

Depth	Min. mud weight, ppg	Max. mud weight, ppg	Median mud weight, ppg	Actual mud weight, ppg
10806 ft, MD 7780 ft, tvd	11.97	14.2	12.6	9.3

Table 8. Predicted and actual mud weight for well C80.

Depth, TVD	Min. mud weight, ppg	Max. mud weight, ppg	Median mud weight, ppg	Actual mud weight, ppg
15565ft, MD 8421 ft, tvd	11.06	11.88	11.47	9.3
16246.5ft, MD 8432 ft,tvd	11.09	11.94	11.5	9.3

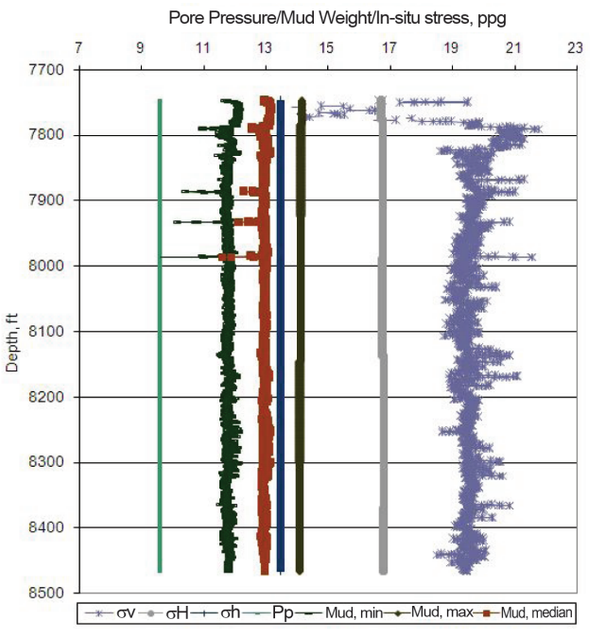


Fig. 9. Mud weight and in-situ profile, C64.

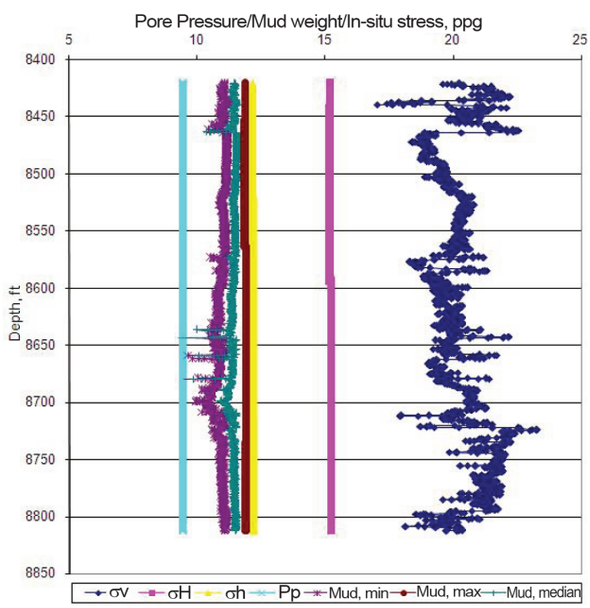


Fig. 10. Mud weight and in-situ profile, C80.

As the drilling operation proceeds, the static mud weight will increase (ECD) as a result of friction pressure which will cause an increase in the borehole pressure (Tables 9 and 10). In order to predict the increase of mud weight while drilling (ECD) different pressure losses are assumed, 200, 300, and 500psi. No ECD measurements are available for both wells to compare with the calculated ECD.

The local stresses around the well bore $ó_{è}$, $ó_z$ and $ó_r$ have been calculated and Tables 11 and 12 show the results at which $ó_{è} > ó_z > ó_r$ for well C64 and C80, respectively.

Table 9. Predicted equivalent circulating density for well C64.

Depth	Mud weight, ppg	ECD, ppg		
		200 psi	300 psi	500 psi
10806 ft, MD 7780 ft, tvd	11.09 (min.)	11.58	11.8	12.3
10806 ft, MD 7780 ft, tvd	12.6 (median)	13.09	13.34	13.8

Table 10. Predicted equivalent circulating density for well C80.

Depth	Mud weight, ppg	ECD, ppg		
		200 psi	300 psi	500psi
15565ft, MD 8421 ft, tvd	11.06 (min.)	11.52	11.76	12.2
16246.5ft, MD 8432 ft, tvd	11.09 (min)	11.55	11.77	12.23
15565ft, MD 8421 ft, tvd	11.47 (median)	11.9	12.2	12.6
16246.5ft, MD 8432 ft, tvd	11.5 (median)	11.96	12.18	12.64

Table 11. The local stresses around the borehole, well C64.

Depth	σ_θ, MPa	σ_z,MPa	σ_r, MPa
10806 ft, MD 7780 ft , tvd	68.24	40.6	33.3

Table 12. The local stresses around the borehole, well C80.

Depth	σ_θ, MPa	σ_z, MPa	σ_r, MPa
15565 ft, MD 8421 ft, tvd	80.41	41.89	33.33
16246.5ft,MD 8432 ft, tvd	86.95	43.42	34.9

CONCLUSIONS

1) Formations of breakout and washout are successfully observed using four arm caliper log data.

2) The key parameters (in-situ stresses and formation material properties) for model construction were derived using density log, sonic log and leak-off tests.

3) Due to the lack of laboratory measurements, impirical relationships where used to derive the unconfined compressive strength.

4) The mud weight window (minimum and maximum mud weight) has been calculated in order to keep the borehole pressure within this window to assure successful drilling operation.

5) The minimum mud weight predicted is higher than the actual mud weight used in drilling through the instable zones for both holes.

6) Minimum and maximum equivalent circulating densities (ECD which represent the borehole pressure

and pressure losses) have been calculated using different assumed pressure losses in both holes.

NOMENCLATURE

ECD: equivalent circulating density.
P_{hyd}: hydrostatic pressure.
ΔP_{fric}: frictional pressure losses.
D: depth
F: applied force.
A: cross sectional area.
Lo: original length.
L: elongated length.
ΔL: the longitudinal strain.
ΔV: change in volume.
Vo: original volume.
εx: lateral strain.
εz: axial strain.
E: Young's modulus.
ν: Poisson's ratio.
G: Shear modulus.
ρ_b: bulk density.
Δts: Shear wave transit time.
ε: strain.
$\sigma x, \sigma y, \sigma z$: Stress tensor as function of location (x,y and z).
σv: vertical stress.
σ_h: minimum horizontal stress.
σ_H: maximum horizontal stress.
g: acceleration of gravity.
P_p: pore pressure.
α: Biot constant.
K_m: rock matrix compressibility.
K_b: bulk rock compressibility.
To: tensile rock strength.
τ: shear stress.
τ: normal stress.
So: Cohesion.
φ: friction angle.
LWD: logging while drilling.
UCS: unconfined compressive strength.
σr: radial stress.
σ_θ: tangential stress.
σz: vertical stress.
θ: azmith angle with respect to minimum horizontal stress.
KCl: Sodium Chloride.
MD: measured depth.
tvd: true vertical depth.
m: meter.
ft: feet.
in.: inch.
C1: caliper one.
C2: caliper two.
V_p: compressional wave.
V_s: shear wave.
$\emptyset$: porosity.
ρ_w: sea water density.
D_w: sea water depth.
LOT: leak-off test.
XLOT: extended leak-off test.
Plot: leak-off pressure.
FIT: formation integrity test.
RFT: repeat formation test.
P_w: borehole pressure.
Co: unconfined Compressive Strength, UCS.
P_f: fluid pressure.

ACKNOWLEDGEMENT

The authors gratefully acknowledge the management of Institute of Pertoleum Enginering, Heriot Watt University for permission to publish this work and would like to thank Dr. Jim Somerville and Prof. Brain Smart for their contributions to the material presented here in.

REFERENCES

[1] Bradley W. B., 1979. Mathematical concept stress cloud can predict borehole failure. *Oil The and Gas Journal, Feb. ed.* .
[2] Zamora M., Broussard P. N. and Stephens M. P., The top 10 mud-related concerns in deep water drilling operations. *SPE* 59019.
[3] Chen, G. and Ewy, R. T., 2002. Investigation of the undrained loading effect and chemical effect on shale stability. *SPE* 78164.
[4] E. Fjaer, R. M. Holt, P. Horsurud, A. M. Raaen and R. Risnes, 1992. Petroleum related rock mechanics, developments in petroleum science, 33.
[5] Walt Aldred, John Cook, Peter Bern, Bill Carpenter, M. Hutchinson, J. Lovell, I. Rezmer and P. Chuleder, Winter, 1998. Using downhole annular pressure measurements to improve drilling performance. *Oil Field Review*.
[6] H. Diaz, S. Miska, N.Takach, M. Yu, 2004. Modeling of ECD in casing, drilling operations and comparison with experimental and field data. IADC/SPE 87149.
[7] Joel D. Walls, M. Turhan Taner, Tom Guidish, Gareth Taylor, David Djmas, Naum Derzhi. North Sea reservoir Characterization Using Rock Physics, Seismic Attributes, and Noval Networks: a case History. Rock Solid Images, Houston, TX.
[8] Hutchinson, M. and Rezmer-Cooper, I., 1998 *Using Downhole Annular Pressure Measurements to Anticipate*

Drilling Problems. *SPE* 49114, SPE Annul Technical Conference and Exhibition, 27-30 Sep., New Orleans, USA.

[9] J. Reinecker, M. Tingay and B. Müller., 2003. *Borehole Breakout Analysis from Four-arm Caliper Logs.* World Stress Map Project.

[10] Tare, U. A. and Mody, F. K., 2002. Managing Borehole Stability Problems. AADE-02-DFWM-OH-31.

[11] Samantha, G, Rama, R, and Toksöz,M. Nafia. *Geomechanical Modeling of In-Situ Stresses Around a Borehole. Massachusetts Institute of Technology*, Cambridge, MA 02139.

[12] Andrew Royle and Sandor Bezdan., 2001. *Shear Wave Velocity Estimation Techniques: A comparison*. CSEG convention,.

[13] Chandong, C., 2004. Empirical rock strength logging in boreholes penetrating sedimentary formations. *Min. Sci. and Geomech*., **7**,3,174-183.

[14] Adrian J. White, Martin O. Traugott and Richard E. Swarbrick., 2002. The use of leak-off tests as means of predicting minimum in-situ stress. .*Petroleum Geosince*, **8**,189-193.

Appendix A

Borehole failure in well C80 (15565 to 15637 ft) MD, (8421 to 8460ft) tvd

The maximum stress is greater than minimum stress: $\sigma_H > \sigma_h$

In case of: $\sigma_\theta > \sigma_z > \sigma_r$

The minimum borehole pressure that failure may occur

$$p_{w,\min} = \frac{2\sigma_h - C_o + P_f(\tan^2\beta - 1)}{\tan^2\beta + 1}$$

$$p_{w,\min} = \frac{2*36.7 - 2.4 + 28(0.89)}{3}$$

$$p_{w,\min} = 33.19MPa$$

To examine the solution the local around the wellbore can be determined as following:

$$\sigma_r = p_w$$

$$\sigma_r = 33.19MPa$$

$$\sigma_\theta = \sigma_h + \sigma_v - 2\cos 2\theta(\sigma_v - \sigma_h) - p_w$$

$\sigma_\theta > \sigma_z e > \sigma_r$

$$\sigma_\theta = 80.41MPa$$

$$\sigma_z = \sigma_h - 2\nu\cos 2\theta(\sigma_v - \sigma_h)$$

$$\sigma_z = 41.89MPa$$

The minimum mud weight can be calculated as follows:

$$\rho_{\max} = \frac{33.19MPa}{9.8\ m/S^2 * 2567m} = 1.32\ gm/cc = 11ppg$$

The maximum borehole pressure and mud weight for impermeable formation:
The maximum borehole pressure for initiating hydraulic fracture in the wellbore wall:

$$p_{w,\max} = 3\sigma_h - \sigma_H - P_p$$

$$p_{w,\max} = 3*36.7 - 45.8 - 28 = 36.3MPa$$

The maximum mud weight from impermeable formation:

$$\rho_{\max} \frac{36.3MPa}{9.8\ m/s^2 * 2567m} = 2.05\ gm/cc = 12.04\ ppg$$

Borehole failure in well C80 (16246.5 to 16370 ft) MD, (8764 to 8856ft) tvd

In case of: $\sigma_\theta > \sigma_z > \sigma_r$

$$p_{w,\min} = \frac{2\sigma_h - C_o + P_f(\tan^2\beta - 1)}{\tan^2\beta + 1}$$

$$p_{w,\min} = \frac{2*38.4 - 3.9 + 29.6(0.89)}{3}$$

$$P_{W,\min} = 34.34MPa$$

$$\rho_{\min} = \frac{34.34MPa}{9.8\ m/s^2 * 2679} = 1.31\ gm/cc = 10.9\ ppg$$

The maximum borehole pressure:

$$p_{w,\max} = 3\sigma_h - \sigma_H - P_f$$

$$p_{w,\max} = 3*38.9 - 48 - 28 = 39.2MPa$$

$$\rho_{\min} = \frac{39.2MPa}{9.8\ m/s^2 * 2679} = 1{,}49\ gm/cc = 12.45\ ppg$$

Petroleum Res. J. Vol. 21 (2008/2009); P. 15–24, 10 Figs.

The Enhancement of Wear Resistance of AISI-316 Austenitic Stainless Steel by Gas Nitriding: Response Surface Analysis and Optimization

Tarek M. Belgasam*, Farag M. Shuaeib* and A. AL-Khatib*

Abstract: Austenitic stainless steels are widely used in industrial applications, mainly due to their good corrosion resistance. However, its low hardness and poor wear performance impose strong limitations in many cases where tribological properties are of prior significance. Nitriding processes has gain acceptance as a technology for surface modification that seems to overcome these problems. In this regard, significant improvements on wear characteristics of stainless steels by gas nitriding have been reported by several workers.. However, previous research attempts on studying the effects of the gas nitriding process parameters on the material performance were made with the old classical method of changing one parameter at a time. This approach is time consuming and did not investigate the interaction effects between the various nitriding parameters. Furthermore, optimization particularly multi-variable type was very difficult to perform. These shortcomings are tackled in the present work by using the Response Surface Methodology (RSM) in the design of experiments (DOE) statistical method. Therefore, this work investigates the wear performance of AISI 316 stainless steel in a designed statistical approach. An austenitic stainless steel type AISI 316 was subjected to gas nitriding processes throughout temperature range of 400 – 600 C^o, nitriding time of 10- 50 hrs and flow rate of ammonia (NH_3) of 100 - 600 liter/hr. Experimental design is first created using composite design method in the response surface methodology. Then gas nitriding and wear tests were performed accordingly. Wear tests were made with an Amsler-Disc- Machine A135 under rolling and sliding conditions. The nitrided layers were investigated using optical microscopy (OM) technique. The phases built-up at the nitrided surfaces were investigated using X-ray diffraction (XRD) method. The microhardness of the nitrided layers was also measured and incorporated in the analysis. Results showed that maximum wear resistance improvement was 93% as compared with the un-nitrided specimen, which is achieved at 528 ^oC for 33 hrs using 260 liter/hr ammonia flow rate. It is also concluded that the RSM is a powerful tool to perform gas nitriding analysis and optimization.

Key words: Ammonia gas nitriding, AISI 316, wear tests. XRD methods, DOE, Response Surface Methodology.

INTRODUCTION

Austenitic stainless steels are well known by their corrosion resistance and, as consequence, are extensively used in chemical, nuclear and food industries. However, they have principal drawbacks, which are low hardness, low wear resistance, and high friction coefficient[1-3]. All these can be summarized as poor tribological characteristics. In the past, different methods have been tried to modify the surface and overcome the weakness mentioned, without affecting the corrosion resistance of the stainless steel. Among those methods, gaseous, salt bath, plasma, and ion beam nitriding methods are dominant. This has been demonstrated by the recent development of various low temperature surface modifications processes (including plasma, ion beam, gaseous and salt bath nitriding methods) and the increasing numbers of academic publications, reflecting rapidly expanding markets in the food, chemical, nuclear and medical sectors. Nitrided parts are being used in various applications such as in the food-processing, biomedical and automotive industries (see Figure 1). In food industry, nitrided stainless steel type 302 piston in a liquid-ammonia pump (in Coca Cola factory) lasted for more than five years when replaced with a piston made of an un-nitrided 300 series alloy that lasted approximately six months. Nitrided stainless steel type 410 cutting

Mechanical Engineering Department, Faculty of Engineering, Garyounis University, Benghazi, Libya., 8B00
elgasam@yahoo.com.

blade showed less wear after completion of five million cuts when used as an alternative of un-nitrided blade, which experienced a normal life of only one million cuts. Also, in another application, nitrided type 321, for a motor shaft used in the aeration of orange juice, exhibits very good life that prolonged nine times increase compared to un-nitrided part[3]. In biomedical sector, the austenitic microstructure of austenitic stainless steel is very important due its superior corrosion resistance and nonmagnetic property. This made it compatible for use in magnetic resonance imaging (*MRI*) systems used as diagnostic tools in the medical field[3]. Furthermore, nitriding can be beneficial in other categories as well, such as automotive parts (engine, transmission, chassis, and accessory components), cold-forming tools, and hot-forming tools. Some special applications include screws and cylinders for plastic extrusion, components for rotary internal combustion engines, and synchronizer components for transmissions are ion nitrided to meet close dimensional tolerances, reduction gears for marine steam turbines, deep-drawing punches and hot-forging dies[1-6].

The research and development of low temperature surface modification of austenitic stainless steels was focused on combining the improvements in wear, and fatigue performance parameters[1-2]. Therefore, this work is part of a comprehensive research program on gas nitriding of austenitic stainless steel, which aims to determine the multi-response (compromise) optimum settings for all performance parameters (Multi-response optimization)[2].

In order to design the experimental program of the present study, a review of the previous work is essential. Even though this research work is focused on the conventional gas nitriding, other process that would produce similar effects is included in this review. This will assist in the nitriding process conditions estimation and will assist in process understanding. In this regard, Ozbaysal[7] studied the structure and properties of ion-nitrided layers on AISI 321 austenitic stainless steel, AISI 410 martensitic stainless steel, and AISI 430 ferritic stainless steel, under varying process conditions. Microhardness-depth correlations, optical microscopy and transmission electron microscopy were used in the analysis. The process variables studied include time (2 - 10 hrs) and temperature (400 - 600 ^{o}C). He found that the highest case depth values and hardness levels were observed in martensitic stainless steels, the lowest case depths were observed in austenitic stainless steel. All three steels showed increasing case depths and decreasing surface hardness with increasing ion-nitriding temperatures and times. Nitriding depth was found to be parabolic with ion nitriding time in all three steels at all ion-nitriding temperatures investigated. Electron microscopy showed that almost no structural difference arises in the core of ferritic and austenitic stainless steels whereas recrystallization of the martensitic structure was observed in the core of martensitic steel following ion nitriding. Kuawahara[8] made comparative study between plasma nitriding and ammonia gas nitriding of austenitic stainless steel type

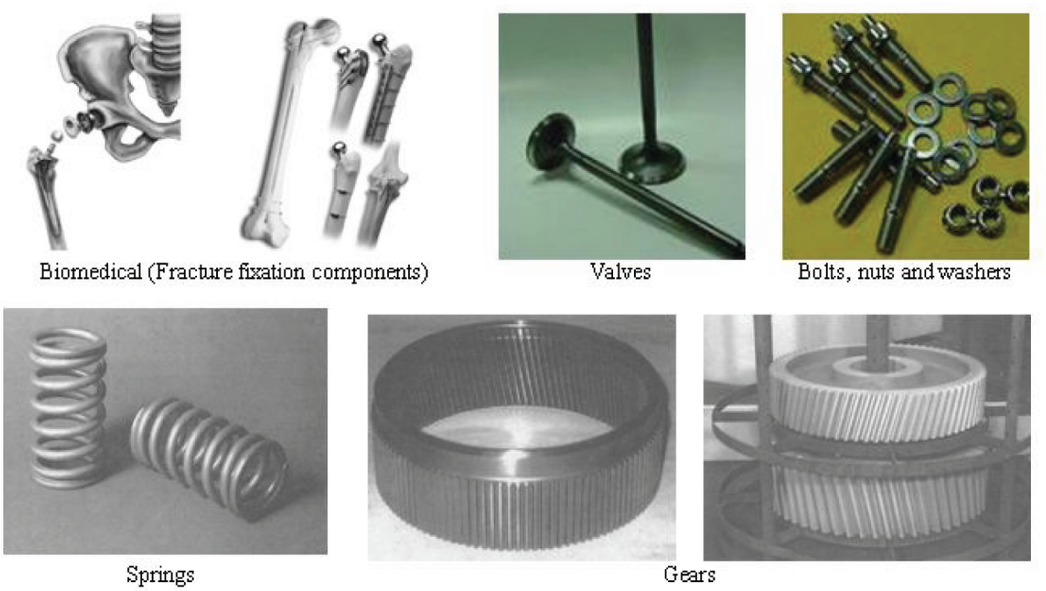


Fig. 1. Nitrided stainless steels parts.

Fe-18Cr-9Ni. Both plasma and gas nitriding were compared with respect to the growth rate of nitrided layer. He concluded that the growth rate of nitrided layer in the plasma nitriding of stainless steel type Fe-18Cr-9Ni is 1 to 2.5 times that in case of gas nitriding. However, his comparison was based on layer growth rate, which cannot be considered as strong indicator for the tribological characteristics of the nitrided stainless steel.

Wei[9] presented the results of a comparative study of beam ion implantation (BII), plasma ion nitriding (PII) and gas nitriding of AISI 304 stainless steel. He concluded that, under controlled conditions (the same treatment time of 30 to 60 min and the same treatment temperature 400°C), the microstructure produced by all techniques are similar. However, the concentrations and nitrogen detectable depths of the nitrogen-enriched layer are significantly different, depending on the process. Both BII and PII produce a thick nitrogen-enriched layer (with higher concentration) compared with gas nitriding. Again, the effect of the nitrogen-enriched layer thickness on the tribological characteristics of the nitrided stainless steel was not investigated. Finding a compromise between increased hardness, increased wear resistance and retained corrosion resistance using nitrogen plasma immersion ion implantation (PIII) on austenitic stainless steel AISI 316 at a treatment temperature of 380°C was investigated[10]. The depth and the distribution of the implanted nitrogen and the phase composition were analyzed with glow discharge optical spectroscopy (GDOS) and X-ray diffraction (XRD). Compared to untreated material, he found that the hardness can be increased up to factor of four and the wear behaviour was improved by 1-2 orders of magnitude. Only a very small fraction of chromium nitride, which is not detrimental to the corrosion resistance, was observed with XRD.

Bell[5] overviewed the development of low temperature thermo-chemical surface modification processes. He reported that the surface hardness and wear resistance of the austenitic stainless steels could be much improved without lowering its corrosion resistance by low temperature nitriding. Menthe[11] investigated the influence of the plasma nitriding process on the mechanical properties of austenitic stainless steel. He conducted plasma nitriding process on AISI 304 steel in a temperature range of 375-475°C using pulsed-DC plasma with different N_2-H_2 gas mixtures and treatment times. He found that the wear resistance significantly increased even at higher loads compared to the untreated material and in the same time, the microhardness of nitrided layers had increased by factor of five as compared untreated material. Menthe's work was focused on the wear and microhardness characteristics and does not mention any thing about corrosion resistance issues. However, the main point which can be obtained from his work, is that wear resistance can be improved by plasma nitriding at low temperature (as low as 375°C). Baranowska[12] studied the morphology of the nitrided layers produced on austenitic steel and their mechanical and tribological behaviour. Using MFM, TEM and XRD techniques, he found that the coatings produced have complex multilayer structures. The specific wear rate was measured using a pin-on-disk test method consisting of an alumina sphere (99.6% Al_2O_3, hardness 1800HV, roughness 0.025-ìm Ra) of diameter 6mm±0.25-ìm sliding against the flat nitrided austenitic steel samples. He found that the low temperature gas nitriding combined with appropriate pre-treatment makes it possible to obtain surface layers with very complex morphology similar to those produced by plasma treatments. Furthermore, he found that by changing the conditions of the gas nitriding parameters, layers with various phase compositions could be obtained. Finally, he concluded that the mechanical properties of the layers are mainly related to nitrogen content and for all kinds of obtained phase compositions the mechanical properties were at least the same as for typical gas-nitrided layers obtained at higher temperature and containing chromium and iron nitrides. Therefore, Baranowska's work confirms the low temperature nitriding benefits and that gas nitriding can produce layers with comparable properties with other more advanced techniques. Ionara[13] presented results of wear tests performed on AISI 316L stainless steel samples nitrided with DC-pulsed plasma equipment for 20 hrs at 400ºC in plasma formed with 25% N_2+75% H_2. The wear tests were made with an Amsler-Disc-Machine A135 under rolling and sliding conditions. The surface and subsurface were studied by optical microscope (OM) and microhardness. Wear debris generated under dry rolling-sliding condition were observed by scanning electron microscope (SEM). The results showed that plasma nitriding significantly improves the wear resistance of the surface of the austenitic stainless steel. However, Ionara work could be more beneficial if parametric studies and process optimization were performed.

Bielawski[14] conducted nitriding process on

chromium steel at a temperature range of 400 – 500 °C in ammonia gas atmosphere. The microstructure of the resulted layers was investigated using scanning electron microscopy (SEM) and light microscopy analysis (LMA) techniques. Its phase build-up was checked by XRD methods, and the thickness and microhardness of the layers were measured. It was found, that it is possible to obtain layers with good mechanical properties (microhardness) and good corrosion resistance (microstructure). Moreover, it was possible, by gas nitriding treatment, to obtain uniform layers at low temperature processing. He found that by nitriding at temperature below 500°C, the obtained layers remained white after etching, which suggested their good corrosion resistance (as they resisted the acidic effect of the etching agent). All the obtained layers showed very good mechanical properties (high hardness) corresponding to a very high nitrogen content in the layers.

In summary, the previous work on gas nitriding process of stainless steel showed that the wear properties of the austenitic stainless steels could be significantly improved after nitriding depending upon the treatment conditions. In addition, there is a common conclusion that low-temperature nitriding is preferable to high-temperature nitriding from corrosion resistance point of view. However, there is no an overall agreement on the effect of other process conditions such as ammonia flow rate or time of nitriding. Furthermore, previous research work was performed using the classical methods of changing one factor at a time while holding the other factors. This methodology requires a lot of specimens and extensive experimental work, which is both costly and time consuming. In addition, the classical method is not capable of investigating the interaction effects between the factors and cannot be used to perform experiment optimization. All these drawbacks are tackled by using the response surface methodology (RSM) in the design of experiment statistical methods. Therefore, in this work an austenitic stainless steel material type AISI 316 is subjected to a conventional gas nitriding process throughout a temperature range of 400–600 ^{o}C, a nitriding time of 10-50 hrs and ammonia (NH_3) flow rate of 100-600 liter/hr; and the wear behaviour of the nitrided specimens were then examined. The ranges of processing parameters (Temperature, time, and flow rate) were estimated based on the previous literature review and few preliminary trials. Conventional gas nitriding is adopted in this research work, because it is cheap and does not require very highly skilled technicians. In addition, it can be used for mass production of industrial and biomedical parts with all sizes and shapes.

MATERIALS AND METHODS

The material used for this investigation was austenitic stainless steel type AISI 316 with a chemical composition shown in Table 1.

The as received material microstructure was fully austenitic and its hardness was 200 HV. The as received material was then stress relieved for 3 hrs at 1100 ^{o}C in nitrogen atmosphere then oil quenched to avoid oxidation. The wear test specimens were fabricated in accordance with Amsler-Disc-Machine A135 specimens' requirements. Specimens were prepared with the shape of discs, 38mm diameter and 10mm thickness machined from annealed stainless steel bar. All specimens were subjected to a pickling pre-treatment using a hot hydrochloric acid (70 ^{o}C and 50%) for oxide film breaking as required by nitriding process. Specimen shape and dimensions are shown schematically in Figure 2 and the physical specimens after nitriding in Figure 3.

Table 1. Chemical composition of AISI 316 austenitic stainless steel used in the experiments.

Alloying element	C	Mn	P	S	Si	Cr	Ni	Mo
Wt.%	0.08	1.53	0.023	0.024	0.69	16.4	10.4	2.00

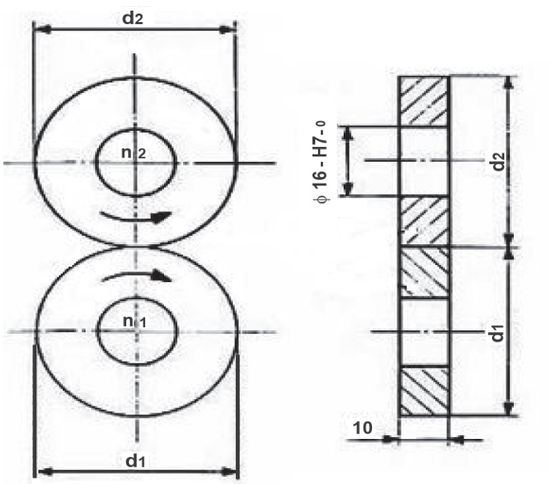


Fig. 2. Rolling and sliding wear test specimen's shape and dimensions.

The response surface methodology (RSM) was then employed to determine the required points of experiments (design points) within the previously mentioned ranges of nitriding temperature, nitriding time and ammonia flow rate. The resulted matrix is shown in Table 2. Anhydrous ammonia gas was used to accomplish the gas nitriding processes. The nitriding processes were conducted using a SIB Furnace (pit furnace type 752) shown in Figure 4.

Table 2. RSM matrix of gas nitriding process with results of wear resistance and microhardness. experimental program.

Exp. No	Time (hrs)	Temperature (^{o}C)	Flow rate (litre /hr)	Wear resistance (relative weight loss) %	Microhardness ($HV_{200\ gr.}$)
1	30	500	350	7	1298.0
2	18	441	201	49	339.9
3	10	500	350	47	458.4
4	42	441	499	52	633.3
5	18	559	201	22	1080.0
6	30	500	100	9	973.0
7	42	559	499	18	1010.0
8	50	500	350	25	1089.0
9	30	500	600	26	915.5
10	42	559	201	12	1061.0
11	30	600	350	23	1081.4
12	30	400	350	71	312.9
13	42	441	201	37	647.0
14	18	559	499	29	1001.0
15	18	441	499	62	388.1
16	30	500	350	9	1118.7
17	30	500	350	8	1166.8



Fig. 3. Wear test specimen after nitriding.

The wear tests were performed on an Amsler Disc-Machine model A 135 shown in Figure 5a. The arrangements of samples are as shown in Figure 5b, where the top sample rotated at 200 rpm and. The bottom sample rotated at 220 rpm to obtain 10% sliding. The wear tests were performed under 500 N load and the wear tests duration was fixed to 2 hours for all specimens. After wear test, the specimens were cleaned with alcohol and acetone using an ultrasonic bath; the specimens were weighted with an ADAM type AAA 260 LE balance (0.0001g sensitivity). After wear test completion, the preparation of specimens for metallography was made by cutting them parallel to the rotation plane (longitudinal) and in a transverse direction. The specimens were then polished up to grade 0.3ì and etched (at room temperature) in an aqueous solution of $FeCl_3$ and NITAL 2% solution (2 ml nitric acid + 98 ml ethanol) to reveal the thickness of nitride layer and the microstructure.

The specimens were examined by optical microscopy (OM). In addition, X-ray diffraction analysis of nitrided surface was performed using a Philips X-ray diffractometer (type PW 1800) with a Cu-radiation. A two theta (2è) range of 2^{o} to 80^{o} was selected with step 0.02^{o}. The hardening effect of the nitrided layer was evaluated by surface hardness measurements using the conventional Vickers micro-hardness technique. Microhardness testing was carried out under an indentation load of 200g. The microhardness measurements were made normal to the surface and on transverse sections of the samples using an equipment Leica VMHT (type 302801) apparatus.

RESULTS AND DISCUSSION

For each wear test, two specimens of each nitriding process were used, and their corresponding weight loss relative to un-nitriding material for wear resistance is determined. Furthermore, the nitrided layers microhardness was measured. The obtained results of the wear resistance of nitrided specimens are entered into the previously created design matrix and then analyzed using the RSM. The wear resistance (weight loss relative to un-nitriding material, the wear %) and the microhardness ($HV_{200gr.}$) of nitrided specimens are presented in Table 2.

As shown in Table 2, generally, for all nitriding processes performed, the wear resistance significantly improved as compared with un-nitriding

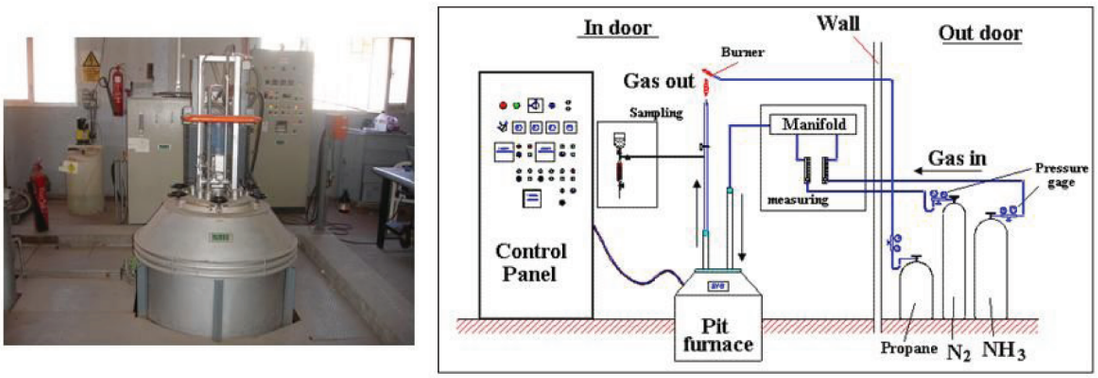
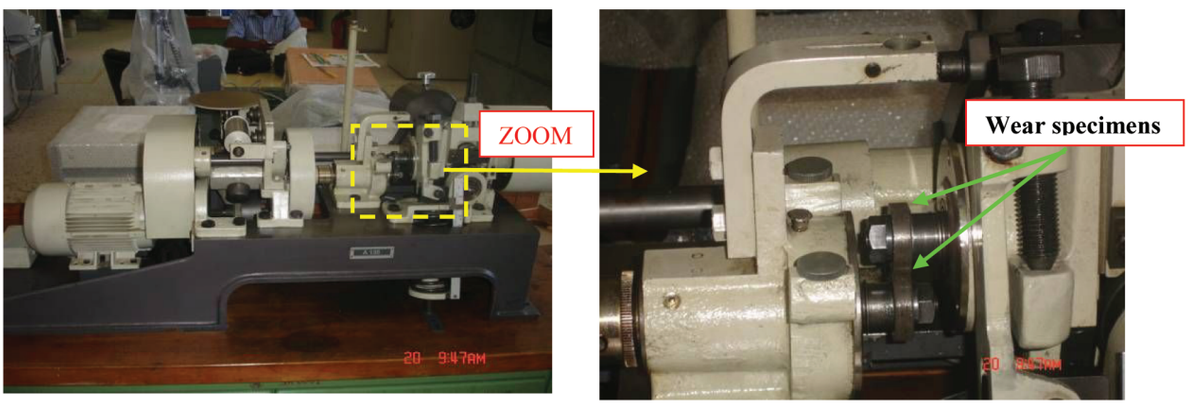


Fig. 4. The SIB Furnace (pit furnace type 752).



(a) (b)

Fig. 5. Photographs showing an Amsler machine model A135 Wear Testing Machine, (a) overall shape of the wear apparatus, (b) zoomed to illustrate the specimens postions.

material. High and low wear resistances were obtained around nitriding process No.1and No.2, respectively. In addition, Table 2 shows the highest and the lowest values obtained from No. 1 and No. 2 nitriding process. Detailed analysis of these results is provided in a separate section hereafter. The point of maximum wear resistance and microhardness (point No.1) will be considered from the microstructure analysis point of view. Further layer thickness and microstructural analysis is provided in another publication. Therefore, Figure 6 shows an optical microscopy (OM) micrograph of a cross section of nitrided specimen (nitriding process No.1 of Table 2). The layer appears uniform and continuous with a total layer thickness of 72 ìm and the diffusion zone can easily be distinguished from the substrate. Figure 7 shows a typical microhardness profile of a sample cross section (nitrided sample experiment No.1 in the design matrix of Table 2). The sharp transition from the high hardness in the surface to the low hardness of the substrate can be observed which is associated with the presence of the nitrided layer.

Figure 8 shows X-ray diffraction patterns for the same nitriding process No 1. The detected chromium nitride (Cr N) is the most responsible for the increased hardness and wear resistance. Ion nitride ã'-Fe_4N is shown, However, the most interesting phase appearing in the nitriding layer is the expanded austenite phase ($ã_N$), which is named after the lattice expansion of the original austenite lattice, as indicated by a shift of X-ray diffraction peaks towards smaller diffraction angles. This phase is reported to retain the corrosion resistance of the nitrided material[2]. Therefore, its presence in the nitrided layer of the maximum wear resistance specimen as depicted by the XRD analysis is a significant indication on the good efficiency of the nitriding process.

Parametric Study

The results of Table 2 were analyzed using response surface methodology (RSM), and the interactions of nitriding processing parameters (nitriding temperature, nitriding time and ammonia flow rate) were identified. The effects of nitriding

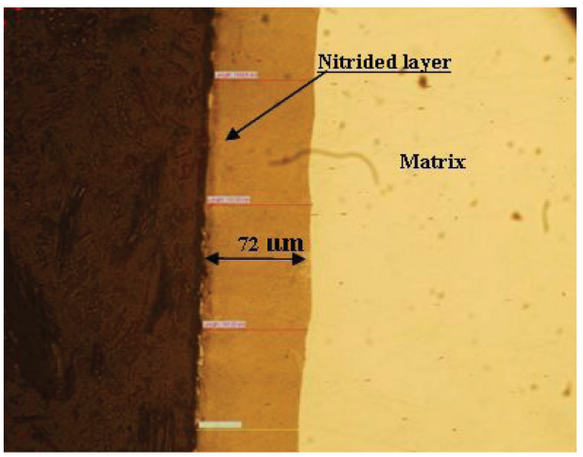


Fig. 6. Optical micrographs (OM) of a nitrided layer of AISI 316 (process No.1).

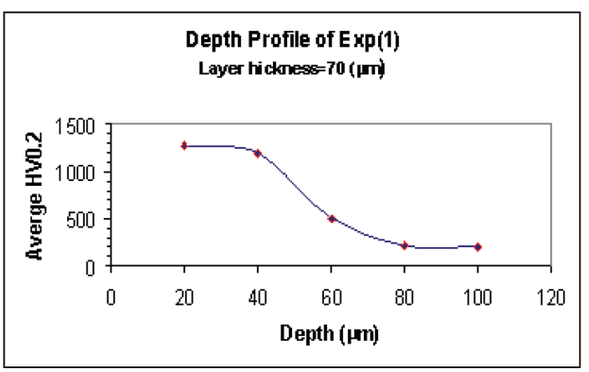


Fig. 7. Hardness profile across the nitrided layer (nitriding process No.1).

processing parameters on wear resistance are shown in three-dimensional graphs and contours in Figure 9a, b, c, d, e, and f. It is clear that an optimum region for the wear resistance do exist (Figs. 9a and b). This is evident from both the decreasing contour circles and the downward curvature of the 3D surface plot. More specifically, referring to Figure 9a, the time and temperature, which provide optimum region of wear resistance (less than 13.991%), is about 32 hrs and 535 ^{o}C respectively. This is also shown in the 3D surface plot of Figure 9b. However, these plots need to be correlated with the other graphs for conclusions. Figure 9c shows the effect of the time and the flow rate on the wear resistance. As shown the time and the flow rate, which provide optimum (minimum wear) region of wear resistance (less than 15%) is about 34 hrs and 260 l/hr respectively. This is also agrees with the 3D surface plot of Figure 9d. However, these plots need to be correlated with the other graphs for conclusion as well. Figure 9e, shows the effect of the temperature and the flow rate on the wear resistance. As shown the temperature and the flow rate, which provide optimum region of wear resistance (less than 18%) is about 530 ^{o}C and 300 l/hr respectively. This is also agrees with the 3D surface plot of Figure 9f. These plots have provided a comprehensive view on the parameters effects and an optimization plot will further confirm these findings,

Response Optimaztion (Minmum Wear)

A third and comprehensive method of presenting the nitriding process parameters effects is by developing the optimization chart of the wear resistance with the nitriding conditions, which is shown in Figure 10. This Figure shows the optimization chart for the performed wear tests on the gas nitrided specimens. The optimization result is shown in the lift column; while the optimum setting of each parameter is shown at meddle of the top row. The behaviour curve of each factor is shown hereunder. As shown, the optimum nitriding time is 33.4 hrs, the optimum temperature setting is 528.2^{o}C and the optimum gas flow rate setting is 260 liter/hr, which resulted in minmum wear of 1.98%. This achievement means that by setting the nitriding conditions to the previous values, a material with an optimum wear resistance will be produced (1.98% wear as compared with the 100% wear of the un-nitrided samples). Furthermore, up to the authors' knowledge, the optimum 33 hrs nitriding times and the 260 l/hr ammonia gas flow rate have not been mentioned in the previous work, which is considered as a further contribution

CONCLUSIONS

From this study, we can conclude that:

- The ammonia gas nitriding, if suitably performed, can improve the wear resistance of austenitic stainless steel type AISI 316. From the results of this study, the considered nitriding process parameters were nitriding temperature, nitriding time and ammonia flow rate and the two dominate factors found to be the nitriding temperature, and the nitriding time, while the ammonia flow rate was found to be of less significance.
- The maximum wear resistance experimentally obtained was 93% (point No.1 in Table 2) as compared with the un-nitrided specimens and the RSM optimization predicts that an optimum wear 1.98% (H" 98% wear resistance) as compared with

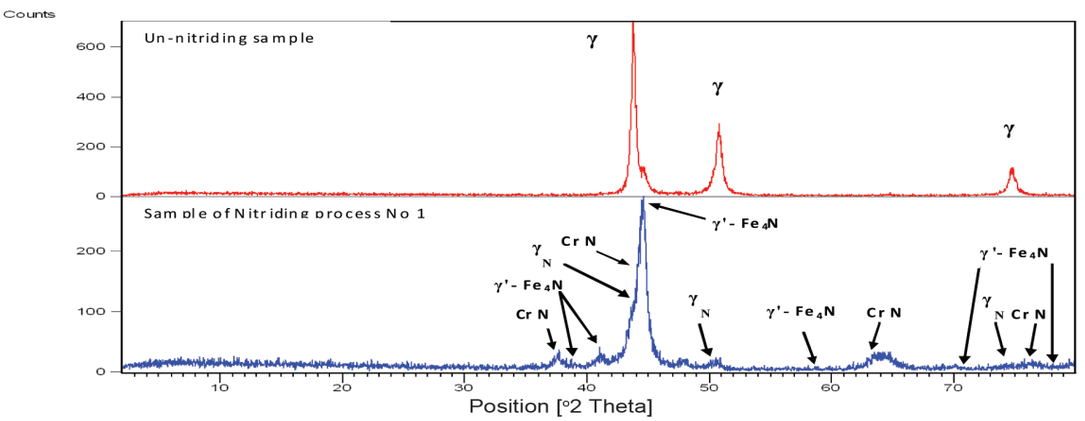


Fig. 8. X-ray diffraction patterns of a nitrided layer of nitriding process No. 1.

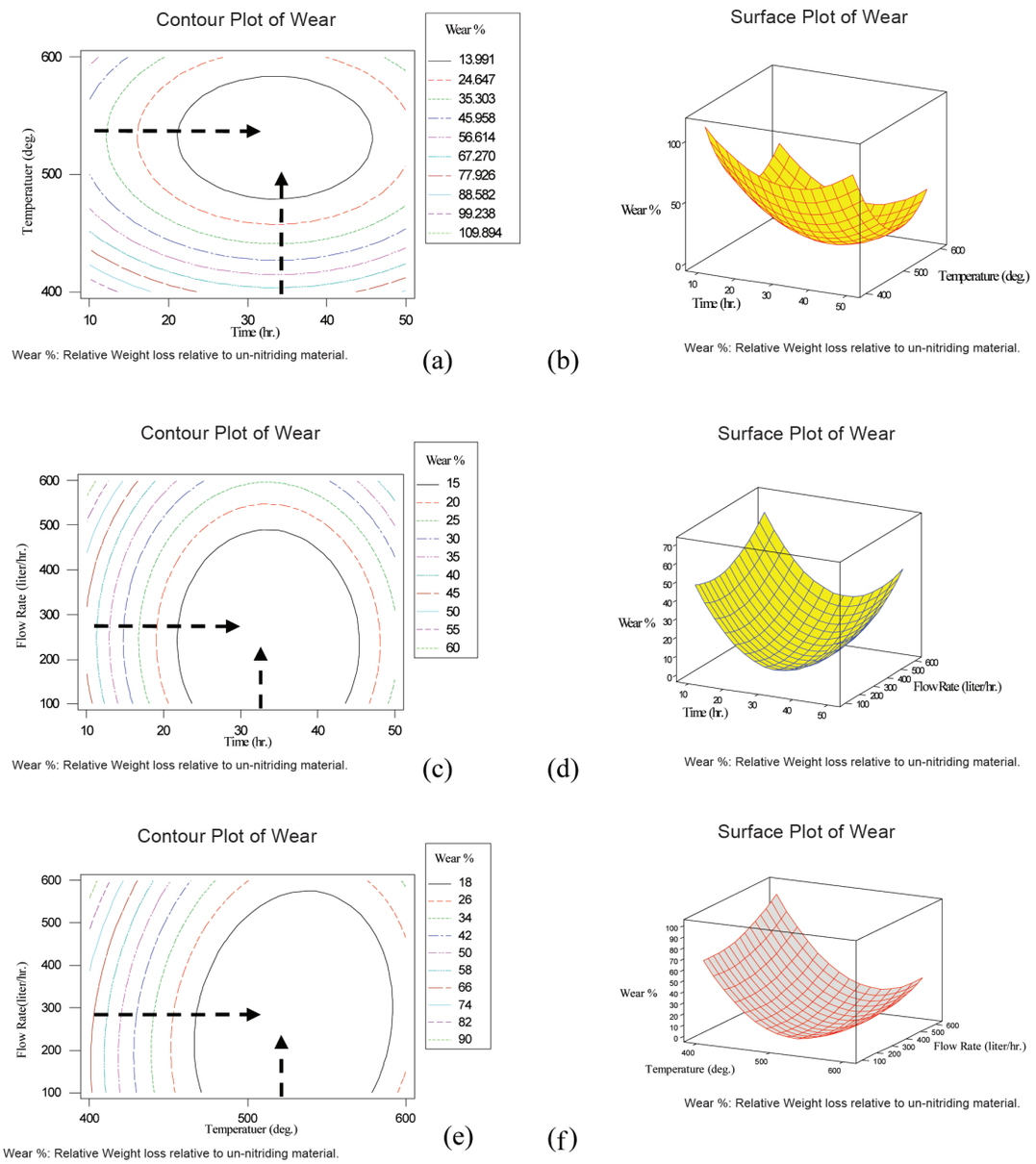


Fig. 9. Effects of nitriding processing parameters on wear resistance (MINITAB).

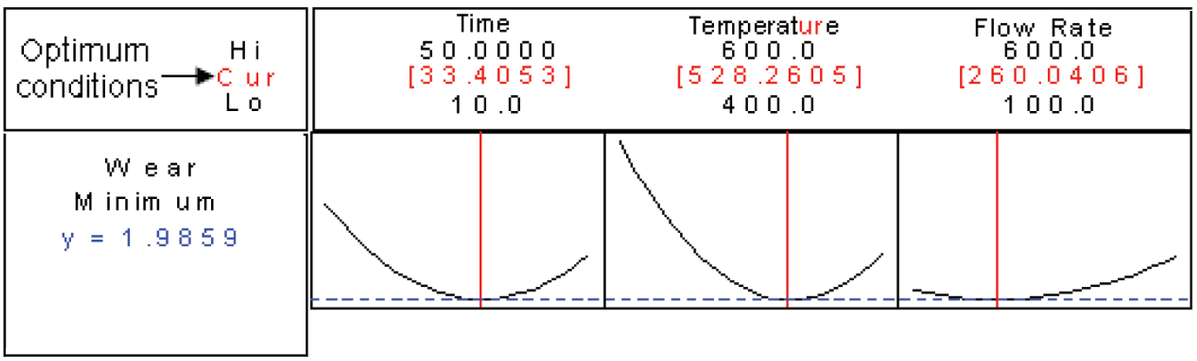


Fig. 10. Optimum nitriding conditions for minimum wear (1.9859 %).

the 100% wear of the un-nitrided specimens could be achieved at 528°C nitriding temperature for 33.4 hrs using 260 liter/hr ammonia flow rate.

- Gas nitriding of AISI 316 stainless steel has been shown to produce the ($\tilde{a}_N$) S-phase. This is reported to improve both corrosion and wear resistance of the of AISI 316 steel. However, a compromise between the wear and corrosion resistance can be achieved by controlling the nitriding process to produce a material suitable for the intended application.

ACKNOWLEDGEMENTS

The authors are thankful to all staff of the Libyan Technical Research Centre-Mechanical Research Branch, and the Libyan Petroleum Institute, Tripoli, for their help and co-operation throughout this research program.

REFERENCES

[1] Michel, J. Korwin, Christopher, D., Morawski, , George J. Tymowskie, and Witold, K. Lilental, 2004. Design of Nitrided and Nitrocarborized Materials. In; *Metallurgical Design Handbook,* Chap.14, by George, E. Totten, Kiyoshi Funtani, and Lin Xie,Marccl Deker Inc, (USA).

[2] Tom Bell, and Katsuya Akamatsu, 2001. *Stainless Steel 2000: Thermochemical Surface Steel*. Published by W.S. Maney and Sons Ltd. UK.

[3] The American Society for Metals (ASM), 1994. *Surface Engineering Handbook*, (Ohio, USA), **5**.

[4] The American Society for Metals (ASM), 2004. *Metallography and Microstructures Handbook* (Ohio, USA), **9.**

[5] Bell,T., 2002. Surface Engineering of Austenitic Stainless Steel. *Surface Engineering,* **18,** No. 6, 415-422.

[6] Lakhtin, Yu. M. and Kohen, Ya.D.1982. *Structure and Strength of Nitrided Alloys.* Metallurgical, Moscow, chaps.1, 2 and 7, in Russian.

[7] Ozbaysal, K. and Inal, O.T., 1986. Structure and properties of ion-nitride stainless steels. *Journal of Materials Sience*, **21**, 4318-4326.

[8] Kuawahara, H., Matsuoka, H., Takada, J., Kikuchi, S., Tomii,Y. and Tamura, I., 1991, Plasma nitriding of Fe-18Cr-9Ni. *Oxidation of Metals*., **36**, No.1-2, 143-156.

[9] Wei, R., 1996. Comparative study of beam ion implantation, plasma ion implantation, and nitriding of AISI 304 stainless steel. *Surface and Coating Technology*, **83**, 235-242.

[10] Mandl, S., Gunzel, R., Richter, R. and Moller,W., 1998. Nitriding of austenitic stainless steel using plasma immersion ion implantation (PIII). *Surface and Coatings Technology*, **100-101**, 372–376.

[11] Menthe, E., Bulak, A., Olfe, J. and Zimmermann, A., 2002. Improvement of the mechanical properties of austenitic stainless steel after plasma nitriding. *Surface and Coatings Technology*, **133-134,** 259–263.

[12] Baranowska, J., Franklin, S. E., and Pelletier, C. G. N., 2005. Tribological behaviour and mechanical properties of low temperature gas nitrided austenitic steel in relation to layer morphology. *Wear*, **259,** 432–438.

[13] Cabo, A., Ionar, S. A., Arias 3422, C1430 CRB Buenos Aires, Argentina ,E. De Las Heras, P. A. Corengia, F. Walther- National Institute of Industrial Technology, C.C. 157, San Martín, Argentin , S. Brühl- National University of Technology, 3260 Concepción del Uruguay, Argentina, http://www biblio.inti.gov.ar/textos/304507.pdf

[14] Bielawski, J., Baranowska, J. and Szczecinski, K., 2005, Microstructure and properties of layers on chromium steel. *Surface and Coatings Technology*, **200** (2006) 6572–6577.

[15] MINITAB, 2003. *Statistical Software Version 13:* User Guide II, USA.

Petroleum Res. J. Vol. 21 (2008/2009); P. 25–38, 19 Figs.

Development of Low and High Chromium Alloyed Creep Resistance Steels for Power Plants and Related Applications

Yousef Elarbi* and Bela Palotas**

Abstract. The development of power plant technology towards larger and more efficient units is linked to the development of Cr alloyed creep resistant steels. These steels that are mainly used in power generating and petrochemical plants, have improved successively by introducing new alloying elements and new microstructures. Around the 1940s, molybdenum was added to low chromium steels such as 2.25 Cr 1Mo to improve their application temperature to about 560 ºC. Niobium that is contained in all the latest high strength steels, which belongs to the group of 9-12% Cr steels, has been one of the most successful new elements. The use of these steels allows the design of power plants with steam temperatures up to 625 °C. Furthermore, ferritic steels are currently under development for steam temperatures of 650°C and more.

Another recent development of the creep strength of creep resistant martensitic steels at higher temperatures was introduced by partial replacement of molybdenum by tungsten such as grade T23, NF616 (T92) and HCM12A (T122). This improvement in creep strength led to the raising of the operating temperatures of power plants using these new grades of steels, resulting in energy savings and reduction of the environmental impact. In addition to high creep strength other material properties are also important, e.g. hardenability, corrosion resistance, and weldability. All product forms of these steel grades such as large forgings and castings are used to build turbines, whereas tubes, pipes, plates and fittings are the typical products for application in pressure vessels, boilers and piping systems.

Keywords: Creep resistant steels, creep strength, oxidation resistance, piping, turbine rotors.

INTRODUCTION

For decades scientific researches into fossil-fired power plants have been carried out through a lot of scientific researches in many countries. These researches have indicated that due to the use of carbon steel as a construction material by the 1920's, the maximum operation limits on steam were at 4 MPa and 370°C. When Mo was added to the steel, the operational conditions were raised to 10 MPa and 480 °C. In the 1940's, the use of Cr-Mo steels allowed operational conditions of 17 MPa and 566°C[1]. Around that time, 2.25Cr-1Mo (T22) and 9Cr-1Mo (T9) steels were introduced for power plant applications, and T22 is still used extensively up to about 538ºC. Over the years, 2.25-3Cr steels with improved properties compared to T22 have been developed. The most recent developments occurred in the 1990s and involved 2.25Cr steels in which the replacement of molybdenum by tungsten was used to develop the steel grade T23 with a nominal composition of (Fe-2.25Cr-1.6W-0.1Mo-0.25V-0.05Nb-0.45Mn-0.20Si-0.003B-0.06C).

Another development was a 2.25Cr-1Mo-0.25V-0.3Si-0.50Mn-0.07Ti-0.005B-0.08C steel (T24) with strength somewhat inferior to that of T23. There has been continued emphasis on higher-operating temperatures for improved efficiency, since increased efficiency generates energy savings and reduces environmental impact. For some applications, this has meant switching to steels with better high temperature performance, such as modified 9Cr-1Mo (T91) developed in the 1970s as an improvement of T9 by the addition of V, Nb, and N to induce the formation of stable carbides, nitrides, and carbonitrides. More recently, steels such as NF616 (T92) and HCM12A (T122) have been developed; these are modifications

*Department of Materials Science and Engineering, Budapest, University of Technology and Economics, H-1111. Budapest, Bertalan L u.7. Tel: 0036-70-5795922,
e-mail: binyusef@yahoo.com
**Department of Materials Science and Engineering, Budapest University of Technology and Economics, H-1111. Budapest, Bertalan L u.7. Tel: (1) 463 1115, e-mail: palotasb@eik.bme.hu

of T91 that involve the replacement of some of the molybdenum by tungsten. For applications at temperatures 600 ºC, the advantages of low-chromium bainitic steels, especially in welding, have made them the continued choice[2].

Table 1 presents an overview on the creep resistant ferritic steels which are used in power plants for tubing and piping. The list of steels can be subdivided into C-Mn steels (No. 1and2), Mo steels (No. 3 and 4), low alloyed Cr-Mo steels (No. 5-9), and 9-12 % Cr steels (No. 10-15). Because of the large number of different steel grades, only a few typical representatives of each group could be included in the Table. The steel grades have been listed according to increasing content of alloying elements where the chemical composition becomes increasingly complex.

As can be seen from Table 1, niobium has been an important element and niobium bearing steels are found in each group. The complexity of chemical composition is reflected by a complexity in microstructure. Different hardening mechanisms have been used to achieve an optimized product. As a result, the creep rupture strength has been raised by a factor of about 10 as shown in Figure 1[3].

The aim of this paper is to overview the historical improvements of the mechanical properties (mainly creep strength) of creep resistant martensitic steels at elevated temperatures and the effect of these developments on the application of these steels in the power and petrochemical plants.

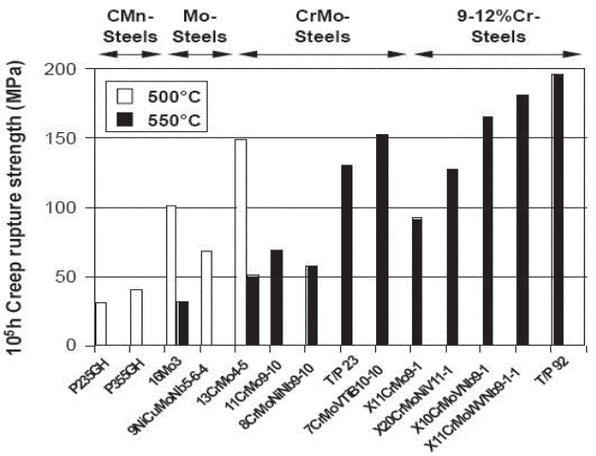


Fig. 1. Creep rupture strength of heat resistant steels for tubes and pipes.

OVERVIEW ON CREEP RESISTANT FERRITIC STEELS

C - Mn Steels

Steel grade P235 can be regarded as typical C-Mn steel having a ferrite pearlite microstructure. C and Mn contents are the major factors influencing the strength properties. Figure 2 shows a plot of the minimum 0.2% proof strength values together with the average 10^5 h creep rupture strength as function of temperature. The European design codes are based on minimum proof strength values at low and creep rupture strength values at high temperatures. Both regimes are separated by

Table1. Chemical composition of Cr-alloyed steels[3].

Steel Designation	Chemical composition (wt. %)										
	C	Si	Mn	Al	Cr	Ni	Mo	V	Nb	B	Others
13CrMo-4-5 (T/P11)	0.1-0.17	0.1-0.35	0.4-0.7	max 0.04	0.7-1.1		0.45-0.65				
11CrMo-9-10 (T/P22)	0.08-0.15	0.15-0.4	0.3-0.7	max 0.04	2.0-2.5		0.9-1.2				
8CrMoNiNb-9-10	max 0.1	0.15-0.5	0.4-0.8	max 0.05	2.0-2.5	0.3-0.8	0.9-1.1		min 10×%C		
7CrMoVTiB-10-10 (T/P24)	0.05-0.1	0.15-0.45	0.3-0.7	max 0.02	2.0-2.6		0.9-1.1	0.2-0.3		0.0015-0.007	0.01N 0.07Ti
7CrWVMoNb-9-6 (T/P23)	0.04-0.1	max 0.5	0.1-0.6	max 0.3	1.9-2.6		0.05-0.3	0.2-0.3	0.02-0.08	0.0005-0.006	0.03N 1.6W
X11CrMo-9-1 (T/P9)	0.08-0.15	0.25-1.0	0.3-0.6	max 0.04	8.0-10.0		0.9-1.0				
X20CrMoNiV-11-1	0.17-.0.23	0.15-0.5	max 1.0	max 0.04	10.0-12.5	0.3-0.8	0.8-1.2	0.23-0.35			
X10CrMoVNb-9-1 (T/P91)	0.08-0.12	0.2-0.5	0.3-0.6	max 0.04	8.0-9.5	max 0.4	0.85-1.05	0.18-0.25	0.06-0.1		0.05N
X11CrMoWVNb-9-1-1	0.08-0.13	0.1-0.5	0.3-0.6	max 0.04	8.5-9.5	0.1-0.4	0.9-1.1	0.18-0.25	0.06-0.1	0.0005-0.005	0.07N 1.0W

the intersection of the proof strength with the creep rupture strength curve. In the case of P235 the intersection point is around 420°C.

Above this temperature, a design becomes time dependent because the lifetime of a component is limited by the creep process. An interesting modification of P235 is the Nb- bearing grade P355. The proof strength values could be raised considerably as a result of Nb- addition due to grain refinement. However, the increase of creep rupture strength is rather small. This increase can be attributed mainly to the increase of Mn, which is a solution hardening element. Since proof and creep rupture strength have not increased by equal amounts, the intersection point between the creep and proof strength regime is shifted to 400°C. The advantage of P355 clearly lies in the application below this temperature.

Mo Steels

A similar effect can also be seen for the Mo-steels, which are also represented in Figure 2. These steels are basically of the same type with about 0.3% Mo, which is a strong solution hardening element. The solution hardening effect is the main cause for the increase of creep rupture strength, which is similar for both steels. Grade 9NiCuMoNb5-6-4, also well known as WB 36, shows a dramatic increase of proof strength, which again is partly caused by the grain-refining effect of Nb[3]. In addition, hardening by copper precipitation increases the proof strength.

Cr-Mo Steels

It has been found that the strengthening effect of Mo cannot fully be used, since creep ductility strongly decreases with increasing Mo content. Another limitation in the application of Mo-steels is the observed decomposition of iron carbides above 500°C (graphitization). A solution to both problems was the use of chromium as an alloying element in combination with molybdenum. In fact Cr-Mo steels were the first ones that allowed power stations to be operated at steam temperatures above 500°C.

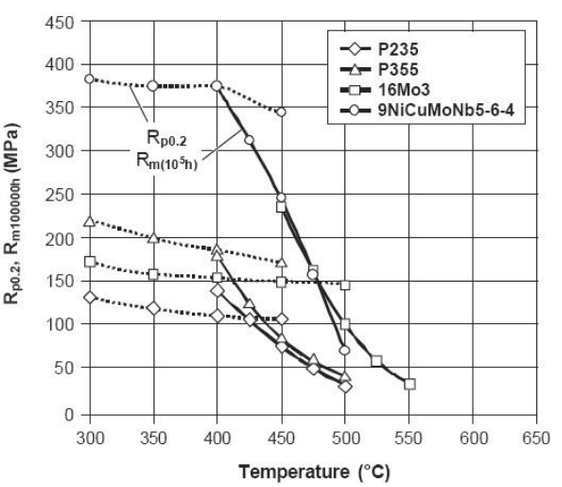


Fig. 2. Strength propertiesof C-Mn and Mo-steels[3].

The classical Cr-Mo steels are 13CrMo4-5 (T/P11) and 11CrMo9-10 (T/P22). Their creep rupture strengths are distinctly higher than the simple Mo-steels (Fig. 3), which is mainly a result of higher Mo-content. Cr-Mo steels form chromium carbides which are stable above 500°C. Therefore, graphitization is no longer a problem. Chromium also promotes the use at higher temperatures due to its positive influence on oxidation resistance.

The steels 7CrMoVTiB10-10 (T/P24) and T/P23, also represented in Figure 3, reveal extremely high strength properties. These are newly developed steels on the basis of T/P22. Having a similar microstructure as T/P22, their strengths properties have been raised considerably by additional alloying with Ti, V and B in the case of T/P24 as well as W, V, Nb and B in T/P23[3].

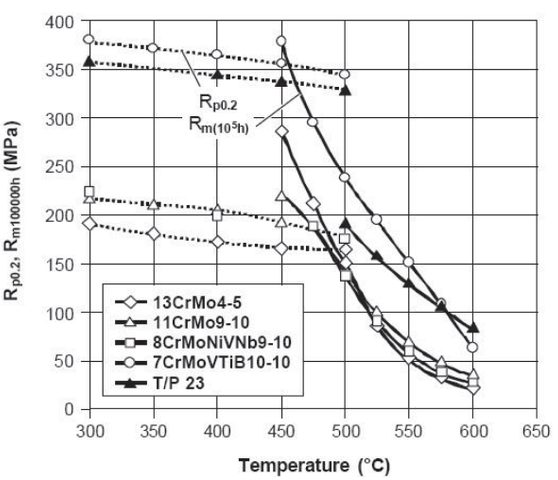


Fig. 3. Strength properties of Cr-Mo steels[3].

9-12 % Cr Steels

The increase of chromium in Cr-Mo steels above 7 % leads to a group of steels which have a martensitic microstructure as a common feature. This microstructure introduces a new element of structural hardening. It is characterized by a high dislocation density and a fine martensite lath structure which is stabilized by $M_{23}C_6$ precipitates. Thus structural hardening is responsible for the large increase in

strength of X11CrMo9-1, as compared to 11CrMo9-10 (Fig. 4). Further improvements of the creep strength have been achieved by alloying with V, Nb, W and B.

The introduction of X20CrMoNiV11-1 at the beginning of the sixties has been a major step to increase power plant efficiency. Its creep rupture strength at a temperature of 540°C is nearly twice that of the low-alloy ferritic steels available at that time (*e.g.* 10CrMo9-10 with 10^5 h- creep rupture strength of 78 MPa compared to 147 MPa for X20CrMoNiV11-1). Transformation behavior and microstructure is comparable to X11CrMo9-1. The higher creep rupture strength of X20CrMoNiV11-1 is mainly caused by the higher amount of $M_{23}C_6$ carbides as result of high carbon content.

After a period of standstill, the material development was reactivated by work carried out in the USA and Japan in the mid seventies. The prototype of the new steels from this development work is the modified 9% Cr steel T/P91 (EN designation: X10CrMoVNb9-1) invented in the USA. Meanwhile, this steel is well known and applied in power plants all over the world. It is used in new plants as well as in refurbishment work of high pressure/high temperature piping systems.

Although the carbon content is lower, the creep rupture strength of T/P91 is distinctly higher than that of X20CrMoNiV11-1. This has been achieved by alloying with V and Nb. T/P91 uses the precipitation of finely dispersed Nb/V carbonitrides of type MX as an additional strengthening effect. It was essential to balance the composition because an optimum dispersion and particle size of MX can only be achieved by an optimized Nb/V-ratio and N content. Subsequently new steel grades have been developed on the basis of T/P91 such as X11CrMoWVNb9-1-1 (T/P911), T/P92 and T/P122. These steel grades represent the current state of development for creep resistant ferritic steels[3].

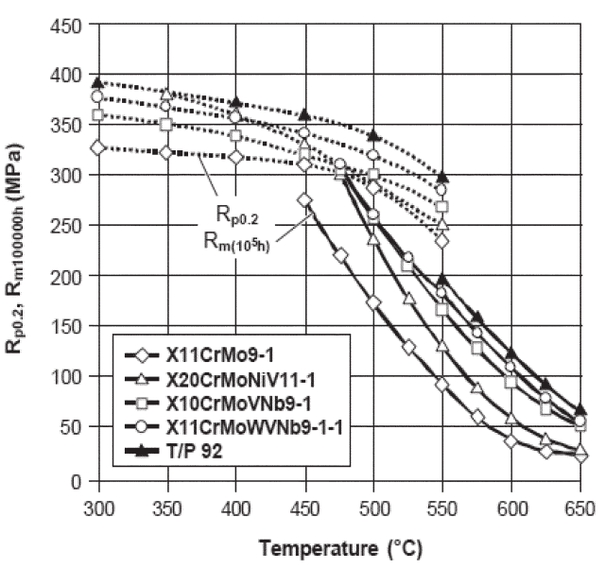


Fig. 4. Strength properties of 9-12% Cr- steels[3].

STEELS FOR PIPING AND TUBING APPLICATIONS

Low Alloyed Cr-Steels

Low-alloy ferritic 2.25Cr-1Mo steel and its recent modified grades are used extensively as structural material in the steam-generating systems of power plants and petrochemical industries. Service conditions in these plants demand the use of a various materials in different sections of components. A modification of this type (2.25%Cr-Nb-V contained W) is also introduced for similar applications due to its improved tensile properties at elevated temperatures to a level equivalent to those of 9Cr-1Mo-Nb-V steels. A unique chemical composition patent for this steel was obtained in the 1980s by JFE Steel Corporation and has realized the follow-ing advantages:

(1) Low C and N contents result in good weldability.

(2) Preheating and post weld heat treatment are unnecessary.

(3) The crack resistance of the heat affected zone (HAZ) was improved.

(4) The low Al content, which was reduced to the mini-mum possible limit, results in good creep properties[4].

The modified steel grade (3Cr-3WVTa) was also developed for elevated-temperature service in the power-generation and petrochemical industries. Creep-rupture strength of this new steel at 600 ºC exceeded those of the two advanced commercial 2.25Cr steels T23 (Fe-2.25Cr-1.6W-0.25V-0.05Nb-0.07C) and T24 (Fe-2.25Cr-1.0Mo-0.25V-0.07Ti-0.005B-0.07C) as it is shown in Figure 5. Moreover, the strength of 3Cr-3WVTa approached that of modified 9Cr-1Mo (T91) at 650 ºC. Elevated-temperature strength in this new steel is obtained from a bainitic microstructure with a high density number of fine needle-like MX precipitates in the matrix.

The presence of tantalum promotes a finer MX precipitate in the 3Cr-3WVTa than in the 3Cr-3WV

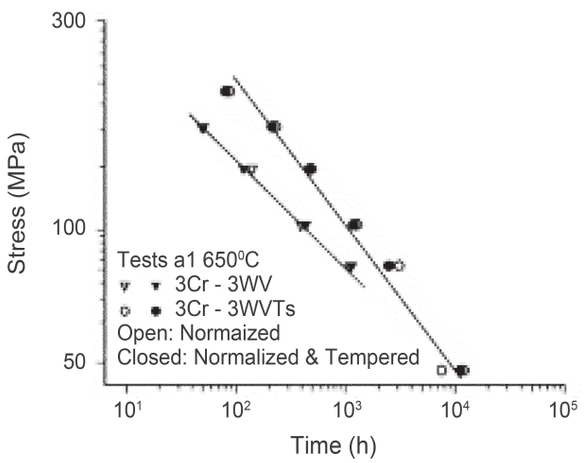


Fig. 5. Creep-rupture curves for 3Cr-3WV and 3Cr-3WVTa at 650ºC[2].

(Figs. 6a and 6b), and it suppresses the coarsening of these fine precipitates during creep.

At Oak Ridge National Laboratory (ORNL), reduced-activation bainitic steels with a base composition of nominally Fe-2.25Cr-2W-0.25V-0.1C (2.25Cr-2WV) were developed. This base composition with H" 0.1% Ta (2.25Cr-2WVTa) showed improved strength relative to even some 9Cr steels, but it suffered from inferior toughness. Prior to work on reduced-activation steels, work at ORNL demonstrated that quenched-and-tempered plates of a Fe-3Cr-1.5Mo-0.25V-0.1C steel had, unexpectedly, better toughness than normalized (air-cooled)-and-tempered plates[2].

P91 Steel

In the 1970s, there was considerable interest in the 9 % Cr steels for components of the fast breeder nuclear reactor. On the basis of the familiar Fe9Cr1Mo steel used since the 1950s in petrochemical plant, improved steel was developed by the Oak Ridge National Laboratory and subsequently incorporated into the ASTM specifications under the designation P91. A remarkable increase in the stress rupture strength was achieved by the addition of 0.2 % V, 0.06 % Nb and 0.05 % N[5]. The heat resistant martensitic steel P91 is being utilized in conventional power plants for piping systems with operating temperatures of 560 – 600ºC and high pressures in the range of 270 bars. These high operating temperatures and pressures require high quality welds to ensure safety of equipment and personnel[6] .

In the early 1980's, tubing of 9Cr-1Mo-V (P91) steel was introduced into the superheaters of power boilers. Because P91 steel is an air-hardenable martensitic high-strength alloy, the specifications of preheating and post weld heat treating conditions are critically important. However, maintaining preheat temperature before post weld heat treatment is essential for minimizing the probability of hydrogen cracking in weld heat-affected zones[7].

P92 Steel

P92 is a development of the now well established steel grade P91, which is modified by reducing the Mo content to about 0.5 % (In order to avoid the formation of delta-ferrite in the microstructure), and adding about 1.7% W plus a few parts per million of B. Controlled microalloying in the form of Nb, V and N is retained. This composition modification gives rise to very stable carbides and carbo-nitrides which improve long term creep strength. This steel is designed to operate at temperatures up to 625°C and it is claimed that high temperature rupture strengths are up to 30 % greater than for P91. For example at 600 °C the 100,000 hour creep rupture strength of P91 base material is about 95 MPa whereas P92 is about 123 MPa. Exploitation of P92 is relatively limited and further confidence and experience in the fabrication and use of the alloy still has to be

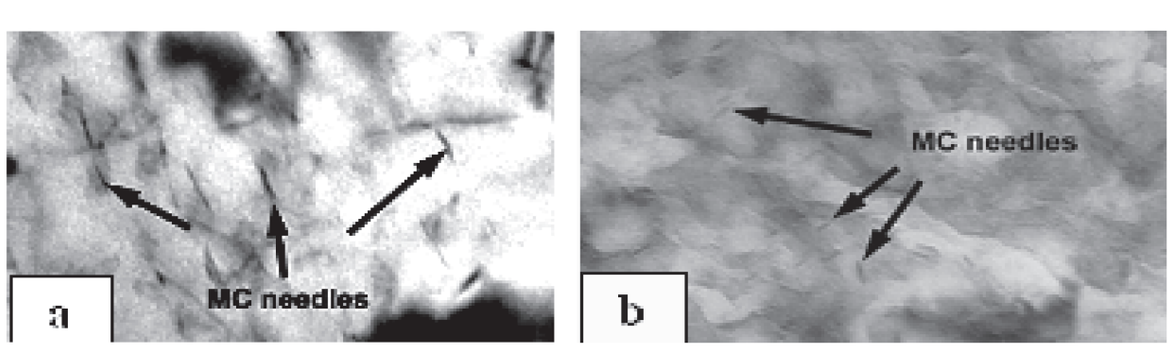


Fig. 6. Ultra-fine precipitate needles in the matrix of(a) 3Cr-3WV and (b) 3Cr-3WVTa steels[2].

developed. However, a number of installations were completed in the late 1990s and more are under construction or being planned[8]. Figure 7 shows the TEM micrographs of austenitised and tempered P92 steel.

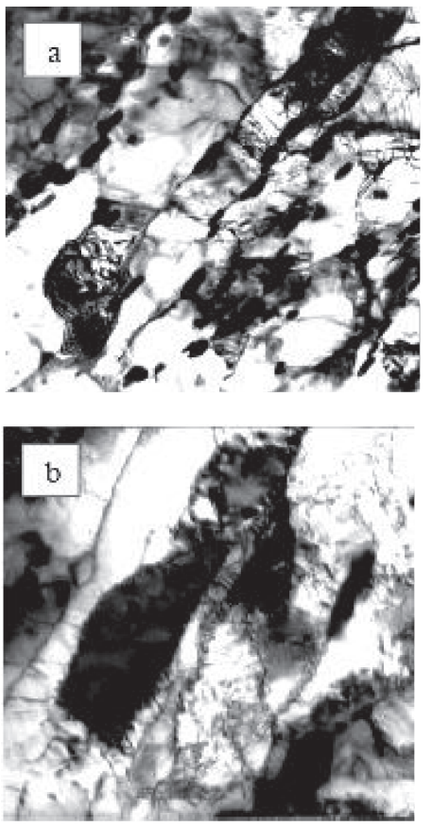


Fig. 7. TEM micrographs of P92 austenitised for 2 h at (a) 970 °C, (b) 1145 °C, followed by tempering for 2 h / 775 °C[5].

E911 Steel

E911 steel (X11CrMoWVNb9-1-1) has been developed by the work carried out in Europe as part of the COST 501 WP11 project, entitled "Advanced Materials for Power Engineering Components - High Efficiency, Low Emission Systems". Its chemical composition is essentially the same as the P91, except it contains 1 % W additionally and also some B. The benefit of B is believed to decrease the coarsening rate of carbides. E911 and P92 are intended for use in main steam lines. E911 and P92 differ only in their Mo and W contents, while the molybdenum equivalent (Mo + 1/2 W) of both steels is nearly the same. The Continuous Cooling Transformation (CCT) diagram of E911, shown in Figure 8 is essentially the same as that of P91 and P92. The M_S and A_{C1b} temperatures as well as martensite hardness are more or less the same for the three steels, and also the location of the ferrite-carbide transformation nose is comparable to that of P91 steel grade[3].

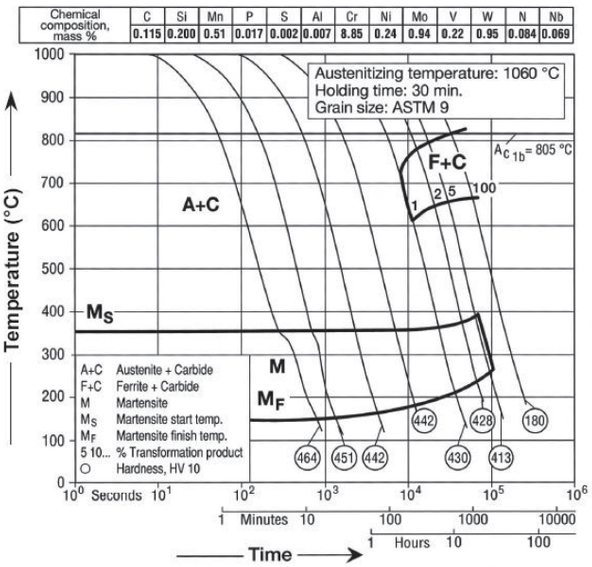


Fig. 8. The CCT-diagram for X11CrMoWVNb9-1 (T/P911)[3].

The optimization of the E911 composition has improved the creep properties at 600 ºC and 625 ºC; however, the most important improvements are to the oxidation performance. At temperatures above approximately 600ºC, it is not the creep strength that limits the high temperature operation of 9 % Cr materials such as E911, but the oxidation rate [9]. The tensile properties of P911 are improved compared with the well established steel P91 as it is indicated in Figure 9[10].

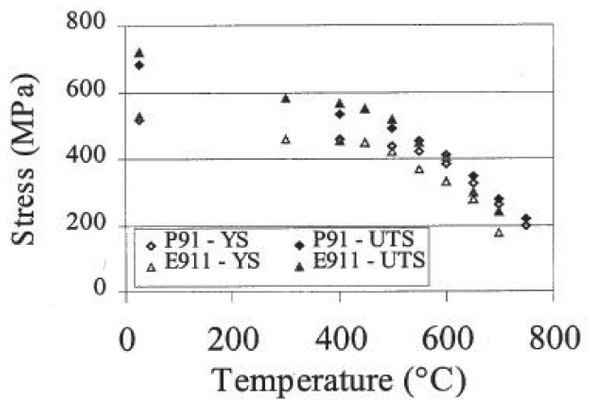


Fig. 9. Comparison of tensile properties versus temperature of the P91 and E911 steel-pipes[10].

Comparison of the Microstructure of P91, P92 and E911 Steels

Ennis and his co-author[5] carried out an

experimental work in which a standard heat treatment for three investigated steels (given in Table 2). They found that the three steels exhibited similar microstructures, as shown in Figure 10. Austenitizing produced a martensitic structure with a high dislocation density within the martensite laths. During tempering recovery caused the formation of sub-grains and dislocation networks.

The creep strength of 9-12 % Cr steels, is correlated inversely with the martensite lath width and therefore with the sub-grain size. Measurements of the average sub-grain width and of the dislocation density within the subgrains, performed by means of quantitative TEM, are presented in Table 3.

Table 2. Standard heat treatment of P91, P92 and E911 steels[5].

P91 Steel	P92 Steel	P911 Steel
1h/1050 °C + 1h/750 °C, air cooled	2h/1070 °C + 2h/775 °C, air cooled	1h/1050 °C + 1h/750 °C, air cooled

Table 3. Dislocation density and mean sub-grain size as received of P91, P92, E911 steels[5].

Steel	Dislocation density $\times 10^{-14}$, m^{-2}	Mean sub grain size, μm
P91	7.5 ± 0.8	0.4 ± 0.06
P92	7.9 ± 0.8	0.4 ± 0.09
E911	6.5 ± 0.6	0.5 ± 0.05

It can be seen that sub-grain size is fairly similar in all investigated steels. The small differences can be attributed to the different prior austenite grain size. Dislocation densities in P91 and P92 steels were similar and little higher than in E911 steel.

Besides recovery processes the precipitation of carbides, carbonitrides and nitrides occurred during tempering of the three steels examined by Ennis and his co-author. They also observed that $M_{23}C_6$ carbides containing Cr, Fe, Mo and W, precipitated preferentially on the prior austenite grain boundaries and on the martensite lath boundaries. These precipitates retard the sub-graingrowth and therefore increase the strength of the materials.

Comparison of the Rupture Strengths of P91, P92 and E911 Steels

From Figure 11, it is clear that the stress rupture strengths of the currently used and the new power station steels are compared on the basis of the maximum service temperature for 10^5 h stress rupture strength of 100 MPa. It may be seen that the maximum service temperature increases with increasing complexity of the steel composition, and the more highly alloyed steels have sufficient stress rupture strength to be considered for application at temperatures in excess of 600°C.

Figure12 shows the secondary creep rates of P91, P92 and E911 at 600 and 650°C plotted against the applied stress. Data taken from the published literature for the same heat are included where available. It can be seen that at high stresses the differences in the secondary creep rates of the three steels are relatively small. In the low stress region, however, the differences between the steels become more pronounced.

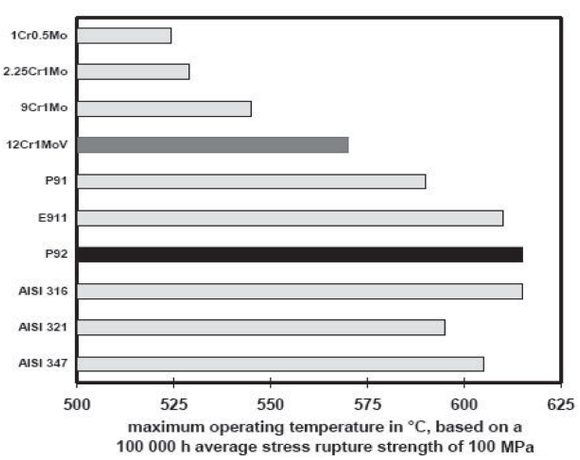


Fig. 11. Stress rupture strengths of the currently usedand newly developed power station steels[5].

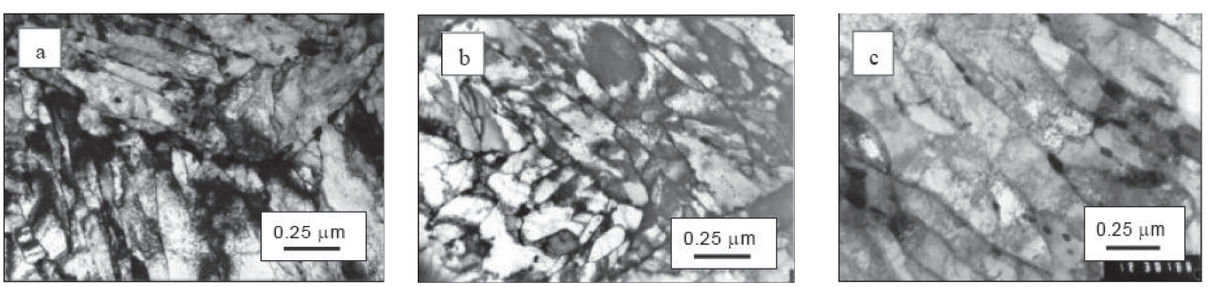


Fig. 10. TEM Micrographs of the as received steels (a) P91, (b) P92 and (c) E911, showing the elongated sub-grains of tempered martensite[5].

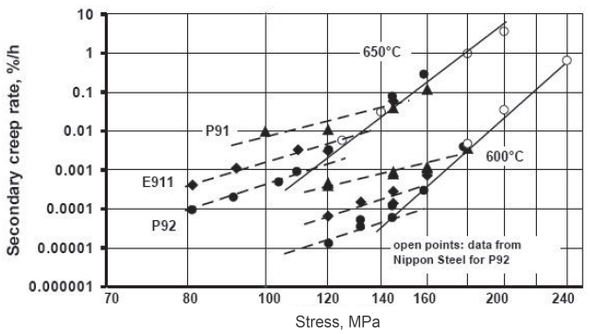


Fig. 12. Secondary creep rates for P91, P92 and E911[5].

The Role of Stress on the Creep Rupture Strength of 9-12 % Cr Steels

The creep deformation characteristics may be described by the Norton equation (minimum creep rate is proportional to the applied stress to the power n) with two different values for the Norton stress exponent n.

$$\dot{\varepsilon} = K \sigma^{n}$$

Where K and n are experimentally derived material constants.

At high stresses, the value of n is around 16 while at lower stresses, the data conform to an n value of 6. The change in n is indicative of a change in the creep characteristics. Figure 12 also shows that at high stresses the differences in the secondary creep rates of the three steels were relatively small and the high dislocation densities resulting from the martensite transformation dominate the deformation.

In the low stress region, however, the differences between the steels became more pronounced. The results of long-term (200000 h) creep rupture strength of different 9-11 % Cr steels are shown in Figure 13. It can be observed that at the usual levels of service temperatures, the relative improvement from X20 to P91 is roughly similar to the improvement observed for the traditional low-alloy steels (10CrMo9-10 and 14MoV6-3) to X20. However, the relative improvement from P91 to newer steels (E911 and P92) is less impressive. Particularly,a small difference seems to now exist between P91 and E911[11]. From the above equation, the time to rupture for the steels exposed to elevated temperatures decreases with the increasing of the applied steel, as shown in Figure 14[12].

NF616 Steel

The use of NF616 (P92), for example, may allow about 35 % increase in the allowable stress at 600°C. This in turn permits a decrease in section thickness (Fig.15), and thereby a reduction in weight, as well as lower welding costs. Consequently, the through-wall temperature gradients will be reduced resulting in a reduction in the thermal fatigue loading experienced[13]. This type of steel has been developed and shown to be capable of operation up to 620 °C[14].

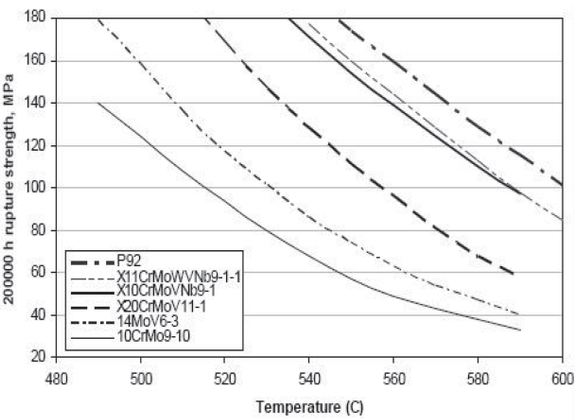


Fig. 13. Comparison of the 200,000 h creep rupture strength of selected 9-11 % Cr steels and the low-alloy steels 14MoV6-3 and 10 CrMo9-10 according to EN 10216-2 and ECCC data sheets[11].

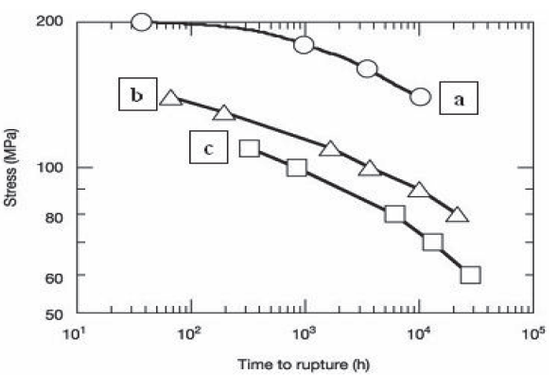


Fig. 14. The stress-time to rupture relationship for (a) New 9% Cr nanostructure carbonitride dispersion steel, (b) P92 steel grade and (c) P91 steel[12].

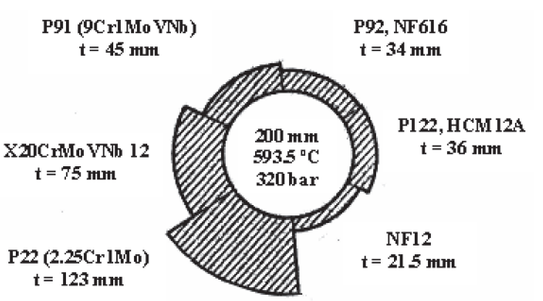


Fig. 15. Variation in wall thickness (t) with material grade (with an internal diameter of 200 mm) for service at 593.3 °C and 320 bar [13].

P122 Steel

In recent years, several new high creep strength ferritic steels have been developed for boiler pressure parts, with 11Cr–0.4Mo–2W–V–Nb–Cu steel (P122) having excellent corrosion resistance and approximately 1.3 times higher creep strength than Modified 9Cr–1Mo steel (P91). This steel has already been used for main steam pipes, high-temperature reheats pipes and headers, as well as SH/RH tubes in modern large capacity fossil power plants.

This steel consists of a tempered martensitic structure that is the same as for P91. The microstructure of the heat affected zone (HAZ) in welds is quite complicated because of the transformation and recovery caused by repeated heat cycles through welding processes[15]. It is well known that welds are weaker in creep strength than base metal under higher temperature and lower stress conditions. Welds usually fracture at the intercritical HAZ adjacent to base metal, known as type IV failure, although the failure mechanism has yet to be elucidated. This type of failure is indicated in Figure 16.

For P122, the chromium content has been raised to about 12 % in order to improve the oxidation resistance. The increased chromium content influences the phase stability and therefore 0.9 % Cu was added to obtain on fully martensitic microstructure. This is because P122 type of ferritic steel is preferred boiler material owing to its higher oxidation resistance. The disadvantages of P122 are mainly found in the area of fabricability. This can be attributed mainly to the high copper content. Low A_{C1} temperature entails longer tempering times at lower temperatures when the steel has to be tempered after hot working and welding[3].



Fig. 16. Microstructure of creep damaged HAZ observed by replica[15].

Reduced Activation (RA) Steels

For martensitic/ferritic steels, the main alloying elements such as molybdenum, niobium and nickel present in ordinary commercial steels are substituted by elements such as tungsten, vanadium and tantalum. These elements have a similar influence on the processing and the structure, but exhibit a lower radiological impact. The development process for the RA alloys can benefit from the many years of experience on power plant materials even though the use of boron or cobalt is not permitted in fusion reactors. The used design procedure is based essentially on the following rules and assumptions:

1. B, Co, Nb and Mo which are present in conventional creep-resistant steels are eliminated.
2. The amount of W is increased as much as possible for solid solution strengthening.
3. The creep resistance of martensitic steels is enhanced by a fine dispersion of non-shearable particles which are resistant to coarsening. V nitrides are good in this context.
4. A fine dispersion of V nitride particles can only be achieved if they all dissolve at the austenitization temperature, which in the industrial context must be 1200 °C or lower.
5. The balance between austenite and ferrite stabilizing elements has to be controlled to avoid the formation of ä ferrite at the solutionizing temperature 1200°C-1250°C. With these criteria, the list of solutes permitted becomes limited to the following elements: Cr, W, V, Ni, Si, Mn, N and C[16]. Table 4 shows the nominal composition of reduced-activation steels in Japan, Europe and USA[17].

T23 and T24 Steels

As shown in Figure 17, the new steels T23 and

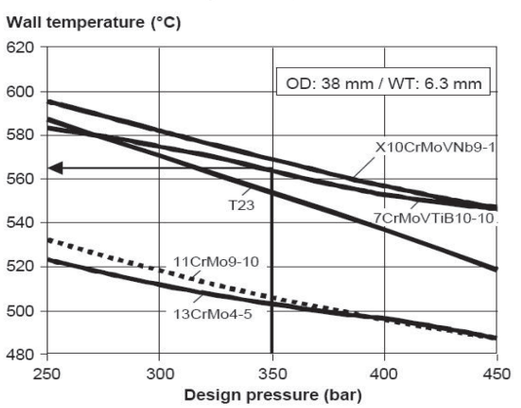


Fig. 17. Allowable temperaturesfor different waterwall materials[3].

7CrMoVTiB10-10 (T24) allow high enough wall temperatures. The steels have been developed in Japan (T23) and Germany (T24). They are both based on 11CrMo9-10. Thanks to their lower carbon content where the maximum hardness at the HAZ lies at 350-360 HV10. The steels are micro-alloyed with V, Nb, Ti and B to achieve high creep rupture strength (see Figure 3). T23 also contains W, while its Mo content is considerably reduced (see Table I). The applied hardening mechanisms are basically the same as have been used for the new 9-12 % Cr steels.

Due to their origin, however, most of the other properties of T23 and T24 are similar to T22 (11CrMo9-10). They belong to the group of Cr-Mo steels with a predominantly bainitic microstructure. As an example, Figure 18 shows the transformation behavior of T24. The main difference to the transformation behavior of T22 is the retardation of ferrite formation, which is caused by the micro-alloying additions. Because of high cooling rate, the thin-wall tubes used as membrane walls exhibit a bainitic martensitic structure. Both steels are used in a normalized and tempered condition[3].

STEELS FOR STEAM TURBINES

Steels for Rotors, Discs and Blades

The most commonly used alloys for steam turbine rotors and/or discs are the CrMoVWNbN steels, which can vary in chromium content from 1 to 13 % depending on the preference of individual manufacturers. These alloys (Table 5) are widely used up to a temperature limit of about 566°C. However, the higher-W, lower-Nb and C versions are capable to be used up to 593°C. The issues for alloys for higher-temperature use are similar to those for materials of steam piping. Versions of these ferritic steels, based on the advanced 9-12% Cr compositions, are already in service at steam temperatures of 600°C, and it is expected to be usable to approximately 620°C (and possibly 650°C). The main manufacturing concern is how rotors, discs and other large castings and forgings components can be made. Very large rotors now can be produced, but experience is related mostly to Cr-Mo-V alloys (used in current 541-566°C plants), and for 12 Cr alloys (needed for advanced steam cycles to 620°C)[18].

For turbine blades, the steel grade 422 which is a

Table 4. Nominal composition of reduced-activation steels (wt %)[17].

Program	Steel	C	Si	Mn	Cr	W	V	Ta	N	B	Others
Japan	F82H	0.1	0.2	0.5	8.0	2.0	0.2	0.04	<0.01	0.003	-
	JLF-1	0.1	0.08	0.45	9.0	2.0	0.2	0.07	0.05	-	-
Europe	OPTIFER Ia	0.1	0.06	0.5	9.3	1.0	0.25	0.07	0.015	0.006	-
	OPTIFER II	0.125	0.04	0.5	9.4	-	0.25	-	0.015	0.006	1.1 Ge
	EUROFER	0.11	0.05	0.5	8.5	1.0	0.25	0.08	0.03	0.005	
USA	ORNL 9Cr2WVTa	0.1	0.3	0.4	9.0	2.0	0.25	0.07	-	-	-

Table 5. Samples of rotor steels[20].

Rotor type	Steel grade	$R_{p0.2}$ (N/mm^2)	R_m (N/mm^2)	A_5 (%)	Impact Energy at 20 °C (J)	Service Temperature (°C)
HP, IP	30CrMoNiV 5 11 21CrMoNiV 5 9	≥550	≤850	15	≥24	≤560
	X22CrMoV 12 1	≥590	≤930	13	≥24	≤600
	X12CrMoWVNbN 10 1 1	≥700	≤1000	13	≥24	≤630
HP-LP	23CrMoNiWV 8 8	≥550	≤850	13	≥80	≤530
S-Rotor	26NiCrMoV 10 10	≥580	≤820	16	≥100	≤350
LP, Ge	26NiCrMoV 11 5 26NiCrMoV 14 5	≥610 / ≥650 ≥705	≤850 / ≤900 ≤980	15 15	≥100 ≥100	≤350 ≤350
LP Disk	26NiCrMoV 14 5	≥750 / ≥820	≤970	15	≥100	≤350

HP = High pressure IP = Intermediate pressure LP = Low pressure S = Saturated steam
Ge = Generator $R_{p0.2}$ = Yield strength R_m = Tensile strength A_5 = Elongation

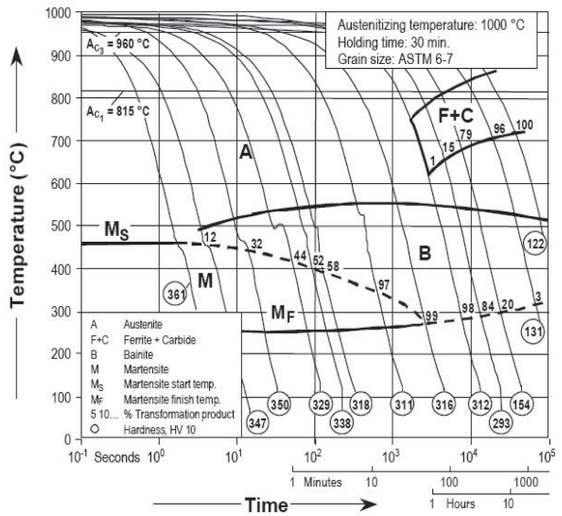


Fig. 18. The CCT diagram for7CrMoVTiB10-10 (T/P24)[3].

modified AISI 420 martensitic stainless steel with Mo and W additions is designed for service temperatures up to 650°C with a satisfactory combination of strength and toughness. This steel can also be used for high-strength fasteners, valves, as well as structural components for aircraft applications. Turbine blades made of martensitic stainless steels, *e.g.* 403 and 422 stainless steels, are used frequently in modern fossil power plants. Type 422 can be heat treated to obtain a wide range of mechanical properties to meet the requirements of a specific application[19].

Steels of Casings/Shells

The casings of steam turbines are typically large structures with complex shapes that must provide the pressure containment for the steam turbine. Depending on the design of the turbine, an inner casing or cylinder may be employed to enclose the hot gas path, so that the main steam from the steam generator first flows into the steam chest, through the inner cylinder, over the vanes and blades, and then returns through the annulus between the inner cylinder and the outer casing before being sent to the reheater.

Because of the size of these components, their cost has a strong impact on the overall cost of the turbine. The materials used currently for inner and outer casings are the 1-2CrMo steels, usually as castings products. The temperature limit of these alloys in this application is approximately 566°C, and is set by their resistance to oxidation in steam. For higher temperatures, cast 9CrMoVNb alloys are considered to be adequate in terms of strength capabilities to 593°C, while the 12Cr steels in either cast or forged form currently appear to be limited to 620 °C, assuming that their steam oxidation resistance is acceptable[18].

STEELS FOR WATER WALLS AND BOILER TUBES/PIPES

Bainitic-ferritic steels, such as 10CrMo4-5 (T12) and 11CrMo9-10 (T22), which have been used so far, do not have adequate creep rupture strengths for use in water walls under the conditions of advanced power plants (Figure 17). From the viewpoint of creep strength T91 (X10CrMoVNb9-1) seems to be a suitable solution. As a requirement of manufacturing, water walls cannot be subjected to a post-weld heat treatment after welding. However, martensitic 9-12% Cr steels attain a maximum hardness between 450 HV_{10} (*e.g.* T91) and 650 HV_{10} (*e.g.* X20CrMoNiV11-1) in the as-welded HAZ, depending mainly upon the carbon content. A reduction of carbon content in these steels is only possible to a limited extent for reasons of microstructural stability. Such high hardness levels are not acceptable, mainly because of the risk of stress corrosion cracking. Therefore, the high strength 9-12% Cr steels are not suitable for use in waterwalls. The aspect of hardness had to be taken into account when developing new steels. As shown in Figure 17, the new steels 7CrWVMoNb9-6 (T23) and 7CrMoVTiB10-10 (T24) allow high enough wall temperatures. Thanks to their lower carbon content, that makes the maximum hardness in the HAZ of their weld joints lies at 350- 360 HV_{10}.

Outside of Europe, T23 is used as tube material for reheaters and superheaters. Due to the low chromium content, however, this application is limited by oxidation and flue gas corrosion. The steel grade 7CrMoVTiB10-10 (T24) could be an interesting alternative to P91 for use in conventional plants with steam temperatures up to about 545°C. With increasing steam temperature the lifetime of components will not only be limited by creep strength but also by oxidation and high temperature corrosion. Service tests have shown that the newly developed steels T/P911 and T/P92 are not suitable for use as boiler tubes with a steam temperature of 600°C. In general 9 % Cr steels have a distinctly lower oxidation resistance than 12 % Cr steels, like X20CrMoNiV11-1. The difference becomes most severe at temperatures above 600°C. Figure 19 illustrates the

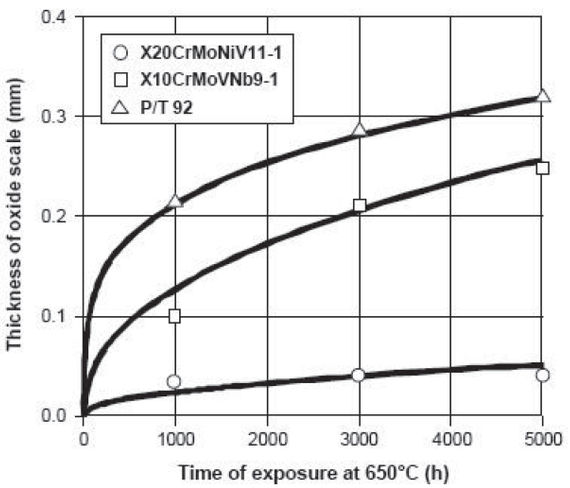


Fig. 19. Steam oxidation of 9-12 % chromium - steels at 650°C[3].

comparison by steam oxiation for the steel grades, X20CrMONiVII-1, X10CrMoVNb9-1 (T/P91) and T/P92. It shows that 9% Cr steels can not be used in steam lines outside the boiler, if the steam temperature is 650°C or over[3]. In recent years, 9-11%Cr ferritic heat resistant steels were developed by addition of Co and/or W, such as NF616 (9Cr-1.8W-0.5Mo), HCM12A(11Cr-2W-0.4Mo-Cu), NF12 (11Cr-2.6W-Mo-Co-V-Nb) and E911(9Cr-1W-1Mo), for thermal power boilers. Due to the high creep rupture strength of these steels, the Ultra Super Critical (USC) boilers with the high steam condition of 25MPa/600°C can be used, and now several USC power plants of 1,000 MW class have been operated in Japan. To achieve higher plant efficiency, a still higher steam condition is expected; therefore further research have been continued in Japan and Europe to increase the creep rupture strength of ferritic steels. The final target of rupture strength of these ferritic steels seems to be MPa at 100,000 hours/650°C.

For example, Takashi Sato and his co-authors in Japan[21], carried out a practical research on the ferritic heat resistant steel 9%Cr-W-Co, and they proposed that this ferritic steel can be used as a candidate material for boiler tube and pipe for up to 650°C application. They confirmed the improvement of creep resistance and formability of the proposed steel by applying both long-term creep rupture and boiler tube manufacturing tests The contents of Al and Ni of the investigated steel were reduced to 0.001% and 0.035% respectively because some researchers believe in their contribution to the reduction of the long term creep rupture strength of the ferritic steels[21].

FERRITIC/MARTENSITIC STEELS FOR HIGH TEMPERATURE APPLICATION

Several investigators have looked beyond the typical Cr-Mo-W-V steels for novel compositions and processing routes to develop new ferritic and martensitic steels for service to 650ºC and higher. One such composition was 9Cr-3.3W-0.2V-0.05Nb-0.05N-0.08C steel containing 1–3% Pd. In another study, 15% Cr ferritic steel with a base composition of Fe-0.1C-15Cr-1Mo-3W-0.2V-0.05Nb-0.07N-0.003B was alloyed with up to an additional 3% W and 3% Co. A combination of 6 % W and 3% Co in this steel provided the best strength properties due to the resulted precipitates (not identified). For nuclear considerations and subsequent activation, the cobalt alloys are probably not an option, although the class of steel may offer other non-cobalt-containing options.

Information on the development of low-carbon (0.002 %) 9Cr-3W-3Co-VNb steel with 0.05 % N has recently been published. Improved creep strength was attributed to nano-sized MX carbonitrides along prior-austenite grain boundaries and lath boundaries. Another recent experimental steel development is a carbon-free martensitic alloy. The steel composition is Fe-11.0Ni-5.0Cr-10.0Mo-0.20Ti-0.12Al-0.005B and has an excellent properties at 700ºC.

Oxide dispersion-strengthened (ODS) ferritic steels are another alternative with the potential of having the advantage of ferritic steels, but being able to push operating temperatures to 650ºC and beyond. These steels are presently receiving an ever increasing amount of attention as possible candidate materials for first wall and blanket structural materials for future fusion reactors and for fuel cladding for fast fission reactors. They have also been considered in the planning for generation IV reactors, as well as for the conventional power-generation industry, as they push for operating temperatures beyond 650ºC. The first ODS steels consisted of a low-carbon, high-chromium (12–17 % Cr) non-transformable ferrite matrix with a high number density of small Titania (TiO_2) and/or Yttria (Y_2O_3) particles as the strengthening dispersion.

Two early compositions studied extensively were: Fe-13Cr-1.5Mo-2.9Ti-1.8Ti_2O_3 (DT2906) and Fe-13Cr-1.5Mo-2.2Ti-0.9Ti_2O_3-0.5Y_2O_3 (DT2203Y05). Elevated-temperature strength is provided by a dispersion of fine Titania and Yttria particles and by ÷-phase (70% Fe, 15% Cr, 7% Ti, and 6% Mo) that forms at grain boundaries. The development programs seek to process the presently available steels (e.g.,

commercial MA957 (Fe-14Cr-1Ti-0.3Mo-0.25Y_2O_3) to produce an equiaxed structure and explore new alloy compositions. Many of the new alloys use tungsten instead of molybdenum, and they usually use Y_2O_3 dispersions with lower titanium concentrations than were used for the earlier versions.

The Central Research Institute of the Electric Power Industry of Japan and Kobe Steel Ltd have presented information on 12Cr-8Mo and 12Cr-8Mo-0.1Y_2O_3 steels fabricated for cladding of metallic fuel for fast breeder reactors. The steels, fabricated by mechanical alloying/powder metallurgy techniques, were shown to have two-to-three times the creep-rupture strength of a conventional 12Cr (HT9) steel. Two attempts have been made to produce dispersion-strengthened steels by more conventional techniques than mechanical alloying/power metallurgy techniques. The first has good creep strength to 650–700°C, and it achieves its excellent elevated temperature properties by dispersion strengthening. The steel, designated A-21 has a nominal composition of Fe-9.5Cr-3Co-1Ni-0.6Mo-0.3Ti-0.07C that is strengthened by a fine dispersion of tiny titanium carbides produced by austenitizing to dissolve all precipitates and then hot working the austenite (ausforming) prior to cooling to form martensite. A some-what similar approach to the A-21 but without the hot working is the development of a steel designed to use precipitation strengthening with vanadium nitrides and carbonitrides. In this case, the steel with the complicated nominal composition of Fe-12Cr-0.5Ni-2Mn-10Co-1.5Mo-0.7V-0.06Nb-0.04Ta-0.04Ti-0.15N-0.03C was austenitized at 1180ºC for 1 h and then ausaged at 700ºC for 120 h, after which it was cooled to room temperature, and finally tempered at 700ºC for 4 h. The objective was to form a high number density of fine precipitates. The properties of the steels produced by the initial attempts at this process were less-than desired, and further work is required[17].

CONCLUDING REMARKS

1- Concerning the steel P92, it is modified from the well established alloy P91, by reducing the Mo-content to about 0.5% (In order to avoid the formation of delta-ferrite in the microstructure), and adding about 1.7% W plus a few parts per million of B, with retained controlled microalloying of Nb, V, and N. This composition modification gives rise to very stable carbides and carbo-nitrides which improve long term creep strength. This steel is designed to operate at temperatures up to 625°C and it is claimed that high temperature rupture strengths are up to 30% greater than for P91.

2- Maximum service temperature increases with increasing complexity of the steel composition, and the more highly alloyed steels have sufficient stress rupture strength to be considered for application at temperatures in excess of 600°C.

3- Creep strength of 9-12% Cr steels is correlated inversely with the martensite lath width and therefore with the sub-grain size.

4- Comparing the long-term (200000 h) creep rupture strength of different 9-11% Cr steels at the usual levels of service temperatures and the relative improvement from X20 to P91 is roughly similar to that observed for the traditional low-alloy steels (10CrMo9-10 and 14MoV6-3) to X20. However, the relative improvement from P91 to newer steels (E911 and P92) is less impressive, where small difference seems to now exist between P91 and E911.

5- Although P122 steel has an excellent corrosion resistance and approximately 1.3 times higher creep strength than P91, the microstructure of its HAZ in welds is quite complicated because of the transformation and recovery caused by repeated heat cycles through welding processes. It was pointed out that such welds are weaker in creep strength than base metal under higher temperature and lower stress conditions. Due to this, P122 is preferred to be used as boiler components because of its higher oxidation resistance. However, it is not favored to be used for thick section components

6- Oxide dispersion-strengthened (ODS) ferritic steels are another alternative that were studied extensively to push operating temperatures up to 650ºC and beyond. Steels such as (DT2906) Fe-13Cr-1.5Mo-2.9Ti-1.8Ti_2O_3, and (DT2203Y05) Fe-13Cr-1.5Mo-2.2Ti-0.9Ti_2O_3-0.5Y2O3 are examples of this. Their elevated-temperature strength is provided by a dispersion of fine Titania and Yttria particles and by ÷-phase (70% Fe, 15% Cr, 7% Ti, 6% Mo) that forms at the grain boundaries.

7- Other improved creep rupture steels (12Cr-8Mo and 12Cr-8Mo-0.1Y_2O_3) were presented by The Central Research Institute of the Electric Power Industry of Japan and Kobe Steel Ltd. These steels were fabricated by mechanical alloying/powder metallurgy techniques and shown to have two-to-three times the creep-

rupture strength of the conventional 12Cr (HT9) steel at 650–700°C.

8- Improvement was made on steels with high service temperature of 700ºC, low-carbon steel (Fe-0.002C-9Cr-3W-3Co-VNb-0.05N) and carbon free steel (Fe-11.0Ni-5.0Cr-10.0Mo-0.20Ti-0.12Al-0.005B) have been publicized and still under investigation.

REFERENCES

[1] Hernandez Sergio, G., and Alberto, N. Conejo, 2005. Creep Properties of 1.25Cr-1Mo-0.25V steels for turbine casings. *Metalurgia and Materiais*, R. Esc. Minas, Ouro Perto, **58(2)**, 165-173.

[2] Klueh, R. L., Evans, N. D,. Maziasz, P. J, and. Sikka, V. K., 2005. Creep-rupture behavior of 3Cr-3W-V bainitic steels. ECCC Creep Conference, 12–14, London. *etd@etd1.co.uk.*

[3] Hagen Ingo von and Bendick Walter. *Creep Resistant Ferritic Steels for Power Plants*. Ehinger Strasse 200, 47259 Duisburg, Germany.

[4] JFE Steel Corporation, 2006. *2.25 % Cr-1.6 % W Ferritic Steel for Boiler Piping and Tubing Applications.* Technical report, No. 7.

[5] Ennis, P. J. and czyrska.-Filemonowicz, A. 2002. Recent advances in creep resistant steels for power plant applications. *OMMI* (**1**).

[6] http://www.btwcan.com/html/tips_page 1.html - Bohler Thyssen Welding.

[7] Santella, M. L., Babu, S. S., Swindeman, R. W, and Specht, E. D., 2003. In-Situ Characterization of Austenite to Martensite Decomposition in 9Cr-1Mo-V Steel Welds. TMS (*The Minerals, Metals and Materials Society*).

[8] Metrode Products Ltd., 2005. P92 *Welding Consumables for the Power Generation Industry*. Issue 2.

[9] Pugh, J. A. and Fleming, A. Clarke, P., Allen, D. J. and Mulvihill, P. *Practical Improvements in Power Plant Efficiency through Materials Engineering*. Scientific report**.**

[10] Di Gianfrancesco, A., Matera, S. and Tassa, O., 2001. Properties and microstructure of modified 9 % Cr steels. *La Revue de Métallurgie*-CIT.

[11] Auerkari ,P., Holmström, S., Veivo, J. and Salonen , J., 2005. Creep damage and expected creep life for welded 9-11%Cr steels. ECCC Creep Conference, 12–14, London. etd@etd1.co.uk.

[12] Masaki Taneike, Fujio Abe and Kota Sawada, 2003. Creep-strengthening of steel at high temperatures using nano-sized carbonitride dispersions. *Nature Journal. **424**. www.nature.com/nature.*

[13] http://www.twi.co.uk/j32k/unprotected/band_1/power_newweldmet.html

[14] Klueh R. L., 2002. *Evolution of Ferritic/Martensitic Steels for Elevated-Temperature Service.* US Fusion Materials Science Program Strategic Planning Meeting.

[15] Nobuyoshi Komai and Fujimitsu Masuyama, 2002. Microstructural degradation of the HAZ in 11Cr–0.4Mo–2W–V–Nb–Cu steel (P122) during Creep. *ISIJ International*, **42,** (12), 1364– 1370.

[16] de Carlan, Y., Murugananth M., Sourmail, T.and. Bhadeshia, H. K. D. H., 2004. Design of new Fe-9CrWV reduced-activation martensitic steels for creep properties at 650°C.
Journal of Nuclear Materials, 329-333,. 238-242.

[17] Klueh, R. L., 2004. *Elevated-Temperature Ferritic and Martensitic Steels and their Application to Future Nuclear Reactors.* ORNL/TM, 176.

[18] http://www.ms.ornl.govF.V/researchgroups/corrosion/staff/pdf/IGW-0417.pdf I.G. Wright,
Maziasz P.J.,. Ellis, Gibbons T B., and Woodford D.A *Materials Issues for Turbines for Operation in Ultra-Supercritical Steam.*

[19] Yang, T. C. and Chen, C., 2004. Laser welding of 422 stainless steel with inconel 625 filler metal. *ISIJ International*, **44**, (5), 852–857.

[20] Wolfgang Janssen. *Welding on Rotors for Power Plant Turbo Sets State of the Art*. Siemens AG, Power Generation, Germany.

[21] Takashi, Sato, Kohji, Tamura, Yuji, Fukuda and, Toshio, Fujita, 2005. *Improvement of Long-Term Creep Rupture strengths of 9-11%Cr Ferritic heat Resistant Steels for Boiler* Component. ECCC Creep Conference, 12–14, London. etd@etd1.co.uk.

Petroleum Res. J. Vol. 21 (2008/2009); P. 39–48, 12 Figs.

Role of Magnetic Field at High PH on Scaling Tendency

Mabrouk Hassan* and Noureddine Boucif **

Abstract: Scale formation has always been a tedious problem to scientists and heating equipment manufacturers as well as production engineers. Scale is encountered most of the time in heat exchangers using hot water or steam as the heating fluid, and in steam production with boilers and various calcium concentrations.

Series of experiments have been undertaken to investigate the formation of calcium carbonate scale on boiler elements. A test rig designed to meet the DGVW testing protocol was used. The effect of physical condition was also investigated. Scaling behavior was assessed and calculated when the flow rate and temperature were kept constant at 25 1/h and 80ºC. The pH was kept at 7-8.5 and the hardness typically greater than 300 mg/1. The tests have shown that reduction in scaling tendency was maximal at 40% and the effect of flow rate was also observed.

Keywords: scaling, hardness, DGVW, calcium carbonate.

INTRODUCTION

The calcium carbonate, which is the preponderant agent for scale, forms a thin layer over the plate or tubing material such that the overall heat transfer is affected negatively. To overcome these shortcomings, manufacturing engineers have to over-design the installation, and production engineers usually have to shut down the production to clean the heat transfer equipments.

It goes without saying that this procedure is of a substantial impact on the budget and maintenance costs. Scientists and engineers have addressed this serious problem since the nineteenth century, suggesting different technical processes to reduce or inhibit the scale formation. The techniques suggested, which differ form one another and apply to specific processes, are chemical (acid washing, inhibitor injection, precipitation, *etc.)* mechanical (over sizing, hydro-blasting, fluidized media, *etc.)* or physical (electric treatment, magnetic treatment, *etc*.)

This paper investigates the scale reduction with a magnetic treatment device plugged on line with two water boilers operated in parallel. The laboratory setup, supplied by Kennikot Ltd., along with a magnetic treatment Aqua Total supplied by BWT , both UK Companies, have been run for a constant surface temperature , a constant liquid flow rate, and various calcium concentrations.

The concept of hardness and alkalinity are closely related to the description of scaling system. Hardness, which is defined as the ability to form a scum with soap[1], is in fact the measure of the water content of and Mg^{2+} both of which tend to form insoluble Ca^{2+} salts with organic anions from detergent. The natural hardness of water is a consequence of the presence in the ground of Ca^{2+} and HCO^{-3}. When natural water boils, calcium and magnesium bicarbonate decompose to carbonates which have a low solubility in water. The amount of hardness, which precipitates in this way, is called the temporary hardness[2]. After all the ions responsible for the temporary hardness have precipitated, the hardness, which is left, is called the permanent hardness.

Alkalinity is the measure of the water's ability to neutralize acid[1]. In natural water, it can be considered as a measure of the waters content in HCO^{-3}. As in the case for hardness, alkalinity is the consequence of the presence in earth's ground of $CaCO_3$. In addition to that, under Henry's law, CO_2 tends to dissolve in water, dissociating into the species responsible for alkalinity.

* Faculty of Health and Wellbeing, Sheffield University, Sheffield, UK;
**Laboratoire LPQ3M, Universte' de Mascara, route de Mamounia, Mascara 29000, Algeria.

Boiler waters contain both carbonate and hydroxide alkalinity. Both are derived from bicarbonates in the feed water. Carbon dioxide is insoluble in boiling water; hence, it is removed with the stream. This causes an increase in the pH and shift in alkalinity from bicarbonate to carbonate and from carbonate to hydroxide. Moreover, under these extreme conditions, pH levels in excess of 11.0 are often obtained[1].

When the solution is heated, CO_2 is removed, favouring the bicarbonate decomposition reaction followed by $CaCO_3$ precipitation. For calcium carbonate to appear in an irreversible manner in a liquid, the sequence of a germination step by growth could take place in the liquid phase. In fact, the germination phenomenon starts with the agglomeration of the hydration ions *i.e.* CO^{-}_{3} and Ca^{2+}

These two ions will then join together to form a colloidal germ having an electrical charge that characterizes the so-called *zeta* potential. Afterwards, this colloidal germ can grow and dehydrate at the same time till a crystal is produced with inherent capability.

If a germ is transferred to a close layer of a metallic wall, it may be adsorbed by the nearby surface, which has a negative electrochemical potential. Hence, one of the two scenarios may take place, either the germ adheres strongly to the wall, and initiates scaling of the metal wall, or it is attracted without being really adsorbed.

A solution is said to be super-saturated when it contains species in concentration such that the corresponding salt's solubility defined by thermodynamic equilibrium is exceeded[3]. This situation arises, if for instance, a solution temperature is modified. Super-saturation is then a consequence of sluggish crystallization kinetics caused by a high activation energy barrier. The formation of crystals (also called nucleation) usually follows and either occurs spontaneously (homogeneous nucleation) or can be aided by the presence of a suitable nuclei, which may be either solid impurities in suspension in the solution or sites on the tubing boiler surface (heterogeneous nucleation). Crystal growth by incorporation of ions into the crystal lattice follows the formation of stable nuclei within the region where super-saturation occurs[4].

One of the characteristics of calcium carbonate is that it possesses an inverse solubility that is to say that the solubility of $CaCO_3$ decreases with temperature. The main consequence of this property is that calcium carbonate will precipitate preferably in areas of high temperature. Heaters are thus particularly exposed to scaling of their surface[4, 5].

When calcium carbonate precipitates, it forms crystals of various defined allotropic structure, or form an amorphous deposit. There are three allotropic forms for $CaCO_3$ crystals: aragonite, calcite and vaterite. Their formation depends on the conditions under which the precipitation occurs, mainly the solution's temperature, and subsequent transformation, particularly in the case of vaterite[5].

Each allotropic form is easily recognized by the shape of the crystal it forms, a needle shape for aragonite, a cubic shape for calcite, and a spherically shape for vaterite.

Water boilers may be considered as heat exchangers in the sense that the heat transmission is similar to that in classical tube and shell heat exchangers. Nevertheless, the heating stream, instead of being a fluid (either liquid or gas), could be a gas combustion or an electrical energy source.

The scaling in water boilers represents a tedious problem. The fouling, due to scaling, can cost a medium size oil refinery as much as one million USD a year in terms of increase in the capital and operating costs. This implies the importance of the market for scaling control. The problems caused by fouling of a water boiler fall into two categories, namely, the operation difficulties and the additional costs. The complexity of these phenomena with their corresponding interaction makes fouling reduction a difficult problem to tackle. In the particular case of scale reduction, it should be noted that crystallization in general, and crystallization of calcium carbonate in particular is a process that is not yet fully understood, and even today is subject to speculation and thorough discussions among chemical scientists[6]. The scale control market incorporates therefore a very wide range of methods based on a variety of fundamental mechanisms, some of which have little scientific credibility. However, scale control methods are generally based on either prevention or inhibition of scale by the injection of chemicals.

The prevention of scale is achieved by eliminating the scale-forming cations (*i.e.* the ions contributing to the hardness) from water. In the case of inhibition, the aim of the technique is to retard as much as possible the appearance of scale formation.

The existing scale controlling techniques can be classified as follow: processes accommodating the effects of scaling in the design of the system, processes using chemical or physico-chemical

treatment of the scaling water, or processes using physical treatment.

The various methods to remove existing scale belong in general to the first category These include acid- washing of the surfaces as well as the various mechanical methods in use, such as brushing and scraping.

Another chemical-based method is precipitation, using for instance soda. This involves separating the precipitates in an additional step using flocculation, sedimentation or filtration processes. This method requires sophisticated process control since the process is highly sensitive to fluctuation of the operating parameters[7, 8].

The pellet softening can also be used as a method of scale reduction. A pellet softener consists of a cylindrical vessel containing a fluidized bed of grains of feed material that provides a large surface on which the crystallization of calcium carbonate takes place in a fast reaction. Softening chemicals such as caustic soda (NaOH*)* lime *(*$Ca(OH)_2$) or soda lime (Na_2CO_3*)* are used to instigate the crystallization. The pellet softening technology presents the advantage of generating recyclable products, solid grains of calcium and bicarbonate cannot be removed to the low concentration produced by conventional softening and the crystallization process only proceeds for as long as the solubility product of calcium carbonate is exceeded. Also, hardly any magnesium is removed.

The physical conditioning can be based on electric, magnetic or ultrasonic treatment. Such treatment does not modify the mineral content of water but the morphology of the precipitated which is then mainly made up of fine particles[9] Moreover by their very nature, these methods do not generally add the chemical content of the water.

The electronic anti-fouling technology (EAF) is based on the use of an induced electrical field that fluctuates with time. An EAF device is usually composed of one or several wires wrapped around a feed pipe to a heat exchanger, forming a solenoid. The two ends of each wire are connected to the EAF, '-control unit, which produces a pulsing current to create time-varying magnetic fields inside the pipe[6].

The ultrasonic treatment is based on a generator which produces electrical impulses at high frequency, which are transmitted via a coaxial to transducers mounted externally. Each transducer contains piezoelectric ceramic crystals which, when excited by the electrical impulses, generate an ultrasonic beam[4, 10].

The magnetic water treatment (MWT) has an extensive history. Based on the application of magnetic field to prevent scale, an early patent by Faunce and Cable was registered in 1890. The MWT works on the principle of forcing oppositely-charged ions to move in opposite directions, hereby producing collisions which result in the formation of microscopic nuclei that cause the calcium carbonate to precipitate within the water instead of on the surfaces of the pipes or heat exchangers.

The process changes the crystalline structure by the use of a magnetic induction field, which when exposed to moving water, interacts with the water's electric dipole moment and applies a torque to the water molecule. The resulting electric double layer of the colloidal particles, when distorted by the external magnetic field, tends to absorb calcium and magnesium ions, thus inhibiting their precipitation on the pipes or heat exchanger surfaces.

MATERIALS AND METHODS

The comprehensive laboratory setup, that is described below has been supplied by Kennicot Ltd, a UK company. Tap water is pumped from a one half-cubic meter tank to two water boilers, with 5.0 liters capacity each, operated in parallel. The flow to each boiler is controlled individually by means of two rotameters. The water, pumped at an approximate pressure of 15 *psig* to the boilers, is heated by an electric source, where the energy is controlled through an electric power recorder. The temperature in both boilers is controlled separately by two digital temperature controllers, as shown in Figure 1. The overflow of the two water boilers is returned to the main water tank after being cooled in a water heat

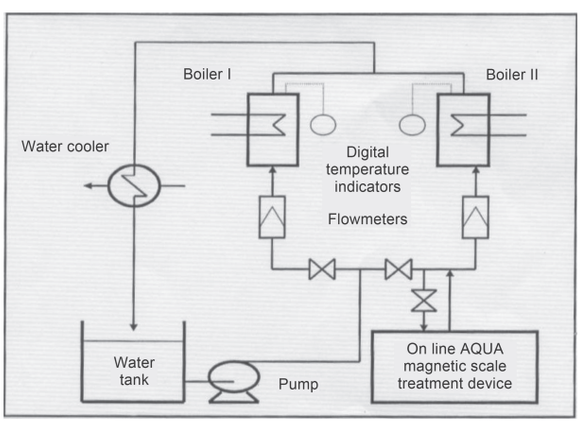


Fig.1. Schematic flowchart of the laboratory setup.

exchanger. The water flow is electrically controlled by a solenoid valve.

The temperature of the water is controlled by the liquid flow rate to each water boiler. The higher is the flowrate; the lower is the temperature in the boiler. The laboratory setup was run at a water temperature nearby 80±1^{0}C which is equivalent to a water flow rate of 25 l/h for most of the experiments carried out in this study.

The magnetic water treatment device plugged on line with a laboratory setup has been supplied by AQUA Total, a UK company, and works according to the DVGW Standard W 512[11] Deutsche Vereinigung des Gas und Was serf aches e.V., English: German Association on Gas and Water[12]. The technical specifications of this device are detailed in Table 1.

Table 1. Technical specifications of the AQUA total 2500.

Characteristic specification	Units	Value
Nominal connector bore	*mm*	25.0
Rated flow	m^3/h	2.50
Pressure drop at rated throughout	*bar*	0.35
Nominal pressure PN	*bar*	10.0
Water temperature max.	^oC	30.0
Ambient temperature max.	^oC	40.0
Dimensions Height Width Length	 *mm* *mm* *mm*	 1060.0 65.0 330.0
Power input	*V/Hz*	230×50
Power consumption max.	*Watts*	60.0
Power consumption approx.	Wh/m^3	55.0
Protection	-	IP54

The water solutions were prepared by adding sodium hydrogen hydroxide to calcium chlorate to form calcium carbonate in a 300 liters capacity tank by adding water and stripping until all the salts were dissolved. The equation below describes the reaction that takes place in the tank:

$$CaCl_2 + NaHCO_3 \rightarrow CaCO_3 + NaCl + HCl$$

Before and after each run, all the equipment was drained and refilled with de-ionized water in order to remove all suspended and scaling matters.

The hardness was measured by the EDTA (ethylene diamine tetra acetic) solution and the alkalinity by the volumetric titration using an N/50 sulphuric acid by means of phenolphthalein and bromocresol colour indicators.

RESULTS AND DISCUSSION

The boiler apparatus has been studied at five different running times in blank and treated modes at different operating conditions (water flowrate and calcium carbonate concentration) as shown in Table 2. The pH was maintained constant around 7.0 to 8.4 during all the different runs.

After each run, the measure of the scaling mass in both boilers was dissolving 5 litres of hydrochloric acid in the boilers. The scaling rate was calculated as the ratio of the scaling amount by the running time. In the first run, when water is circulated at 981/h, the scaling rate is 1.97 mg/h whereas it decreases to 0.98 mg/h, nearly by half, when the flow rate is lowered to 25 l/h. The flow rate has a substantial effect on the scaling rate, in the sense that the scaling rate increases as the fluid velocity is augmented.

The laboratory setup has been run for quite long times to enhance scale deposit as much as possible. The hardness decay of the prepared solution in the water tank during both treated and untreated runs were linear as shown in Figure 2. The behavior of the alkalinity decay in the water tank observed during different runs was also linear as shown in Figure 3.

Figure 4 shows that the pH fluctuated from 7.9 to 8.1 which represent a 2.5 % change. There was slightly no effect on the pH while running the experimental setup in a blank regime. However, a substantial change on the pH was observed when the magnetic treatment was incorporated in the loop. The pH fluctuated from 7.6 to 8.3 in a parabolic

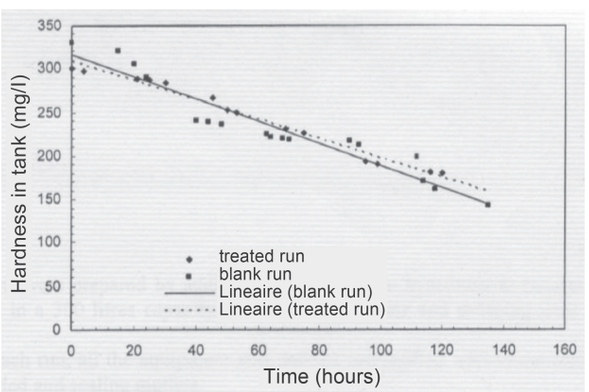


Fig. 2. Depletion of hardness in treated and untreated regimes.

behavior. Some authors[13, 14] have mentioned that the influence of the magnetic treatment on low pH, whereas for high pH's the impact is considerable.

The incorporation of the magnetic treatment device in the experimental station loop reduces drastically the scaling rate as shown in Figure 5. A considerable decay of around 40% has been observed between the treated and untreated regimes as exhibited by Figure 6. The scale amount deposited in boiler I (left) is slightly higher compared to that in boiler II (right) due to the fact that the latter is located nearer to the magnetic device and, henceforth the circulating water benefits from a better treatment (Fig. 7).

The morphology analyzed by SEM (Scanning Electronic Microscope) of the scale crystals deposited at the walls and elements of both left and right boilers at the end of run 1 (blank) and run 3 (treated) are summarized in Table 3. The scales deposited at the walls of the right boiler are needle shape and smooth, whereas those deposited on the left one are soft.

Figures 8 and 9 show SEM pictures of the scale deposited on hot surface areas qualified usually as if calcite, a hard scale, and aragonite are soft scale. This depends on the solution chemistry and surface temperature. It has been reported[13] that aragonite shape formed at around 60°C. The soft scale has formed on walls and hard scale on elements during the blank run while in the treated one, the formation of scale on elements is soft and deposit as aragonite and calcite with a larger size.

The trace amounts of iron in water form paramagnetic FeOOH clusters that are retained and

Table 2. Operating conditions of scale laboratory setup.

	Run#1	Run#2	Run#3	Run#4	Run#5
Mode of running	Blank	Blank	Treated	Treated	Blank
Flow rate (l/h)	98 25	25	25	25	25
Running time (h)	75 151	109	105	116	123
Tank temperature (°C)	33 20	35	35	30	30
Left boiler temperature (°C)	80	80	80	80	80
Right boiler temperature (°C)	80	80	80	80	80
Initial hardness (mg/l)	300	450	340	300	300
Initial alkalinity (mg/l)	450	450	340	340	340

Table 3. SEM of scale crystals formation during run 1 (blank) and 3 (treated).

Run. No.	Right boiler				Left boiler			
	Element		Wall		Element		Wall	
	Shape	Size	Shape	Size	Shape	Size	Shape	Size
Run1 (blank)	Aragonite	25-30 microns	Needle shape	Tiny	Aragonite	20 microns	Soft scale	Small
Run 3 (treated)	Aragonite	200-300 microns long	-	-	Calcite	150-200	-	-

Table 4. Summary of changes on water quality in the tank.

Run number	Amount of dosing	Change in Ca	Change in HCO_3	Change in pH	Time	Flow rate	Reduction rate
	mg/1	mg/1	mg/1		h	L/h	$g/h10^{-3}$
Run 1(B)							
Dosing 1	280	132	216	0.36	75	98	1.75
Dosing 2	290	186	0.14	0.14	30	25	6.20
Dosing 3	300	162	0.38	0.38	25	25	5.40
Dosing 4	298	176	0.19	0.19	23	25	7.60
Run 2 (B)							
Dosing 1	422	292	176	-0.88	85	25	3.43
Dosing 2	290	120	192	0.13	24	25	5.00
Run 3 (M)	340	142	101	0.57	105	25	1.35
Run 4 (M)	300	121	150	-0.71	116	25	1.04
Run 5 (B)	330	170	165	-0.31	123	25	1.98

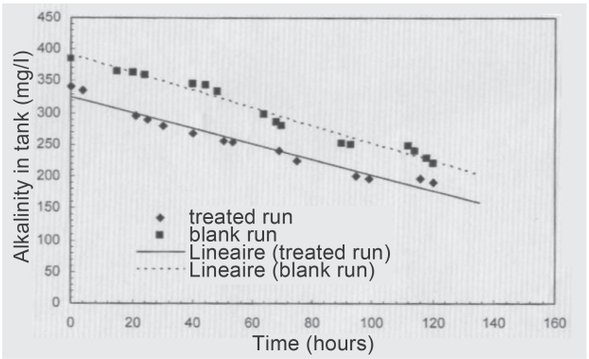


Fig. 3. Depletion of alkalinity in treated and untreated regimes.

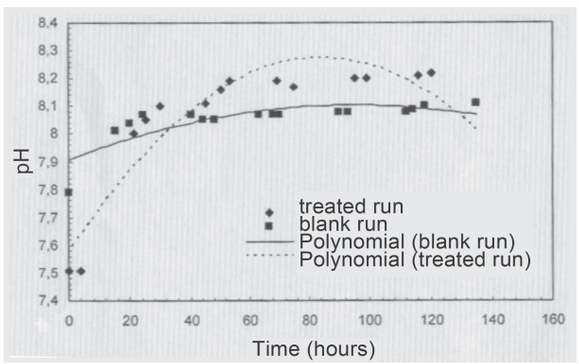


Fig. 4. Effect of the scaling on the pH.

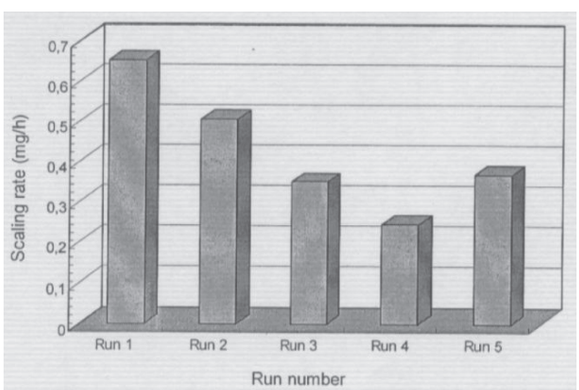


Fig. 5. The evolution of the scaling rate.

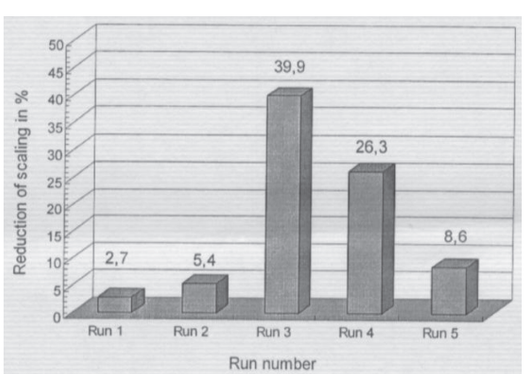


Fig. 6. The reduction of scale deposited in both boilers in %.

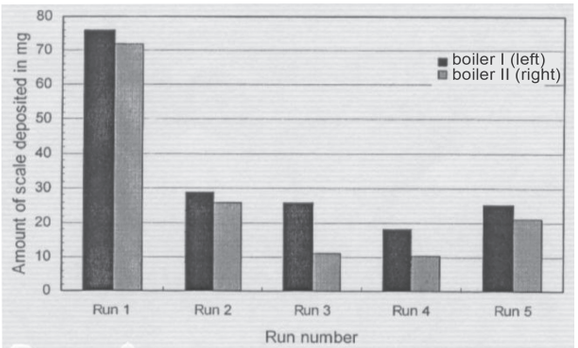


Fig. 7. The amount of scale deposited in both boilers.

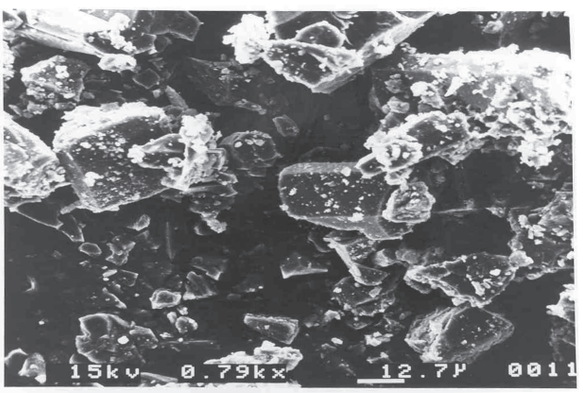


Fig. 8. SEM photograph of calcite crystals deposited in a treated run.

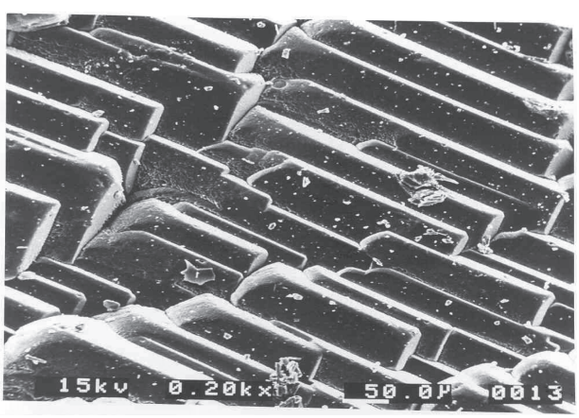


Fig. 9. SEM photograph of aragonite crystals deposited in a treated run.

which serve as nucleation centers which enhance the development of aragonite formation. The aragonite, being slightly less stable than calcite, tends to form elongated needle-like crystals as pictured in Figure 9.

Calcium carbonate samples of scale formed on water boiler deposited on the wall and the elements were taken at the end of run 1 from left and right boilers and analysed by Scanning Electronic Microscope (Table 4).

The scale shown in Figures 10(a) and (b) is that of the right boiler whereas Figures 11 (a) and (b) show the crystals formed in the wall region from the left boiler. Different types of scales can be clearly recognized:

- needled smooth shape in the wall, nearly 10 mm in size, classified as soft scale.
- aragonite shape in the elements (both from left and right boiler) near 20mm in size, and classified as hard scale.

From the three calcium carbonate po1ymorphs (calcite, aragonite and vaterite), calcite is the most thermodynamically stable form at standard temperatures and pressures[15]. However, at the surface temperature commonly encountered in systems such as heat exchangers and boilers, aragonite is normally the first phase to precipitate out of solution. In this case, recrystallisation of the aragonite into calcite overtime may enhance the formation of a more tenacious encrustation [16].

Magnetic treatment has been found to cause occasional difference in the precipitated crystal habit in order to determine any possible influence of the magnetic treatment on the structure of the $CaCO_3$ layers. Two studies were undertaken: first, SEM pictures of the scale samples were taken, and secondly, the relative proportion of the two main allotropic forms of calcium carbonate was evaluated. The two studies were made possible because of the difference in physical properties of the two allotropic forms of $CaCO_3$ (calcite and aragonite). The calcite tends to form what was referred in literature as hard scale, whereas the aragonite referred to as soft scale.

The main difference in the macroscopic level between these two types of scale is that calcite tends to adhere quite strongly to the surface it crystallises on, whereas aragonite adheres rather weakly. In our experimental work, the boilers were consisted with copper element. It basically describes the ($CaCO_3$ crystallised on the copper element according to the simple graph of Figure 12. In addition, by gently removing the scaled copper element on the hard surface, it was possible to separate the two types of scale as illustrated in that figure.

The treatment of calcium carbonate solutions with

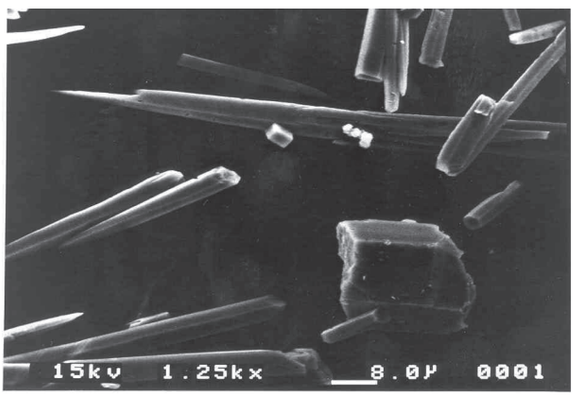


Fig. 10a. SEM photograph of scale formed on boiler wall during run 1.

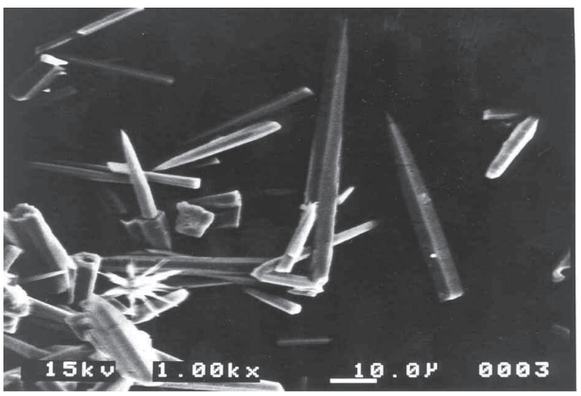


Fig. 11a. SEM photograph of scale formed in boiler wall in run1.

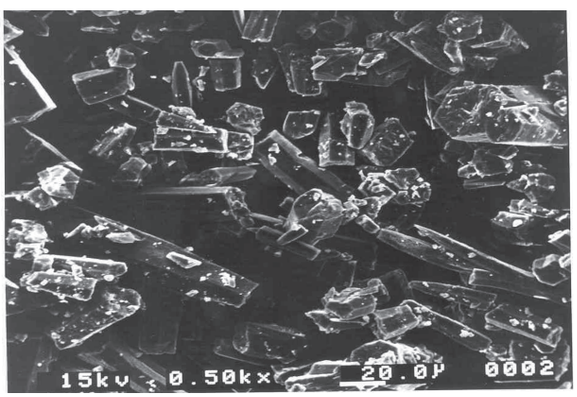


Fig. 10b. SEM photograph of scale formed on the element during run 1.

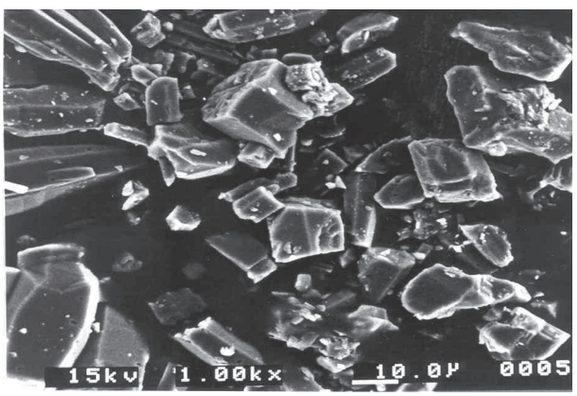


Fig. 11b. SEM photograph of scale formed in element boiler in run 1.

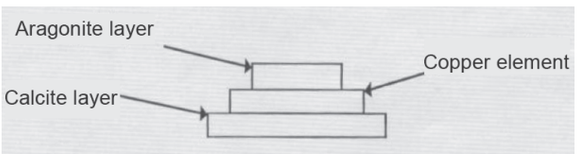


Fig. 12. Cross section of the scale deposits.

substantial orthogonal fields [7000 Gauss] can, depending on the chemistry, reduce precipitation of calcium carbonate and calcium sulphate. Scaling of surfaces on heat exchangers can be reduced by 80% as mentioned by Coetzee[17], and by 90% as mentioned by Aqua Total on DGVW. An effect has been shown quantitatively in both static and flowing systems, results have shown that colloidal stability is influenced by the application of a magnetic field that will lead to accelerated coagulation confirmed by the increasing agglomerates found in the scale, nucleation and crystal growth rates are also reduced leading to the formation of irregularly shaped crystal forms.

HOW DOES IT WORK?

There was a wide range of mechanisms proposed for how magnetic treatment works, but most of them are unproven yet. The most likely mechanism is the effect of micro contaminants[17], interfacial phenomena-macroscopic or surface/interfacial phenomenon. The intra-atomic effect will be on stages which can be summarised as the following process: electron excitation - electron spin interaction -electron transfer - molecular bond breaking. In recent works, it was identified that the key roles of micro-contaminants which affect the crystal nucleation grout rate[17]. Gotezee[18] reported a reduction in carbonate precipitation following adsorption of free Zn (II) cations present at the ppb level.

CONCLUSION

The conditions of running the experimental setup were similar to the DGVW test.

The application of temperature, pH and concentration, was reached through the blank run.

The use of photographic images from SEM analysis proved too subjective from use as a qualitative indication in the change of crystal morphology. It was apparent that the microscope operator could manipulate selection of the crystal images to illustrate the difference in morphology.

In addition, it can be said that magnetic treatment can reduce the scaling under the correct conditions of temperature, pH, hardness and flow. Also the once through magnetic treatment can reduce the scaling.

- Morphology of scale different between treated run and untreated run.
- No scale despite on wall boiler in treated run.
- Maximum reduction on hardness in tank 30-35% were $5x10^{-3}$ g/h.
- Reduction rate in tank were high at small flow rate.
- No effect of flowrate on scale formation, were observed at a rate of 98 l/h.
- Effect of flow rate on surface temperature.
- Maximum reduction of 40% in scaling formation in boilers.
- The scale in left boiler was less than in right one.
- Formation of scale on surface at high hardness.

The magnetic anti scale treatment knows, since the last few years, an overwhelming interest among the" specialized scientific community as a scaling inhibitor. The experimental study of this process has clearly shown that this one is capable of reducing the scale formation by up to 40 % with a negligible effect on the pH of the circulating water. In a future work, higher initial concentrations with longer running times will be investigated for collecting a wide range of data with the laboratory setup run at different operating conditions. A budgetary and investment study is aimed to be performed for comparison with the classical treatments processes.

REFERENCES

[1] Sawyer, C. N.,Cathy, P. L.Mc. and Perkin, G. E., 1994. *Chemistry of Environmental Engineering*. McGraw Hill International 4th edition, Singapore

[2] Porteous, P.,1996. *Dictionary of Environmental Science and Technology*. John Wiley & Sons Ltd. New-York 2nedition

[3] Bott,T. R.,1997. Aspects of crystallization fouling. *Thermal and Fluid Science Experimental*, **14**, 356-360.

[4] Sanchez, G. E., 1998. *Scale Control in Heat Exchangers*. M. Phil. Thesis, Cranfield University

[5] Coetzee, P. P.,Yacoby, M. and Howell, S., 1996. The role of zinc in magnetite and other physical water treatment methods for the preventation of scale. *Water S. A*., **22**, 319-326.

[6] Cho, Y.I., Fan, C. F. and Drazner, B. J., 1998. Theory of electronic anti-fouling technology to control precipitation fouling in heat exchanger. *Heat International Communication and Mass Transfer*, **24**, 747-756.

[7] Rautenbach, R. and Albrecht, R., 1989. *Pretreatment Method against $CaCO_3$,Scaling in Membrane Processes*. 233-238, John Wiley & Son,UK.

[8] www.accepta.com/Industry Water Treatment/Magnatic treatment.asp. Acces date 18.3.2005.

[9] Euvrard, M., Leroy, P. and Ledion, J., 1997. Effects and consequences of electric treatment in preventing scaling of drinking water systems. *J. of Water Supply Research and Technology- Aqua*, **46**, 71-83.

[10] Anonymous, 1997 (Feb.). Seawater intake pipe-work kept clear by electronic and ultrasonic anti-fouling. *Mer-Marine Engineers Review***,**

[11] DVGW-Arbeitsblatt W 512(Ausgabe 9/96). Verfahren zur beurteilung der wirksamkeit von wasserbehandlung-sanlagen zur verminderung von steinbildung.

[12] DVGW, Wächter, S., 2000. From the main office department. Private communication (dated 1-09-2000).

[13] Baker, J., Judd, S. J. and Parsons, S. A., 1997. Anti-scale magnetic pre- treatment of reverse osmosis feed water. *Desalination*, **11**, 151-166.

[14] Coey, J. M. D. and Cass, S., 2000. Magnetic water treatment. *J. of Magnetism and Magnetic Materials*, **209**, 71-74.

[15] Parsons, S.,1999 (April). *Overview of Recent Magnetic Treatment Researches*. 3rd Cranfield University Conference on Magnetic Treatment.

[16] Hrzo R. E., Shi, Q. H., Patil, J. N.,and Katz, J. L., 1989. Magnetic water treatment : the effect of iron on calcium carbonate nucleation. Langmuir, 861-867.

[17] Coetzee, P., Yacobsy, M. and Howell, S. 1996. The role of zinc in magnatic and other physical water treatment methods for the prevention of scale. *Water S. A*., **22**,319-326.

[18] Coetzee, P. P.M.,1999 (April). The Role of Zinc in Physical Water Conditioning. 3rd Cranfield Univ. Conf. on magnatic treatment .

Petroleum Res. J. Vol. 21 (2008/2009); P. 49–56, 11 Figs.

A Study of the Predictive Thermodynamic Models for the Wax Deposition of Synthetic Fuels

Layla Alghanduri*, Abdulghani .A., Nhaesi** and Mohamed M. Elgarni*

Abstract: Local composition models (UNIQUAC, Wilson and NRTL) and regular solution models (Won and Pedersen) were applied to predict the cloud point temperature of systems with n-alkanes and acceptable results were obtained by these models. The prediction of wax formation and the composition below cloud point temperature were done by UNIQUAC model using two different structural parameter for solid phase activity coefficient (UNIQUAC10 and Coutinho 2000). The results that are more accurate for calculating the wax content and the composition at different temperatures below cloud point were obtained using UNIQUAC10.

Keywords: Cloud point, model, solid-liquid equilibrium.

INTRODUCTION

The majority of petroleum fluids contain heavy hydrocarbons, which at low temperatures may precipitate as a wax phase. The presence of wax phase causes problems during oil production, transport and use of both crude oil and refined products. This phenomenon is responsible for losses of billions of dollars per year in the petroleum industries. Under-standing the wax phase and modeling this behavior are fundamental in dealing with this problem. Thermodynamically, this problem treated for along time as solid liquid equilibria models. Different models are presented in the literature. The models differ in the approach for describing the non-ideality of solid and liquid phases. In this study, computer programs have been developed on the basis of thermodynamic models.

The main purpose of this paper is to apply some thermodynamic models that can be used to predict cloud point temperature based on literature experimental data. A comparison between the predictions of these models and experimental data is presented. The models selected in this study are regular solution models (Won and Pedersen) and local composition models (UNIQUAC, Wilson, and NRTL).

THERMODYNAMIC MODELS

The cloud point is defined as the temperature at which the first crystal appears in petroleum fluids. The formation of wax is treated as solid liquid equilibrium between a solution (liquid phase) and solid phase (wax) in a hydrocarbon mixture.

The general solid-liquid equilibrium equation relates the composition in both phases with the non ideality of the phases and the pure component thermophysical properties.

The equilibrium equation relating the composition in the liquid and solid phases with the non ideality of the phases and the thermophysical properties of the pure components can be written for each component i present at equilibrium as[1]:

$$\left(\frac{x_i^s \gamma_i^s}{x_i^l \gamma_i^l}\right) = \frac{\Delta h_{m,i}}{RT_{m,i}}\left(\frac{T_{m,i}}{T} - 1\right) + \frac{\Delta h_{tr,i}}{RT_{tr,i}}\left(\frac{T_{tr,i}}{T} - 1\right) - \frac{\Delta cp_{m,i}}{R} \left(\ln\left(\frac{T}{T_{m,i}}\right) + \frac{T_{m,i}}{T} - 1\right) \quad (1)$$

Where $\Delta h_{m,i}$ is the enthalpy of melting for component i, $T_{m,i}$ is the melting temperature, $\Delta h_{tr,i}$ is the transition enthalpy of component i, $T_{tr,i}$ is the transition temperature of component i, ΔCp_m is the heat capacity at melting temperature, and γ_i^s, γ_i^l are the activity coefficients for both liquid and solid phases respectively.

Regular solution models: Won and Pedersen

Won model

Two simplifications in equation (1) were done by Won[2]. First the heat capacity differences were neglected in the equilibrium ratio. Secondly, the melting temperatures and solid-solid transition

*Libyan Petroleum Institute, Tripoli, Libya P.O.BOX 6431.
** University of Bahrain, Bahrain, P.O.BOX 38032.

temperatures are considered as equal, and then the general expression can be written as:

$$\ln\left(\frac{x_i^s \gamma_i^s}{x_i^l \gamma_i^l}\right) = \frac{\Delta h_{m,i}}{RT_{m,i}}\left(\frac{T_{m,i}}{T} - 1\right) \quad (2)$$

Won[2] used the regular solution theory in order to describe the nonideality in the oil (liquid) and wax (solid) which means that the activity coefficients are determined from the solubility parameters of the individual components

$$\ln \gamma_i = V_i \frac{(\bar{\delta} - \delta_i)^2}{RT} \quad (3)$$

$$\bar{\delta} = \sum \Phi_i \delta_i \quad (4)$$

$$\Phi_i^l = \frac{x_i v_i}{\sum x_i v_i} \quad (5)$$

$$\Phi_i^S = \frac{S_i v_i}{\sum S_i v_i} \quad (6)$$

Where v_i is the molar volume, δ_i is the solubility parameter, Φ_i is the volume fraction of component i, is the average solubility parameter of the mixture, S_i and Xi are the mole fractions for solid and liquid phases. Won used the following expression to determine for the melting enthalpy (cal/mol) of component i:

$$\Delta H_{m,i} = 0.1426\, Mw_i T_{m,i} \quad (7)$$

Where Mw_i is the molecular weight and $T_{m,i}$ the melting temperature in Kelvin and has the following expression:

$$T_{m,i} = 374.5 + 0.02617\, Mw_i - \frac{20172}{Mw_i} \quad (8)$$

The molar volume, v_{i-} in the equations 5 and 6 was calculated by the following correlation[2]:

$$V_i = \frac{Mw_i}{d} \quad (9)$$

Where:

$$d = 0.8155 + 0.6272 * 10^{-4} Mw_i - \frac{13.06}{Mw_i} \quad (10)$$

The solubility parameters, for both liquid and solid phases of the normal paraffin up to C_{40}, which were used by Won[2] are presented in Table (1).

Pedersen model

Pedersen et al.[3] have made two modifications of Won's model. The first modification takes the heat capacity difference into account in the equilibrium equation, and has the following form:

$$\Delta Cp_i = (0.3033 Mw_i - 4.635 * 10^4 Mw_i T) \quad (11)$$

The second is that the solubility parameters are function of carbon number of components according to[3]:

$$\delta_i^l = 7.41 + 0.5914(\ln C_n - \ln 7) \quad (12)$$

$$\delta_i^S = 8.5 + 5.763(\ln C_n - \ln 7) \quad (13)$$

Where: C_n is carbon number.

Table 1. Solubility Parameters $(cal/cm^3)^{0.5}$ for paraffinic components used in Won's model[2].

COMPONENT	δ^L	δ^S
C_{10}	7.71	9.17
C_{11}	7.78	9.32
C_{12}	7.83	9.44
C_{13}	7.88	9.55
C_{14}	7.92	9.64
C_{15}	7.96	9.72
C_{16}	7.99	9.79
C_{17}	8.02	9.86
C_{18}	8.05	9.92
C_{19}	8.07	9.97
C_{20}	8.09	10.0
C_{21}	8.11	10.1
C_{22}	8.13	10.1
C_{23}	8.15	10.1
C_{24}	8.17	10.2
C_{25}	8.18	10.2
C_{26}	8.20	10.3
C_{27}	8.21	10.3
C_{28}	8.22	10.3
C_{29}	8.24	10.3
C_{30}	8.25	10.4
C_{31}	8.26	10.4
C_{32}	8.27	10.4
C_{33}	8.28	10.4
C_{34}	8.29	10.4
C_{35}	8.30	10.5
C_{36}	8.31	10.5
C_{37}	8.32	10.5
C_{38}	8.33	10.5
C_{39}	8.34	10.5
C_{40}	8.35	10.6

Local composition models: UNIQUAC, Wilson, and NRTL

These models are based on the concept that the composition of the system in the neighborhood of a given molecule is not the same as the bulk composition and presumed to account for the short-

range order and nonrandom molecular orientations that result from differences in molecular size and intermolecular forces. The heat capacity term of equation (1) is neglected and is not used in the modeling of the local composition model[4,5].

The Liquid Phase Nonideality

The activity coefficient model used for the liquid phase can be described as:

$$\ln \gamma_i^{l} = \ln \gamma_i^{res} + \ln \gamma_i^{comb-fv} \quad (14)$$

Where the residual contribution for the activity coefficient, γ^{res}, is estimated by UNIFAC model and the Flory-free volume equation[6,7] were used to provide the combinatorial term

$$\gamma_i^{comb-fv} = \ln \frac{\Phi_i}{x_i} + 1 - \frac{\Phi_i}{x_i} \quad (15)$$

with:

$$\Phi_i = \frac{x_i (v_i^{0.333} - v_{wi}^{0.333})^{0.333}}{\sum_{j=1}^{n} x_j (v_j^{0.333} - v_{wj}^{0.333})^{0.333}} \quad (16)$$

Where v_i is the molar volume, and v_{wi} is the van der waals volume of component i

The Solid Phase Nonideality

The solid phase non-ideality was described using three different predictive local composition models: UNIQUAC, Wilson, and NRTL[8,9].

UNIQUAC model for solid phase activity coefficient: The UNIQUAC model for solid phase used has the following form:

$$\ln \gamma_i^s = \ln\frac{\Phi_i}{x_i^s} + 1 - \frac{\Phi_i}{x_i^s} - Z/2\, q_i \left[\ln\frac{\Phi_i}{\theta_i} + 1 - \frac{\Phi_i}{\theta_i}\right] + q_i - q_i \ln\left[\sum_{j=1}^{n}\theta_j \tau_{ji}\right] - q_i \ln \sum_{j=1}^{n} \frac{\theta_j \tau_{ij}}{\sum_{k=1}^{n}\theta_k \tau_{kj}} \quad (17)$$

With:

$$\Phi_i = \frac{x_i r_i}{\sum_{j=1}^{n} x_j r_j} \quad (18)$$

$$\theta_i = \frac{x_i q_i}{\sum_{j=1}^{n} x_j q_j} \quad (19)$$

τ_{ji} is the interaction parameter.

Subscript i identifies species and j is a dummy index. All summations are over all species.

The structural parameters r_i (relative molecular volume) and q_i (a relative molecular surface area) are function of paraffin chain length. The correlations used for r and q are[10,11]:

$$r_i = 0.0148 C_n + 0.0096 \quad (20)$$

$$q_i = 0.0185 C_n + 0.0211 \quad (21)$$

***Wilson model for solid phase activity coefficient*:** The Wilson equation used to predict the nonideality of solid phase is a modification of the original Wilson equation, where the contribution of the molar volumes to the local compositions is not taken into account and q_i (area parameter) was added to the interaction parameter.

$$\gamma_i^s = 1 - \ln \sum_{j}^{n} x_j A_{ij} - \sum_{k}^{n} \frac{x_k A_{ki}}{\sum_{j}^{n} x_j A_{kj}} \quad (22)$$

Where: $A_{ij} = \exp\left(-\frac{\lambda_{ij} - \lambda_{ii}}{RT}\right)$

***NRTL model for solid phase activity coefficient*:** The NRTL model for solid phase was used without modifications of the original NRTL model and has the following form:

$$\gamma_i^s = \frac{\sum_{j=1}^{n} \tau_{ij} G_{ij} x_j^s}{\sum_{k=1}^{n} G_{ki} x_k^s} + \sum_{j=1}^{n}\left[\frac{x_j^s G_{ij}}{\sum_{k=1}^{n} G_{kj} x_k^s}\left(\tau_{ij} - \frac{\sum_{k=1}^{n} x_k^s \tau_{kj} G_{kj}}{\sum_{k=1}^{n} G_{kj} x_k^s}\right)\right] \quad (23)$$

Where: $G_{ij} = \exp\left(-\alpha_{ji}\tau_{ji}\right)$

Where á is a measure of the non-randomness of the mixture and for the solid phase has a value of $\alpha=2/Z$, and Z is the coordination number for solid phase having a value of 6.

For these three models studied, the estimation of the local compositions is based on the interaction energies between pairs of molecules, λij. The pair interaction energies between two identical molecules were predicted using the enthalpy of sublimation of the orthorhombic crystalline phase of the pure component:

$$\lambda_{ii} = -\frac{2}{z}\left(\Delta_{sub,i} H - RT\right) \quad (24)$$

Where *z* is the coordination number with a value of 6 for the n-alkanes in the orthorhombic crystals[11] and is the enthalpy of sublimation of the pure n-alkanes defines as:

$$\Delta_{sub,i} H = \Delta H_{vap} + \Delta H_{fus} + \Delta H_{tr}. \quad (25)$$

THERMOPHYSICAL PROPERTIES FOR THE N-ALKANES

The following correlations were used to calculate the parameters needed to obtain the the thermophysical properties of the n-alkanes in local composition models used in this paper[12]:

$$T_{fus,i}[K] = 421.63 - 1936412\exp\left(-7.8945(Cn_i - 1)^{0.07194}\right) \quad (26)$$

$$T_{tr,i}[K] = 420.42 - 13487\exp(-4.344\left(Cn_i + 1\right)^{0.14627}) \quad (27)$$

and

$$\Delta H_{tot,i}[KJ/mol] = 3.7791Cn_i - 12.654 \quad (28)$$

$$\Delta H_{fus,i}[KJ/mol] = 0.0035Cn_i^3 - 0.2376Cn_i^2 + 7.400Cn_i - 34.814 \quad (29)$$

with

$$\Delta H_{tr,i} = \Delta H_{tot,i} - \Delta H_{fus,i}$$

Where C_{ni} is the number of carbon atoms in n-alkanes.

Morgan and Kobayashi correlations were used to predict the heat of vaporization[13].

$$\frac{\Delta H_{vap,i}}{RT} = \Delta H_v^{(0)} + \omega\Delta H_v^{(1)} + \omega^2\Delta H_v^{(2)}$$

With

$$\Delta H_v^{(0)} = 5.2804X^{0.3333} + 12.865X^{0.8333} + 1.171X^{1.2083} - 13.116X + 0.4858X^2 - 1.088X^3 \quad (30)$$

$$\Delta H_v^{(1)} = 0.80022X^{0.333} + 273.23X^{0.8333} + 465.08X^{1.2083} - 638.51X - 145.12X^2 + 74.049X^3 \quad (31)$$

$$\Delta H_v^{(2)} = 7.2543X^{0.3333} - 346.45X^{0.8333} - 610.48X^{1.2083} + 839.89X + 160.05X^2 - 50.711X^3 \quad (32)$$

where: $X = \left(1 - \frac{T}{T_C}\right)$

The acentric factor is a function of the carbon number, C_{ni},

$$\omega = -0.000185397\,Cn_i^2 + 0.0448946\,Cn_i - 0.0520750 \quad (33)$$

The critical properties are obtained from the correlations of Twu[14]:

$$\theta = \ln(Mw)$$

$$T_b[K] = \left[\exp\left(5.71419 + 2.715790 - 0.2865902 - \frac{39.8544}{\theta} - \frac{0.122488}{\theta^2}\right) - 24.7522\theta + 35.31550^2\right]/1.8 \quad (34)$$

$$T_C[k] = T_b\left(0.533272 + 0.343831\times10^{-3}T_b + 2.52617\times10^{-7}T_b^2 - 1.65848\times10^{-10}T_b^3 + \frac{4.60774\times10^{24}}{T_b^{13}}\right)^{-1} \quad (35)$$

$$P_C[atm] = \left(1.0 + 0.312\left(1 - \frac{T_b}{T_C}\right)^{0.5} + 9.1\left(1 - \frac{T_b}{T_C}\right) + 9.4417\left(1 - \frac{T_b}{T_C}\right)^2 + 27.1793\left(1 - \frac{T_b}{T_C}\right)^3\right)^2 \quad (36)$$

Ideal solution model

The simplest model also has been tested in which liquid and solid phases are assumed an ideal solution,

$$\gamma_i^l = 1\,, \quad \gamma_i^s = 1 \quad (37)$$

RESULTS AND DISCUSSION

Experimental data of synthetic fuel[15] have been used to test the predictive capabilities of these various models for predicting the cloud point temperature. Also UNIQUAC model was used to predict the composition and contents of wax below this point. This synthetic fuel, Table(2) consists of five synthesis paraffinic systems. These systems were made up of

Table 2: Composition in mass % of the paraffinic system.

	BIM0	BIM3	BIM5	BIM9	BIM13	Purity
$n.C_{10}$	63.84	64.25	64.65	65.59	66.65	>99.0
$n.C_{18}$	4.276	4.872	5.383	6.958	10.57	>99.0
$n.C_{19}$	3.871	4.411	4.874	6.301	9.571	99.0
$n.C_{20}$	3.494	3.981	4.400	5.688	8.641	99.0
$n.C_{21}$	3.149	3.587	3.963	5.124	-	>98.0
$n.C_{22}$	2.828	3.221	3.561	4.603	-	99.0
$n.C_{23}$	2.536	2.889	3.193	-	-	99.0
$n.C_{24}$	2.270	2.586	2.858	-	-	>99.0
$n.C_{25}$	2.028	2.310	-	-	-	>98.0
$n.C_{26}$	1.811	-	-	-	-	>99.0
$n.C_{27}$	1.612	-	-	-	-	>98.0
$n.C_{28}$	1.441	-	-	-	-	>98.0
$n.C_{29}$	1.274	1.451	-	-	-	>99.5
$n.C_{30}$	1.130	1.290	1.424	-	-	>99.0
$n.C_{31}$	1.004	1.142	1.262	-	-	>97.0
$n.C_{32}$	0.887	1.011	1.119	1.444	-	>98.0
$n.C_{33}$	0.788	0.895	0.989	1.280	-	>99.5
$n.C_{34}$	0.695	0.790	0.873	1.129	1.716	>98.0
$n.C_{35}$	0.522	0.698	0.771	0.998	1.516	>99.5
$n.C_{36}$	0.541	0.616	0.682	0.881	1.337	>98.0

a solvent (n-decane) plus synthetic wax in the proportion of 4 moles of n-decane to 1 mole of wax. The composition of waxes is essentially made up of heavy n-paraffins whose carbon number varies from 18 to 36.

Comparison between predicted values using the various models and experimental values is reported in Table (3).

It can be clearly seen from this table that the use of local composition models in general provides satisfactory prediction of the cloud point temperatures with the deviation less than experimental error. In the regular solution models, the results were satisfactory for Pedersen model. This model gave better prediction than Won model as shown in Table (3). This can be attributed to the fact that Pederson model considered the difference between solid and liquid heat capacities, a term has been neglected in Won model. Also it seemed the estimation values of solubility parameter necessary to increase the values of the solid phase solubility parameters as compared with Won model.

The large deviation was clear in an ideal solution model, this leads to a clear indication of the importance of using a description of the non-ideality in the solid-liquid equilibrium.

Composition of solid phase at cloud point

The composition of the solid phase at cloud point for the synthetic fuel were predicted by the models carried out in this work, and exponential decay of normal alkanes can be seen clearly from Figures 1 and 2 for BIM0 system .

A study of solid deposit at cloud point, by these different models leads to similar prediction. The heavy components are present in the first solid bulk, whereas the lightest do not precipitate. This means that only the heaviest components are contained in the solid phase at the cloud point temperature.

Table 3: Deviation "T" between experimental and calculated cloud points.

MODEL	BIM0	BIM3	BIM5	BIM9	BIM13
Texp/K	308.75	309.65	310.37	311.33	312.31
Won	-4.51	-3.71	-1.02	-1.71	4.42
Pedersen	-0.1	0.17	0.67	0.93	1.85
UNIQUAC	-1.94	-1.72	-1.23	-1.03	0.35
Wilson	0.05	-0.07	0.16	-0.17	-0.01
NRTL	-1.91	-1.04	0.03	1.75	3.73
Ideal solution	-7	-6.33	-5.55	-4.75	-4.45

Wax solid content and liquid- solid equilibrium

Solid liquid equilibrium model at temperatures below cloud point was calculated using UNIQUAC model. The solution of the model was based on the methodology prepared by Leivobici and Neoschil[16].

To test the UNIQUAC model ability to predict liquid-solid phase composition below cloud point, experimental data, Table (2), were used[15]. In the prediction, two different structural parameters r and q of the solid phase have been used; the first is mentioned above in equations 20, 21 and its named as Coutinho 2000[10]. The second is UNIQUAC10[17], it has the following form:

$$r_i = 0.1C_n + 0.0672 \quad (38)$$

$$q_i = 0.1C_n + 0.1141 \quad (39)$$

Figures 3 to 6 show the comparison between the experimental and calculated composition in the solid phase at different temperatures. Also Figure 7 shows the comparison between the experimental wax solid composition content and that predicted by the two different structural parameters. It can be seen that the UNIQUAC 10 gives better results in comparison with Coutinho 2000[10].

For liquid phase, the UNIQUAC model provides an excellent description of the experimental data for all of the systems studied using these two structural parameter correlations, equations. Figures 8 to 11 show the comparison between the experimental and calculated composition in the liquid phase at different temperatures for the different systems.

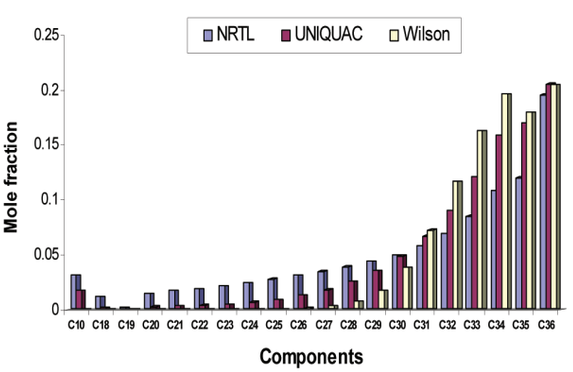


Fig. 1. Solid phase composition at cloud point for BIM0 system by local composition models.

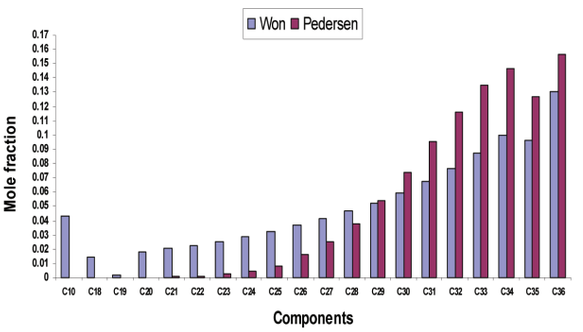


Fig. 2. Solid phase composition at cloud point for BIM0 system by regular solution models.

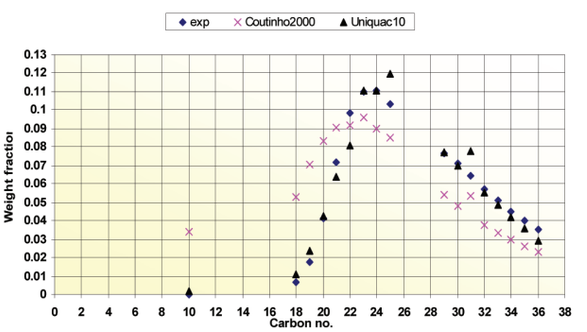


Fig. 3. Comparison between experimental [15] and predicted solid phase composition of BIM3 system at 278.35K by two different structural parameters.

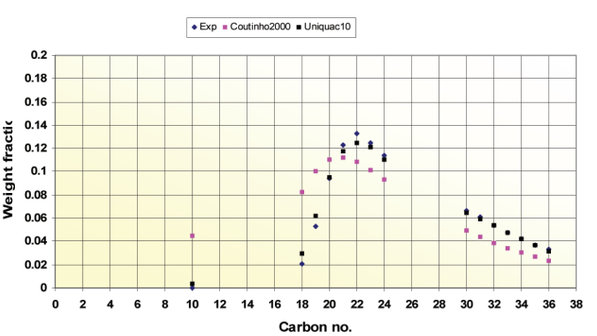


Fig. 4. Comparison between experimental [15] and predicted solid phase composition of BIM5 system at 273.45K by two different structural parameters.

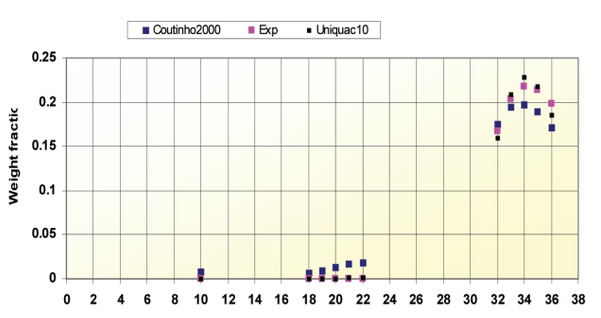


Fig. 5. Comparison between experimental [15] and predicted solid phase composition of BIM9 system at 303.15K by two different structural parameters.

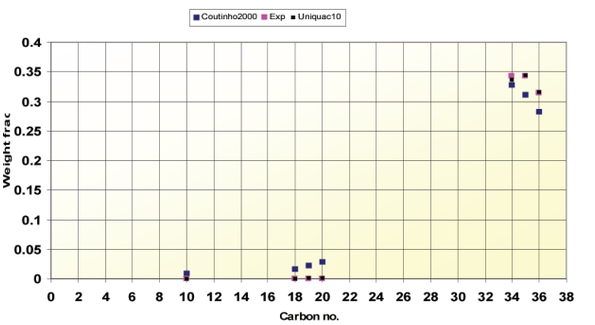


Fig. 6. Comparison between experimental [15] and predicted solid phase composition of BIM13 system at 299.15K by two different structural parameters.

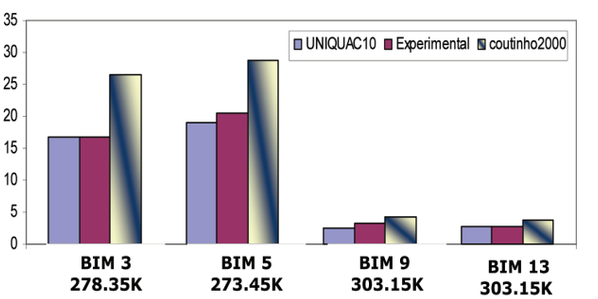


Fig. 7. Wax solid content at some temperatures for the studied system.

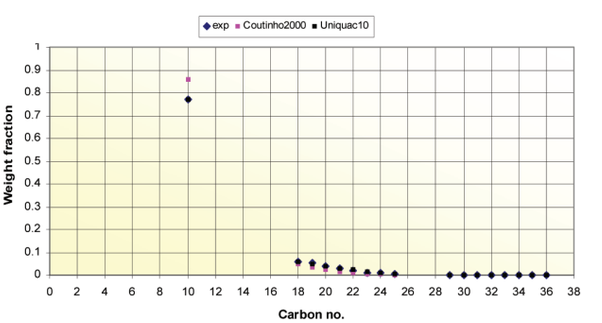


Fig. 8. Comparison between experimental [15] and predicted liquid phase composition of BIM3 system at 278.35K by two different structural parameters.

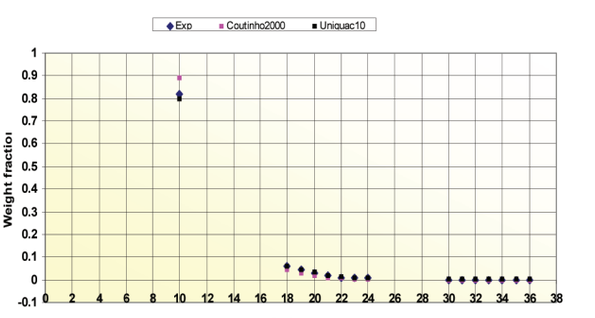


Fig. 9. Comparison between experimental [15] and predicted liquid phase composition of BIM5 system at 273.45K by two different structural parameters.

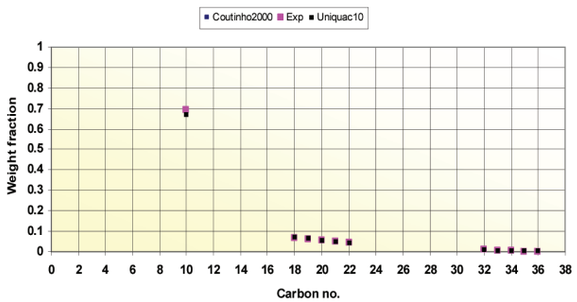


Fig. 10. Comparison between experimental [15] and predicted liquid phase composition of BIM9 system at 303.15K by two different structural parameters.

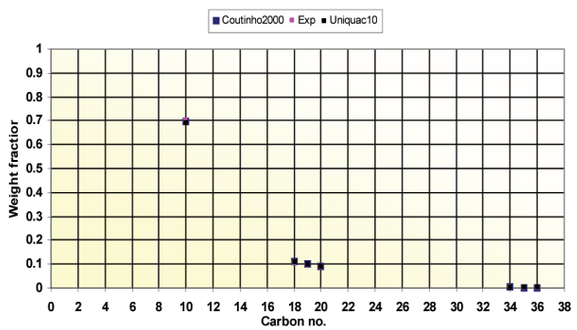


Fig. 11. Comparison between experimental [15] and predicted liquid phase composition of BIM13 system at 299.15K by two different structural parameters.

CONCLUSION

Six thermodynamic models namely, Won, Pedersen, UNIQUAC, Wilson, NRTL and ideal solution have been used to predict the cloud point temperature of defined liquid mixtures (synthetic fuel). The predicted cloud point temperatures have been compared with the literature experimental cloud point data. Good agreement between the predicted and experimental values was obtained using models that are based on solid activity coefficients as compared with those that neglect the non-ideality in the solid phase. Also, the UNIQUAC model was applied to predict the wax formation and the composition of liquid and solid phase below the cloud point temperature. This model was found to provide a remarkably good description of the low-temperature phase behavior for different types of synthetic fuel in broad temperature region.

NOMENCLATURE

A_{ij} is the binary interaction parameter for pair ij in the Wilson model.

C_{ni} is carbon number, i=10 to 40

d density of the component, g/cc

G_{ij} is the binary interaction parameter for pair ij in the NRTL model.

Mw_i is the molecular weight.

q_i relative molecular surface area of the paraffinic constituent.

P_c is the critical pressure in atm.

r_i relative molecular volume of the paraffinic constituent.

S_i is the mole fraction for solid phase.

T_b is the boiling point temperature in Kelvin.

T_c is the critical temperature in Kelvin.

$T_{m,i}$ the melting temperature in Kelvin.

$T_{tr,i}$ is the transition temperature of component i in Kelvin.

$T_{fus,i}$ is the fusion temperature of component i in Kelvin.

v_i is the molar volume of component i cc/gmol

V_{wi} is the van der waals volume of component i cc/gmol.

Xi is the mole fraction for liquid phase.

Z is the coordination number for solid phase.

α is a measure of the non-randomness of the mixture.

λij. The pair interaction energies between two identical molecules, area the activity coefficients for both liquid and solid phases respectively

δ_i is the solubility parameter

Φ_i is the volume fraction of component i

is the average solubility parameter of the mixture

γ^{res} residual part of the activity coefficient

$\gamma^{comb\text{-}fv}$ combinatorial part of the activity coefficient.

is the interaction parameter for the UIQUAC model.

ΔCp_m is the heat capacity at melting temperature

$\Delta h_{m,i}$ is the enthalpy of melting for componenti

$\Delta h_{tr,i}$ is the transition enthalpy of componenti

is the enthalpy of sublimation of the pure n-alkanes

"H_{vap} heat of vaporization, kJ/mol

"H_{fus} heat of fusion, kJ/mol

"H_{tr} heat of transition, kJ/mol

REFERENCES

1. Prausnitz, J.M., 1969. *Molecular Thermodynamics of Fluid Phase Equilibria, Prentice-Halll*. Englewood Cliffs, NJ.
2. Won, K.W., 1986. *Fluid Phase Equilibria*, **30**, 265-279.
3. Pedersen, K.S., Skovborg, P., Ronningsen, H.P., 1991. *Energy & Fuels* **5**, 924.

4. Coutinho, J.A.P., Andersen, S.I., Stenby, E.H., 1998. *Fluid Phase Equilibria*, **103**, 23.
5. Smith, J.M., Van Ness, H.C., 1987. *Introduction to Chemical Engineering Thermodynamics*, 4rth Edition, McGraw, HILL.
6. Coutinho, J.A.P., Stenby, E.H., 1996. *Ind. Eng. Chem. Res*. **35**, 918-925.
7. Helle, S.E., Age, F., Peter, R., 1991. *Ind. Eng. Chem. Res*. **30**, 2576-2582.
8. Bondi, A., 1968. *Physical Properties of Molecular Crystals, Liquids and Glasses*, Wiley, New York.
9. Mirrante, F.I.C., Coutinho, J.A.P., 2001. *Fluid Phase Equilibria*. **180**, 247-255.
10. Coutinho, J.A.P., 2000. *Energy and Fuels*, **14**, 625-631.
11. Coutinho, J.A.P., Knudsen, K., Andersen, S.I., Stenby, E.H., 1996. *Chem. Eng. Sci*. **51**, 3273.
12. Coutinho, J.A.P., Pauly, J., Daridon, J.L., 2001. *Barazilian journal of chemical Engineering*, **18**, 411-422.
13. Morgan, D. L., Kobayashi, R., 1994. *Fluid Phase Equilibria*, **94**, 51.
14. Twu, C.H., 1984. *Fluid Phase Equilibria*, **16**, 137.
15. Dauphin, C., Daridon, J.L., Coutinho, J., Baylere, P., Potin-Gautier, M., 1999. *Fluid Phase Equilibria*, **161**, 135-151.
16. Leibovici, C.F., Neoschil, J., 1995. *Fluid Phase Equilibria*, **112**, 217-221.
17. Coutinho, J.A.P., 1999. *Fluid Phase Equilibria*, **158**, 447.

Petroleum Res. J. Vol. 21 (2008/2009); P. 57–66, 6 Figs.

A Stratigraphic Review of the Al Bayda Formation, NE Libya: Calcareous Nannofossils versus Foraminifera

Esam O. Abdulsamad* and Ahmed F.A.Tmalla*

Abstract: Different groups of Eocene and Early Oligocene fossils have been reported from the Al Bayda Formation at Cyrenaica, northeast Libya by several authors. The formation is detrital in its lower part, and separated by disconformities from both the Darnah Formation below and the Al Abraq Formation above.

In this review, it is confirmed that all Eocene taxa reported from the lower member of the Al Bayda Formation (the Shahhat Marl Member) are allochthonous, representing reworked bioclasts from the Eocene Darnah Formation. The Early Oligocene micro- and macrofossils reported by several authors from the Shahhat Marl Member and from the upper member (the Algal Limestone) of this formation are considered here as autochthonous, in situ biota, confirming its Early Oligocene age.

The contradictory conclusion of El Mehaghag and Ashahomi, 2005, based on calcareous nannofossils, that the Al Bayda Formation is Middle to Late Eocene, is not accepted in this present work**.**

Key words: Eocene-Oligocene, Cyrenaica, Shahhat Marl Member, Allochthonous, Autochthonous, Nannofossils, Foraminifera

INTRODUCTION

Larger foraminifera form an important constituent of many warm-water; shallow marine carbonates shelf-sequences. They are normally the most important age-diagnostic fossils present within these carbonate shelf deposits. They went through rapid evolution, therefore age datings based on them are considered as fine, in resolution, as those of the deeper marine planktonic foraminifera (Cavelier and Pomerol, 1986 and Racey, 1994). Consequently, they are of great use in carbonate shelf sequences, such as those of Cyrenaica, where planktonic foraminifera and nannofossils are limited to certain lithological levels representing deeper marine conditions.

The current review discusses the stratigraphy of Al Bayda Formation based on published and unpublished data collected by the authors in different occasions. The discussion aims at minimizing the contradictory conclusions about the stratigraphic position of this formation and investigating its age, based on foraminifera and other microfossils reported by different workers in the region. All foraminiferal taxa reported here are listed, authored and referenced in Abdulsamad(1999) Abdulsamad and Barbieri (1999) and Abdulsamad (2000). The nannofossils are authored and referenced in Perch-Nielsen (1985) and Hay *in* Ramsay (1977). For detailed regional background and the geological and tectonic development of the region, the reader is referred to the works of Röhlich (1978; 1980) and El Hawat and Abdulsamad, (2004).

GEOLOGICAL BACKGROUND

The Al Bayda Formation typically crops out between the towns of Al Bayda and Darnah in northern Cyrenaica, northeast Libya (Fig. 1). This formation is further subdivided into two members (Fig. 2). Röhlich (1974) introduced the term Al Bayda Formation to include the lower Shahhat Marl Member and the upper Algal Limestone Member of the Al Kuf Formation of Kleinsmiede and van den Berg (19680). The main reason for upgrading these two members to form one formation was because they corresponded to a separate cycle of sedimentation, separated from both the underlying and overlying beds by disconformities (Röhlich, 1974, p. 39). Hammuda

* Earth Sciences Department, Garyounis University, P. O. Box: 9480, Binghazi, Libya. Email: esam000@yahoo.com

** Department of Palaeontology, Nationaal Natuurhistorisch Museum Naturalis, Postbus 9517, 2300 RA Leiden, The Netherlands. Email:aftmalla@yahoo.co.uk

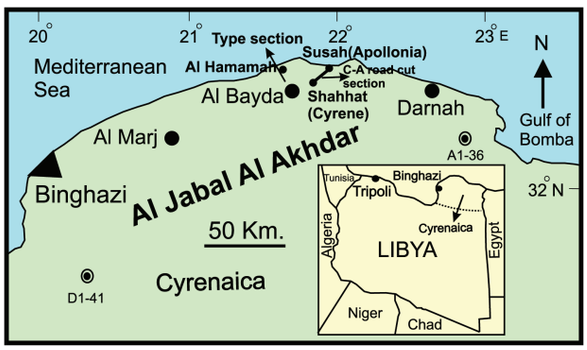


Fig. 1. Index map of NE Libya and the location of the Cyrene-Apollonia road cut section (C-A), well A1-36 and well D1-41.

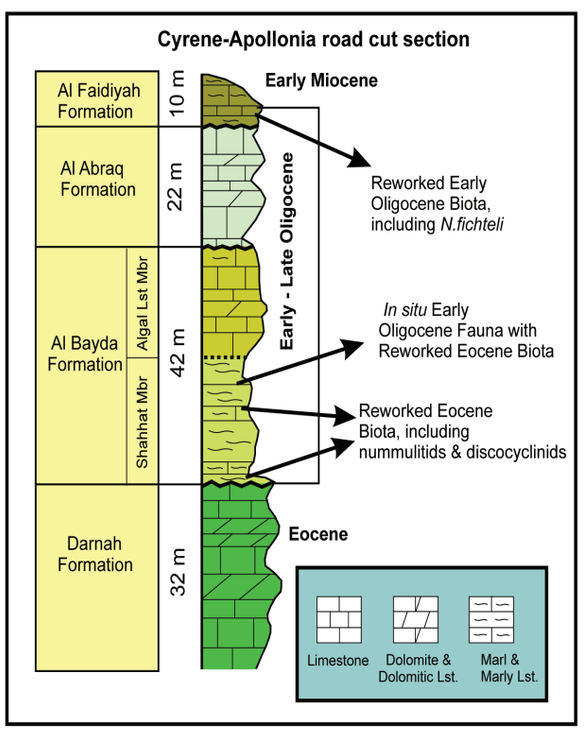


Fig. 2. Stratigraphic log of Cyrene-Apollonia road cut section.

(1973) also noted the unconformity separating the Eocene from the Early Oligocene detrital deposits in Darnah area.

Lithologically, the Shahhat Marl Member consists of yellow marls and marly and chalky limestones with fine to coarse-grained matrix that largely consists of skeletal remnants of echinoderms, mollusks, reworked Eocene discocyclinids and nummulitids (Plate 1: Figs. 1, 2). The upper Algal Limestone Member is characterized by poorly sorted packstone and grainstone cemented by micrite to sparite. The biotic content shows common assemblage of non-geniculate coralline red algae, nummulitids, corals, mollusks, and echinoids (Plate 1: Figs. 3, 4). The geographic extent and development of the Al Bayda Formation is shown in Figure 3 and the type locality is about 2.5 km NW of al Bayda Town, at the road leading to al Hamámah Village, where it is separated from both the underlying Darnah Formation and the overlying Al Abraq Formation by major disconformities.

Kleinsmiede and Van den Berg (1968 indicated that the basal part of their Al Kuf Formation (= the Shahhat Marl Member) was detrital with reworked Eocene fauna, in agreement with Gregory (1911). The Shahhat Marl Member was regarded by Gregory (1911) to belong partly to the underlying Eocene Darnah Formation. However, Stefanini (1923) distinguished the Eocene Darnah Formation from the Oligocene Al Bayda Formation based on the presence of an unconformable surface that separates the two formations. All the above authors confirmed that the contact between the Darnah Formation (Eocene) and the base of the Al Bayda Formation (Shahhat Marl Member) is disconformable.

The recovery of Early Oligocene fauna, including *Nummulites fichteli* and *N. vascus* by Kleinsmiede and Van den Berg (1968) and by Hanzliková *in* Röhlich (1974) allowed assigning the Al Bayda Formation to the Early Oligocene.

DISCUSSION

Based on foraminiferal assemblages, the major part of the Al Bayda Formation belongs to the Early Oligocene. This is based on the recovery of *Nummulites fichteli* (Plate 1: Figs. 4, 11) and *N. vascus* (Plate 1: Figs. 4, 8, 9) from the middle and upper parts of the formation in several outcrops and subcrops. These deposits are largely confined to the larger foraminiferal zones SB21-SB22a of Cahuzac and Poignant (1997) which essentially correspond to the planktonic foraminiferal zones P18-P19 of Berggren *et al.*(1995). This conclusion is supported by the diverse Oligocene planktonic foraminiferal assemblages, recovered from the Al Bayda Formation at Well A1-36, about 150 km southeast of the Cyrene–Apollonia road cut exposure, by Abdulsamad and Barbieri (1999). These assemblages include *Catapsydrax dissimilis, Tenuitellinata angustiumbilicata, Globigerina ouachitaensis gnaucki, G. ciperoensis ciperoensis, G. praebulloides*, *G. yeguaensis*, *G. euapertura* and *G. angulioficinalis.* The stratigraphic use of the planktonic foraminifera in this well was based on the last stratigraphic occurrence of the species *(i.e.* first appearance going down the borehole) in order to eliminate the assumption of caving (see Haynes, 1981

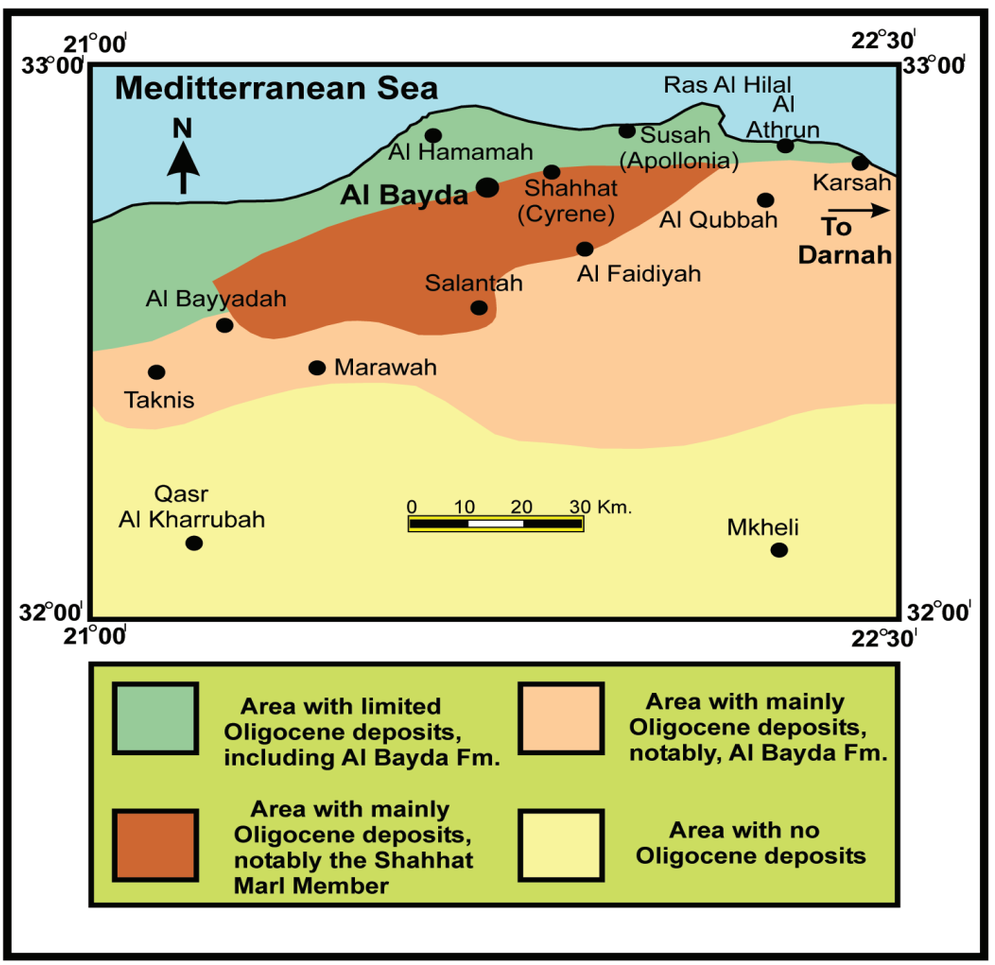


Fig. 3. Extent and development of the Al Bayda Formation in northern Cyrenaica (modified after Röhlich, 1974).

and Tmalla, 1996). However, the recovery of *Nummulites fabianii* at Wadi al Kuf, near al Bayda Town, led Moody *et al.*(2004) to assign the deposits of the Shahhat Marl Member to the Late Eocene.

In 2005, Tmalla confirmed, in a written communication to Moody-Sandman Associates, the presence of *N. fabianii* from Wadi al Kuf section. He also recovered *N. vascus* from the same deposits at the Cyrene-Apollonia road cut section (near al Bayda Town). Similar findings were also reported by Abdulsamad (1999), by Muftah and Erhoma (2002) from the same outcrop, and recently, by Abdulsamad from Daryanah-al Abyar area, near Binghazi City.

Abdulsamad and Barbieri (1999) regarded the Eocene nummulitids and discocyclinids in the Shahhat Marl deposits as reworked, and though *N. fabianii* has forms transitional to *N. fichteli*, the latter species and the transitional forms belong to the Early Oligocene (Abdulsamad, 2000). Moreover, reworked lithoclasts and bioclasts (notably, nummulitids) are major constituents of the sedimentary rocks of the Al Bayda Formation. They are considerably older than the surrounding allochems, thus confirming the presence of reworked allochthonous material in the formation. In fact, reworked specimens of nummulites (including *N. fabianii* and related forms such as *N.* cf. *fabianii* and *N.* aff. *fabianii*) have been found throughout the Late Oligocene and the Early Miocene sedimentary rocks of Cyrenaica (Plate 1: Figs. 5, 7); see also Abdulsamad and Bu-Argoub (2006). Reworking in several stratigraphic levels in the region is well known. It is caused primarily by syndepositional tectonics (El Hawat, 2005) and examples of this trend can be seen in El Hawat and Abdulsamad (2004). The recovery of reworked Cretaceous nannofossils by Haq and Aubry, 1980 in the Eocene Apollonia Formation at Wadi al Athrun section is another example of this trend. Elements of reworking have also been noted by most workers in the region, including, Abdulsamad and Barbieri (1999).

Imam (1999) studied outcrops in the al Bardia

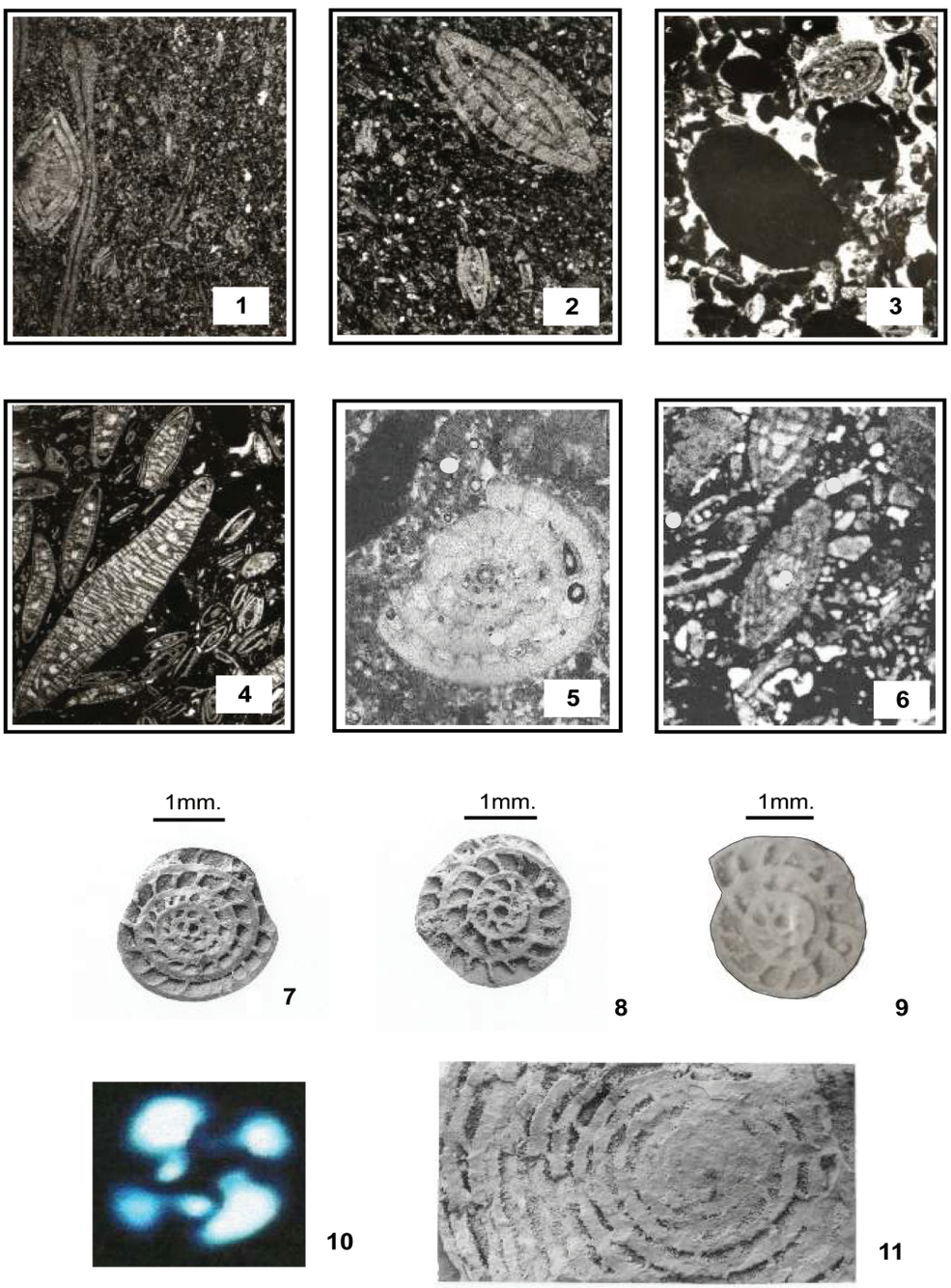


Plate - I

Plate I - 1, 2. The lower and mid-upper parts of the Shahhat Marl Member at Cyrene-Apollonia (C-A) road cut section. They show wackestone to packstone with reworked nummulitids and discocyclinids. X10

Plate I - 3, 4. The lower and upper parts of the Algal Limestone Member at Cyrene-Apollonia (C-A) road cut section. They show packstone to grainstone with N. vascus (small specimens) and N. fichteli (large specimens). X10

Plate I - 5. The lower part of the Shahhat Marl Member at Deryanah-al Abyar area (East of Binghazi). It represents wackestone to packstone with reworked N. cf. fabianii, (from El-Salmi, 2001). X10

Plate I - 6. The lower part of the Al Faidiyah Formation at Deryanah-al Abyar area (East of Binghazi) with reworked N. fichteli. This microfacies is similar to the one found in the basal part of the Al Faidiyah Formation at Cyrene-Apollonia (C-A) road cut section, (from El-Salmi, 2001). X10

Plate I - 7. N. aff. fabianii, Ain al-Dabbusiyah section, upper part of the Darnah Formation.

Plate I - 8, 9. N. vascus, at Cyrene-Apollonia (C-A) road cut section, upper part of the Shahhat Marl Member.

Plate I - 10. Cyclicargolithus abisectus, mid-upper part of the Shahhat Marl Member at Deryanah - al Abyar area (East of Binghazi), (from El-Salmi, 2001). X5000

Plate I - 11. N. fichteli, upper part of the Shahhat Marl Member at well D1-41. X10

area at the most northeastern part of Cyrenaica including what he called Al Khowaymat Formation of El Defter and Issawi (1977). Not withstanding the enigmatic status of the Al Khowaymat Formation and the recommendation of Megerisi and Mamgain (1980) to suppress the term, we still find Imam's report on the larger foraminiferal assemblage in his study relative to the present discussion. Imam (1999, p. 625) reported the following about the Lower Member of the Al Khowaymat Formation: "This unit is highly fossiliferous with larger foraminifers such as *Nummulites intermedius* dÁrchiac (= *N. fichteli* Michelotti), *N. fabianii* Prever, *N. boucheri* de la Harpe (= *N. vascus* Joly-Leymerie), *N gizehensis* (Forskål), *N. beaumonti* dÁrchiac, especially in the lowermost part of the member, *Operculina complanata* (Defrance), *Assilina* sp. and other undefined oyster shell fragments together with echinoid remains." He assigned this member, with the above mixed larger foraminiferal assemblage, to the Late Eocene (Priabonian).

The logical geologic interpretation of the above mixed larger foraminiferal assemblage reported by Imam (1999) is an Eocene fossil assemblage reworked into Early Oligocene deposits. *N. intermedius* (=*N. fichteli*) and *N. boucheri* (=*N. vascus*), which he reported (p. 625) also from the Upper Member, are restricted to the Early Oligocene throughout the Mediterranean region; *Operculina complanata* (also in the upper Member) Early Oligocene – Middle Miocene, while *N. fabianii* is a typical Late Eocene species and *N. gizehensis* and *N. beaumonti*, are not younger than the Middle Eocene (see Abdulsamad, 2000).

The above larger foraminiferal assemblage encountered by Imam in his Al Khuwaymat Formation, indicates that the Lower Member is equivalent to the Shahhat Marl Member of the Al Bayda Formation of Röhlich (1974) and the Al Khuwaymat Upper Member, which is unconformably overlain by what he called Al Faidiyah Formation, is equivalent to the Algal Limestone Member of the Al Bayda Formation.

Röhlich (1974) recorded several fossils from the Shahhat Marl Member including the following ostracods: *Paracypris aerodynamica* Oertli (1956); *Pterigocythereis retinodosa* Oertli, (1956) (recorded as *P.* cf. *retinosa*); *Echinocythereis scabra* (Münster); *Cytherella gracilis* Lienenklaus (recorded as *C.* cf. *gracilis*) and *Bairdia subdeltoidea* (Münster). Oertli, (1956) described all the above ostracod species (excluding *B. subdeltoidea*) from the Rupelian (Early Oligocene) of the Swiss Molasse.

El Mehaghag and Ashahomi (2005) studied the nannofossil content of fifteen outcrop samples from the Cyrene-Apollonia road cut exposure, 10 km NE of Shahhat City. Two samples were from the uppermost part of the Darnah Formation that was barren of nannofossils and eight samples from the lower member of the Al Bayda Formation (the Shahhat Marl Member). Five samples from the upper member of Al Bayda Formation (the Algal Limestone Member) were also barren of nannofossils. They recorded and identified eighteen known nannoplankton species and two other species identified to the generic level from the Shahhat Marl Member. Only *Discoaster barbadiensis* and *Reticulofenestra dictyoda* are indicative of Late Eocene. Most of the species were recorded as rare on their Table 1. Apart from the Early Eocene species *Discoaster lodoensis* and *D. salisburgensis* (see Hay *in* Ramsay, 1977) and other long ranging species, at least eight of the recorded species are known to range into the Oligocene, including *Helicosphaera euphratis*, *Reticulofenestra umbilica, R. hillae, Dictyococcites bisecta*, *Pedinocyclus larvalis* and *Coccolithus pelagicus* (see Pearch-Nielsen, 1985). *C. pelagicus* was reported by Haq and Aubry, 1980 from the Early Paleocene deposits of El Haria Formation at El Kef section in Tunisia and from the Early to Middle Eocene deposits of Apollonia Formation at Wadi al Athrun section at al Jabal al Akhdar. The stratigraphic range of *C. pelagicus* extends to the Late Oligocene in Italy (Beckmann *et al*., 1981) and to the Late Miocene in southern Spain (Flores *et al.*, 2005).

El Mehaghag and Ashahomi (2005 p.17) concluded that the Shahhat Marl Member is Middle to Late Eocene in age and considered the two Early Eocene nannoplankton species (see above) and *Discoaster gemmeus,* as reworked. Hence, they also confirm the presence of reworked fossils in the Shahhat Marl Member of the Al Bayda Formation. They also added: "Although barren of calcareous nannofossils, the overlying Algal Limestone Member must be Late Eocene (NP20) or younger". This is in contradiction to all published literature about the area (see Kleinsmiede and van den Berg, 1968; Barr and Weegar, 1972; Röhlich, 1974; Banerjee, 1980; Abdulsamad, 2000; Muftah and Erhoma, 2002; El Hawat and Abdulsamad, 2004).

Moreover, a conflicting result to the conclusion of El Mehaghag and Ashahomi (2005) comes from

El-Salmi (2001) who recovered the Oligocene nannoplankton *Cyclicargolithus abisectus* (Plate 1: Fig. 10) from the Shahhat Marl Member in Wadi Azzad near Binghazi City.

The conclusion of El Mehaghag and Ashahomi (2005) was essentially based on a few Eocene species, which were recorded as common to rare (1 to 10 specimens per field of view) in their study. It should be noted that in terms of nannofossils, the recovery of rare and few species should be regarded as inadequate in age determination. It is worth noting that, inner-shelf sediments commonly contain as many as 1 billion of specimens/cm^3. A light-microscope smear-slide with evenly spaced nannofossils usually contains 100 000 to 1 million specimens (Siesser *in* Lipps, 1993).

We strongly believe that the conclusions of El Mehaghag and Ashahomi (2005) need to be re-evaluated and compared with the study of other outcrops, including the type area. We also encourage that such research should consider the depositional environment and the physical gaps (unconformity/ disconformity) in the field. The lack of zonal marker species should also be commented on in such research.

Because the two samples examined by El Mehaghag and Ashahomi (2005) from the Darnah Formation, immediately below the Al Bayda Formation were barren of nannofossils, they did not mention any thing about the nature of the contact between these two formations (conformable or not). The same can be said about the contact between the Shahhat Member and the Algal Limestone Member, because the five samples they examined from the basal part of the latter member were also barren of nannofossils.

The unconformable contact between the Darnah Formation and the Shahhat Marl Member (Figs. 4 and 5) is the key for the geologic interpretation of the reworked Eocene fauna from the Darnah Formation into the Shahhat Member, which is partly detrital. Moreover, the Shahhat Marl Member was deposited in a platform fore-reef slope (Abdulsamad, 1998), where the possibility of transportation and reworking of fauna and flora were extremely high (see, for example, Hohenegger *et al.,* 1999 and Zellers and Gray, 2007). Beavington-Penney *et al.,* (2005) however, discuss examples related to the dynamics of sediment and fossil shell-transportation, in detail.

Nannofossils clearly have marked advantages for use in biostratigraphy, but there are also serious factors, which should be considered. The most important of these factors are ecologic control, diagenetic alteration and reworking (Siesser *in* Lipps, 1993). The minute size of nannofossils makes them almost destructible by mechanical abrasion. They can be carried for long distances and reworked into

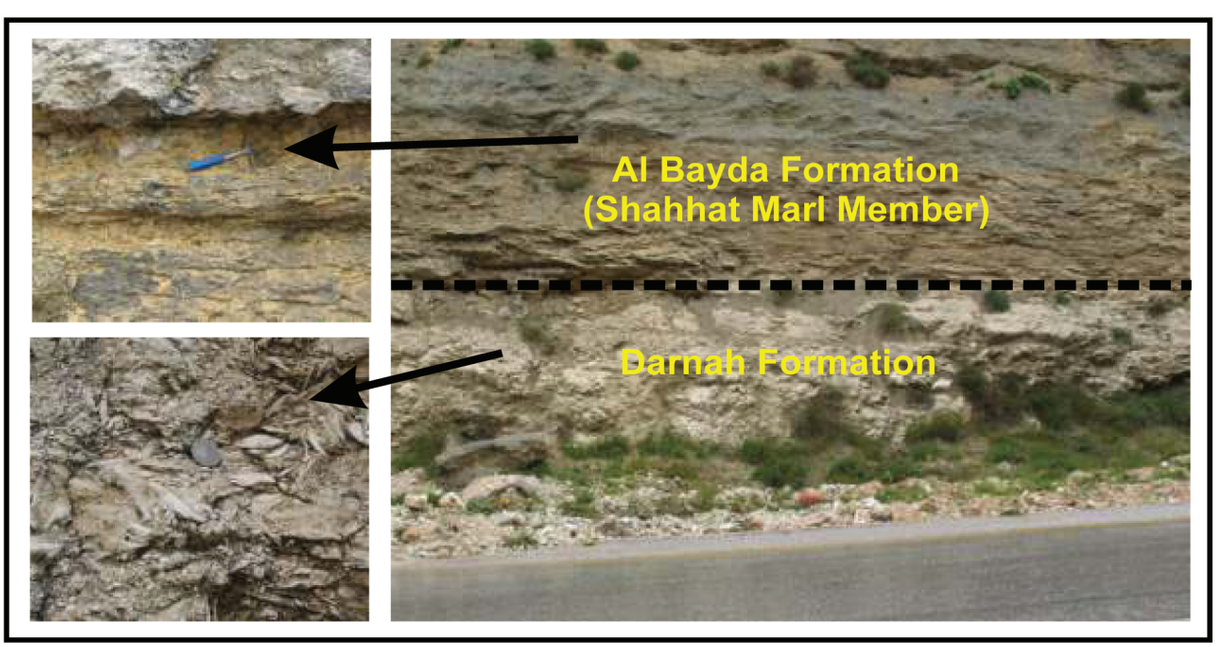


Fig. 4. The Eocene-Oligocene boundary (dashed line) at Cyrene-Apollonia road cut section, it shows the Darnah Formation (below) and the Al Bayda Formation (above), with close-up views of the lower part of the Shahhat Marl Member (left upper view) and the upper part of the Darnah Formation with A and B forms of Nummulites lyelli (left lower view).

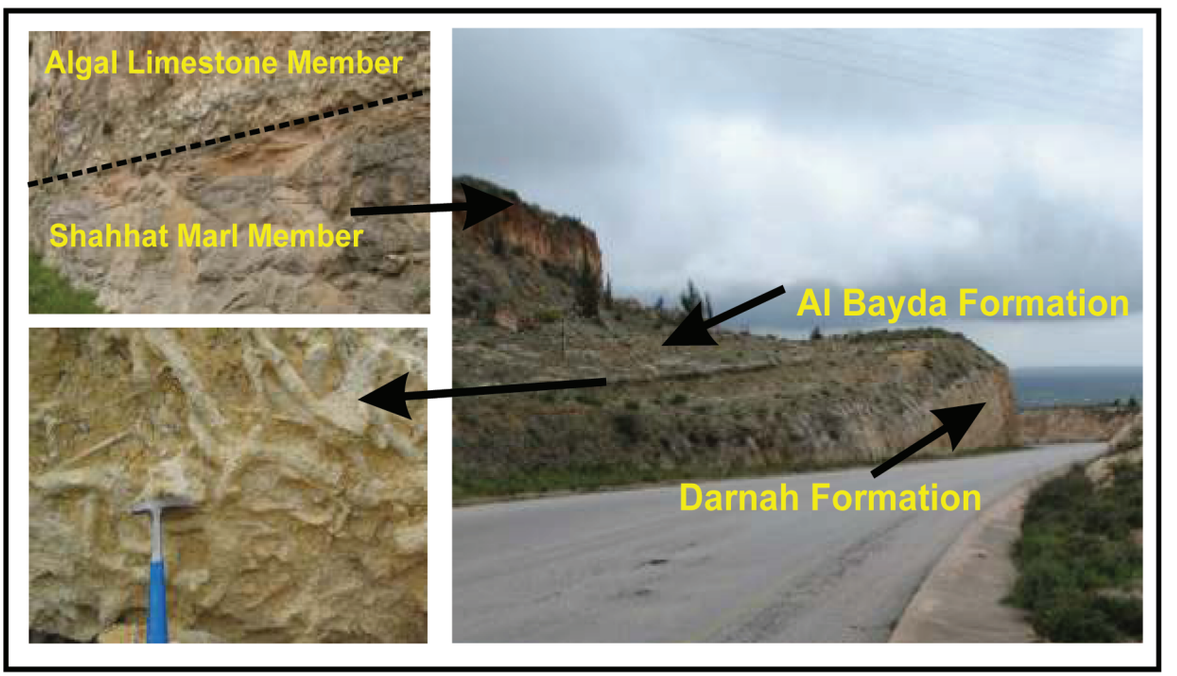


Fig. 5. The Eocene-Oligocene boundary at Cyrene-Apollonia road cut section, with close-up views showing trace fossils (bioturbation) directly above the contact (left lower view) and the contact between the Shahhat Marl and the Algal limestone members (left upper view).

younger deposits where they will not be the true indicators for neither the depositional environment nor the age of these deposits (see Pomerol, 1982). The roles of nannofossils in sedimentation, transportation, preservation and contamination, are discussed by numerous authors such as Bramlette (1958) and recently by Agnini *et al.*, (2007).

In contrary, the characteristics and typical appearance of larger foraminifera such as nummulites can usually be evaluated in order to resolve reworking problems. Identification of *in situ* (undamaged) specimens from moderately transported (partly damaged) specimens or extensively transported (considerably damaged, wave reworked) specimens can be achieved with different successes (see Beavington-Penney, 2004). Shell fragmentation by reworking can be easily differentiated from other taphonomic processes such as compaction. For example, the latter shows skeletal fragmentation at points of contact between bioclasts and fragments from individual bioclasts are found together in the rock (see for example Dodd and Stanton, 1981). Examples of compaction in nummulite accumulations, however, are discussed in Beavington-Penney (2004). Normally nummulite accumulations show evidence that both physical reworking (scouring, winnowing and imbrication) and biological processes (reproduction strategies and bioturbation) have influenced their formation (Racey, 2001). A general model for discriminating between physical and ecologically produced biofabrics is outlined by Racey (2001).

Based on lithology and faunal content, the Al Bayda Formation represents a shallowing-upward sedimentary sequence (Abdulsamad and Barbieri, 1999). Normally, the change in lithology of the Al Bayda Formation, from the yellowish soft marl and fine argillaceous limestone with allochthonous, coarse litho- and bioclasts of the Shahhat Marl Member to the generally white, hard and coarse grained algal limestone of the Algal Limestone Member, can be traced in time and space in the field. Consequently, bedsets of the Al Bayda Formation are obviously genetically related and in general harmony with Walther's Law. It is recommended to consider the Al Bayda Formation as a depositional sequence, which certainly represents a single episode of progradation (Abdulsamad, in preparation). From the stratigraphical point of view, appropriate age dating of the Al Bayda Formation can only be achieved through the analyses of all biota recovered from the total bedsets and to consider the geologic history of the region. It is inadequate to set age for the lower part (the Shahhat Marl Member) and the upper part (the Algal Limestone Member) separately. Accordingly, we feel that the suggested Early

Oligocene age for the Al Bayda Formation is more acceptable, simply because we consider the Eocene fauna and flora in the lower part of the formation as allochthonous, reworked particles, and the Early Oligocene taxa up-section as *in situ* constituents of the rock. This is supported by the confirmed hiatus between the Darnah Formation and the Al Bayda Formation, particularly at the type locality (Fig. 6).

SUMMARY AND CONCLUSION

Based on the above discussion, it seems that both foraminifera and calcareous nannofossils are in harmony as regards the age of Al Bayda Formation. Both groups show some reworking of Eocene taxa in the lower part and if we consider the presence of the Oligocene nannofossil (*Cyclicargolithus abisectus*), then the middle (top part of the Shahhat Marl Member) and the upper parts of the formation belong to the Early Oligocene. It is obvious, however, that the conflicting conclusions regarding the age of Al Bayda Formation are largely related to misinterpretation of the fossil record. It is inadequate to jump to conclusions based on rare and poorly preserved taxa without considering the depositional history of the region and ignoring the physical gabs present in the field. Unfortunately, similar attempts regarding other rock units in Cyrenaica have been seen in the recent years (see for more details Tmalla, 2007). Some of the problems influencing biostratigraphic interpretation are local variation in species ranges, phenotypic variation, preservation, contamination, reworking of older sediments and infrequent misidentification of species. These problems can be minimized by using quantitative faunal analysis (see Keller, 1985). Other palaeontologic strategies dealing with sedimentary displacement and stratigraphic disorder can be found in Cutler and Flessa (1990) and in Finger *et al*. (2007) respectively.

In conclusion, the present review, suggests that the Al Bayda Formation is mainly Early Oligocene in age based on the recovery of *Nummulites vascus* (Plate 1: Figs. 4, 8, 9) and *N. fichteli* (Plate 1, Figs. 4, 11) and other fossils from the formation (see above). The Eocene biota in the lower Shahhat Marl Member is confirmed as reworking by almost all workers in the region. Based on the above discussion, the present work does not agree with the conclusion of El Mehaghag and Ashahomi (2005) that the Al Bayda Formation at the Cyrene Apollonia road cut section is Middle to Late Eocene. Further more, the latter authors confirmed the presence of reworked Eocene nannofossils in the Al Bayda Formation and, at least, eight of the species they recorded from the formation, range into the Early Oligocene.

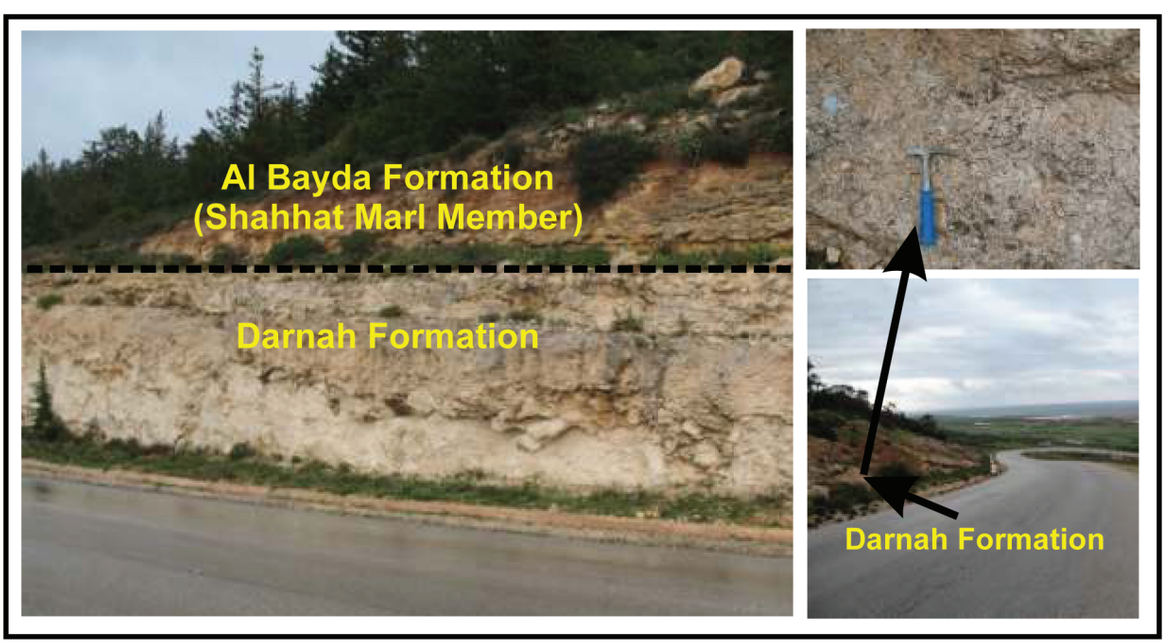


Fig. 6. The Eocene-Oligocene boundary (dashed line) at the road leading to Al Hamámah (the type locality of the Al Bayda Formation, 2.5 km NW of Al Bayda), it shows also the lower part of the Darnah Formation (bioclastic limestone unit with gastropods, pelecypods and small sized-nummulites) near the coast of Al Hamámah.

ACKNOWLEDGEMENTS

We are especially grateful to Profs. A. El Hawat, A. El-Arnauti (Garyounis University), M. J. Salem (Al Fateh University), Dr. S.J. Beavington-Penney (British Gas Group) and Prof. R. Barbieri (Bologna University) for their critical reading and useful suggestions for improving the manuscript. Our thanks are due also to Mr. S. Emhana and Mr. N. Al-Selini (Garyounis University) and Mr. F. Bu-Argoub (Gulf Oil Company) for their support and assistance during the fieldwork.

REFERENCES

Abdulsamad, E. O., 1998. Palaeoenvironmental distribution of Tertiary foraminifera from th carbonate depositional facies of northern Cyrenaica (NE Libya). Abstract toconference on Tertiary to Recent larger foraminifera, Kingston University, UK.

Abdulsamad,,E.O.,1999. Stratigraphy and palaeobiogeography of Tertiary larger foraminifera fromAI Jabal al Akhdar (Cyrenaica, NE Libya). *Giornale di Geologia* ,**61**, 75-98, Bologna.

Abdulsamad,E. O.,2000. Contribution to the *nummulites* taxonomy from the Palaeogene sequences of Al Jabal al Akhdar (Cyrenaica, NE Libya). *Revue de Paleobiologie*,**19**(1),19-45.

Abdulsamad, E. O. and Barbieri, R., 1999. Foraminiferal distribution and palaeoecological interpretation of the Eocene – Miocene carbonates at al Jabal al Akhdar (northeast Libya). *Journal of Micropalaeontology*, **18**, 45-65.

Abdulsamad, E.O. and Bu-argoub, F. M., 2006. Sedimentary facies and foraminifera of the Miocene carbonates of the Ar Rajmah Group in Cyrenaica, NE-Libya. *Petroleum Res. J.*, **19**, 49-60, Tripoli.

Agnini, C., Fornaciari, E., Rio, D., Tateo, F., Backman, J. and GiusbertiI, L., 2007. Responses of calcareous nannofossil assemblages, mineralogy and geochemistry to the environmental perturbations across the Paleocene/Eocene boundary in the Venetian Pre-Alps. *Marine Micropaleontology*, **63**, 19-38.

Banerjee, S., 1980. Stratigraphic Lexicon of Libya. Department of Geological Researches and Mining, *Bull.* **13**. *Industrial Research Centre*, Tripoli, 300 pp.

Barr, F.T. and Weegar, A.A., 1972. *Stratigraphic Nomenclature of the Sirte Basin, Libya,* Petroleum Exploration Society of Libya, Tripoli, 179 pp.

Beavington-penney, S. J., 2004. Analysis of the effects of abrasion on the test of *Palaeonummulites venosus*: implications for the origin of nummulithoclastic sediments. *Palaios*, **19**, 143-155.

Beavington-penney, S.J., Wright, V.P. and Racey, A., 2005. Sediment production and dispersal on foraminifera-dominated early Tertiary ramps: the Eocene El Garia Formation, Tunisia. *Sedimentology,* **52**,537-569.

Beckman, J. P., Bolli, H.M., Perch-neilsen, K., Decima, F. P., Saunders, J. B. and Ttoumarkine, M., 1981. Major calcareous nannofossils and foraminiferaleEvents between the Middle Eocene and Early Miocene. *Palaeogeography, Palaeoclimatology, Palaeoecology*, **36**, 155-190.

Berggren, W.A., Kent, D., Swisher, C.C. and Aubry, M.-P., 1995. A revised Cenozoic geochronology and chronostratigraphy. In*:* Berggren, W. A. and Kent, D. (eds), *Geochronology Time Scales and Global Stratigraphic Correlation. SEPM*, Special Publication No. **54**, 134-175.

Bramlette, M. N., 1958. Significance of coccolithophorids in calcium carbonate deposition. *Bull. Geol. Soc. Am.,* **69**, 121-126.

Cahuzac, B. and Poignant, A., 1997. Essai de biozonation l'Oligo-Miocène dans les bassins européens à l'aide des grands foraminiferes ncritiques. *Bull. Soc. géol*. *Francce*, **168**, 155-169.

Cavelier, C. and Pomerol, C. ,1986. Stratigraphy of the Palaeogene. *Bull. Soc. géol*. France, Ser. 11, No. **2**, 225-265.

Cutler, A.H. and Flessa, K.W., 1990. Fossils out of sequence; computer simulations and strategies for dealing with stratigraphic disorder. *Palaios;* **5** (3), 227-235.

Dodd, J.R. and Stanton, R. J. JR., 1981. *Paleoecology, Concepts and Applications.* John Wiley and Sons, Inc. 559 pp.

El Defter, T. and Issawi, B., 1977. Geological map of Libya; 1:250000, Sheet Al Bardia NH35-1. Explanatory Booklet. *Industrial Research Centre*, Tripoli, 93 pp.

EL Hawat, A.S., 2005. The dynamic stratigraphy of Cyrenaica: an implication of the Mediterranean tectonics. Abstract to the Cretaceous-Tertiary Biostratigraphy of Cyrenaica, Hannover, Germany.

El Hawat, A.S. and Abdulsamad, E. O. 2004. *The Geology of Cyrenaica: A Field Seminar*. Special Publication, Earth Sciences Society of Libya (ESSL), Tripoli, 130 pp.

El Mehaghag A.A. and Ashahomi, K. A., 2005. Calcareous nannofossils biostratigraphy of the Al Bayda Formation, Al Jabal al Akhdar, NE Libya: a short note. *Journal Nannoplankton Research*, **27** (1), 15-19.

El-Salmi, T. F., 2001. *Geology of the Area Between Wadi Malag-Krah and Wadi Ekhil at Al Jabal al Akhdar, Sector (4), Northeastern, Libya*. Unpublished B.Sc. thesis, University of Garyounis, Benghazi. 78 pp.

Finger, K.L., Nielsen, S.N., Devries, T.J., Encinas, A. and Peterson, D., 2007. Paleontologic evidence for sedimentary displacement in Neogene forearc basins of Central Chile. *Palaios,* **22** (1), 3-16.

Flores, J-A., Sierro, F.J., Filippelli, G.M., Barcena, M.A., Perez-Folgado, M., Vazquez, A. and Utrilla, R., 2005. Surface water dynamics and phytoplankton communities during deposition of cyclic late Messinian Sapropel sequences in the western Mediterranean. *Marine Micropaleontology,* **56**(1-2), 50-79

Gregory, J.W., 1911. Contribution to the geology of Cyrenaica. *Quarterly Journal, Geological Society*, **67**,572-615.

Hammuda, O. S., 1973. *Eocene Biostratigraphy of the Derna area, Northeast Libya*. Unpublished PhD Thesis, Univ. Colorado.

Haq, B.U. and Aubry, M-P., 1980. Early Cenozoic calcareous nannoplankton biostratigraphy and palaeobiogeography of North Africa and the Middle East and Trans-Tethyan orrelations. In: M.J. Salem and M.T. Busrewil (eds). *The Geology of Libya,* Academic Press, London, **1**, 271-304.

Haynes, J.R, 1981. *Foraminifera*. Macmillan, London, 433 pp.

Hohenegger, J., Yordanova, E., Nakano, Y. and Tatzreiter, F., 1999. Habitats of larger foraminifera on the upper reef slope of Sesoko Island, Okinawa, Japan. *Marine Micropaleontology,* **36**(2-3), 109-168.

Imam, M.M., 1999. Lithostratigraphy and planktonic foraminiferal biostratigraphy of the Late Eocene-Middle Miocene sequence in the area between wadi Al Zeitun and wadi Al Rahib, Al Bardia area, northeast Libya. *Journal of African Earth Sciences*, **28** (3), 619-639.

Keller, G., 1985. Eocene and Oligocene stratigraphy and erosional unconformities in the Gulf of Mexico and Gulf Coast. *Journal of paleontology*, **59** (4), 882-903.

Kleinsmiede, W. F. J. and Van Den Berg, N. J., 1968. Surface geology of the Jabal al Akhdar, northern Cyrenaica, Libya In*:* Barr, F. T. (ed.), *Geology and Archaeology of Northern Cyrenaica, Libya*. The Petroleum Exploration Society of Libya, Tripoli, 10th Annual Conference: 115-123.

LIPPS, J. H. (ed.) 1993. *Fossil Prokaryotes and Protists*. Blackwell Scientific Publications, Inc., London, 342 pp.

Megerisi, M. and Mamgain, V. D.,1980. Al Khowaymat Formation – an enigma in the stratigraphy of northeast Libya. In*:* M.J. Salem and M.T. Busrewil (eds), *The Geology of Libya*, Academic Press, London, **1,** 73-88.

Moody, R.T.J., Sandman, R.I. and Hassan, H. M., 2004. The deposition, distribution and stratigraphy of the Eocene-Oligocene carbonates of the Soluq Basin and Jabal al Akhdar region. Geology of the East Libya. 3rd Symposium on Sedimentary Basins of Libya. ESSL, Benghazi, Abstract: p. 73.

Muftah, A.M. and Erhoma, A. H., 2002. Coralline red algae of the algal limestone member of Al-Bayda Formation, NE Libya: biostratigraphic and paleoenvironmental significance, 633-638. In: El- Sayed, A. A. and Yousef, P. (eds) *Proceedings of the sixth International Conference on the Geology of the Arab World*, Cairo University.

Oertli, H.J., 1956. Ostrakoden aus der Oligozänen und Miozänen molasse der schweiz. *Schweizerische Palaeontologische Abhandlungen*, **74**, 1-119 + 16 plates

Perch-Nielsen, K., 1985. Cenozoic calcareous nannofossils. In*:* H.M. Bolli, J.B. Saunders and K. Perch-Nielsen (eds.). *Plankton Stratigraphy*. Cambridge University Press, 427-554.

Pomerol, C.,1982. *The Cenozoic Era, Tertiary and Quaternary*. Ellis Horwood Limited Publishers, England. 272 pp.

Racey, A.,1994. Biostratigraphy and palaeobiogeographic significance of Tertiary nummulitids (foraminifera) from northern Oman. In*:* Simmons, M. D. (ed.), *Micropalaeontology and Hydrocarbon Exploration in the Middle East*, 343-370, Chapman and Hall, London.

Racey, A.,2001. A Review of Eocene nummulite accumulations: structure, formation and reservoir potential. *Journal of Petroleum Geology*, **24** (1), 79-100.

Ramsay, A.T.S. (ed.), 1977. *Oceanic Micropalaeontology*. 2 vols. London, Academic Press.

Röhlich, P., 1974. Geological Map of Libya, 1: 250 000. Sheet : Al Bayda (NI 34-15). Explanatory booklet, *Industrial Research Centre*, Tripoli, 70 pp.

Röhlich, P., 1978. Geological development of Jabal al Akhdar, Libya. *Geologische Rundschau*, **67**, 401-412.

Röhlich, P., 1980. Tectonic development of Al Jabal al Akhdar. In: Salem, M. J. and Buserwil, M.T. (eds), *The Geology of Libya*, **III**, 923-931, Academic Press, London.

Stefanini, G., 1923. Fossili Terziari della Cirenaica. *Paleontographia Italica*, **27**:,101-146.

Tmalla, A.F.A. 1996. Latest Maastrichtian and Palaeocene planktonic foraminiferal biostratigraphy of well A1a-NC29A, northern Sirt Basin, Libya In*:* M.J. Salem, A.J. Mouzughi and, O. S. Hammuda (eds), The Geology of Sirt Basin **1**,195-232, Elsevier, Amsterdam.

Tmalla, A.F.A., 2007. The Stratigraphic positions of wadi Dukhan and Al Uwayliah formations, northeast Libya- a review. *Scripta Geologica*, **134**, 119-130

Zellers, S. D. and Gary, A., 2007. Unmixing foraminiferal assemblages: polytopic vector analysis applied to Yakataga Formation sequences in the offshore gulf of Alaska. *Palaios*, **22** (1), 47-59.

Petroleum Res. J. Vol. 21 (2008/2009); P. 81–98, 14 Figs.

Petrography, Diagenetic Aspects and Isotopes of the An Nagaza Member of the Al Khums Formation, NW Libya

Mahmoud T. Elbakai*, Aisha, K. Shalghum* and Lila I. Hafez*

Abstract: Petrographic, and geochemical analyses were carried out on a total of 33 samples from the An Nagaza Member of the Al Khums Formation in NW Libya. The An Nagaza sediments have been divided into five lithofacies. These lithofacies are mainly of grainsupported and they started with sediments resulted from transgression over a Cretaceous and/or Triassic surface of moderate relief. Various fossils and abundance of silisiclastic materials suggest a shallow marine environment. The complete succession of the An Nagaza sediments is interpreted as a transgressive sequence over the Cenomanian succession, passing from marginal marine possibly to fully marine deposits. Several diagenetic events took place during deposition of the sediments of the An Nagaza Member in a different diagenetic environments. These events include micritization, cementation, compaction and dissolution. These diagenetic processes occurred in marine phreatic zone, mixed marine and meteoric zone, meteoric zone and shallow burial environment. Low concentration of Sr and Mn of the An Nagaza samples could be attributed to the diagenetic effects produced by meteoric solutions. High concentration of Fe in the An Nagaza samples suggest that all samples are not exclusively carbonate and contain appreciable amounts of clay minerals and quartz grains. Depleted or negative values of $\delta^{18}O$ in the An Nagaza samples probably indicate the influence of sea-level fluctuation during Miocene, influx of meteoric water and recrystallization of early carbonate cements. Furthermore, changes of $\delta^{13}C$ from low values in the bottom to relatively higher values and return to a low $\delta^{13}C$ values in top of the sequence may indicate a move from restricted basin with high productivity to more marine conditions and back again. Analysis of Sr isotopes suggest that an Early Miocene age is postulated for the An Nagaza Member of the Al Khums Formation.

Keywords: Al Khums Formation, An Nagaza, marine phreatic, meteoric, $\delta^{13}C$, $\delta^{18}O$.

INTRODUCTION

The succession of the exposed outcrop unites in northwestern Libya (Fig 1) ranges from Triassic to Late Miocene (Fig. 2).

Al Khums Formation is the only record of the Tertiary in this area, although Tertiary strata occur both to the southwest and to the east, in the Sirt Basin (Barr and Weegar, 1972). Al Khums Formation consists chiefly of a limestone, chalk and marly limestone interbedded with thin layers of sandy limestone and clay, much of it contains both mega fossils and microfossils. Al Khums Formation has been divided by Salem and Spreng (1980) into two members named the lower An Naggazah member (the target of this study), and upper Ras El Manubyah Member.

The thickness of An Naggazah Member in the study area is approximately 95m, and unconformably overlies Mesozoic rocks. An Naggazah Member can be divided into two units (Salem and Spreng, 1980); the lower Unit (1) consists predominantly of bioclastic, biostormal, and biohermal limestone. This unit was deposited in low areas on eroded Mesozoic rocks, so its thickness is variable and is controlled by the topography of pre-Miocene. Unit (2) is brownish, yellow, marlstone, argillaceous limestone and sandy to silty detrital limestone. Both interbedded with green gypseferous clay beds.

The most common fossils are pectins, high spiral gastropods, oysters, corals, bryozoans, algae and echinoids. (Fig. 3a and b).

Previous Work

Many works have been done on Al Khums

* Libyan Petroleum Institute (LPI), P. O. Box 6431, Tripoli, Libya

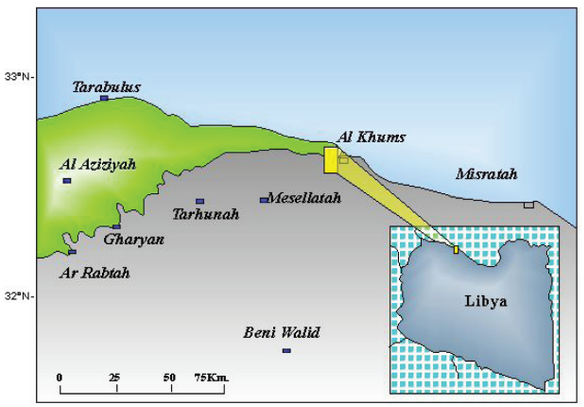


Fig. 1. Location map of Al Khums area.

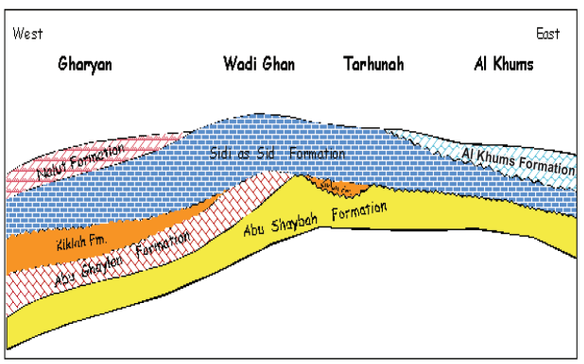


Fig. 2. East-west cross-section through Gharyan Al Khums area (after Fatmi and Sbeta, 1991).

Formation, but most of them concentrated on a stratigraphy and age determination.

The sediments of Al Khums were first distinguished as Middle Miocene. Floridia (1939) and Mann (1975) have introduced the term of Al Khums on the Mediterranean Coast in Tripoli and suggesting a Middle Miocene age during the regional mapping of Libya (1975 to 1984) for IRC.

Zivanovich (1977) added more details on the lower and upper part of Al Khums Formation exposed in Bani Walid and Al Qaddahyah sheets.

Mijalkovic (1977), established the persistence of Al Khums Formation from Al Khums area eastwards as far as An Nawfliya, and all of them attributed it to a Middle Miocene age. The formation was studied and subsequently divided by Salem and Spreng (1980) into two members, a lower An Naggazah Member and an upper Ras Al Mannubya Member. Innocenti and Pertusati (1984) studied the sediments of the formation and determined their age as Late Miocene. El Waer (1988 and 1991) had studied the ostracoda in this area and agreed with the others about the Middle Miocene age. Sherif (1991) determined the same age in his study of the area.

MATERIALS AND METHODS

Several fieldtrips were carried out to the study area in order to measure and log the An Nagaza Member section. A total of 33 samples from 95 meter exposure of this member were collected.

All samples were used for thin-section preparation, subsequently all samples were grinded for atomic absorption analysis in the Libyan Petroleum Institute laboratories and stables isotopes contents in the NERC Isotope Geosciences Laboratory, UK.

Two additional unconsolidated sandstone samples were sieve analyzed in order to help identification of the environment of deposition of this member. All thin-sections were stained according to Dickson's (1965) technique.

The powder of these samples was reacted with anhydrous phosphoric acid in *vacuo* overnight at a constant temperature of 25°C. The CO_2 liberated was separated from water vapour and collected for analysis in the NERC Isotope Geosciences Laboratory, UK. Measurements were made on a VG SIRA mass spectrometer. Overall analytical reproducibility for these samples and standard materials was better than 0.1% for both $\delta^{13}C$ and $\delta^{18}O$ (2σ). Isotope values ($\delta^{13}C$, $\delta^{18}O$) are reported as per mil (‰) deviations of the isotopic ratios ($^{13}C/^{12}C$, $^{18}O/^{16}O$) on the VPDB scale.

150 milligrams of powder were leached overnight with 3mls of IN Romil® ultrapure acetic acid in order to dissolve only the carbonate fraction. Each sample was centrifuged and the supernatant liquid pipetted into a Savillex® FEP beaker and reduced to dryness. The residue was converted to chloride with 1μL double quartz-distilled 6N hydrochloric acid, evaporated until dry and then dissolved in 200 μL of 2.5N HCL. After centrifuging, 100μL of each sample was located onto a standard Biorad® AG50-X8 cation exchange column and eluted in 2.5N HCL. Strontium was loaded on a single tantalum filament with phosphoric acid. Isotope ratios were measured on a Finnegan Triton mass spectrometer run in static mode with mass fractionation normalized to a $^{87}Sr/^{86}Sr$ ratio of 0.1194. At least 170 ratios were collected which resulted in a 'within run' precision of better than 7 x 10^{-6} (2σ). Each sample was analysed twice and the mean of the data is used in this study. Replicate analysis (n = 25) of the international strontium isotope standard NBS-987 yielded a mean value of 0.7102446 ± 0.0000012 (2σ). 16 determinations of the North Atlantic Seawater standard yield a mean $^{87}Sr/^{86}Sr$ ratio of 0.7091689 ± 0.0000091 (2σ).

PETROGRAPHY

The vertical variation in lithology of An Nagaza Member of the Al Khums Formation can be divided into various lithological units or lithofacies started with sediments resulted from transgression onto a Cretaceous surface of moderate relief. Generally, these sediments are of fossiliferous, reef-bearing with basal sand and limestone (Salem and Spreng, 1980). Five lithofacies can be distinguished on bases of field observation; faunal diversity and petrographic analysis (see also Fig. 12). These lithofacies in ascending order are as following:

Lithofacies 1: This lithofacies overlying Cretaceous sediments of Ain Tobi Member of the Sidi as Said Formation and is characterized by transgressive sandstone at its base (Fig. 3c and d). Lithofacies 1 exhibits 13 metres of yellowish, highly fossiliferous (gastropods, bivalves, echinoderms, foraminifera and algae) and irregularly to horizontally bedding marly limestone. The lower 2m of Lithofacies 1 are mainly sandstones composed of quartz grains scattered and float in fine micrite matrix (Fig. 4a and b).

Quartz grains are fine to medium-grained, well rounded to subrounded, rarely subangular, calcareous and unicrystalline. This sandstone containing scattered fossils including (plecypods, foraminifera, echinoderms, corals and gastropods, Fig. 4c). The sand is conglomerate in places, containing flat pebbles and cobbles of limestone. The main non-skeletal allochems occurred in Lithofacies 1 are ooids and pellets (Fig. 4b). They are observed only in the lower part. Ooids are of different size or poorly sorted (very fine to medium) with relatively thin cortices coating detrital quartz nuclei. The early ooids laminae fill in depression on the surface of quartz grains and are absent from angular corners. Ooids with no nucleus seem to be partially and/or completely micritized to form pellets. The skeletal allochems of Lithofacies 1 consist also of large single crystals of echinoderm with early syntaxial calcite overgrowth cement (Figs. 4d and 5a). Small transverse cross-sections of echinoderm spins showing single calcite crystal structure are also observed and scattered within micrite matrix (Fig. 5b). Large fragments of red coralline algae are also present, some of them are well preserved (Fig. 5c) with very thin micrite walls separating small cells and others are fractured.

Both uniserial and biserial and various shapes of miliolid foraminifera are observed within sediments of Lithofacies 1 and are surrounded by micrite envelopes and their typical chambers are filled by sparry calcite (Figs. 5d and 6a). Poorly preserved pryozoa fragments are scattered throughout the

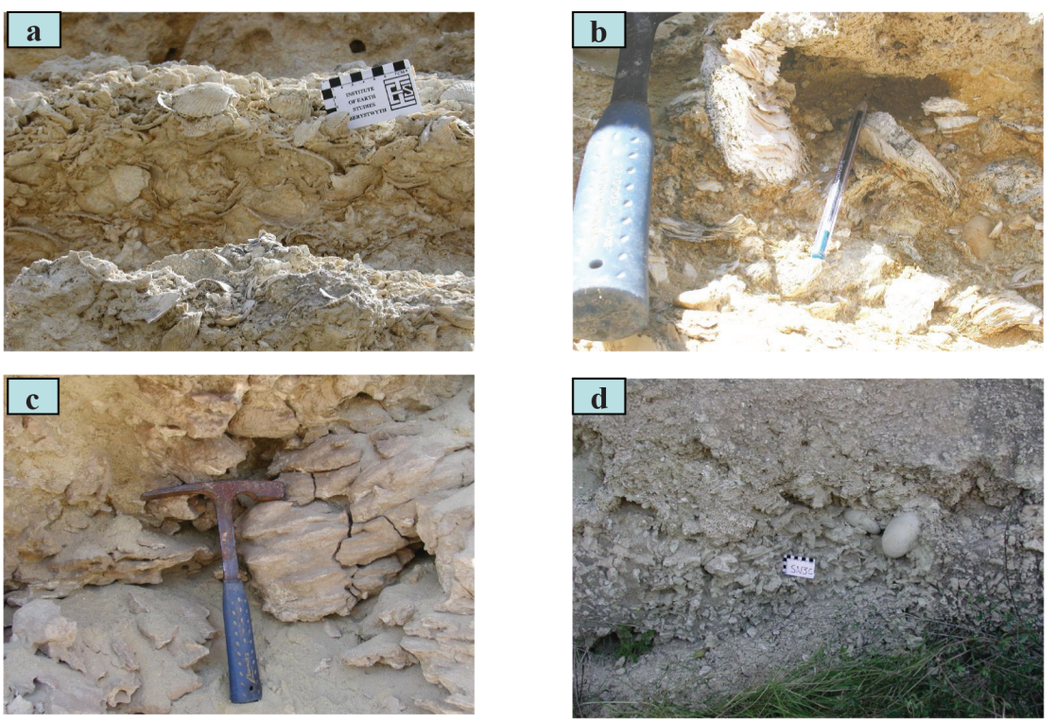


Fig. 3. Field views showing common fossils in An Nagaza sediments (a and b) and the basal sandstone and conglomerate of the An Nagaza Member (c and d)

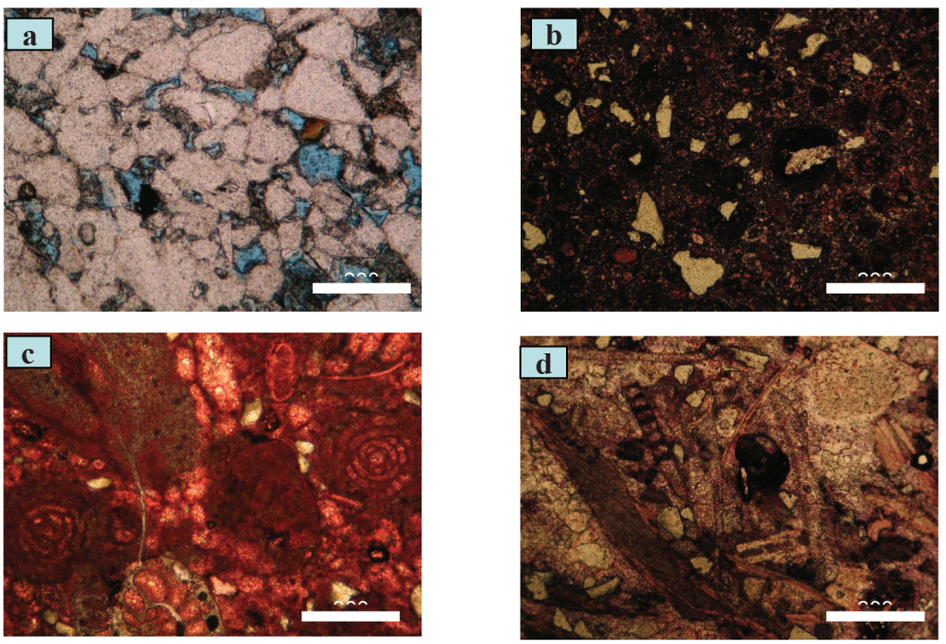


Fig. 4 Microphotographs from An Nagaza Member of the Al Khums Formation. a) Microphotograph showing quartz grains. b) Microphotograph showing ooids within micrite matrix. c) Microphotograph showing different types of foraminifera. d) Microphotograph of uniserial forams and echinoderm plates with syntaxial overgrowth cement.

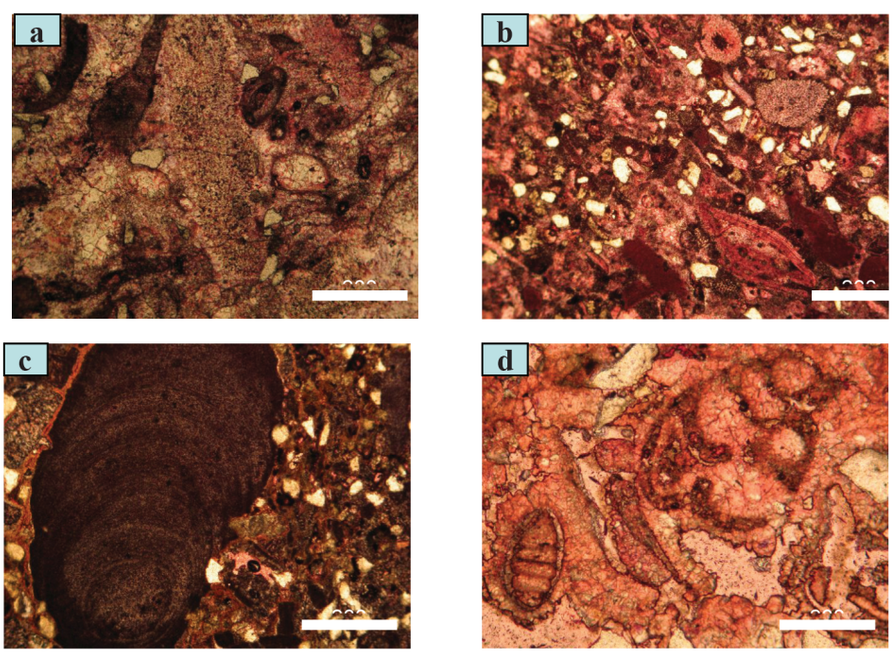


Fig. 5. Microphotographs of An Nagaza Member of the Al Khums Formation: a) Microphotograph of echinoderm plates with syntaxial overgrowth cement. b) Microphotograph showing plates of echinodem and numulites. c) Microphotograph showing good preserved coraline algae. d) Microphotograph of gastropoda shells with micrite envelope. Note also interparticle porosity.

upper part of this lithofacies. Rare transverse sections of brachiopod spins with thick foliated walls (Fig. 6b) are also occurred. No visible porosity observed in most of these sediments.

Sediments of this lithofacies exposed to many diagenetic events; such as cementation and micritization. Lithofacies 1 can be classified as bioclastic wackestone dominated by sandstone at the lower part.

Lithofacies 2: This lithofacies composed of 20 meter of yellowish-grey, irregularly to massively bedded and hard limestone. Sediments of Lithofacies 2 consist of algae, corals, and plecypods, these

organic accumulations thicken locally to form biohermal structure (Salem and Spreng, 1980). Corals are concentrated in the lower part of the lithofacies (Fig. 6c), while echinoderms, bryozoans and plecypods locally form coquinal masses in the upper part. The most common skeletal particles are small, longitudinal and not very well preserved red algae (Fig. 6d). Different sizes of mainly rounded and well preserved echinoderm plates and cross-sections of crinoid spins are also common (Fig. 7a). All cemented by calcite, mainly of syntaxial overgrowth type.

Bryozoa fragments are observed in Lithofacies 2, their cells are separated by thin walls of micrite. These cells are mainly filled by drusy mosaic calcite cement. Some of the bryozoan fragments are influenced by pressure solution event. Cells of bryozoans are similar in the shape to the bees cells (Fig. 7b). Corals are relatively unaltered and illustrating high initial intragranular pore spaces. Some of these pores are filled by sparite.

Miliolids, Numulites (Fig. 7c), fusulinds and biserial forams are rarely observed within sediments of Lithofacies 2. They are mainly characterized by thick micrite walls and their chambers are filled by different texture of calcite.

Quartz grains are the only non-carbonate constituents observed in Lithofacies 2. They are fine, moderately sorted and subrounded unicrystalline grains scattered throughout matrix. Lithofacies 2 can be classified as packstone, becoming grainstone at the top.

Lithofacies 3: This lithofacies begins with sandy limestone. Sand grains are mainly composed of fine, subrounded to subangular quartz grains, scattered throughout the whole lithofacies. The thickness of Lithofacies 3 is 27 metres and it is characterized by very common echinoderms. These echinoid plates are still with their original structure and well preserved spins are also occurred (Figs. 7d and 8a), some of them have syntaxial calcite overgrowth cement.

Rare uniserial and biserial forams are observed in Lithofacies 3. Algae are not common (some of them are completely micritized) and bryozoa cross-sections exhibit fenestral structure, whereas large and very common bryozoan fragments have thick fibrous walls (similar to brachiopod structure) and shows honey-comb structure-like (Fig. 8b). All cells are filled with drusy mosaic cement. Gastropods occur as transversal or longitudinal section within Lithofacies 3. Their chambers are filled by either drusy cement or micrite and outlined by thin micrite envelopes (Fig. 8c). In the upper part of this lithofacies, large fragments of corals composed of typical rounded chambers are common. Some of these chambers are filled by micrite and their outlines are sparite, whereas others are filled by sparite with micrite envelopes outlining them. Rare valves of ostracoda enclosed drusy calcite cement are also observed in the upper

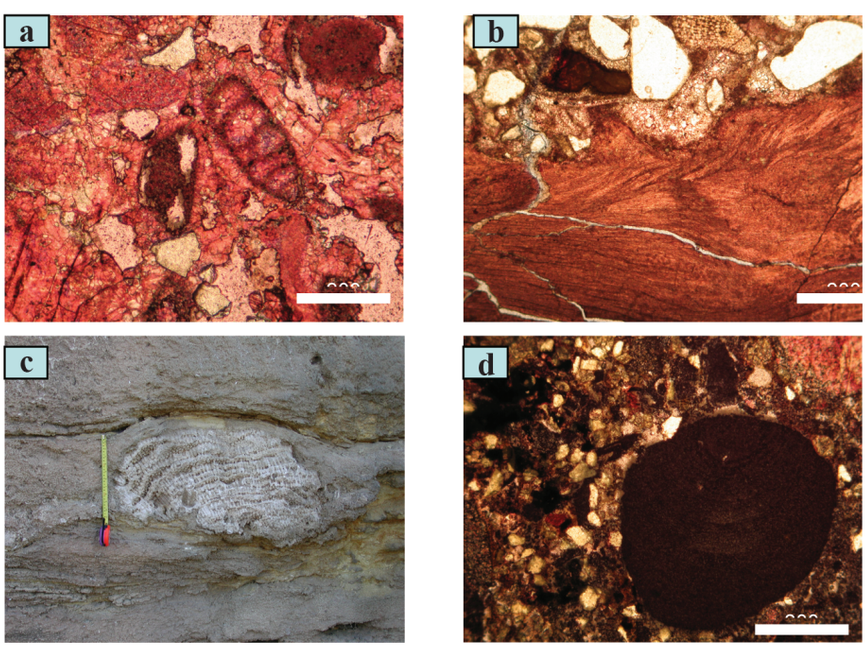


Fig. 6. Microphotographs of An Nagaza Member of the Al Khums Formation: a) Microphotograph of gastropoda shells with micrite envelope. b) Microphotograph showing foliated mollusk fragments. c) Field view of a large corals. d) Microphotograph of well preserved coraline algae.

part of this lithofacies. Sediments of Lithofacies 3 can be classified as biomicrite sandy packstone.

Lithofacies 4: The 16 meter thick sediments of this lithofacies are characterized by brownish-yellow marlstone, argillaceous limestone, and sandy to silty detrital limestone, interbedded with green, gypsiferous clay beds. Lithofacies 4 is the most fossiliferous beds in the entire Al Khums Formation. The common fossils are pectons (Fig. 8d), highly spired gastropods, corals, echinoderms (Fig. 9a) and shallow marine foraminifera. Corals of Lithofacies 4 represented by large fragments exhibit very thick walls with wavy micrite laminae and various chamber sizes. Chambers are outlined by micrite envelopes and mainly filled by drusy calcite cement. Longitudinal

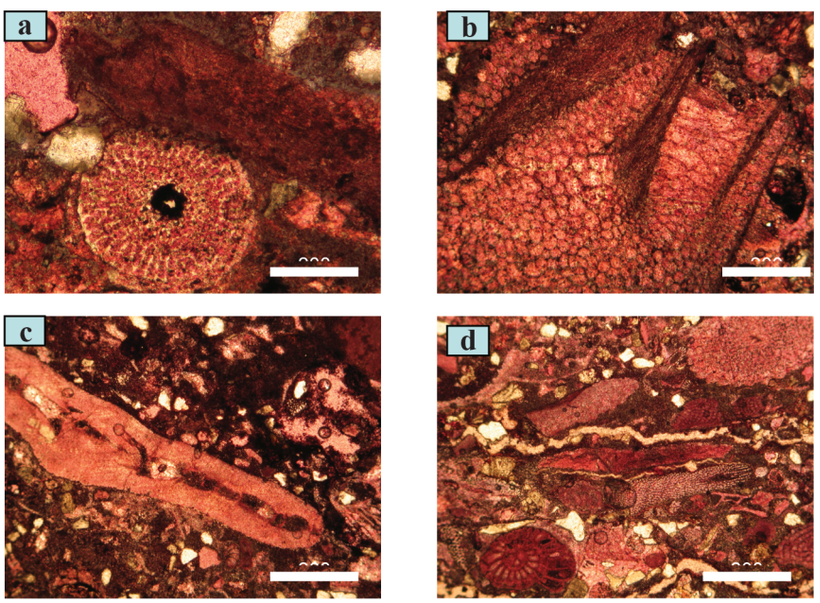


Fig. 7. Microphotographs of An Nagaza Member of the Al Khums Formation: a) Microphotograph showing echinoderm plates and may show influence of compaction on particle grains. b) Microphotograph showing typical structure of bryozoan fragment. c) Microphotograph showing well preserved foraminifera. d) Microphotograph of echinoderm plates and foraminifera + quartz grains. Note the fracture caused by physical compaction.

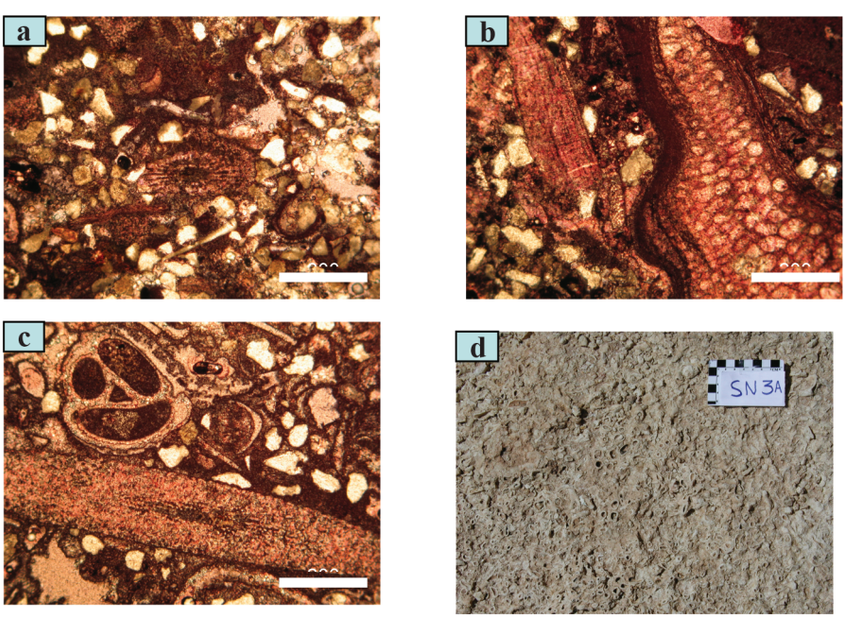


Fig. 8. Microphotographs of An Nagaza Member of the Al Khums Formation: a) Microphotograph showing echinoderm spins (in the centre of photo) with common quartz grains. b) Microphotograph showing typical structure of bryozoan fragment. c) Microphotograph showing well preserved echinoderm spins and transverse section of gastropoda. d) field view showing highly fossiliferous layer.

plates of echinoderm are not common and composed of single calcite crystal; some of them are well preserved.

Transverse section of highly spired gastropods also occurred. They are replaced by non-ferroan calcite. Common, shallow marine uniserial forams are observed at the uppermost part of Lithofacies 4. Forams are outlined by micrite envelopes and filled by recrystallized calcite cement. Sediments of Lithofacies 4 are dominated by bioclastic sandy packstone/grainstone.

Lithofacies 5: The 20 meter thick limestone of this lithofacies may represent shallower marine sediments compared with Lithofacies 4. Lithofacies 5 consists of cross section of bryozoans, with drusy mosaic cement filling chambers. Rare uniserial, biserial and miliolid forams are also observed. Very well preserved longitudinal and rounded plates of echinoderm occurred within the whole lithofacies and exhibit syntaxial calcite overgrowth cement (Fig. 9b). Very common large fragments of corals occur and showing thick wavy micrite walls.

The non-skeletal particles occurred in this facies are ooids. They are rounded and poorly sorted, some of them are enclosed single and foliated crystal of calcite (probably of coral fragments) or quartz grain (Fig. 9c), whereas others are partially or completely micritized. Sediments of Lithofacies 5 can be correlated (on bases of constituents) with those of Lithofacies 1. The top of this lithofacies is dominated by marly limestone with very common algae and branched bryozoans (Fig. 9d). Quartz grains of Lithofacies 5 are moderately sorted, rounded to sub-rounded and unicrystalline. This lithofacies can be classified as biomicrite sandy wackestone/packstone.

DIAGENESIS

The sediments of the Al Khums Formation, particularly the An Nagaza Member) were exposed to several different diagenetic processes. These lead to modification of their original textural and compositional characteristics.

Micritization

Here, blue green algae bore into skeletal material in the shallow marine environment. The borings, re filled with micrite after death of the algae. This process continued and the margin of a shell fragment may become completely replaced by micrite (Fig. 4c) to form micrite envelope (Adams *et al*, 1984, Bathurst, 1975). Micrite envelopes developed on possibly brachiopod (Fig. 9c), brayozoa shells (Fig. 8b) and foraminifera (Figs. 5d and 6a).

Repeated formation of micrite envelopes, may lead to the production of a grain completely micritized with no remaining recognizable structure.

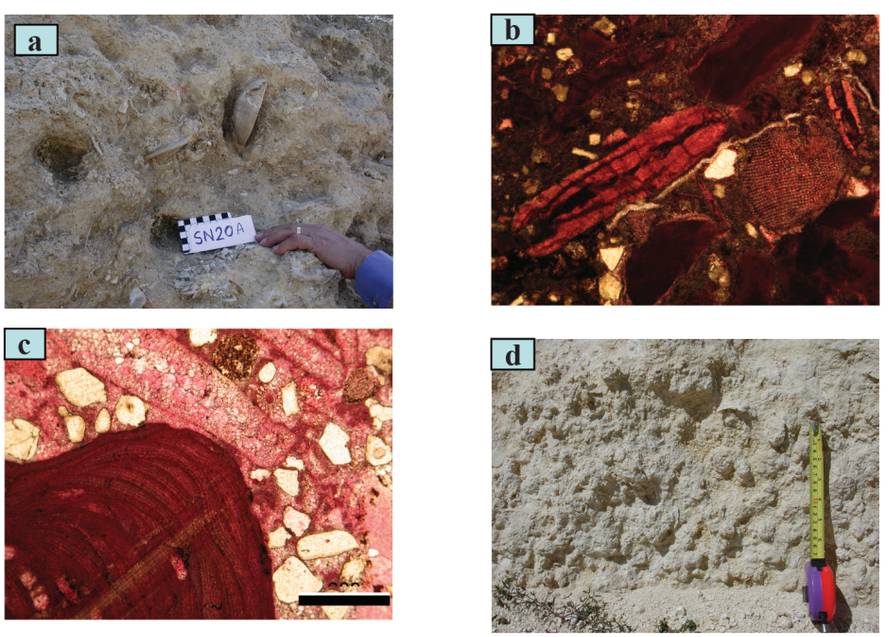


Fig. 9. Field view and microphotograph of An Nagaza Member of the Al Khums Formation: a) field view showing large and well preserved echinoderms. b) Microphotograph showing echinoderms, numulites and micritized grains. c) Microphotograph showing well preserved coraline algae, micrite envelopes, drusy mosaic cement and quartz grains. d) Field view showing a layer of algae and branching bryozoans.

Cementation

The sediments of the An Nagaza Member exhibit four types of cementation. They are syntaxial overgrowth cement, isopachous cement, drusy mosaic cement and meniscus calcite cement.

***Syntaxial overgrowth cement*:** The syntaxial calcite overgrowths exist frequently around echinoderm debris (Figs. 4d and 5a). They exist in form of rims of variable thicknesses and of clean, coarse and bladed crystals with optical continuity with the grains (Evamy and Shearman, 1965).

***Isopachous cement*:** It appears as a rim of crystals of equal thickness on grains such as foraminifera (Fig. 10a). This cement exhibits a radial-fibrous fabric, and it may originally have been aragonite, details of the texture having been lost during inversion to calcite or during dissolution.

***Drusy mosaic cement*:** This type of calcite cement exhibits different crystal sizes, and it occurs as a drusy filling in many skeletal cavities of fossils, such as foraminifera tests, mollusk or bryozoans. The crystal size of the drusy mosaic cement increases towards the centre of cavities (Figs. 5d and 6a; 7b; 9c).

***Meniscus cement*:** Meniscus cement is irregularly distributed and it is precipitated in the vadoze zone as a result of water being held by capillarity between grains where it is concentrated. The crystals of this type of cement are fine to very fine mainly non-ferroan calcite at the grain contacts (Fig. 9c).

Compaction

The rocks of An Nagaza Member were likely subjected to only shallow burial. Mechanical compaction, i.e. grain to grain suture contact (Fig. 7a) and chemical compaction (Fig. 7d) are frequent and were the major diagenetic processes that existed in the shallow burial environment. The fractures within the carbonate and quartz grains probably resulted from physical compaction, during which they were filled by sparite or micrite respectively.

Dissolution

Dissolution and leaching features are present in all carbonates of the Al Khums Formation (An Nagaza Member). Dissolution resulted in the development of several types of porosity including interparticle or intergranular (see Fig. 4a), and moldic which mainly filled by later calcite cement (see Figs. 5d and 6a).

GEOCHEMISTRY RESULTS

Trace elements

Table 1 presents the results of the chemical analyses of the carbonates of samples selected from

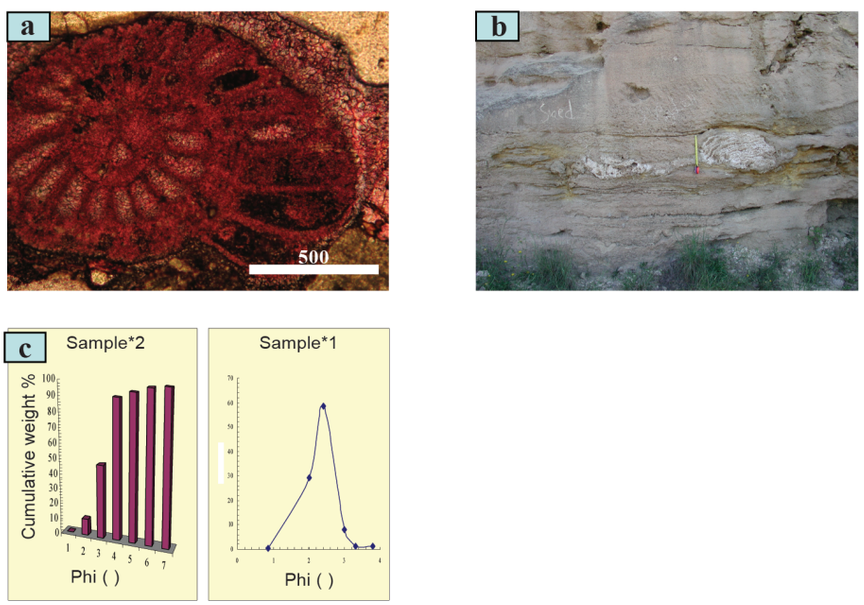


Fig. 10. a) Microphotograph of foraminifera from An Nagaza Member of the Al Khums Formation with probably isopachous cement. b) Field view showing different orientation of corals resulted from reworking. c) Cumulative curves illustrating sediments of beach environment.

Table 1. Chemical analyses (ppm) of selected samples from An Nagaza Member.

Sample no	Fe (ppm)	Mn (ppm)	Mg (ppm)	Sr (ppm)	Na (ppm)
SN1	2000	17	4000	300	31
SN2	1000	63	2000	82	57
SN3	8000	84	18000	70	86
SN4	9000	80	16000	100	95
SN5	7000	241	2000	58	59
SN6	2000	116	3000	100	93
SN7	2000	58	5000	100	69
SN7a	1000	60	1000	200	
SN8	4000	149	6000	54	62
SN9	1000	105	2000	300	79
SN10	4000	139	2000	500	175
SN11	1000	41	1000	100	59
SN12	1000	39	1000	28	55
SN14	2000	54	20000	31	24
SN15	2000	87	6000	100	31
SN16	2000	71	3000	100	58
SN17	2000	68	3000	67	72
SN18	2000	78	3000	81	66
SN19	1000	65	3000	82	79
SN20	3600	51	10000	66	43
SN21	2000	51	10000	76	44
SN22	1000	48	3000	90	52
SN23	2000	66	1000	100	44
SN24	2000	56	2000	91	38
SN25	2000	55	1000	100	11
SN26	3000	48	2000	100	6
SN27	2000	85	5000	89	28
SN28	3000	68	9000	100	27
SN29	5000	33	7000	200	180
SN30	3000	24	3000	200	21
SN31	7000	155	1000	100	3
SN32	1000	35	1000	100	9
SN33	1000	35	2000	100	80

An Nagaza Member of the Al Khums Formation. The variations in concentration of the elements analyzed reflect the diversity of their mineralogical compositions.

Fe contents in Lithofacies 1 range from 1000 to 9000ppm, with an average 4000ppm. The highest Fe content is concentrated at the base of Lithofacies 1, just above the sandstone bed where marl and clay increase. This may indicate that Fe concentration is mainly controlled by clay minerals. Fe concentration decreases significantly at the middle part of the Member (Lithofacies 2 and Lithofacies 3). It increases again towards the top of the Member (Lithofacies 4 and Lithofacies 5, Fig. 11).

Mn concentration increases from Lithofacies 1 (average 87ppm) to Lithofacies 2 (average 95ppm), but decreases towards the top of the Member (Fig. 11), averaging 71ppm and 62ppm in Lithofacies 3 and Lithofacies 5 respectively, with the lowest value observed in Lithofacies 4 (average 53ppm).

The lowest value of Mg was seen in Lithofacies 2 (average 2400ppm), whereas all other lithofacies exhibit more or less similar values.

Sr contents in all lithofacies are low with highest value recorded in Lithofacies 2 (average 196ppm). Generally, Sr contents increases from Lithofacies 1 (average 126ppm) to Lithofacies 2 (average 196ppm) and started to decrease towards Lithofacies 3 (average 77ppm), but increases again towards the top of the Member in Lithofacies 4 and Lithofacies 5 (89 and 127ppm in average respectively, Fig. 11).

Na concentrations in An Nagaza Member are low with highest value was observed in Lithofacies 2 (average 86ppm), whereas, the Na values in other lithofacies are 70ppm,55ppm, 34ppm and 50ppm in Lithofacies 1, 3, 4 and 5 respectively.

Isotopes

Oxygen Isotopes: Oxygen values for sediments of Lithofacies 1 (Table 2) vary from -3.9 to -7.5 ‰ (PDB). They are generally decreasing upward (Fig. 12), with maximum value recorded at the bottom of the lithofacies (-3.9‰), whereas the minimum being at top of the lithofacies (-7.5‰). The range narrows considerably at the middle of the lithofacies (-5.4 to -7.2‰). Oxygen isotopes do not vary greatly and exhibit narrow range in sediments designated as Lithofacies 2. They range from -5.2 to -7.8‰ (Fig. 12), with highest value observed at 22 metres (-5.2‰).

The variation in oxygen isotopes is very limited in Lithofacies 3. They range from -7.9 to -7.1‰), with a mean value of -7.5‰. Similarly, no great changes in the oxygen isotope values recorded in sediments of Lithofacies 4. They range from -7.4 to -5.9‰, with an average of -7.0‰. The range is quite wide of the oxygen isotope values in Lithofacies 5, from -7.3 to -2.2‰, with an average of -5.5‰. The highest values are observed at the middle of the lithofacies which correspond with decreasing $^{87}Sr/^{86}Sr$ (Fig. 12).

Carbon Isotopes: The $\delta^{13}C$- values of the lithofacies of the An Nagaza Member (Table 2) analyzed cover a wide range (-8.1 to 0.0‰), typical of carbonates formed in a near by continental environments, where decaying organic matter serves as a significant source of carbon for the dissolved inorganic carbon pool (Mayayo *et al*, 1996).

The lightest $\delta^{13}C$- values are found at the base of Lithofacies 1, with values from -8.1 to -3.3‰, and a mean of -4.7‰. Fig. 12, obviously shows that the

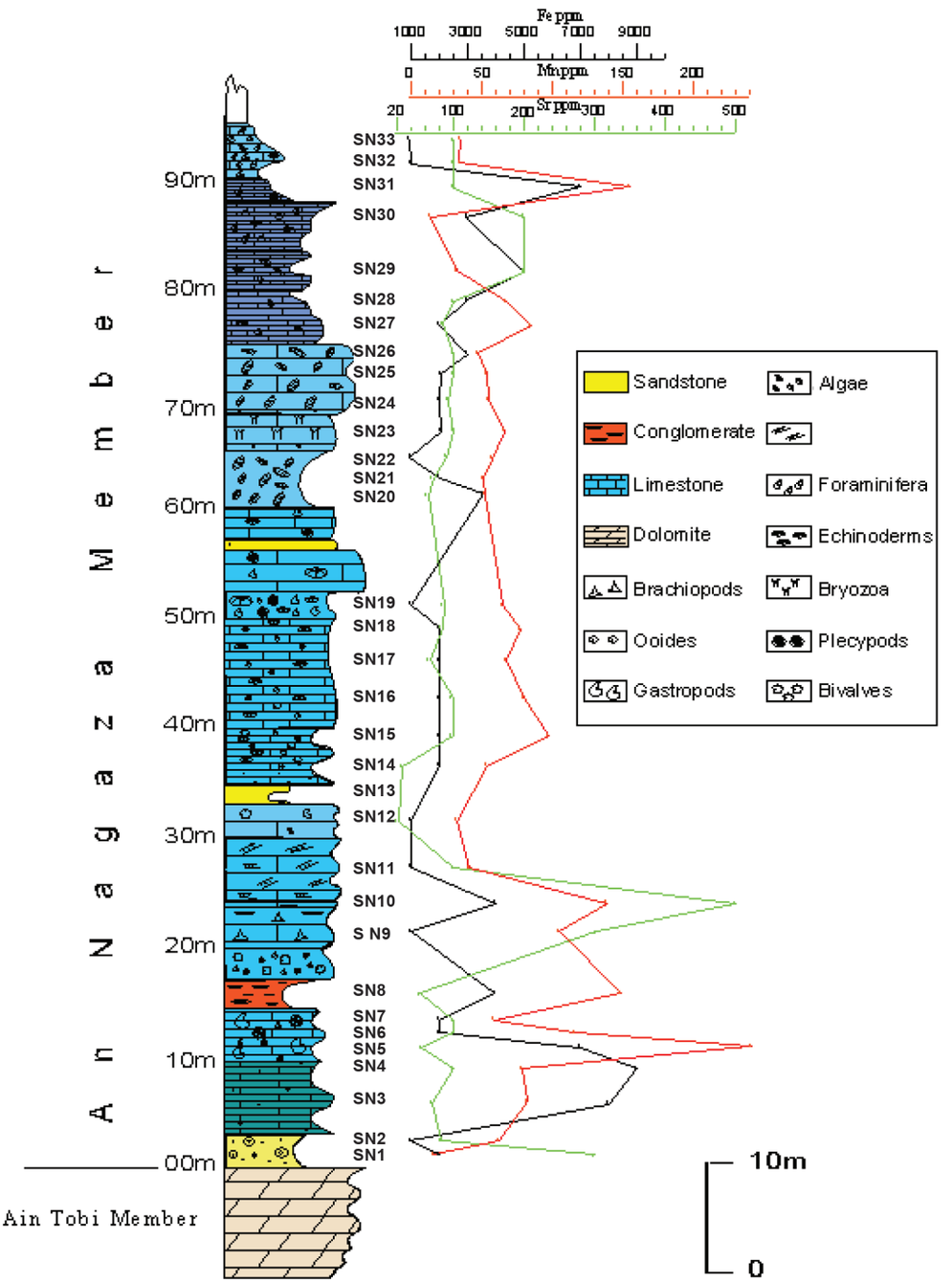


Fig. 11. Fe, Mn & Sr contents.

$\delta^{13}C$ getting heavier towards the top of the lithofacies. Carbon isotope values in sediments of Lithofacies 2 range from -5.6 to -2.3‰, with an average of (3.8‰). The highest value is observed at the bottom of the lithofacies. Generally, $\delta^{13}C$- values in Lithofacies 2 becoming lighter toward the top.

$\delta^{13}C$- values in both Lithofacies 3 and Lithofacies 4 cover narrow range (-3.6 to -1.1‰) and (-2.4 to 0.0‰) respectively. Lithofacies 3 shows slightly enriched carbon isotope values toward its top, on the other hand, $\delta^{13}C$- values in sediments of Lithofacies 4 are gradually depleted towards the top. Lithofacies 5 exhibits slightly wide range of $\delta^{13}C$- values (-6.9 to -2.1‰), with an average of -4.9‰. The $\delta^{13}C$- values of Lithofacies 5 getting lighter towards the top of the facies. Generally, $\delta^{13}C$- values are heavier towards the top of the member (Fig.12), with exception of Lithofacies 5, where the values

Table 2. Carbon and oxygen isotopic analyses of the selected samples from An Nagaza Member.

Sample no	$s^{13}C$	$s^{18}O$
SN1	-8.1	-3.9
SN2	-6.5	-6.3
SN3	-4.3	-7.2
SN4	-4.6	-6.9
SN5	-4.5	-7.5
SN6	-3.9	-5.4
SN7	-4.2	-7.2
SN7a	-3.3	-7.5
SN8	-2.4	-7.8
SN9	-2.3	-5.2
SN10	-3.7	-7.7
SN11	-4.9	-7.4
SN12	-5.6	-7.5
SN14	-3.6	-7.4
SN15	-3	-7.5
SN16	-2.3	-7.8
SN17	-1.5	-7.4
SN18	-2.2	-7.9
SN19	-1.1	-7.1
SN20	0	-5.9
SN21	-1.5	-7.4
SN22	-2.4	-6.9
SN23	-2.2	-7.1
SN24	-2.3	-6.8
SN25	-2	-6.8
SN26	-1.4	-6.8
SN27	-2.1	-7.3
SN28	-2.6	-5.8
SN29	-6.9	-2.9
SN30	-5.9	-2.2
SN31	-5.4	-7.2
SN32	-5.1	-7.1
SN33	-6.1	-6.3

are slightly lighter. It has been noticed that the highest values of $\delta^{13}C$ for most samples are opposite to the lowest values of $\delta^{18}O$ (Fig. 12).

Strontium Isotopes: Strontium isotope ratios presented in Table 3 ranges from 0.708438 to 0.708692. Corresponding ages have been calculated using the regression equations developed by Miller *et al*. (1991a) and Oslick *et al*. (1994). The former are based on the geomagnetic and polarity timescale of Berggren *et al*. (1985) whereas Oslick *et al*. (1994) also use the magnetic timescale of Cande and Kent (1992) to facilitate comparison with other studies. In each age calculation the measured $^{87}Sr/^{86}Sr$ ratios for the An Nagaza Member samples have been normalized to the relevant values obtained for the NBS 987 international isotope standard (0.710252 Miller *et al* and 0.710256 Oslick *et al*).

DISCUSSION AND INTERPRETATION

Environment of deposition: Desio (1971) mentioned the early Miocene transgression and the uplift of the area in the Late Miocene which resulted in the emergence of the area from the sea. Various fossils are indicative of shallow, neritic environment (Mann, 1975). The abundance of shallow water foraminifera as well as thick-shelled oyster, corals and the coralline algae with silisiclastic material suggest the shallow marine environment and were supplied into an outer neritic setting during Early Miocene.

Presence of horizons of limestone conglomerate and reworked fossils indicate periodic sea level rise and fall or times of increased wave action (Salem and Spreng, 1980). Furthermore, occurrence of ooids in the sediments of both Lithofacies 1 and Lithofacies 5 supporting the periodic sea level fluctuation and the mean temperature exceed $18^{O}C$. The grain supported nature of most of the lithofacies suggests

Table 3. Age determination (Ma) of the selected samples from An Nagaza Member.

Sample no	Sr87/Sr86	Age, Ma (Miller *et al*, 1991)	Age, Ma (Oslick *et al*, 1994)	
		BKF 1985	C & K 1992	BKF 1985
SN1	0.7086841	17.08	16.98	17.27
SN2	0.7086786	17.17	17.06	17.35
SN3	0.7085713	18.97	18.63	18.9
SN4	0.7085825	18.78	18.47	18.74
SN5	0.7085033	20.11	19.63	19.88
SN6	0.7086196	18.16	17.92	18.2
SN7	0.7086233	18.1	17.87	18.15
SN7a	0.7086233	18.1	17.87	18.15
SN8	0.7085522	19.29	18.91	19.18
SN9	0.7086809	17.13	17.03	17.32
SN10	0.7085939	18.59	18.3	18.57
SN11	0.7086689	17.33	17.2	17.49
SN12	0.7086634	17.43	17.28	17.57
SN14	0.7084986	20.19	19.7	19.95
SN15	0.7084989	20.19	19.69	19.95
SN16	0.7085038	20.1	19.62	19.88
SN17	0.7084877	20.37	19.86	20.11
SN18	0.7084557	20.91	20.32	20.57
SN19	0.7085054	20.08	19.6	19.85
SN20	0.7085315	19.64	19.21	19.47
SN21	0.7085203	19.83	19.38	19.64
SN22	0.7085455	19.4	19.01	19.27
SN23	0.7085639	19.1	18.74	19.01
SN24	0.7085681	19.03	18.68	18.95
SN25	0.7085608	19.15	18.79	19.05
SN26	0.7085303	19.66	19.23	19.49
SN27	0.7085566	19.22	18.85	19.11
SN28	0.7086432	17.77	17.58	17.86
SN29	0.7086562	17.55	17.39	17.67
SN30	0.7086497	17.66	17.48	17.77
SN31	0.7085687	19.02	18.67	18.94
SN32	0.7084377	21.21	20.59	20.83
SN33	0.708617	18.21	17.96	18.24

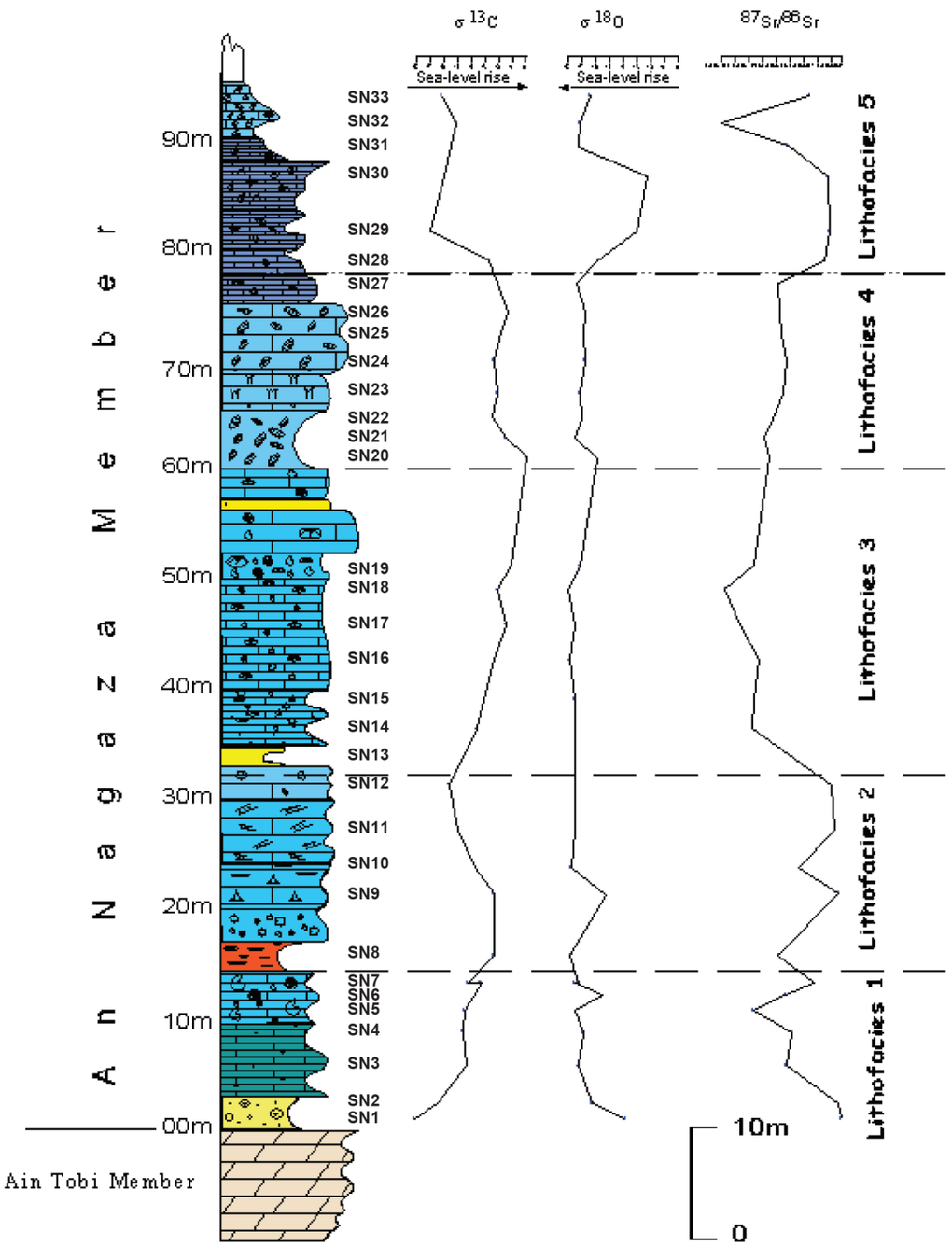


Fig. 12. Isotopes concentration of the An Nagaza Member (see Fig. 11. For symbols).

that the An Nagaza sediments were deposited in a medium to very high-energy marine environment. Vertical lithofacies variations and the presence of algae and branching bryozoans dominant lithofacies at the top of An Nagaza (Fig. 9d), suggest repeated shallowing upwards and elevated salinity. Corals and abundance of fossils indicate a warm water environment and probably normal salinity.

According to the results gained from the sieve analysis of two samples (standard deviation and skewness, Fig. 10c) the sandstones in the base of Lithofacies 1 seem to be deposited in a high-energy beach environment. The dominance of sandy grains in certain levels and less dominance in others of the An Nagaza sequence may also indicate fluctuation of sea level. Silisiclastic material is inferred to be recycled from older formations, perhaps exposed on nearby land areas, which were easily mobilized by marine coastal erosion during Miocene transgression.

Warm water, normal marine, moderate- to high-

energy, middle to outer neritic shelfal area, with reefoidal development, is postulated for An Nagaza sequence during Miocene. In summary, the complete succession of the An Nagaza sediments is interpreted as a transgressive sequence over the Cenomanian deposits, passing from marginal marine possibly to fully marine deposits.

***Diagenesis*:** The diagenetic features of the An Nagaza sediments of the Al Khums Formation seem to have occurred in different diagenetic environments. These are marine phreatic, mixed marine-meteoric and meteoric (Fig. 13).

***Micritization*:** Micritization is one of the early diagenetic processes and is inferred to have taken place in shallow marine environment. Micritization has preferentially affected shallow-water deposits and was most prevalent in low energy deposits. Micritization formed by combination of boring (by algae) and precipitation where the ambient waters are super saturated by calcium carbonate (Bathurst, 1966, 1975; Hook *et al*, 1984).

Micritization of skeletal grains in the An Nagaza sediments form micrite envelopes, which played an important role in preserving the fossil fragments during diagenesis. These envelopes have varying thicknesses and likely formed strictly within the marine phreatic environment near the sediment-water contact. The boundary between the micrite envelope and cement filled the molds and chambers of forams are irregular. This characteristic can be used to distinguish micrite envelopes from micrite coating around skeletal fragments. Also it can be taken as an evidence that this process occurred by blue-green algae (Adams *et al*, 1984).

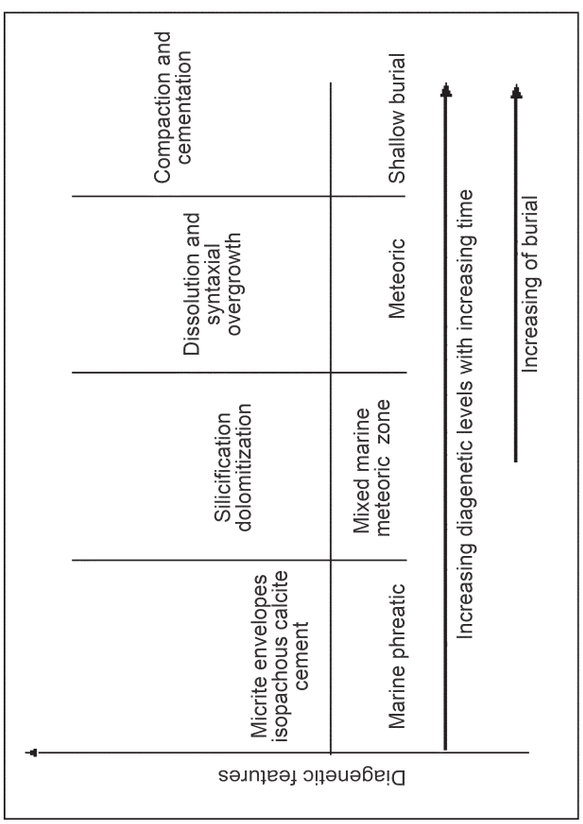


Fig. 13. Different diagenetic features during time and diagenetic environments detected in the An Nagaza Member.

***Compaction and Cementation*:** Lack of compaction in ancient carbonates is a sign of early cementation (Pray, 1960; and Steinen, 1978) and a shallow burial. Cementation in the An Nagaza deposits predates the mechanical compaction, as indicated by the random orientation of the components. In the uncemented beds, foraminifer's tests are broken and the components show a preferred orientation due to wave and current action, boring and mechanical compaction. Biogenic reworking would have destroyed any primary sedimentary structure within the beds. Chemical compaction through pressure dissolution is not able to rotate allochems such as corals (Bathurst, 1987; Figs. 6c and 10b); hence only mechanical compaction is suitable to explain this phenomenon. Pressure dissolution seems to play a minor role in the diagenesis of the examined sediments.

The diagenetic system in shallow-water carbonates with high initial aragonite content such as An Nagaza sequence is thought to be dominantly open (Bathurst, 1987 and Ricken, 1993). Relatively low aragonite content of the cemented (uncompacted) layers, in combination with the relatively high abundance of recrystallized allochems, shows that these layers were diagenetically altered. The onset of cementation in the carbonate layers is probably related to a formerly higher content of unstable carbonate components. In few examples, fracturing probably due to currents activity or mechanical compaction occurred after the development of syntaxial overgrowths on echinoid plates and postdates the formation of drusy non-ferroan spary calcite cement. These fractures remained open and unfilled by any cement, which taken as an evidence of later occurrences.

Syntaxial overgrowths form a minor cement phase restricted to echinoid plates or spins present in different facies of An Nagaza Member. Syntaxial overgrowths usually formed after Micritization (Fig.

13), and may either pre- or post-dates dissolution of aragonite.

The timing relationship of this cement phase relative to other diagenetic events suggests precipitation in a marine to meteoric or very shallow burial environment.

In the coral-rich facies non-ferroan isopachous cement is present around the bioclasts (Fig. 10a). This cement has often been overgrown by bladed or blocky cement, and may be replaced by equant, non-ferroan spary calcite, suggesting alteration of original aragonite. Isopachous cement is most likely represents early marine cement lost by dissolution, followed by recrystallization. This suggests the influence of meteoric water onto the sediments. The occurrence of recrystallization more than the leaching, is probably indicative of submarine precipitation, where nearly all of the pores were permanently filled with sea water. This conclusion is consistent with the suggestions of Land and Goreau (1970) and Marshal and Davis (1981).

Non-ferroan drusy calcite spar is the most common type of cement in the An Nagaza lithofacies, partially or completely occluding intergranular or biomoldic porosity (Figs. 5a and b and 6a). Drusy cements were precipitated after the formation of micrite envelopes. Where aragonite has been dissolved, drusy cements are often better developed between the bioclasts rather than within the biomolds. This suggests that dissolution coincide with the formation of drusy cements in the meteoric phreatic zone (Tucker and Wright, 1990). It is considered likely that calcite for the spar was derived from marine aragonitic bioclasts or cements. Equant, non-ferroan calcite spar is a minor cement phase replacing aragonitic bioclasts or micrite matrix in some sediments of the An Nagaza. It is inferred from the partial replacement nature of this cement that it formed in a shallow pre-burial or possibly meteoric environment.

Meniscus cement is composed of very small size crystals and occurred at the grain contacts. This type of cement is attributed to meteoric environment and it can forms from marine pore waters in the intertidal and supratidal zones as well as from meteoric waters.

***Trace Elements*:** Strontium concentration in diagenetic carbonates ranges from 20ppm to more than 10,000ppm (Land, 1973; Kimbell and Humphrey, 1994). Samples of the An Nagaza sediments have strontium concentration range from 28ppm to 500ppm (Table 1) typically reflects formation from a diagenetic fluid whose composition has been modified by the aragonite to calcite transformation.

Strontium concentration of a diagenetic carbonate samples such as An Nagaza may be a consequence of any combination of a variety of factors, including diagenetic fluid composition, temperature, biological effects, precipitation-rate, extent of recrystallization, type of mineral-solution reaction and crystal growth (Banner, 1995).

The low concentration of Sr and Mn in almost all samples of the An Nagaza Member could be attributed to the diagenetic effects produced by meteoric solutions which, in open systems, modify the chemical composition of carbonates in this way (Brand and Veizer, 1980; and Mayayo *et al*, 1996).

All samples of An Nagaza Member have high concentration of Fe (more than 1000ppm). This means that all samples are not exclusively carbonate and contain appreciable amounts of clay minerals and quartz grains.

Isotopes: The evaluation of the isotope values is somewhat complicated by the fact that bulk samples always contain different carbonate phases, organic carbon and components.

As $\sigma^{18}O$ values depend mainly on the temperature during precipitation (Morse and Mackenzie, 1991). Swart (2000) showed that the changes in the $\sigma^{18}O$ of pore waters along the Bahamas transect resulted from the recrystallization of metastable carbonates in the presence of a geothermal gradient.

The different fractionation factors of calcite and aragonite minerals would lead us to expect a shift towards lighter $\sigma^{18}O$ values in calcitic beds. However, the opposite is observed, the aragonitic beds are depleted in $\sigma^{18}O$. $\sigma^{18}O$ enrichment in the more cemented beds is consistent with a temperature decrease (Fig. 14) as indicated by Erez and Luz (1983).

It is evident that the $\sigma^{18}O$ values can be sensitive indicators of the degree of alteration of the initial metastable minerals comprising the matrix, which was probably formed from a mixture of aragonite and high-Mg calcite and the benthic fossils such as aragonitic mollusks and high-magnesium calcite forams (Shaaban, 2004).

The present $CaCO_3$ components (all are low-Mg calcite) represent the ultimate and product of the stabilization of the initial metastable $CaCO_3$ mineral phase. The close and depleted $\sigma^{18}O$ values of both rock matrix and benthic fossil particles indicate that fabric components probably suffered diagenetic

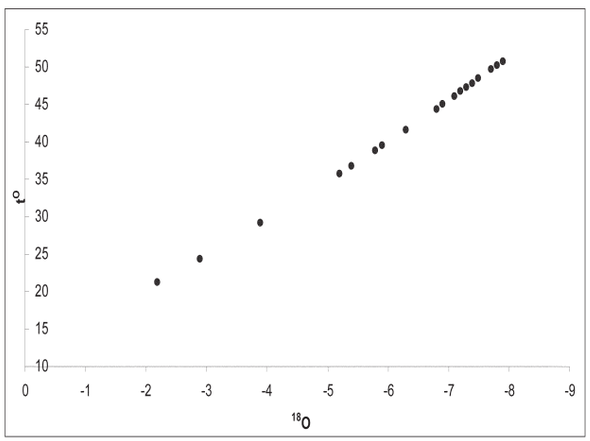


Fig. 14. Cross plot between temperature and oxygen isotope.

stabilization from freshwater dominated solutions undersaturated with respect to both high-Mg calcite and aragonite (Shaaban, 2004). This is true if we apply the following equation given by Hoefs (1973) on samples taken from An Nagaza sequence:

$Z = a(\sigma^{13}C+50) + b(\sigma^{18}O+50)$; where a= 2.048 and b= 0.498. Carbonate with a Z value above 120 would be classified as marine; those with a Z value below 120, as freshwater types. Most of the An Nagaza samples exhibit a Z values below 120, which suggest the strong influence of the freshwater solution.

Oxygen isotope data, compiled in Table 2, range from -2 to -7.9‰. These values are, possibly lower than expected from Miocene marine carbonates (Jacobs *et al*, 1996) and suggest that there may have been exchange with isotopically lighter meteoric water at one or more times in the past which has been approved by using the Hoefs (1973) equation. It may be argued that sample no. SN30 also suffered reworking. $\sigma^{18}O$ values of An Nagaza facies are significantly depleted (Table 2) compared to marine carbonate shells (Woo & Khim, 2006). Processes that can cause the depletion in $\sigma^{18}O$ for early diagenetic carbonates in marine silisiclastic deposits are summarized by Morad *et al* (1996); the influx of meteoric water, the oxidation of organic matter in sulphate-reduction zone, the interaction between seawater and sediments, the upwelling of hot fluids to near-surface, and the recrystallization or replacement of early carbonate cements during burial.

Neritic carbonates are enriched in ^{13}C compared to pelagic counterparts by 2-5‰ (Milliman, 1974). Hence, lithofacies (2, 3 and 4) with high neritic carbonate content display high $\sigma^{13}C$ values whereas; pelagic-rich lithofacies (1 and 5) have relatively low $\sigma^{13}C$ values.

The carbon isotope data range from 0.0 to -8.1‰. It is more difficult to assess the stability of the carbon isotopes because in marginal marine environment the carbon isotopes can be controlled by a number of factors. However, the relatively smooth change from low $\sigma^{13}C$ values in the bottom of the sequence (SN1 and SN2) to higher values, more typical of open marine water, and return to a low $\sigma^{13}C$ value in the top (SN33) may be an indication that a primary signal is preserved. This may be caused by a move from a restricted basin with high productivity, to more marine conditions, and back again (see the environment of deposition discussion section).

The Sr isotope composition of the An Nagaza samples of the Al Khums Formation corresponds to that of Early Miocene age. The calculated ages vary from 17 to 21 Ma, but not, as would be expected, in a systematic fashion which suggests that the carbonate samples may not be well preserved. The data scatter widely, suggesting mixing between a less radiogenic (marine) and more radiogenic meteoric components. Miller *et al* (1991a) related the changes of Sr isotopic in late Eocene to Miocene to glaciations and deglaciations of the Antarctica Craton. They explained the higher rate of change of $^{87}Sr/^{86}Sr$ during the early Miocene by an increase in the frequency of glaciations and the lower rate of change in the Middle Miocene by the development of a permanent ice cap in east Antarctica. Hodell *et al* (1991) and Raymo (1991) attributed the bulk of the Late Neogene $^{87}Sr/^{86}Sr$ increase to mountain uplift.

Sea Level Fluctuation: A $\sigma^{18}O$ decrease at the lower Miocene indicates that there was a large (more than 50m) glacioeustatic event (Miller, *et al*, 1991b). A $\sigma^{18}O$ decrease occurred in the middle of the Early Miocene suggest or may reflect glacioeustatic lowering of sea level and to the permanent ice sheet on Antarctica. Oslick *et al*, 1994 found that the increases in Sr isotopes are empirically linked to the oxygen isotope record. Oslick *et al* (1994) suggested that both mountain uplift and ice volume fluctuations contributed to the Neogene Sr isotopic signal. However, in the An Nagaza samples, the decrease of $\sigma^{18}O$ and increase of Sr isotopes could be attributed to the mountain uplift and glacioeustatic lowering of sea level.

Rises and falls of global sea-level, affecting the oxygen isotopic composition of sea-water. Thus, there should be a casual link between the record of $\sigma^{18}O$ in sea-water and the sedimentary record of sea-level fluctuations. Indeed, the composite isotope record of

the An Nagaza sequence does show several eustatic episodes at the time of deposition (Fig. 12) that are consistent with the geological record of ice-sheets evolution (Abreu and Anderson, 1998). In particular, negative excursions of the $\sigma^{18}O$ values should correspond to high sea-level stands and less negative or positive excursions to low sea-level stands. Furthermore, light $\sigma^{13}C$ observed in sediments deposited during low sea-level, while less negative or positive $\sigma^{13}C$ observed within sediments deposited during sea-level rise.

$\sigma^{18}O$ values record of the An Nagaza sequence are all negative indicating high sea-level stands during Early Miocene. At the beginning, sea transgressed over Cenomanian rocks, but its level was low as indicated by dominance of sandstone influx into the sequence, common shallow water fossils, depleted $\sigma^{13}C$ and less negative values of $\sigma^{18}O$, followed by relatively high stand for a short time (Fig. 12). This were succeeded by short lived regression of sea-water, followed again by sea-level rise for a considerable period of time as indicated by thick sequence of sediments rich in fossils of relatively deep marine (Fig. 12). At the end of the An Nagaza sequence, regression event took place followed by high sea-level stand.

In summary, the depletion of oxygen isotopes of the An Nagaza sediments were influenced by the following: 1- Temperature (Fig. 14), where less negative $\sigma^{18}O$ values consistent with decrease of temperature. 2- Diagenesis, including alteration of aragonite and high Mg-calcite to low Mg-calcite. 3- Lowering of sea-level during Miocene period. 4- Influx of meteoric water into the carbonate of the An Nagaza Member.

CONCLUSION

This study dealt with petrography and diagenesis of the An Nagaza Member of the Al Khums Formation in NW Libya. A total of 33 samples were collected for petrographic, stable isotopic and trace elements analysis. The samples of the An Nagaza were divided into five lithofacies; started with sediments resulted from transgression onto a Cretaceous surface of moderate relief. These sediments are of fossiliferous, reef-bearing with basal sand and limestone (Salem and Spreng, 1980). Lithofacies of the An Nagaza Member are mainly grain-supported and dominated by sandy packston to grainstone.

Various fossils present in the An Nagaza lithofacies are indicative of shallow, neritic environment. Furthermore, the abundance of silisiclastic material suggest the shallow marine environment and were supplied into an outer neritic setting during Early Miocene. The complete succession of the An Nagaza Member is interpreted as a transgressive sequence, passing from marginal marine to fully marine deposits.

The lithofacies of the An Nagaza sequence exposed to several different diagenetic events, which include both early and late stages. These lead to modification of their original textural and compositional characteristics. The diagenetic events occurred within this sequence including; micritization (formation of micrite envelopes and complete micritization), cementation (syntaxial overgrowth on echinoderms, isopachous, drusy mosaic and rarely meniscus), compaction and dissolution.

Micritization and formation of micrite envelopes are thought to be the first diagenetic event occurred within the An Nagaza sediments. They played an important role in preserving the fossil fragments during diagenesis. This process took place in the marine phreatic environment. The timing relationship of the syntaxial overgrowth cement phase relative to other diagenetic events suggests precipitation in a marine to meteoric or very shallow burial environment. Non-ferroan drusy calcite spar is the most common type of cement in the An Nagaza lithofacies. Drusy cements were precipitated after the formation of micrite envelopes and are often better developed where the aragonite has been dissolved. This suggests that dissolution coincide with the formation of drusy cements in the meteoric phreatic zone (Tucker & Wright, 1990).

The isotopes analysis of the An Nagaza samples shows that the oxygen isotope values range from -2.2‰ to -7.9‰ and carbon isotope values range from 0 to -8.2‰. Oxygen and carbon isotopes indicate that the sequence of the An Nagaza had exposed to sea-level fluctuation. Oxygen values are depleted; possibly because of exchange with isotopically lighter meteoric water at one or more times in the past. The smooth change from low $\sigma^{13}C$ values in the bottom of the sequence (SN1 and SN2) to higher values, more typical of open marine water, and a return to low $\sigma^{13}C$ value in the top (SN33) may be an indication that a primary signal is preserved. This may be caused by a move from a restricted basin with high productivity, to more marine conditions, and back again.

The Sr isotope composition of the An Nagaza samples of the Al Khums Formation corresponds to that of Early Miocene age. The calculated ages vary from 17 to 21 Ma. The changes of Sr isotopic in late Eocene to Miocene are related to glaciations and deglaciations of the Antarctica Craton (Miller *et al,* 1991a). Hodell *et al* (1991) and Raymo, 1991 attributed the bulk of the Late Neogene $^{87}Sr/^{86}Sr$ increase to mountain uplift. The Sr isotope increases of the An Nagaza samples may be related to both glaciations and deglaciations of the Antarctica Craton and to the mountain uplift.

Low Sr concentration in the An Nagaza sediments typically reflects formation from a diagenetic fluid whose composition has been modified by the aragonite to calcite transformation. This low concentration may be caused by extent of recrystallization and crystal growth. High Fe concentration of all samples indicates that they are not exclusively carbonate.

ACKNOWLEDGEMENTS

The authors would like to express their sincere thanks and appreciation to Dr Burima A. Belgasim, the former General Manager and all management of the Libyan Petroleum Institute (formerly, Petroleum Research Centre) for financing this work. Thanks go to the Dr. Mustafa J. Salem for guiding the field trips. We would also like to express our sincere thanks to Dr Mustafa Idris, the former General Manager of the Petroleum Research Centre for his help and cooperation during all stages of this work. We shall not forget to thank all our friends and colleges in the LPI, specially the Exploration and Exploitation Research Department staff for their help and support. Finally, we would like to thank the scientific committee members of the Exploration Researches, particularly its Chairman Prof. Ali Sbeta for his critical review and comments of the manuscript.

REFERENCES

Abreu, V. S. and Anderson, J. B., 1998. Glacial eustasy during the Cenozoic: sequence stratigraphic implications. *Bull. Am.Assoc.Petrol.Geol.,* ***82***, 1385-1400.

Adams, A. E., MacKenzie, W. S. and Guilford, C., 1984. *Atlas of Sedimentary Rocks Under the Microscope.* Halsted Press, John Wiley and Sons Inc, USA, 104p

Banner, J. L., 1995. Application of the trace element and isotope geochemistry of strontium to studies of carbonate diagenesis. *Sedimentology,* ***42***, 805-824.

Barr, F. T. and Weegar, A. A., 1972. *Stratigraphic Nomenclature of the Sirte Basin, Libya.* Publ. of the Petrol. Expl. Soc. of Libya, 179p.

Bathurst, R. G. C., 1966. Boring algae, micrite envelopes, and lithification of molluscan biosparites. *Geol. J.,* ***5***, 15-23.

Bathurst, R. G. C., 1975. Carbonate sediments and their diagenesis. *Development in Sedimentology,* ***12***, 658p.

Bathurst, R. G. C., 1983. Neomorphic spar versus cement in some Jurassic grainstones: significance for evaluation of porosity evolution and compaction. *J. Geol. Soc.,* ***14***, 229-237.

Bathurst, R. G. C., 1987. Diagenetically enhanced bedding in argillaceous platform limestones: stratified cementation and selective compaction. *Sedimentology,* ***34***, 749-778.

Berggren, W. A, Kent, D. V. and Flyn, J. J., 1985. Neogene geochronology and chronostratigraphy. *Mem. Geol. Soc. London,* ***10***, 211-259.

Brand, U. & Veizer, J., 1980. Chemical diagenesis of a multi-component carbonate system, 1. Trace elements. *J. Sediment. Petrol.,* ***50***, 1219-1236.

Cande, S. C. and Kent, D. V., 1992. A new geomagnetic polarity timescale for the Late Cretaceous and Cenozoic. *J. Geophysical Res.,* ***97***, 13917-13951.

Desio, A., 1971. Outlines and problems of the geomorphological evolution of Libya from the Tertiary to the present day. In: C. Gray, (ed.) *the Geology of Libya*, *First Symposium,* Faculty of Science, University of Libya, Tripoli, 11-36.

Dickson, J. A. D., 1965. A modified staining technique for carbonates in thin section. *Nature,* ***205***, p. 587

El-Waer, A. A., 1988. Miocene ostracoda from NW Libya. *J. Micropalaeontology,* ***7(1)***, 45-52.

El-Waer, A. A., 1991. Miocene ostracoda from the Al Khums Formation, NW Libya. In: M. J. Salem and M. N. Belaid (eds.), *The Geology of Libya,* ***V***., 1457-1482. Elsevier, Amsterdam.

Erez, J. and Luz, B., 1983. Experimental paleotemperature equation from planktonic foraminifera. *Geochim. Cosmochim. Acta,* ***47***, 1025-1031.

Evamy, B. D. and Shearman, D. J., 1965.The development of overgrowths from echinoderm fragments in limestones. *Sedimentology,* ***5***, 211-233.

Fatmi, A. N. and Sbeta, A. M., 1991. The significance of the occurrence of Abu Ghaylan and Kiklah formations east of Wadi Ghan, eastern Jabal Nafusah. In:. Salem, M. J., Sbeta, A. M. and Bakbak, M. R. (eds.) *The Geology of Libya*, ***VI***:,2227-2233.Elsevier,Amsterdam.

Floridia, G. B., 1939. Osservazioni sul Miocene del dintorni di Homs. *Boll. Soc. Geol. Ital.,* ***58***, 245-260.

Folk, R. L., 1965. Spectral subdivision of limestone types. In: W. E. Ham (ed.), Classification of Carbonate Rocks. *Mem. Am. Assoc. Petrol. Geol.,* ***1***, 62-84.

Hodell D. A., Mueller, P. A. and Garrido, J. R., 1991. Variations in the strontium isotope composition of seawater during the Neogene. *Geology,* ***19***, 24-27.

Hoefs, J., 1973. *Stable Isotope Geochemistry*. Springer-Verlag, New York: 208p.

Hook, J. E., Golubic, S. and Milliman, J. D., 1984. Micrite cement in microborings is not necessarily a shalow-water indicator. *J. Sed. Petrol.,* ***54***, 425-431.

Innocenti, F. and Pertusati, P., 1984. Sheet Al Aqaylah (NH 34-5), geological map of Libya, scale 1: 250,000, with explanatory booklet. *Industrial Research Centre*, Tripoli.

Jacobs, E., Weissert, H. and Shields, G., 1996. The monterey event in the Mediterranean: a record from the shelf sediments of Malta. *Palaeoceanography, **11***, 717-728.

Kimbell, T. N. and Humphrey, J. D., 1994. Geochemistry and crystal morphology of aragonite cements of mixing-zone origin, Barbadose, West Indies. *J. Sed. Res., **A64***, 604-614.

Land, L. S., 1973. Holocene meteoric dolomitization of Pleistocene limestones, north Jamaica. *Sedimentology, **20***, 411-424.

Land, L. S. and Goreau, U. F. (1970). Submarine lithification of Jamaican reefs. *J. Sed. Petrol., **40***, 457-462.

Mann, K., 1975. Sheet Al Khums (NI 33-14), geological map of Libya, scale 1: 250,000,with explanatory booklet. *Industrial Research Centre*, Tripol, Libya.

Marshal, F. F. and Davis, P. J., 1981. Submarine lithification on windward reef slopes: Capricom-Bunker group, southern great barrier reef. *J. Sed. Petrol., **51***, 953-960.

Mayayo, M. J., Bauluz, B, Lopez-Galindo, A.and Gonzalez-Lopez, J. M., 1996. Mineralogy and geochemistry of the carbonates in the Calatayud Basin (Zaragoza, Spain). *Chemical Geology, **130***, 123-136.

Milliman, J. D., 1974. *Marine Carbonates*. Springer-Verlag, Berlin: 375p.

Mijalkovic, N. (1977). Sheet Al Qaddahiyah (NH 33-3), Geological map of Libya, scale 1: 250,000,with explanatory booklet. *Industrial Research Centre*, Tripol, Libya.

Miller, K. G., Feigenson, M. D., Wright, J. D. and Clement, B. M., 1991a. Miocene isotope reference section, Deep Sea Drilling Project Site 608: An evaluation of isotope and biostratigraphic resolution. *Palaeoceanography, **6***, 33-52.

Miller, K. G., Wright, J. D. and Fairbanks, R. G., 1991b. Unlocking the ice-house. *J. Geophys. Res., **96***, 6829-6848.

Morad, S. De Ros, L. F. and Al-Aasm, I. S., 1996. Origin of low $\sigma^{18}O$, precompactional ferroan carbonates in the marine Sto Formation (Middle Jurassic), offshore NW Norway. *Mari. Petolr. Geolg., **13***, 263-276.

Morse, J. W. and MacKenzie, F. T., 1991. Influence of solution chemistry and reaction kinetics on $CaCO_3$ transport in subsurface environments. *Geol. Soc. Amer., Abstr. with program, **23***, A318.

Oslick, J. S., Miller, K. G., Feigenson, M. D. and Wright, J. D., 1994. Oligocene – Miocene strontium isotopes: stratigraphic revisions and correlations to an inferred glacioeustatic record. *Palaeoceanography, **9***, 427-443.

Pray, L. C., 1960. Compaction in calcilutites (abstract), *Bull. Geol. Soc. Am., **71***, p. 1946.

Raymo, M. E., 1991. Geochemical evidence supporting T. C. Chamberlin's theory of glaciation. *Geology, **19***, 344-347.

Ricken, W., 1993. *Sedimentation as a Three-component System.* Lecture Notes in Earth Science, **51**. Springer, Berlin: 211p.

Salem, M. J. and Spreng, A. C., 1980. Middle Miocene stratigraphy, Al Khums area, northwestern Libya. In: M. J. Salem, and M. T. Busrewil (edts.), *Second Symposium on the Geology of Libya. **I,*** 97-116, London Academic Press.

Shaaban, M. N., 2004. Diagenesis of the lower Eocene Thebes Formation, Gebel Rewagen area, eastern desert, Egypt. *Sedim. Geol., **165(1-2,*** 53-65.

Sherif, K., 1991. Biostratigraphy of the Miocene in Al Khums area, northwest Libya. In: M. J. Salem and M. N. Belaid (eds.), *The Geology of Libya, **V***., 1421-1456, Elsevier, Amsterdam.

Steinen, R. P., 1978. On the diagenesis of lime mud: scanning electron microscopic observations on sub-surface material from Barbados. *J. Sed. Petrol., **48***, 1139-1147.

Swart, P. K. (2000). The Oxygen Isotopic Composition of Interstitial Waters: Evidence for Fluid Flow and Recrystallization in the Margin of Great Bahama Bank. In: P. K. Swart, G. P. Eberli, M. J. Malone, J. F. Sarg (eds.), *Proc. ODP Sci., Results, **166***, 91-98.

Tucker, M. E. & Wright, V. P., 1990. *Carbonate Sedimentology*. Blackwell Scientific Publications, Oxford: 482p.

Woo, K. S. & Khim, B., 2006. Stable oxygen and carbon isotopes of carbonate concretions of the Miocene Yeonil Group in the Pohang Basin, Korea: types of concretions and formation condition. *Sediment. Geol., **183(1-2)***, 15-30.

Zivanovich, M., 1977. Sheet Bani Walid (NH 33-2), *Geological map of Libya, scale 1: 250,000, with explanatory booklet.* Industrial Research Centre, Tripoli, Libya.

Petroleum Res. J. Vol. 21 (2008/2009); P. 99–106, 19 Figs.

Basic Nitrogen Compounds Identification in Rasco Crude Oil Blend and in its Distillates and Residue

Youssef A. Al Mestiri* and Abeer A. Al Shiki

Abstract: The basic nitrogen content in Rasco crude oil and light gas oil (LGO), heavy gas oil (HGO) and in naphtha and kerosene produced from Rasco crude oil a 50% Sarir/50% Mesla crude blend; a feedstock for Ras Lanuf refinery was determined; Rasco crude oil, LGO and HGO contain 47, 13 and 88 ppm nitrogen respectively whilst naphtha and kerosene contain zero ppm basic nitrogen. Some of the physical and the chemical properties of Rasco crude oil and its LGO, HGO and residue were determined, followed by extraction of basic nitrogen compounds from Rasco crude oil and from its LGO, HGO and residue by hydrochloric acid extraction method. Separation and identification of these types of compounds was attained by a GC-MS technique and the identified basic nitrogen compounds are quinoline, isoquinoline and acridine derivatives and the identified non basic nitrogen compounds are the indole derivatives.

INTRODUCTION

Basic and non basic nitrogen compounds naturally occurring in petroleum and petroleum distillates influence different stages of petroleum refining[1, 2].

Nitrogen compounds reduce stability of petroleum distillates by colour, odour and sediment formation[2-4]. Similarly basic nitrogen compounds are strong inhibitors in cracking, hydrocraking reforming processes, hydrodenitrogenation and in hydrodesulfurization reactions by interacting with the acidic sites of the catalyst employed causing catalyst poisoning. In this reaction basic nitrogen compounds are electron pair donors (EPD) and the catalyst is electron pair acceptors (EPA)[2,4-7] Non basic nitrogen compounds inhibition in hydrodesulphurization reactions has been observed and described;hydrogenation reduction reaction of these compounds that take place in hydrodesulphurization reactions process leading to the formation of basic type[7-9], or by a strong adsorption of non basic nitrogen compounds over the support surface of the catalyst [7,10,11].

Methods of separation, identification and characterization as well as methods of quantitative determination of basic and non basic nitrogen compounds in petroleum distillates are available and can be found in references [1-8, 12-23].

Since no work is available related to basic nitrogen compounds in Rasco crude oil, the aim of this work is to determine quantitatively basic nitrogen content in Rasco crude oil and in its kerosene, naphtha, LGO and HGO as well as extraction, separation and identification of basic nitrogen compounds from this crude oil blend and from its LGO, HGO and residue; by following a slight modification of the Hartung and Jewel separation scheme[1] and subsequent separation and identification of basic nitrogen compounds by a GC-MS technique[2,7,20].

EXPERIMENTAL

The properties of Rasco crude oil blend and its LGO, HGO and residue were obtained following ASTM standard methods, whilst basic nitrogen content in Naphtha (IBP 40^0C), Kerosene (IBP 155^0C), LGO, HGO and Rasco crude oil blend was determined following, UOP-312, UOP-313 and UOP-269-70 standard methods[7,24-26]. All samples were taken from the Ras Lanuf refinery.

Before basic nitrogen compounds extraction the samples were diluted and dissolved in the proper solvent as follow, a raw Rasco crude oil blend sample was diluted with an n-heptane, HGO sample was dissolved and diluted with an n-heptane whilst residue sample was dissolved and diluted with a 1:1 toluene/

* Ras Lanuf Oil & Gas Processing Co,Technical Service Department, Laboratory Section. P.O.Box 1971,Benghazi – Libya, E-mail address: yelmisteri@yahoo.com

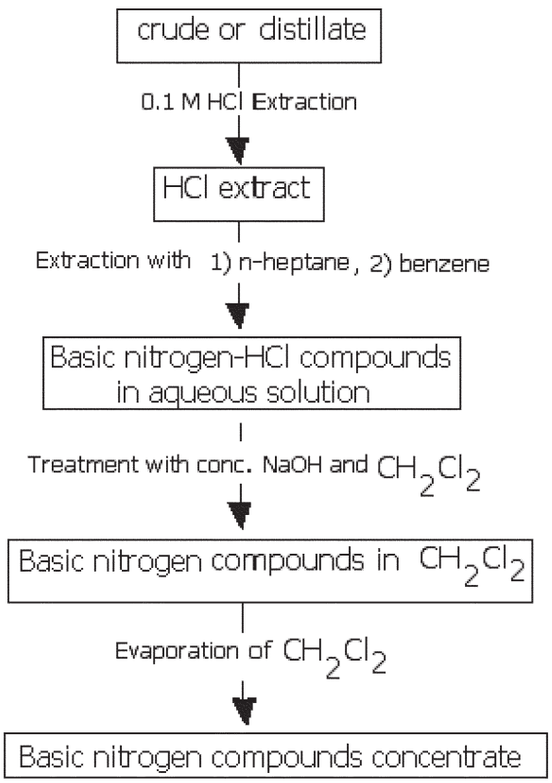


Fig. 1. Basic nitrogen compounds separation scheme.

xylene mixture. Figure 1 shows the separation scheme of basic nitrogen compounds from the samples; basic nitrogen compounds were extracted from each sample with 0.1M HCl acid solution; the acid extract of each sample was extracted with n-heptane followed by benzene and the resulting acidic aqueous solution was reacted with concentrated NaOH in the presence of dichloromethane to raise the pH to 12-13. The liberated basic nitrogen compounds were extracted from the NaOH solution with dichloromethane. The light-yellow dichloro-methane layer was evaporated to about 1-2 ml for GC-MS separation and identification of basic nitrogen compounds. Samples, solvents and reagent volume are tabulated in Table 1.

Basic nitrogen compounds were separated and identified by GC-MS (Thermo Finnigan Trace GC and Trace DSQ). 2-4 µl of each basic nitrogen compounds concentrate from each sample was injected into the GC fitted with a 30 m, 0.25 mm id, 0.25 ìm df capillary column (5% diphenyl-95% dimethyl polysiloxane), coupled directly to MS spectrometer detector; operating in the electron impact mode at 70 eV, mass detector gain 1.00 KV, ionization current 100 ìA, full scan 40-300 µ. GC operating temperature was as follows initial temperature was 85^0C for 1 min, 5^0C / min to 200^0C, for 20 min and 5^0C / min to 270^0C, for 5 min, injector temperature was 280^0C at constant temperature split mode, carrier gas was helium flow rate 1.0 ml/min; at constant flow, MS transfer line and the ion source temperature were 250^0C. The nitrogen compounds in each sample were identified by a computer matching method, comparing their spectra with those of the NIST Library of Mass Spectral Data.

Table 1. Volume of samples, HCL and solvents.

Sample	Volume litre	Solvents	0.1M HCl	CH_2Cl_2
Rasco crude blend	2.4	n-Heptane 600 ml	6 x 500 ml	700 ml
LGO	2.0	-	5 x 500 ml	700 ml
HGO	2.0	n-Heptane 500 ml	5 x 500 ml	700 ml
Residue	1.0	1:1 toluene/xylene 2 L	6 x 250 ml	700 ml

RESULTS AND DISCUSSION

Basic nitrogen compounds were extracted by HCl according to the following basis; basic nitrogen compounds are electrons pair donor (EPD) and acids are electrons pair acceptor (EPA)[2,4-7]; in basic nitrogen compounds, the nitrogen atom has a pair of electrons out of the ring that is available for sharing with an acid forming a water soluble salt, this can be simplified by writing the equation for the reaction between a basic nitrogen compound as dimethylquinoline in crude or distillates $(C_{11}H_{11}N{:})_{org}$ and aqueous hydrochloric acid solution $(HCl)_{aq}$ forming the water soluble dimethylquinoline hydrochloride salt[1,27-29].

$$(C_{11}H_{11}N{:})_{org} + HCl_{aq} \rightarrow \underset{\text{dimethylquinoline hydrochloride}}{(C_{11}H_{11}NH^{+}Cl)_{aq}}$$

Dimethylquinoline can be regenerated from its water soluble salt dimethylquinoline hydrochloride by adding up a concentrated aqueous NaOH solution in the presence of organic solvent as dichloromethane, the regenerated dimethylquinoline dissolve in the organic solvent and can be separated from the aqueous layer by extraction with the added organic solvent[1,15,28-29].

$$(C_{11}H_{11}NH^{+}Cl^{-})_{aq} + NaOH \rightarrow (C_{11}H_{11}N{:})_{org} + NaCl$$

In the other hand the extracted non basic nitrogen

compounds as trimethylindole ($C_{11}H_{12}NH$); in this type of nitrogen compounds, the nitrogen's extra out of the ring pair of electrons is not available to share with acids. By the same token these nitrogen compounds have a high electron density in the ring and can accept an acid only at the expense of the aromatic ring character that is by strong adsorption to an acid[7, 27, and 28].

Table 1 shows that a large volume of samples and reagent were used to perform the separation of basic nitrogen compounds from the samples in order to acquire a quite concentrated basic nitrogen compounds mixture suitable for a GC-MS analysis.

The physical and some of the chemical properties of Rasco crude oil blend, LGO, HGO and residue are tabulated in Table 2, from Table 2 it is clear that basic nitrogen content in LGO is very low whilst HGO contains the highest basic nitrogen content, the percentage of total basic nitrogen to the total nitrogen content is 23.5%. UOP-312 control plant test results gave that basic nitrogen content is zero in both Naphtha and Kerosene; it is clear that basic nitrogen content increases as the boiling point of the distillation cut increases.

GC-MS technique revealed that the extracted basic nitrogen compounds contain some non basic nitrogen compounds (the indole derivatives); GC-MS was able to separate and identify both basic nitrogen compounds and the accompanied non basic nitrogen compounds effectively, all the identified basic nitrogen and non basic nitrogen compounds are tabulated in Table 3.

All the identified basic nitrogen compounds in a raw Rasco crude oil blend sample and in LGO, HGO and residue produced from this crude oil blend did not show any structure alteration or rearrangement.

Total ion chromatograms of the separated basic nitrogen compounds from Rasco crude oil blend, LGO, HGO and residue are shown in Figures 2, 3, 4, and 5 the numbers associated with the peaks refer to the retention time of the compounds in the samples.

The mass spectra of the identified basic nitrogen compounds in the samples are shown in Figures 6-15 whilst mass spectra of non basic nitrogen compounds are shown in Figures 16-19.

Figures 6-9 are reproduced mass spectra of dimethyl, ethyl-methyl, trimethyl quinoline, and 1,2-dimethyl-5,6-dihydro-4H-pyrrolo[3,2,1-ij]quinoline; molecular ion peaks of these compounds appear at m/z 157, 171, 171 and 185 whilst the base peaks appear at m/z 157, 170, 171 and 185 respectively.

Figures 10 – 13 are reproduced mass spectra of substituted alkyl hydroacridine and acridine and these are 7-ethyl-1,2,3,4-tetrahydroacridine, ethylacridine, 1,2,3,4,7,8,9,10-Octahydro-12-methylbenzoacridine, and 1,2,3,4,8,9,10,11- Octahydro-7-methyl-benzoacridine; molecular ion peaks of these compounds appear at m/z 207, 211, 251 and 251 whilst the base peaks appear at m/z 196, 206, 251 and 251 respectively.

Figure 14 are reproduced the mass spectrum of 2,3,4-trimethylbenzoquinoline; the molecular ion peak of this compound appears at m/z 221 and the base peak appears at m/z 220, and the only identified alkyl substituted benzoisoquinoline compound is

Table 2. Properties of Rasco crude oil blend, LGO, HGO and residue.

Property	Method	RCOB	LGO	HGO	Residue
Specific gravity @15.6 °C	ASTM D-1298	0.8340	0.8192	0.8480	0.9104
Density @15.6 °C	ASTM D-1298	0.8336	0.8188	0.8476	0.9099
API° gravity	ASTM D-1298	38	41	35	24
Initial boiling point (IBP) °C	ASTM D-86	-	207	279	-
Final boiling point (°C)	ASTM D-86	-	338	-	-
Flash point (°C)	ASTM D-93	-	89	-	124
Pour point (°C)	ASTM D-97	18	-9	27	41
Cloud point (°C)	ASTM D-2500	-	-3	-	-
Aniline point (°C)	ASTM D-611	-	81	94	-
Total Aromatic (wt %)		-	9.27	9.30	-
Cetane index	ASTM D-976	-	59	-	-
Total sulfur (wt %)	ASTM D-4294	0.1393	0.0414	0.1372	0.2532
Total nitrogen (wppm)	ASTM D-3228	200	-	-	-
Basic nitrogen (wppm)	UOP-269 and 313	47	13	88	-

RCOB = Rasco crude oil blend

Table 3. Basic and non basic nitrogen compounds identified in Rasco crude oil blend, LGO, HGO and residue.

m/z	Identified compounds	RT. Min	Fraction
157	2,7-dimethylquinoline	12.09	RCOB, LGO
171	ethyl-methylquinoline	13.57	RCOB, LGO
171	Trimethylquinoline	14.61	RCOB, LGO, HGO
159	Trimethylindole	16.44	RCOB, HGO
173	Tetramethylindole	17.07	RCOB, HGO, R
185	1,2-Dimethyl-5,6-dihydro-4H-pyrrolo[3,2,1-ij]quinoline	17.56	RCOB, LGO, HGO
187	Pentamethyl indole	18.52	RCOB, LGO, HGO
211	7-ethyl-1,2,3,4-tetrahydroacridine	21.45	RCOB, LGO
213	6-methyl-2-(2-thienyl)-1H-indole	24.83	RCOB, LGO
207	Ethylacridine	26.35	all
221	Trimethylbenzoisoquinoline	30.01	all
251	1,2,3,4,7,8,9,10-octahydro-12-methylbenzoacridine	31.49	RCOB, HGO
251	1,2,3,4,8,9,10,11-octahydro-7-methylbenzoacridine	34.17	RCOB, HGO
221	2,3,4-trimethylbenzoquinoline	34.83	RCOB, HGO

R = Residue

trimethylbenzoisoquinoline the mass spectrum of this compound is shown in Figure 15 the molecular ion peak of this compound appears at m/z 221 and the base peak appears at m/z 220.

Non basic nitrogen compounds are shown in Figures 16-19; these are tri, tetra and penta methylindole and 6-methyl-2-(2-thienyl)-1H-indole (a non basic nitrogen compound containing sulfur), the molecular ion peaks of these compounds appear at m/z 159, 173, 187 and 213 and the base peaks appear at m/z 158, 173, 186 and 213 respectively. The mass spectrum of 6-methyl-2-(2-thienyl)-1H-indole shows an M + 2 ion peak of about 4% of the abundance of the main molecular ion peak that is a typical of ^{32}S containing compound.

The base peaks of all the identified basic and non basic nitrogen compounds show a 100% relative abundance this is due to the high stability of the cation radical through the aromatic ring of the nitrogen compounds as well mass spectra of these compounds show a loss of the stable HCN neutral molecule; a typical fragmentation pattern of nitrogen compounds.

The identified basic nitrogen compounds in Rasco crude oil blend and in its LGO, HGO and residue are quinoline, isoquinoline and acridine derivatives whilst the non-basic nitrogen compounds come with the separated basic nitrogen compounds are only the indole derivatives.

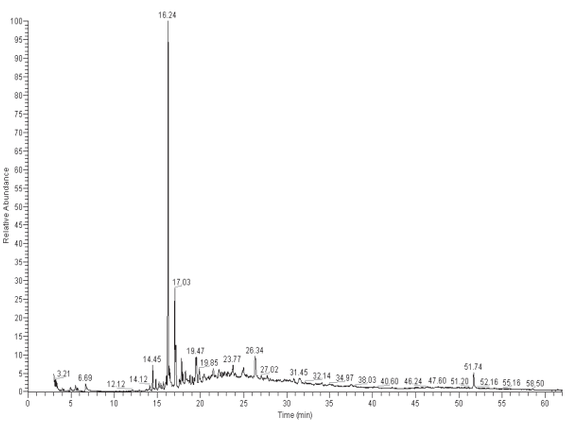


Fig. 2. Total ion chromatogram of nitrogen compounds in Rasco crude oil.

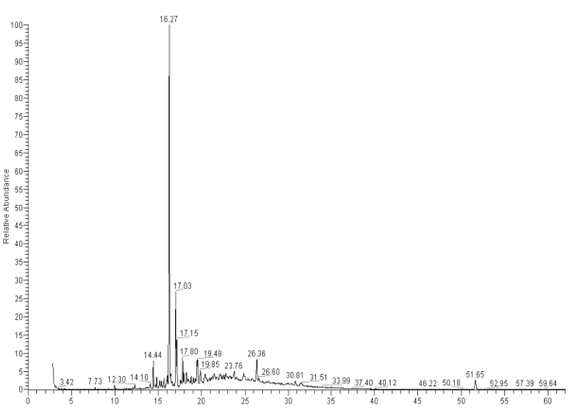


Fig. 3. Total ion chromatogram of nitrogen compounds in LGO.

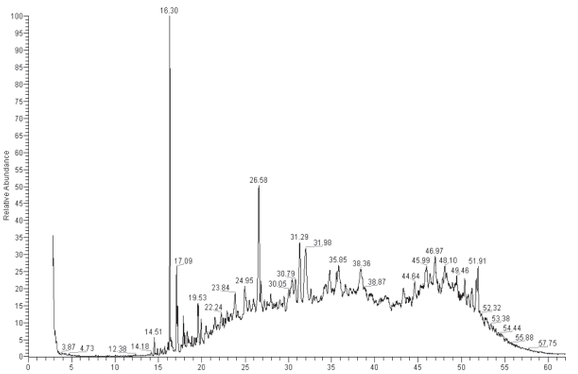


Fig. 4. Total ion chromatogram of nitrogen compounds in HGO.

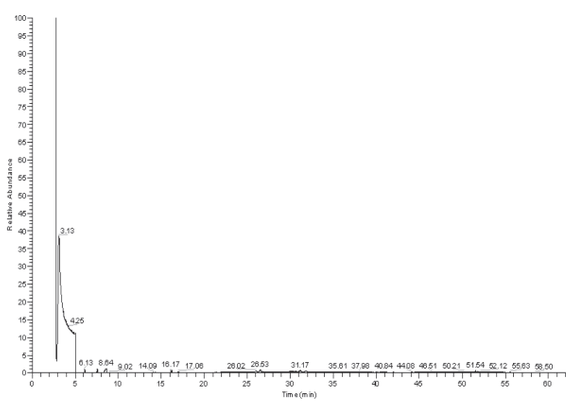


Fig. 5. Total ion chromatogram of nitrogen compounds in residue.

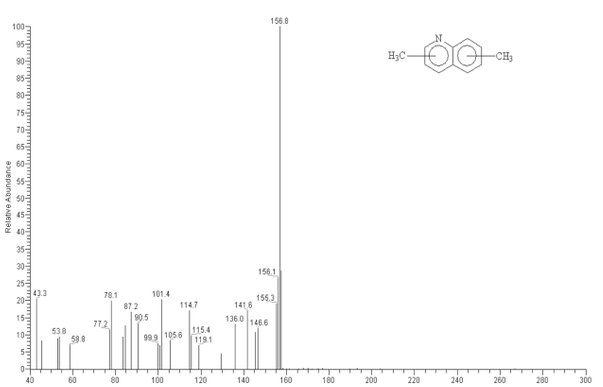


Fig. 6. Dimethylquinoline mass spectrum.

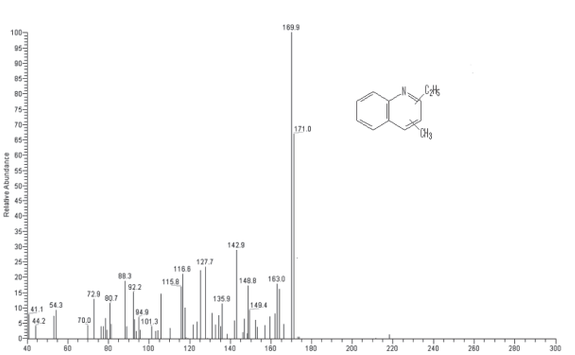


Fig. 7. Ethyl-methylquinoline mass spectrum.

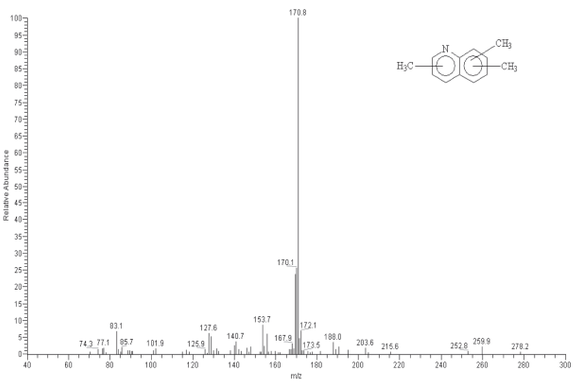


Fig. 8. Trimethylquinoline mass spectrum.

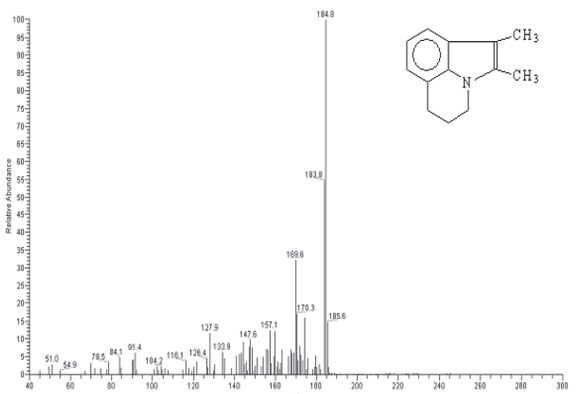


Fig. 9. 1,2-dimethyl-5,6-dihydro-4H-pyrrolo[3,2,1-ij]quinoline mass spectrum.

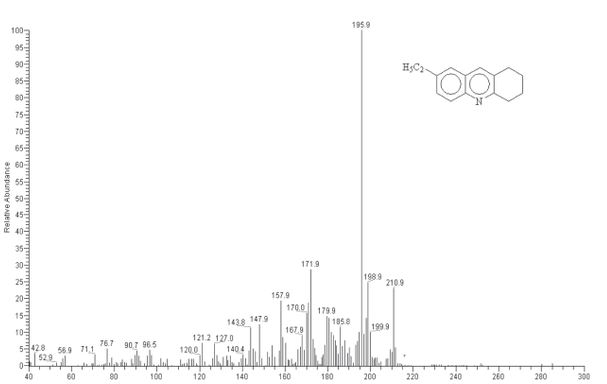


Fig. 10. 7- ethyl-1,2,3,4-tetrahydroacridine mass spectrum.

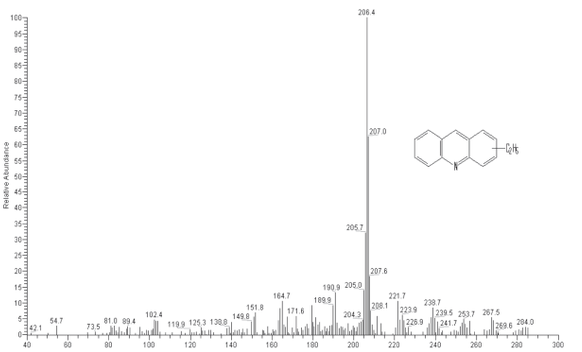


Fig. 11. Ethylacridine mass spectrum.

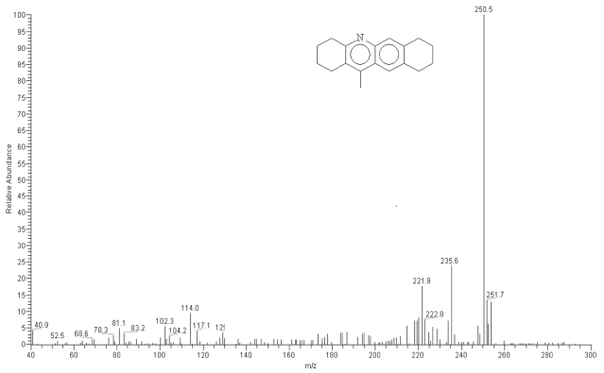


Fig. 12. 1,2,3,4,7,8,9,10-Octahydro-12-methylbenzoacridine mass spectrum.

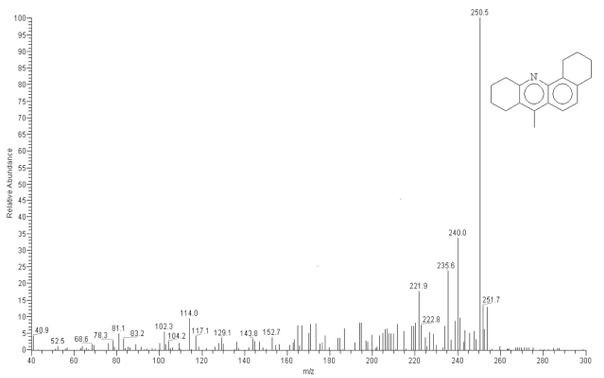


Fig. 13. 1,2,3,4,8,9,10,11-Octahydro-7-methylbenzoacridine mass spectrum.

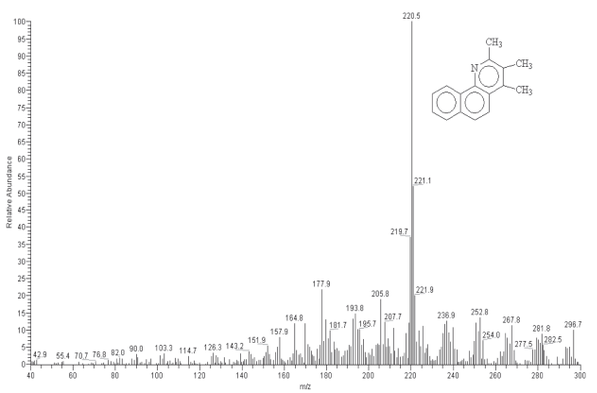


Fig. 14. 2,3,4-trimethylbenzoquinoline mass spectrum.

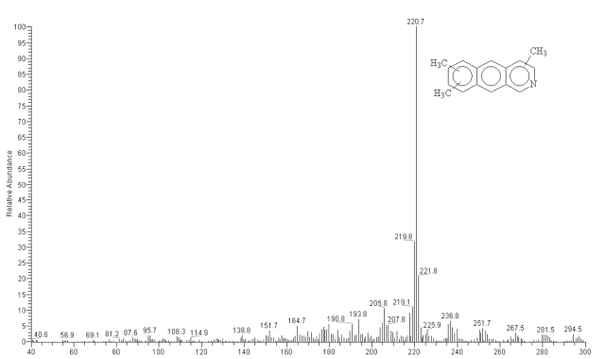


Fig. 15. Trimethylbenzoisoqionoline mass spectrum.

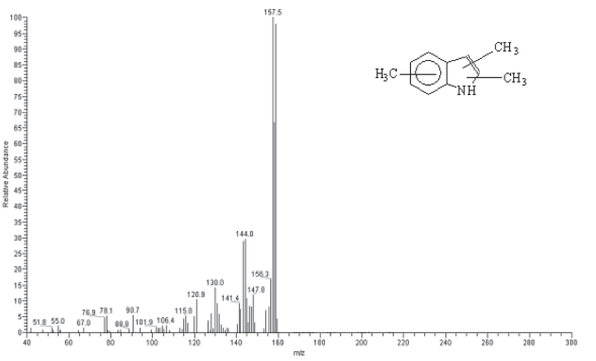


Fig. 16. Trimethylindole mass spectrum.

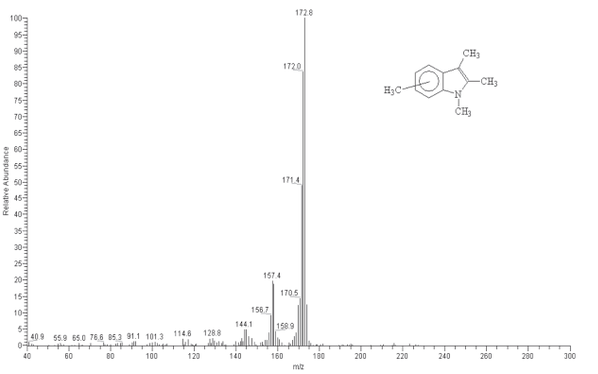


Fig. 17. Tetramethylindole mass spectrum.

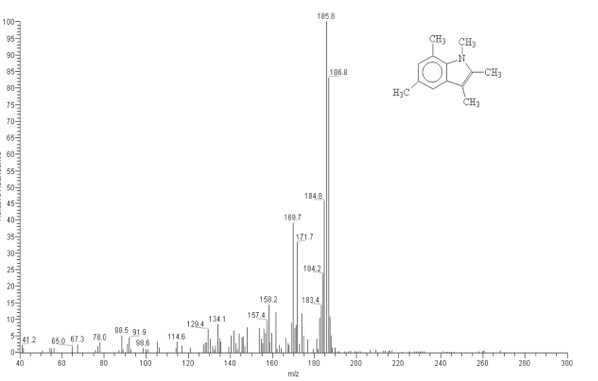


Fig. 18. Pentamethylindole mass spectrum.

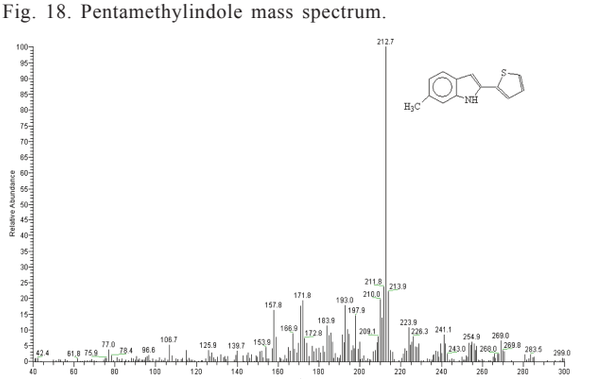


Fig. 19. 6-methyl-2-(2-thienyl)-1H-indole mass spectrum.

CONCLUSION

Basic nitrogen content was quantitatively determined in Rasco crude oil and in its naphtha, kerosene, LGO and HGO. Although the basic nitrogen compounds present in low concentration, these compounds were successfully extracted, concentrated, separated and identified in Rasco crudes oil in its LGO, HGO and residue accompanied with some basic nitrogen compounds.

The identified basic nitrogen compounds are quinoline, isoquinoline and acridine derivatives and the identified non basic nitrogen compounds are the indole derivatives.

The identified basic and non basic nitrogen compounds in Rasco crudes oil are thermally stable through the refining processes parameters of this crude oil.

The identified basic nitrogen compounds in residue are only trapped basic nitrogen compounds molecules.

ACKNOWLEDGEMENT

We are much grateful to Ras Lanuf refinery operation staff for collecting and providing the samples. The preparation of the reagent by the special analysis lab of Ras Lanuf is gratefully acknowledged.

REFERENCES

[1] Hartung, G. K. and Jewell, D. M., 1962. *Anal. Chim. Acta*, **26**, 514.
[2] Mao, J. Pacheco, R. C., Traficante D.D. and Rosen, W., 1962. *Fuel* , **74**, 880.
[3] Worstell, J. H. Daniel, S. R. and Fruenhoff, G., 1981. *Fuel*, **60**, 485.
[4] Qi, J. Yan, Y., Fei, W., Su, Y. and Dai, Y., 1998. *Fuel*, **77**, 255.
[5] Furimsky, E., Massoth, F. E., 1999. *Catal. Today*, **52**,381.
[6] Girgis, M. J. and Gates, B. C., 1991. *Ind. Engng. Chem. Res.*, **30**,2021.
[7] Laredo, C. G., Leyva, S., Ma, A.R., Mares, T. Castillo, J., and Luis, Cano, J., 2002, *Fuel,* **81**,134.
[8] Nagai, M. and Kabe, T., 1983. *J. Catal.,* **81**, 440.
[9] Odebunmi, E. O.and Ollis, D. F., 1983. *J. Catal.*, **80**,76.
[10] Yang, S.H.and Satterfield, C. N., 1984. *Ind. Engng. Chem. Process Des. Dev*.,**23**, 20.
[11] Dong, D., Jeong, S.and Massoth, F. E., 1997. *Catal. Today*, **37**, 267.
[12] Wiwel, P., Knudsen, K., Zeuthen, P., Whitehurst, D., 2002. *Industrial & Chemistry Research*, **39**, 533.
[13] Briker, Y., Ring, Z., Lacchelli, A. and McLean, N., 2003. *Fuel*, **82**,1621.
[14] Ellis, J. and Korth, J., 1994. *Fuel*, **73**, 1569.
[15] Nwadinigwe, C. A. and Maduka, C. M., 1993. *Fuel*, **72**, 1139.
[16] Jewell, D. M., Weber, J. H., Bunger, J. W., Plancher, H. and Latham, D. R., 1972. *Anal. Chem.,* **44**,1391.
[17] Severin, D., and David, T., 2001. *Pet. Sci. Technol.,* **19**(5/6),469.
[18] Okuno, I., Latham, D.R., Haines, W. E., 1965. *Anal. Chem*., **37**, 55.
[19] Li, M., Larter, S. R., Stodaart, D.,1992. *Anal. Chem*., **64**,1337.
[20] Drobon, M., Ignatiadis, I., Schmitter, J. M., Arpino, P. J., Guiochon, G., Toulhoat, H. and Huc, A.,1984. *Fuel* , **63**, 565.
[21] Helm, R. V., Latham, D.R., Ferrin, C. R., Ball, J. S., 1960. *Anal. Chem*., **32**, 1765.
[22] Drobon, M. and Bernasconi, C.,1989. *Fuel*, **68**,1067.
[23] Schmitter, J. M., Ignatiadis, I., Arpino, P. J., Guiochon, G., 1983. *Anal. Chem.,* **55**, 1685.
[24] UOP Laboratory Test Methods for petroleum and its products, vols. 1 and 2 1984 and references therein. methods@uop.com
[25] Wilson, H. N.,1948. *J. Soc. Chem. Ind*., **67**, 237.
[26] UOP Laboratory Test Methods for petroleum and its products on Disc, January 2006. UOP LLC. scott.gunderson@uop.com and references therein.
[27] Acheson, R. M., 1967. *An Introduction to the Chemistry of Heterocyclic Compounds*. 2nd edition. Wily International edition, New York, 151-164.
[28] Morison, R. T. and Boyd, R. N.,1971. *Organic Chemistry.,* 2nd edition. Allyn and Bacon, Inc, Boston, 740 and 1075-1084.
[29] Skoog, D. A. and West, D. M., 1971. *Fundamentals of Analytical Chemistry.* 2nd edition. Holt, Rinehart and Winston, Inc, London, 324.

Petroleum Res. J. Vol. 21 (2008/2009); P. 107–112, 3 Figs.

Distribution and Identification of Some Sulfur Compounds in Rasco Light Gas Oil (Diesel Oil)

Abeer A. AL Shiki*

Abstract: Sulfur compounds play an important factor in the specification of diesel oils. The identification of these compounds and their distribution in light gas oil (LGO) cut give useful information for refinery operation, production and instillation of hydrodesulphurization unit. In this study the isolation and characterization of sulfur compounds (0.043 wt %) in LGO produced by Ras Lanuf refinery (RASCO) were carried out. The LGO fraction was distilled from Messla + Sarir crude oil mixture at RASCO toping unit of temperature ranging from 200 to 340°C. LGO cut was separated into three fractions by atmospheric distillation (ASTM D86). The LGO fractions [F1 205-250 °C], [F2 250-290 °C], and [F3 290-336 °C] were fractionated by column chromatography in order to isolate the respective aromatic fraction and thiophenic compounds. Sulfur compounds in LGO fractions were characterized and identified by Gas chromatography mass spectrometry (GC-MS).

INTRODUCTION

Sulfur compounds play an important factor in the specification of diesel oils. A number of workers have successfully isolated sulfur compounds from petroleum by controlled oxidation of the sulfur compounds to sulfoxid with hydrogen peroxide[1]. The use of novel separation and analysis techniques (such as gas chromatography-mass spectrometry (GC-MS), high resolution gas chromatography, *etc*.) allowed recognition of several new classes of sulfur containing compounds [2-12].

The identification of these compounds and their distribution in light gas oil (LGO) cut give useful information for refinery operation, production and instillation of hydrodesulphurization unit. The organic sulfur exists either in aromatic rings or in aliphatic functional groups, usually categorized as mercaptans, aliphatic and aryl sulphides, disulfides and thiophenes[13]. Most thiol and disulfiedes decompose under 450 ^{0}C, alkyl-and aryl-sulfides lose H_2S between 440 and 630 ^{0}C and thiophenes lose H_2S above 600 ^{0}C[14, 15, 16].

Heteroatom organic compounds like sulfides, mercaptanes, thiophenes, pyrrols and indanes are known to be carcinogenic and mutagenic to animals and humans. Therefore, their presence in petroleum based products raises a health issue. In recent years, allowable sulfur levels in transportation fuels have been drastically lowered by many countries to combat air pollution. So the characterization of sulfur compounds in LGO has been and still is a major topic of interest, both from the point of view of environmental concerns with respect to the application of sulfur-rich petroleum fuels and their chemical significance. Different sulfur compounds have different structures and properties, which cause difficulties in the development of desulphurization technology. The knowledge of desulphurization reactants and products is useful for the optimization of sulfur removal processes. Therefore, analysis of sulfur compounds, especially the characterization of individual sulfur compounds in light gas oil, is fundamental for the production of ultra-low sulfur content diesel.

In this study the isolation and characterization of sulfur compounds (0.043 wt. %) in LGO produced by Ras Lanuf refinery (RASCO) were carried out. LGO cut was separated into three fractions by atmospheric distillation (ASTM D86). The LGO fractions [F1 205-250 ^{0}C], [F2 250-290 ^{0}C], and [F3 290-336 ^{0}C] were fractionated by column chromatography in order to isolate the respective aromatic fractions and thiophenic compounds. The sulfur compounds in LGO fractions were Characterized and identified by Gas Chromatography-Mass Spectrometry (GC-MS).

* Ras Lanuf Oil & Gas Processing Company Analysis and Quality Control Laboratory

EXPERIMENTAL AND RESULTS

The RASCO LGO cut was collected from refinery on 19-5-2006; Table (1) shows some physical properties of LGO. It was further separated by atmospheric distillation (ASTM D86) into three new fractions named LGOF1 (205-250^{0}C), LGOF2 (250-290^{0}C) and LGOF3 (290-336^{0}C). The four samples LGO, LGOF1, LGOF2 and LGOF3 were fractionated by column chromatography (CC), (Fig. 1), to isolate the respective aromatic fractions (LGOA, LGOF1A, LGOF2A and LGOF3A) and thiophenic compounds (LGOT, LGOF1T, LGOF2T and LGOF3T).

The chromatography was performed by diluting 5 g of LGO fraction in n-hexane and introducing the sample at the top of a 32 ×2.6 cm^2 (i.d) column packed with 100 g of silica gel (60-120 mesh, particle size 0.13-0.25 mm), which was previously activated for 12 h at 200 ^{0}C. Saturated compounds were eluted with 250 ml of n-hexane. The aromatic compounds were eluted with 250 ml of toluene. The UV- VIS spectrum (at 239 nm wavelength) of the hexane fraction confirmed that no aromatics were eluted with the saturated compounds. A second CC was carried out in a column packed with 110 g of SiO_2/Al_2O_3 (25/20, w/w) and performed for the previously concentrated aromatic fraction. The sample was eluted first with 250 ml of hexane to extract the possible remaining saturated compounds from the previous separation stage.

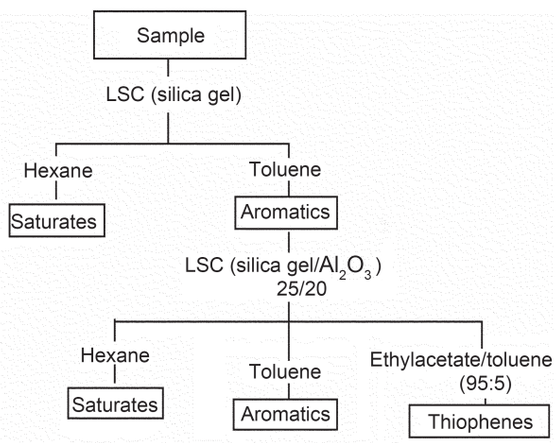


Fig. 1. Fractionating scheme for thiophenic compounds separation by CC.

The remaining aromatic compounds were eluted with 200 ml of toluene while the thiophenes were eluted with 250 ml of ethyl acetate/toluene (95:5) mixture[17] . All the fractions were evaporated to reduce the volume to about 1 ml.

Gas Chromatography-Mass Spectrometric (GC-MS) Analsis

The samples were injected into GC part (30 mm 0.25 mm id, 0.25 df, capillary column), held for 2 min at 80 ^{0}C, programmed at 2 ^{0}C / min to 160 ^{0}C, then programmed at 8 ^{0}C / min to 180 ^{0}C, where it is held for 20 min., the injector temperature was set at 100^{0}C, the split flow was at 100 ml/ min, mode CT splitless, the carrier gas was helium at constant flow rate of 1 ml/min, MS transfer line at 250 ^{0}C, ion source at 250 ^{0}C; 70 ev ionizing voltage, full scan (40-400) mass range.

The Distribution of the Sulfur Compounds in RASCO LGO

The distribution of the sulfur compounds in LGO were studied in the RASCO laboratory by distillation of LGO into three small fractions ranging between IBP 205 ^{0}C and FBP 336^{0}C of LGO (Fig. 2). The total sulfur content (weight %) of the fractions was obtained by an x-ray fluorescence method (ASTM-D2494).

Table 1. Physical properties of RASCO Light Gas Oil (LGO).

Method	Test	Unit	Result
ASTM D.1298	Specific gravity @15.6 ^{0}C	/	0.8185
ASTM D.1298	Density @15 ^{0}C	Kg/lit	0.8181
ASTM D.1298	API gravity	/	41.38
ASTM D.4294	Total sulfur	wt %	0.043
ASTM D.86	Distillation:- I.B.P F.B.P	^{0}C	 205 336
ASTM D.445	Viscosity at 37.8 ^{0}C	Cst	3.10
ASTM D.97	Pour point	^{0}C	-9
ASTM D.93	Flash point	^{0}C	86

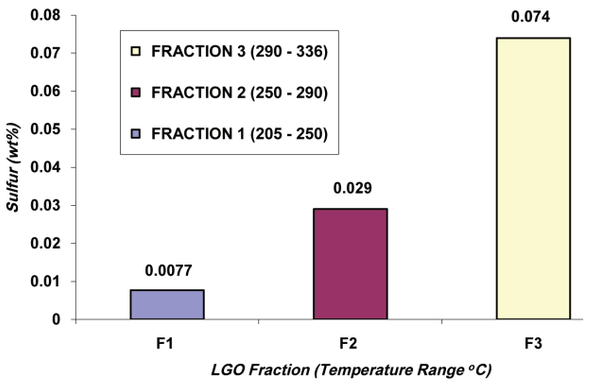


Fig. 2. The total weight % of sulfur compounds in LGO fractions.

DISCUSSION

Distribution of Sulfur in RASCO LGO

The high content of sulfur in the fuels is the main source for the air pollution. This forces the countries to set limitations for the total sulfur in the oil fractions specially diesel fuel. The recommended total sulfur in the diesel fuel for the European Countries in year 2009 is 10 ppm[18]. Figure 2 shows that the distribution of sulfur content is not linear, that means the amount of sulfur does not decrease gradually by decreasing the final boiling point of the fraction. Sulfur compounds may condense more in a specific boiling range of the fraction compared to other fraction of the same LGO cut, depending on the chemical composition of sulfur compounds and its boiling point temperature. Furthermore the percentage of some sulfur compounds increase with increasing the boiling point of the fraction which is depends on the type of crude oil. For example in sulphide and thiophene oils, the sulfur content increases with increasing boiling point of the fraction. In mercaptan oils the total sulfur content decreases with increasing boiling point of the fractions and dependent mainly on the thermal stability of the mercaptan compounds.

Identification of Sulfur Compounds in RASCO LGO

The GC-MS technique was used to identify all the sulfur compounds in LGO fractions Table 2. The sulfur compounds obtained was corresponding to Benzothiophene, alkyl Benzothiophene, dibenzothiophene, alkyl dibenzothiophene, thioxanthene and dimethylnaphtho [2,3-b]thiophene (Fig. 3). Because there were no available sulfur standards, we identified these compounds by two ways:

a) By comparing the mass spectra of the peaks

Table 2. Sulfur compounds identified in LGO cut.

Peak no.[a]	Molecular mass and major fragments[b]	Possible identity
A	176(70),161(100),159(35),128(15),115(15)	2,5,7-tri-methyl-benzo[b]thiophene
B	184(100), 152(15),139(20)	Dibenzothiophene
C,D	198 (100),197(50), 165(5),152(5),99(10)	Methyldibenzothiophene (2isomers)
E	198 (60),197(100), 165(15),152(10),99(5)	Thioxanthene
F,G,K	212(100), 211(50),197(15),105(35)	dimethyldibenzothiophene(3isomers)
H,L	212(100), 211(35),197(30),106(10)	dimethylnaphtho[2,3-b]thiophene(2isomers)
I	149(100),148(61),122(19), 104(18),77(15)	4-methylthieno[2,3-b] pyridine
J	149(100),148(25), 122 (10), 96(10), 77(5)	5-methylthieno[3,2-b] pyridine

[a] In Figure 3, [b] Figures in parentheses denote relative abundances in mass spectrum.

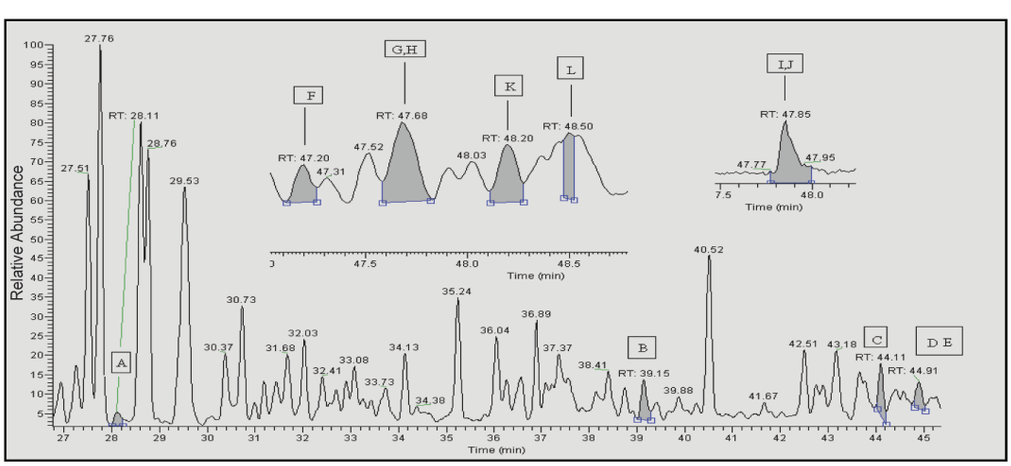


Fig. 3. Gas chromatographic and mass spectrometric data of LGO cut.

present in molecular ion mass fragmentograms with those of reference data (computerized library search) and characteristic fragmentation rules of thiophenic compounds [19,20,21,22] .

b) By using the chromatographically relationships between the retention time and the molecule weight for these compounds and their boiling points.

Fraction 1 (205-250 ^{0}C), contained 0.0077 wt% sulfur, which by GC-MS appears as 4-methylthino [2, 3-b] pyridine and 5- methylthino [3, 2-b] pyridine, while in fraction 2 (250-290 ^{0}C), 0.029 wt% sulfur, the major sulfur compound identified ,was dibenzothiophene and in addition to traces of methyl dibenzothiophene, di-methyldibenzothiophene.

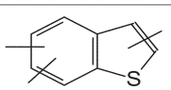
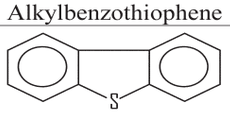
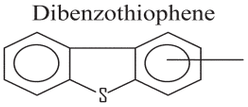
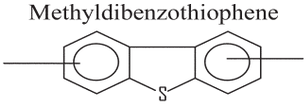
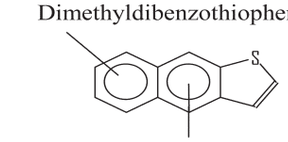
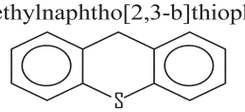
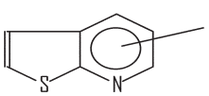
The sulfur content (0.074 wt.%) in fraction 3 (290-336^{0}C), appears as methyldibenzothiophene, dimethylbenzothiophene, thioxanthene, naphtho[2,3,b] thiophe-ne-dimethyl.

Benzo and dibenzothiophenes is the major compound present in the LGO, Table 3. Benzothiophenes and thiophenonaphthalenes would be easier to hydrodesulfurize than dibenzothiophenes. The large increase in alkylbenzenes in the product probably results from the hydrodesulfrurization of benzothiophenes. Similarly, the increase in the Tetralin and indane category may be a reflection of the hydrodesulfurization of dibenzothiophenes to yield a series of cyclohexylbenzenes which would contribute to this category. A dibenzothiophene desulfurization mechanisum to yield biphenyl, as some Russian works have claimed, would cause an increase in the acenaphthenes category[1].

CONCLUSIONS

The distribution of sulfur in distillates fractions of crude oil increases or decrease depending on the boiling point and the type of sulfur compound found in the crude oil. Benthothiophenes, dibenzothiophene, naphthanothiophenes and their alkyl analogous are major sulfur compound present in RASCO LGO.

Table 3. Probable Structures of Major and Minor Sulfur Compounds Represented by Significant Mass Series for LGO.

Empirical formula	Estimated percentage	Probable structures
$C_nH_{2n-10}S$	Minor	 Alkylbenzothiophene
	Minor	 Dibenzothiophene
	Minor	 Methyldibenzothiophene
	Major	 Dimethyldibenzothiophene
	Major	 Dimethylnaphtho[2,3-b]thiophene
	Minor	 Thioxanthene
$C_nH_{2n-9}SN$	Minor	 Methylthieno[2,3-b]pyridine

REFERENCES

[1] Drushel Harry, V. and Sommers, A. L., 1967. *Anal.Chem*., **39**,14

[2] Damste, J.S.S., Elington, T. I., de Leeuw, J.W. *et al*.,1989. *Geochem. Cosmochim. Acta*, **53**, 873.

[3] Anderson, J.T., 198. *Anal. Chem*., **59**, 2007.

[4] Nishioka, M., Bradshaw, J.S., Lee, M.L., *et al,* 1985. *Anal. Chem*., **57**,309.

[5] Kong, R. C., Lee, M.L., Iwao, M.*et al*., 1984. *Fuel*, **63**,702.

[6] Damste, J.S.S., Haven, H.L.T., de Leeuw, J.W.*et al*., 1986. *Org. Geochem*., **10**, 691.

[7] Brassel, S. C., Lewis, C.A., de Leeuw, J.W. *et al*. 1986. *Nature*, **320**, 160.

[8] Valisolalao, J., Perakis, N., Chappe, B. *et al*. 1984. *Tetrahedron Lett*., **25**, 1183.

[9] Demste,J.S.S., Kock-van Dalen, A.C., de Leeuw, J.W. *et al.* 1987. *Tetrahedron Lett*., **28** 957.

[10] Demste,J.S.S., van Koert, E.R., Kock-van Dalen, A.C. *et al.,*1989. *Org. Geochem*., **14**, 555.

[11] Demste, J.S.S., Rijpstra, W.I. C., Kock-van Dalen, A.C. *eal*.,1989.*Geochem.Cosmochim*. *Acta,* **53**, 1343.

[12] Payzant, J.D., McIntyre, D.D., Mojelsky, T.W. *et al*., 1989. *Org. Geochem*, **14**, 461.

[13] Garcia-Labiano F., Hampartsoumian, E. Williams, A., 1995. *Fuel*, **74 (7)**,1072.

[14] Van Aelst J., Alvarez Rodriguez ,R., Yperman ,J., Clemente Jue C., Franco DV, Mullens, J. *et al*., 2000. *Fuel,* **69**, 537.

[15] Rutkowski, P., Mullens, S., Yperman ,J., Gryglewicz, G. ,2002 . *Fuel Process Technol.*, **76,** 121.

[16] Yperman, J., Maes II, van den Rul, H. Mullenens, S. van Aelst, J., Franko, D.V., *et al.* 1999. *Anal Chem Acta*, **395**, 143.

[17] Trends of Automative Fuels standards in European Union, source: Directives 98/70 CE e 2003/17/CE.

[18] Damste, J.S.S., Kock van-dalen, A.C., de Leeuw, J.W.*et al*., 1988. J. *Chromatogr*., **435**,435.

[19] Beynon, J.H., Saunders, R.A Williams, A.E., 1968. *The Mass Spectra of Organic Molecules*. Elsevier, Amsterdam, 354-358.

[20] Budzikiewcz, H., Djerassi, C. and Williams, D.H., 1964. *Interpretation of Mass Spectra of Organic Compounds*. Holden-Day Inc., San Francisco, 231-237.

[21] Afonso,Julio,C. Cardoso, Jari, N. and Schmal Martin,1992. *Fuel,* **71**, 409.

Petroleum Res. J. Vol. 21 (2008/2009); P. 67–80, 13 Figs.

Analysis of Fault Zone Characteristics Using Potential Field and Seismic Data, Al Hagfa Trough, Sirt Basin - Libya

Hussein Ghanoush* and Milad Elmaradi*

Abstract: In this study, gravity data has been used in conjunction with seismic data to map and model the structural and stratigraphic elements in and around Al Hagfa Trough of central Sirt Basin. 2D seismic data show that the erosion and truncation of pre-rift strata and the thinning and onlapping of syn-depositional sequences onto fault scarp suggest that the area has experienced rifting activities and erosion during basin evolution. The mapped fault zone attached to rifting is about 150 km long and is composed of three 45 – 50 km long normal planar segments. These segments are bounded on the east by an area of local gravity high (NW-SE orientation) which results from low contrast between the Palaeozoic basement and Mesozoic - Cenozoic rocks and defines the Zaltan Platform structural trend. The western boundaries are marked by both gravity highs and lows which includes Al Bayda Platform and Al Hagfa Trough. The gravity minima are associated to longitudinal synclines or growth nuclei best explained by recognizing that it is a thick sequence of predominantly sedimentary wedges, including syn and post-sediments. Gravity modeling demonstrates the nature and structure of the mapped troughs and platforms, for a particular fault segments. Tilted segments can be observed also on the Bouguer and horizontal gradient maps. The southern portion of the fault block has a nearly N-S trend due to tilting. The mode of extension has important consequences for the Cretaceous hydrocarbon plays associated with the rifted province of Al Hagfa Trough. A breached relay ramp as evidenced from seismic and gravity data probably has a great influence on the hydrocarbon migration and entrapment in the study area.

INTRODUCTION

Geophysical methods (gravity and seismic) are used to provide control on the structure and stratigraphy of the subsurface related to faulting along a major fault zone separating the Zaltan Platform and Al Hagfa Trough in the central Sirt Basin (Fig 1). The area under study comprises large scale fault systems combined with broad syn-rift sequences evolved during time of basin evolution. Several significant features that reflects the nature of the subsurface are: (1) the anomalous low and high gradient in the area between the Zaltan Platform and Al Hagfa Trough, (2) the anomalous orientation of the anticlines and synclines like structures with respect to fault system evolution. The timing of rifting episodes in the Sirt Basin is thought to have commenced in Triassic, intensified in the Jurassic - Lower Cretaceous and terminated in Upper Cretaceous, (Busrewil et al., 2008). Overburden was largely deposited during the post-rift sedimentation stage (Oligocene and younger). Pre-rift and early syn-rift deposition (Fig. 2) was largely clastic whereas later syn-rift deposition was dominated by carbonate deposition. The deepest troughs in the basin, such as Ajdabiya Trough, (Fig. 1), have more than 7,000m of sediments, of which 5,500m are of Tertiary age (Hallett and El Ghoul 1996). Eighty percent of the drilling programmed in the province have been on platform horst areas at depths less than 3,000m. The Precambrian basement depth within the Sirt Basin approaches 5,000m within the southern part of the Ajdabiya Trough and is generally around 2,000m in the platform areas. The basement is generally deeper in the southern part of the Sirt Basin than in the northern part, and it is deeper in the eastern part than in the western part.

Al Hagfa Trough (Fig. 1) is characterized by high subsidence rates during the Late-Maastrichian and a slow subsidence rate during the Palaeocene (Ahlbrandt, 2001). The Zaltan Platform with the same time is characterized by continuous subsidence during the Late-Maastrichtian and Palaeocene (Meer and Cloetingh, 1993).

* Libyan Petroleum Institute.

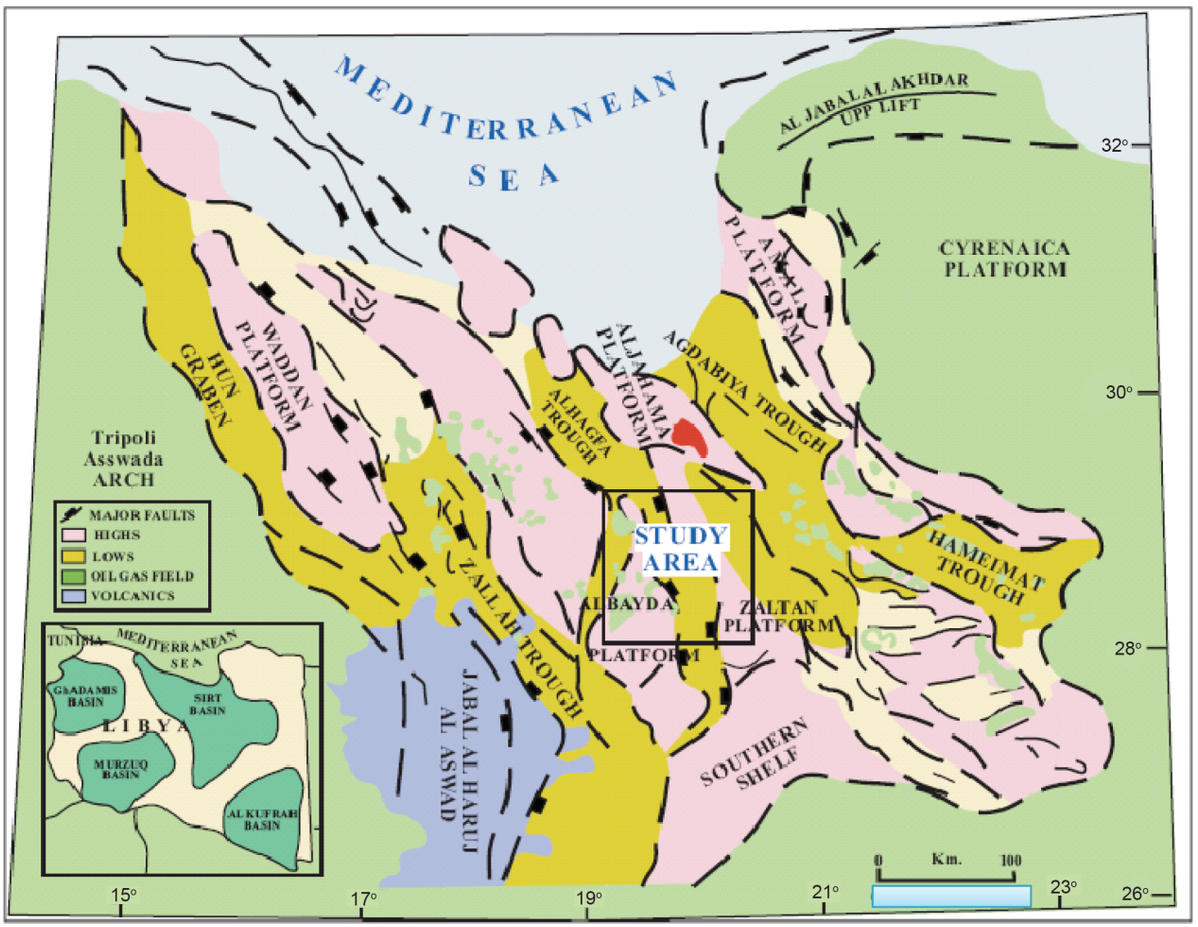


Fig. 1. Sirt Basin tectonic elements and location of the study area, modified form Lasmo Grand - Magreb map (1998).

The differences in both magnitude and direction (uplift or subsidence) of movement of all the basement blocks, with respect to each other, indicate syn-sedimentary normal faulting typical during rifting events. These rifting phases are followed by a period characterized by decelerating subsidence rates during the Eocene to Early Miocene. During the Eocene, deviations from this subsidence pattern can be observed, and affect the analyzed basement blocks in the Sirt Basin. The subsidence rates decelerate to very low levels during the Oligocene – Early Miocene (Meer, and Cloetingh, 1993). Previous geophysical publications focusing on fault zone evolution in the study area are very limited, although several regional studies are available (Andrew, 1994). Gravity and magnetic maps of the Sirt Basin region have demonstrated the value of these data for mapping general basin structures, basement morphology (Libyan Gravity Compilation Project LPI 2002).

Previous seismic studies have focused on the local near-surface features such as thickness of surficial sediments and basin structures required for hydrocarbon exploration. It is aimed through this study to outline the general context of the study area by using integrated geophysical data.

GEOPHYSICAL DATA AND METHODOLOGY

Complete Bouguer Gravity Map

The gravity data used in this investigation (Fig. 3) was taken from the Libyan Petroleum Institute (LPI) data base. The LPI staff compiled and processed data from a number of local surveys. The processing included projecting the data onto a 2 km regular grid using a minimum curvature interpolation technique, and a Bouguer correction using a density of 2.67 g/cm3. The residual Bouguer gravity map of the study area (Fig. 4) is produced and mapped according to a standard colour code, representing the Bouguer gravity values). Red colours represent regions of high

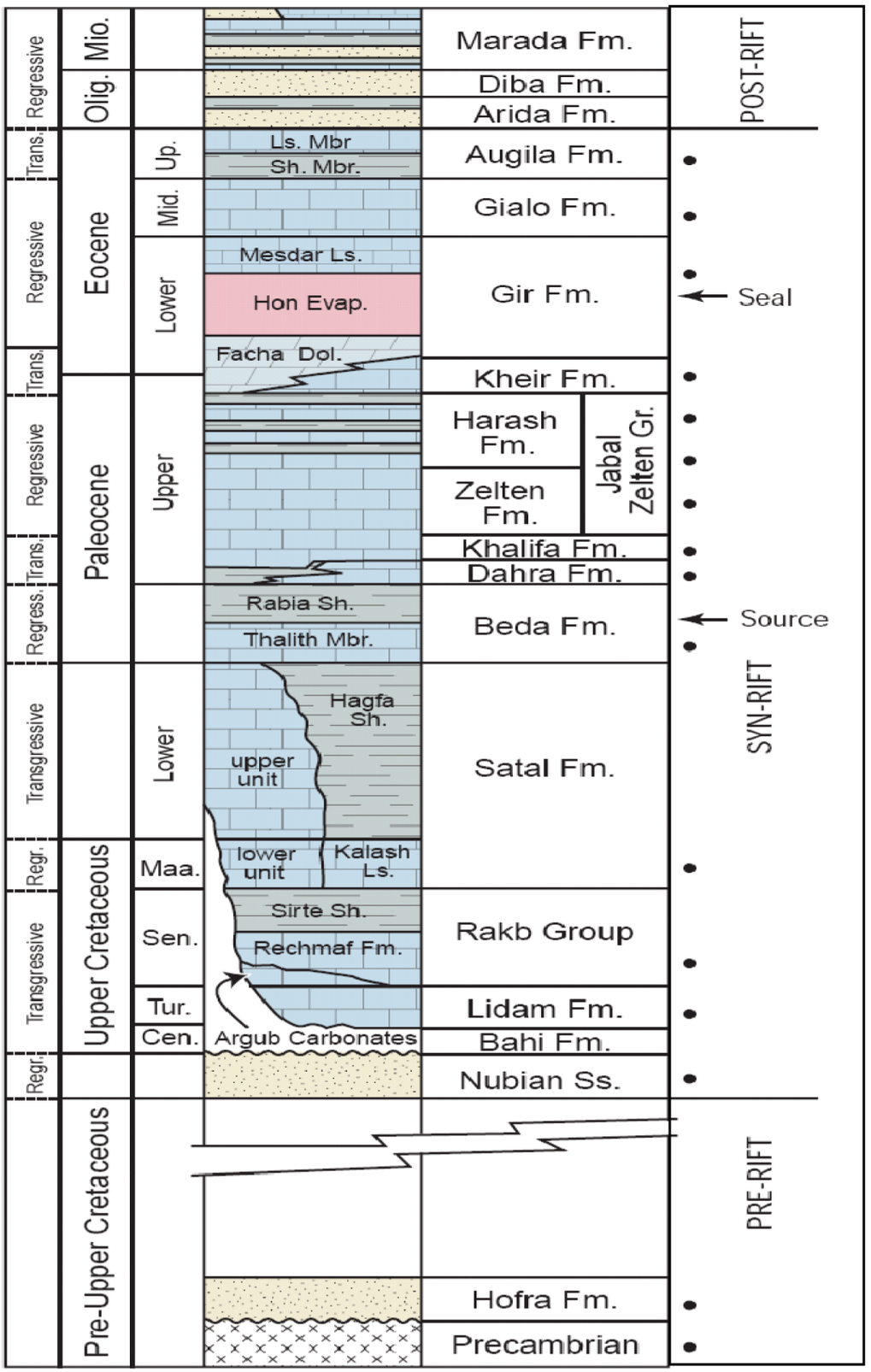


Fig. 2. Stratigraphic section in central Sirt Basin (after Ahlbrandt, 2001).

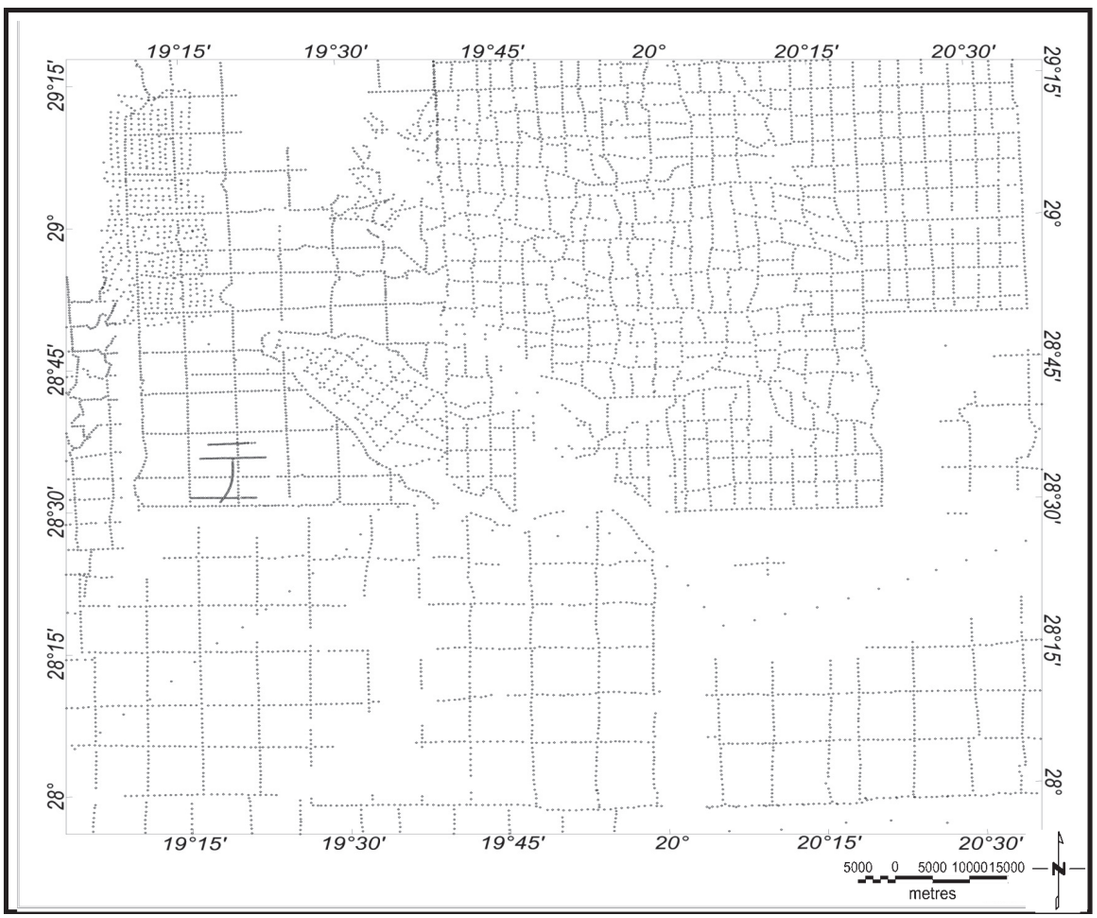


Fig. 3. Gravity station coverage over the study area.

relative density and blue colours represent regions of low relative density.

To remove the regional trend caused by the mantle- crust interference and to bring out local details in the gravity field as displayed in Figure 4, the original Bouguer gravity data (not displayed) were input to a spatial filter (the two-order polynomial filter), designed to attenuate the component of the gravity field. The resulting data are shown in (Fig. 4) with geologic contacts superimposed.

The filtered data (Fig. 4) show the characteristic Bouguer gravity high (red) associated with the Zaltan and Al Bayda platforms, the (blue) associated with sedimentary sub-basin structures representing Al Hagfa and Al Wadayat Troughs, and the intermediate values (yellow) probably associated with signatures of remnant Palaeozoic and Mesozoic rocks. The gravity signature varies considerably along the axial trend of the mapped sub-basins. In the western portion of the study area (Al Hagfa Trough) a large gravity low is observed. This implies a large density contrast between the basin fill and the basement. A filtered total horizontal gradient of the residual Bouguer gravity (Fig. 5) shows clearly the structures and the contacts superimposed.

Al Hagfa Trough is bounded by the major fault as shown in the Bouguer and gradient maps (Red colours). This fault is segmented along the strike and comprised of three fault segments. This suggests that Al Hagfa Trough may contains variable basin fill sequences, but a portion of this low gravity response may be attributable to the regional effect of the denser crust in the region.

In addition to the gravity imaging, 2D forward models demonstrating the identified features were constructed from the residual gravity data. Time unit densities were assumed for these models based on previous studies.

Seismic Data

Three migrated seismic lines from block NC 144 and concession 71 were used. The lines extended

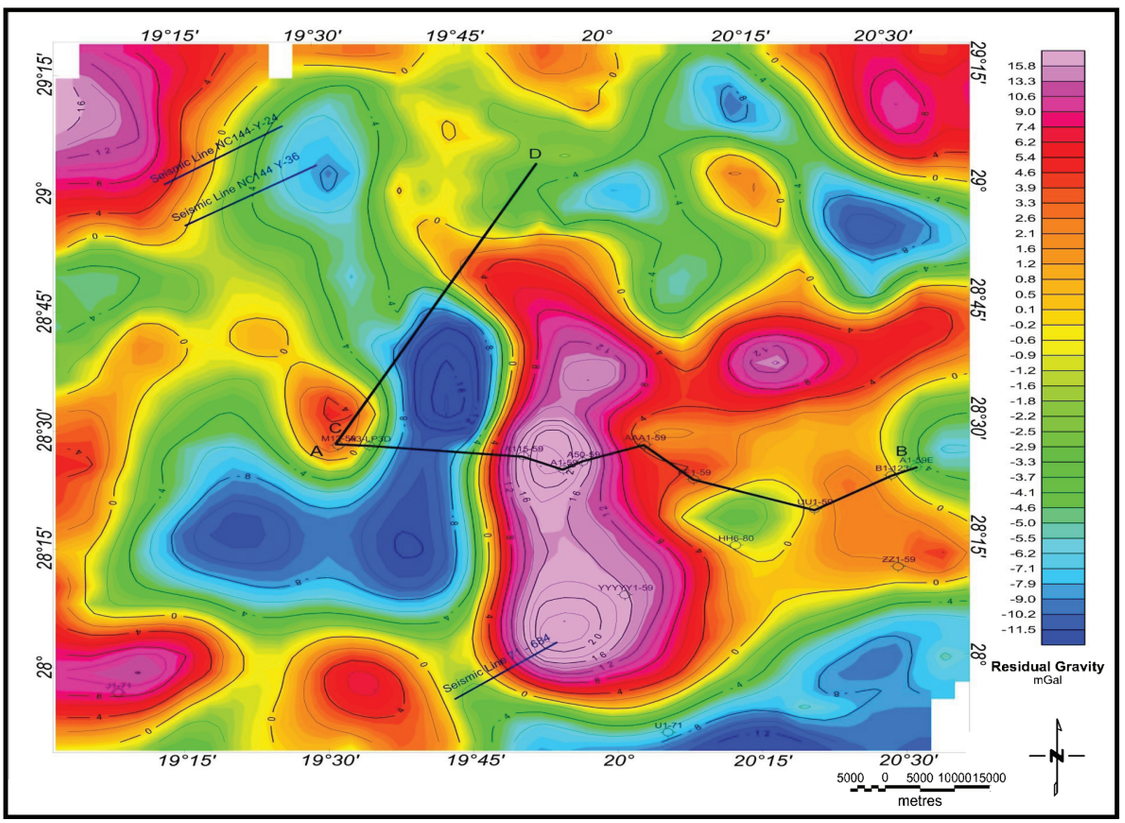


Fig. 4. Bouguer gravity map of the study area with locations of gravity profiles and seismic sections.

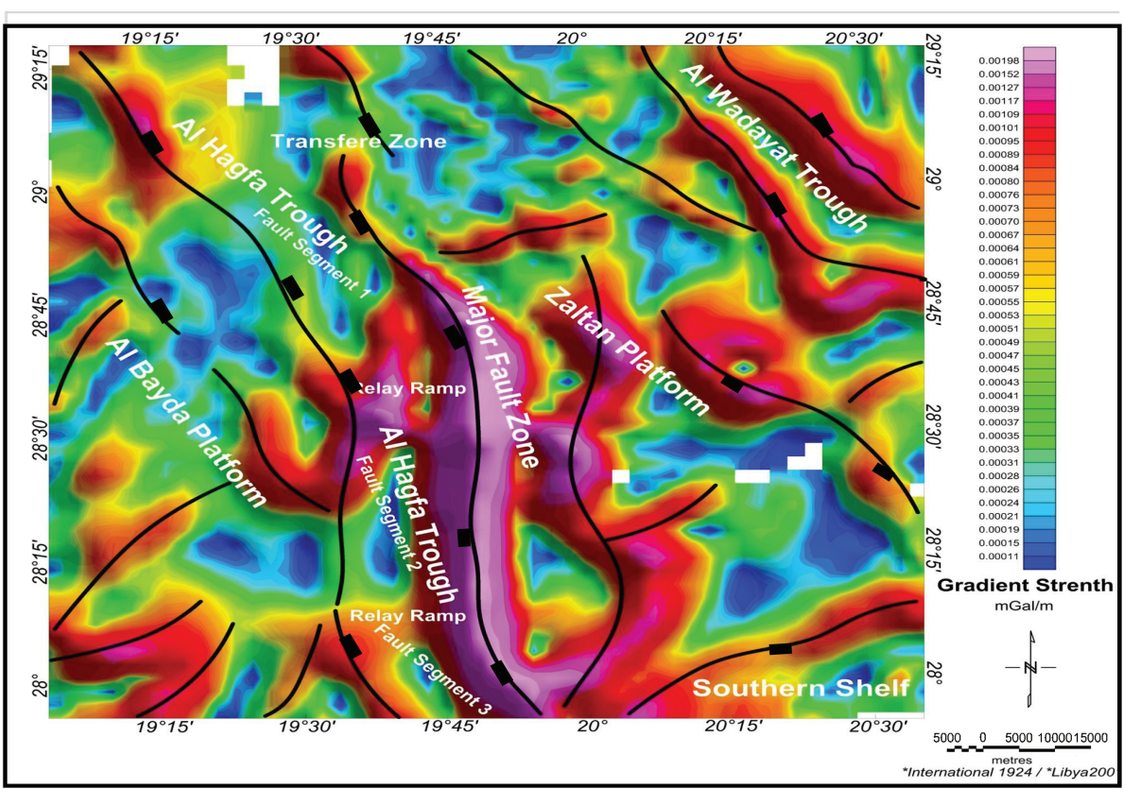


Fig. 5. Total horizontal gradient map of the Bouguer anomaly showing location of fault zones and boundaries of troughs and platforms.

NE – SW and some of them crosses the mapped fault zone.

INTERPRETATION CONFIDENCE

The residual Bouguer gravity anomaly map of the study area (Fig. 4) shows various trends and structures. Negative anomalies are found to be consistent with sub-basins whereas positive anomalies reflect structural highs. The complex pattern of the gravity anomalies can be used to define three main structural domains, comprising from east to west: (1) Zaltan Platform domain, with a NW–SE positive anomaly (2) Al Hagfa Trough domain, characterized by a gravity low and bounded from the east by a major fault zone trending NW – SE direction, and (3) Al Bayda Platform domain, marked by a broad NW–SE trending positive anomaly (Fig. 5). The three domains coincide with high and low structures characterized by a gradual displacement variations along-strike. Approximate limits are proposed to better define the boundaries of the three zones or domains.

The Al Hagfa Trough domain is better defined from the east with the major fault zone of about 150 km long, and combined of three fault segments (normal and planar). Each fault segment has a length of about 45-50km. The segments are bounded from the east by an area of regional gravity high (NW-SE orientation) which results from low contrast between Palaeozoic basement and Mesozoic - Cenozoic sedimentary sequences and defines the Zaltan Platform structural trend. The western boundaries are marked by both gravity highs and lows, and comprise the Al Bayda Platform structural domain. Segments tilting can be observed in the horizontal gradient map. The southern portion has a nearly N-S trend due to tilting. The change in fault orientation along strike gives the fault zone a zigzag pattern in plan view (Figs. 5 and 6 A - D).

Rollover structures within longitudinal synclines may be formed as a result of block tilting and/or probably due to radial propagation during fault growth. There are a number of NW-SE trending

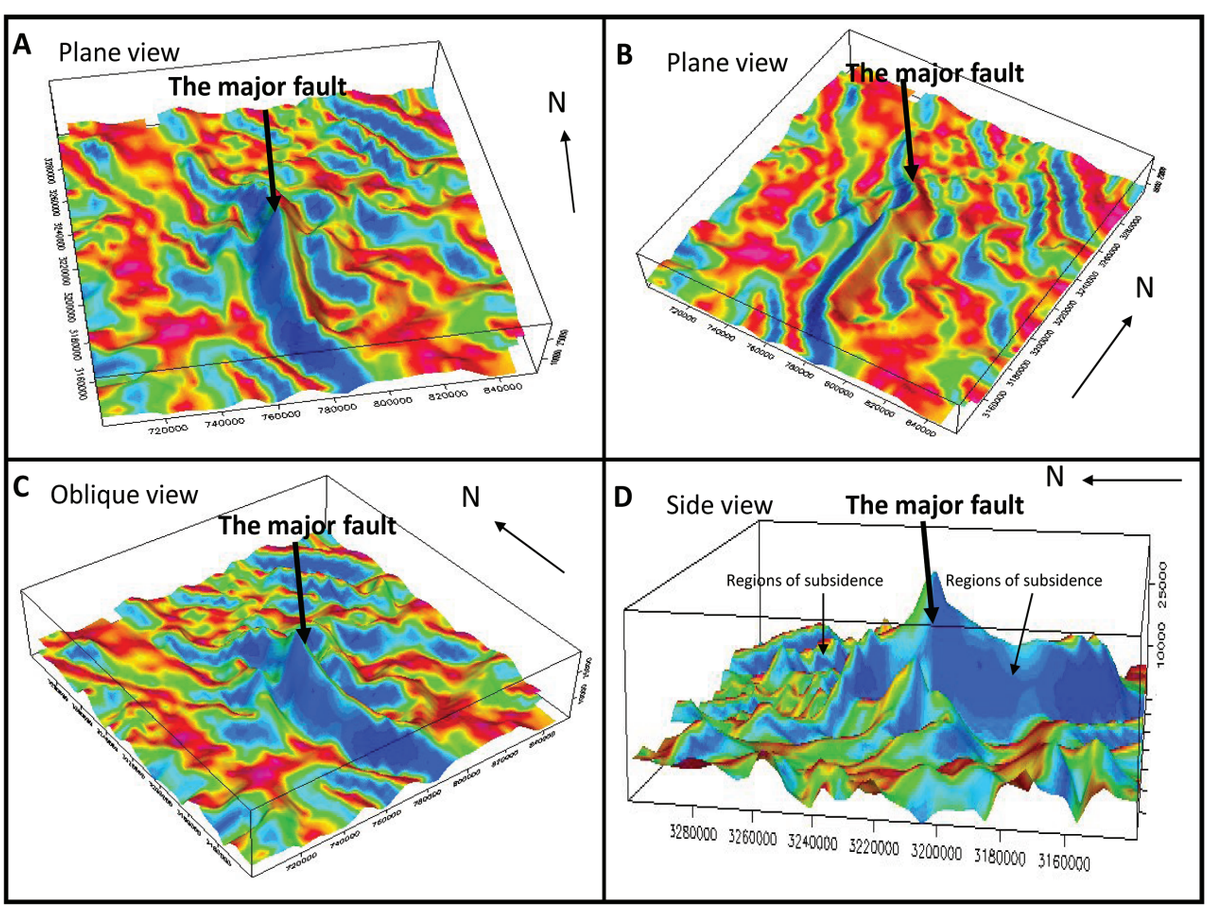


Fig. 6. 3D perspectives of the horizontal gradient surface depicting the major fault zone and structural highs (warm colours) and adjoining regions of subsidence such as longitudinal synclines (blue colours).

faults separated into sub-populations of probably synthetic and antithetic faults of variable arrays that can be observed in the residual anomaly and the horizontal gradient maps (Figs. 4 and 5). Other E-W trends can be observed in the maps which terminate against the major fault at relay zones and crossing the foot-wall and the hanging-wall in some places.

They were formed during interactions between different fault segments during segment linkage processes. In other cases the gravity minima are associated with longitudinal synclines or growth nucleus which related to fault evolution and rifting, best explained by recognizing that they are thick sequences of dominantly sedimentary rocks, including syn and post sediments.

Syn and post rift structures can be observed from seismic section (Fig. 7). The character of the seismic reflections shows evidences of rift patterns. It has been concluded that the attached graben to the bounding fault shows a model of hanging-wall with characteristics of different stacking patterns which in general reflect the nature of the rift features along the fault strike. It is suggested that, within and around the defined fault block, the uplifted area or crest is eroded and the eroded materials were transported and deposited on both sides of the crest forming initial syn-rift sediment wedges, with the greatest thickness at the immediate hanging-wall of the fault. The syn-rift and post-rift sediments of the hanging-wall of the large fault typically show monoclinal structures dipping into Al Hagfa Trough. These structures are interpreted to have been generated either by fault propagation during fault growth processes or through compaction of the sediments over the fault step in the basement.

Fault displacement folds, related to segmentation and fault growth process are common in the northern segment of the master fault. Many intra basin faults are formed sub parallel to the border fault zone (Figs. 8 and 9). Rollover structures (anticlines and synclines) developed within the hanging-wall of this segment

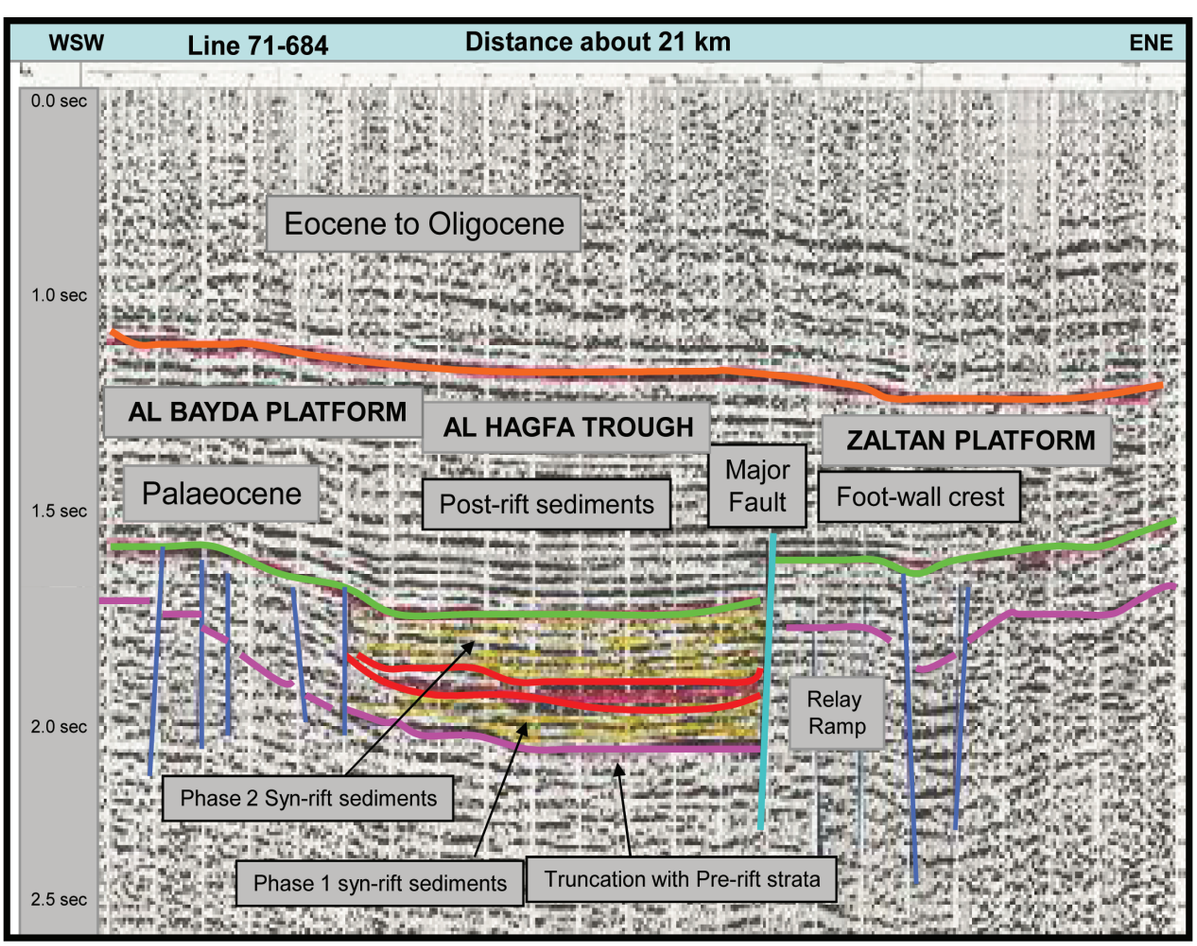


Fig..7. Interpretation of line 71-684 depicting faults, ramp at relay zone, stratigraphic, and structural configuration of a syn -rift wedges.

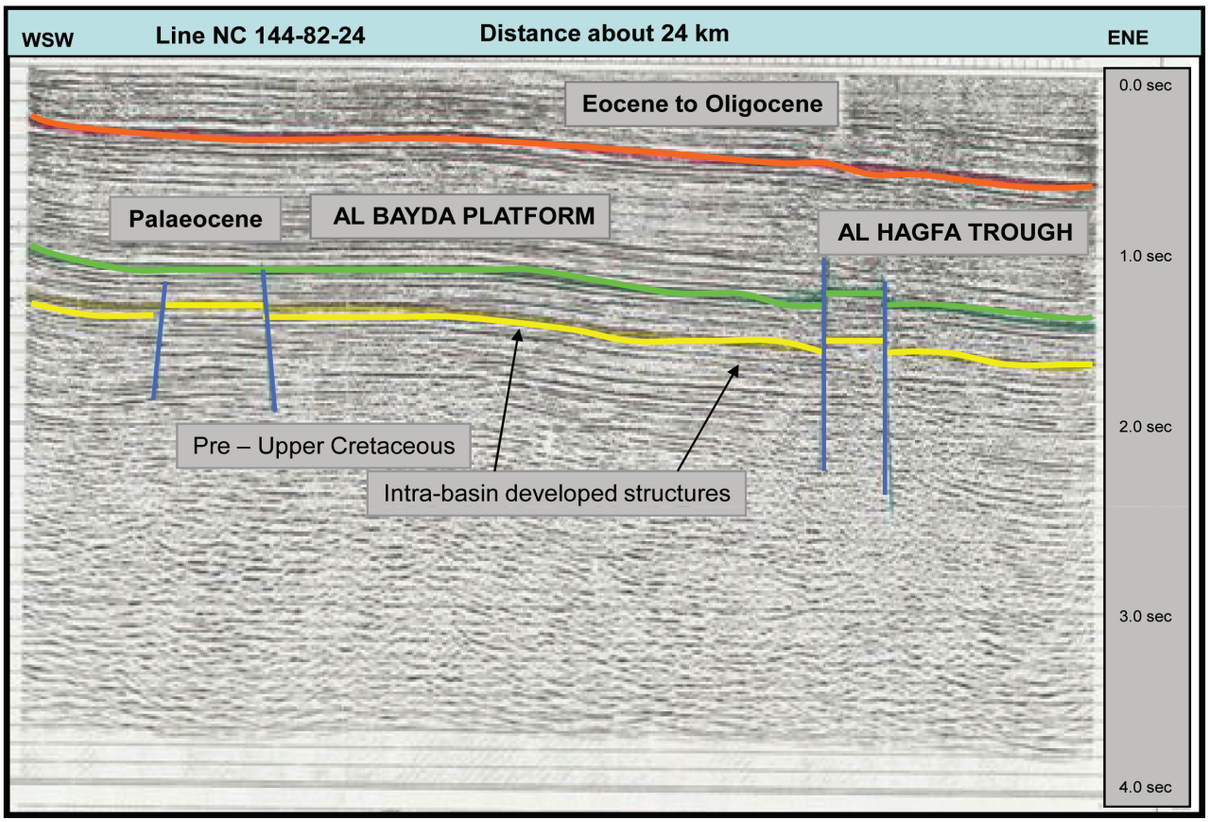


Fig. 8. Interpretation of line NC 144-82-024, showing horizons separating main time units with rollover structures (anticline like structures, synclines and folds) that have been developed with time and space during basin evolution.

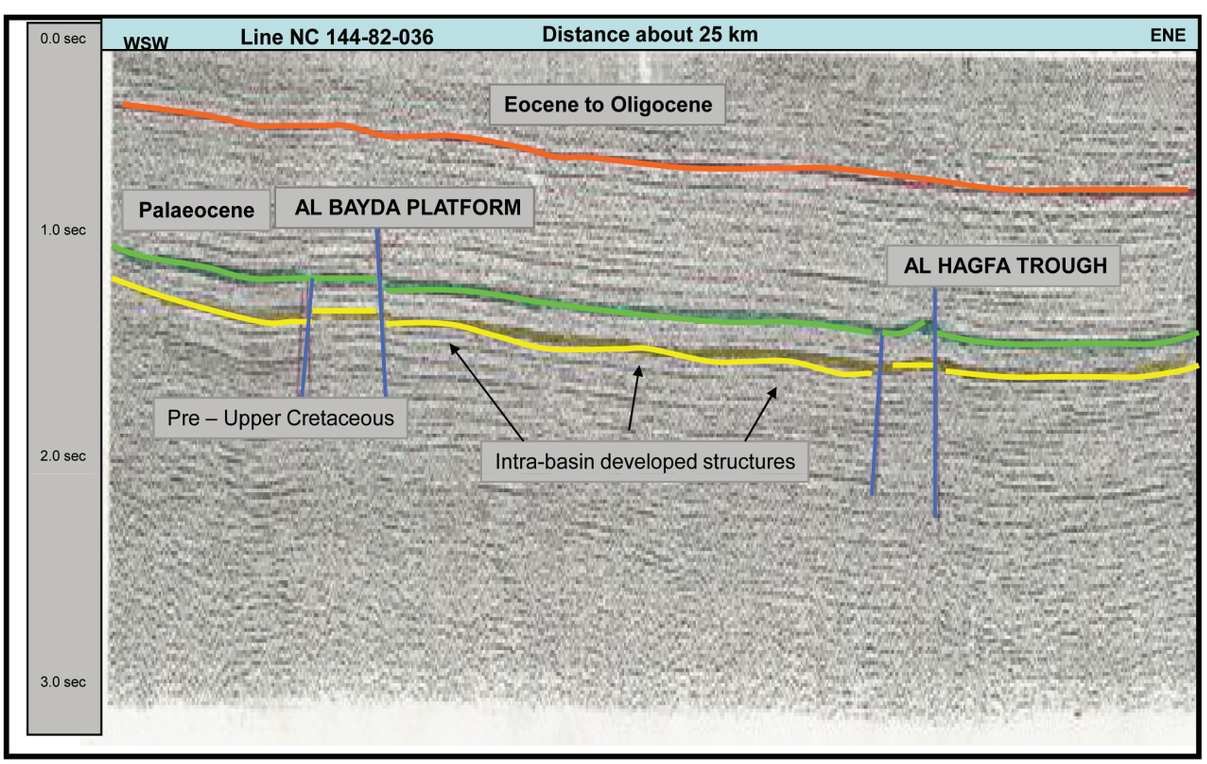


Fig. 9. Interpretation of line NC 144-82-036. It shows horizons separating main time units with rollover structures (anticlines, synclines, and folds) that have been developed with time and space during basin evolution.

mainly formed during radial propagation of this segment culminated with topographic changes associated with a transfer zone that form an important structural elements and has a marked influence on the area stratigraphy.

Computed forward models (Figs. 10 and 11) illustrate the nature and morphology of strata across the identified troughs and platforms. The models show typical sedimentary growth across the fault zone which in general is sufficient to produce structures similar in geometry and magnitude to the observed features.

Generally, in any extensional regime compaction is one of the most important mechanisms in the deformation of normal fault hanging-walls even in areas where basement is not involved in the faulting (Andrew, 1994). Despite the difference in location between gravity profiles and seismic sections, the gravity models (Figs. 10 and 11) and the interpreted seismic section (Fig. 7) show evidences of syn-depositional features and compaction within the hanging-wall. Under certain circumstances anticlines in the hanging – wall can also form as a sole result of compaction. The mode of extension has important consequences for the Cretaceous hydrocarbon entrapment associated with the rifted province of Al Hagfa Trough. It can be observed from the seismic section (Fig. 7) and the horizontal gradient map (Fig. 5) that there is a system of southwest-dipping, sub-parallel intrabasinal normal faults offsetting Cretaceous - Tertiary sediments and perhaps separating fault segments at the relay zones.

Evaluation of the main structures suggests that Al Hagfa Trough area could be reconsidered as a target for future hydrocarbon exploration. The major gravity minima over the trough can best be accommodated by a major rift zone, filled with probable Cretaceous and younger sedimentary sequences of about 3 - 5 km thick. The gravity minima associated with the bathymetric highs of the trough are best explained by recognizing that it is a thick sequence of dominantly sedimentary rocks, probably deposited on thinned continental crust bordering the rift.

Brief Review of Magnetic Data

The preliminary produced maps (Figs 12 and 13) show northeast – southwest and east - west striking magnetic highs that extended across Zaltan Platform and Al Bayda Platform respectively. It seems that the anomalies produced by these highs are caused by high magnetic rocks, probably coincides with the locations of magma tracks. In addition to that many northerly and easterly trending magnetic lineaments are visible on the total intensity magnetic maps (Figs

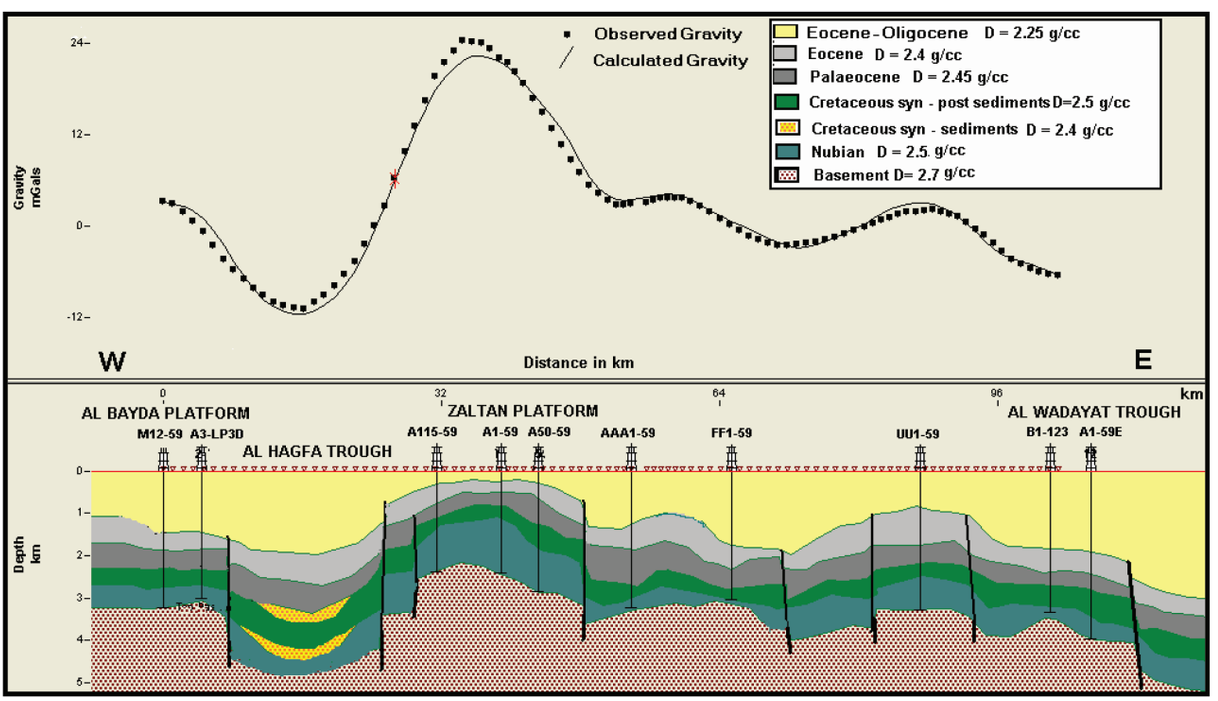


Fig. 10. E-W residual gravity model along profile A – B, showing major and minor faults with subsurface cross section across the mapped platforms and troughs.

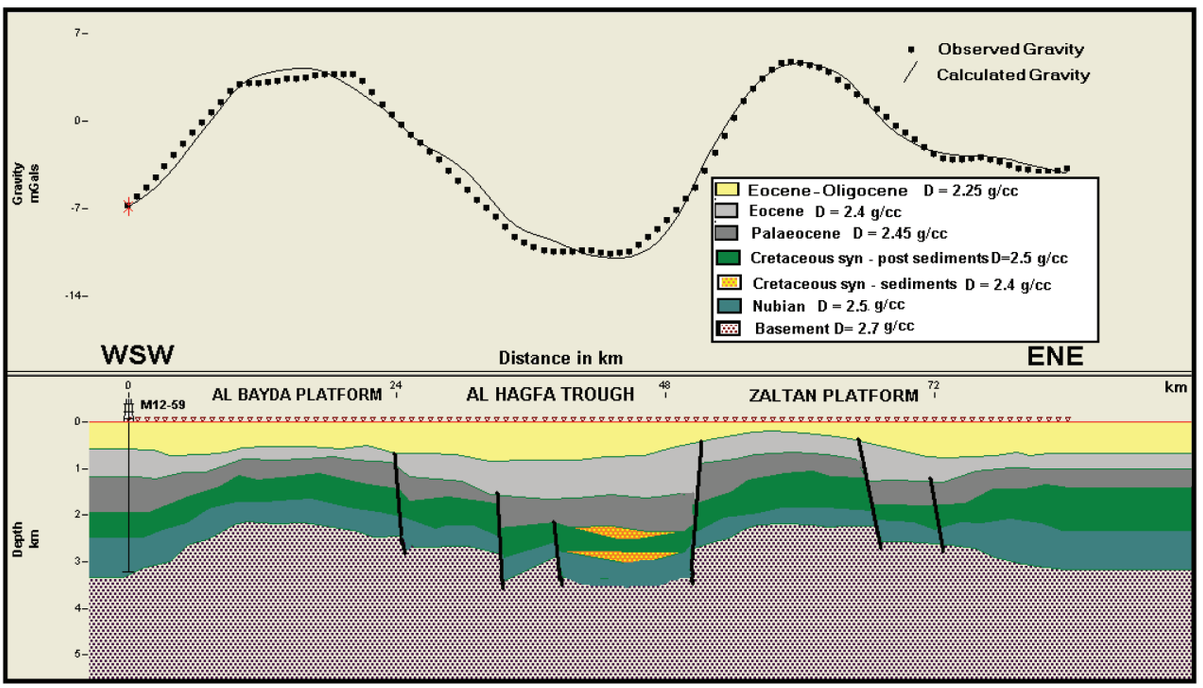


Fig. 11. ENE-WSW residual gravity model along profile C – D, showing major and minor faults with subsurface cross section across the mapped platforms and troughs.

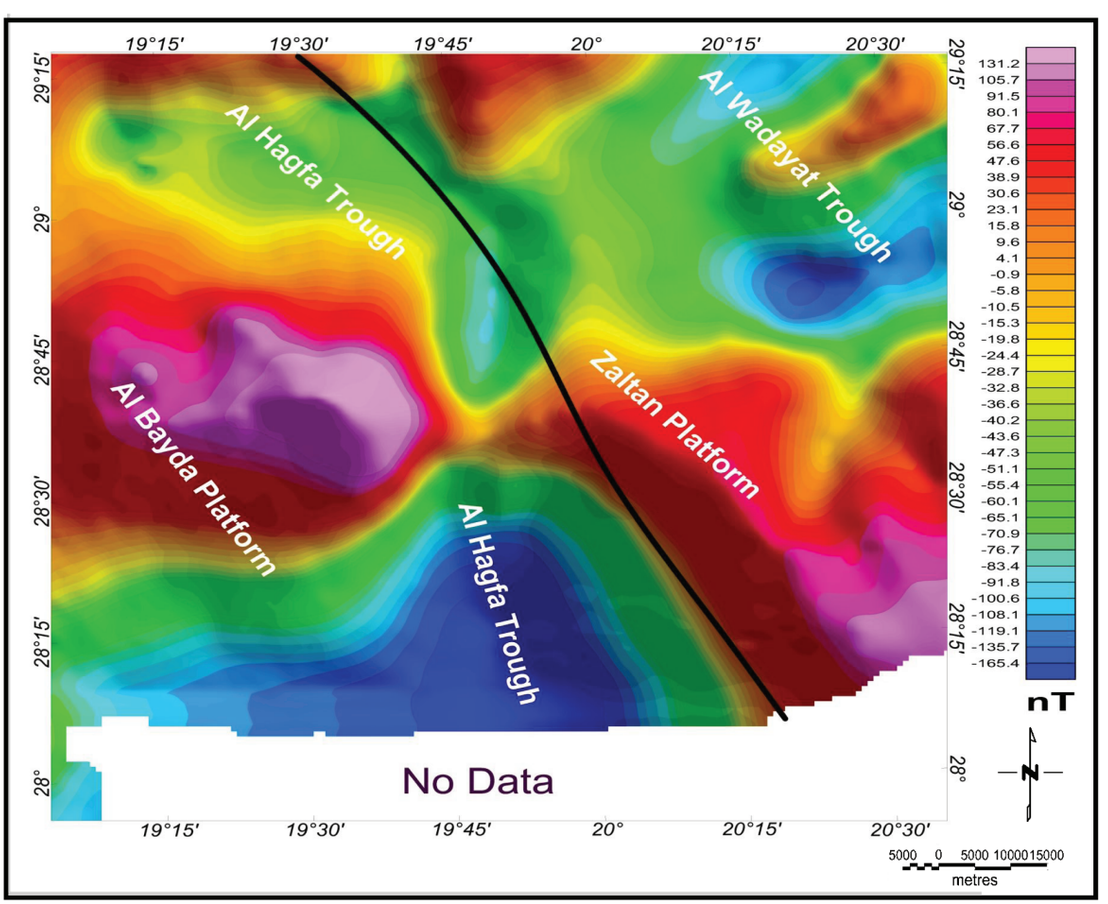


Fig. 12 Total magnetic intensity map of the study area.

12 and 13). The lineaments probably follow lithological contacts in the basement and/or basement shearing trends. Northwest-southeast and northwest-southeast fault trends can be seen to offset the lineaments.

The diagonal fault represents a major fault zone that was traced on the gravity maps. Further work is needed to confirm these preliminary interpretations.

DISCUSSION

Fault Geometry and Graben Evolution

The discussion that follows introduce the implementation of gravity and seismic dataset to locate major structures (horst and graben features) and associated faults evolved during rift evolution in part of the Sirt Basin, (Al Hagfa Trough region and the nearby areas).

The interpretation and modeling of the main structures were accomplished using Bouguer gravity and seismic data. Several trends related to the basin evolution were identified: (1) a northwest to southeast trend, indicates northeast to southwest extension throughout the study area, and (2) a predominantly northeast to southwest directed trend, indicate northwest to southeast extension, primarily in southern regions.

The study area is characterized by a dominant northwest-southeast trend. This is clearly evidenced from the horizontal derivative of the residual Bouguer gravity, with east-northeast and west-southwest trends takes over, characterized by broad gravity highs and lows. This is mainly related to the development of the tectonic zone.

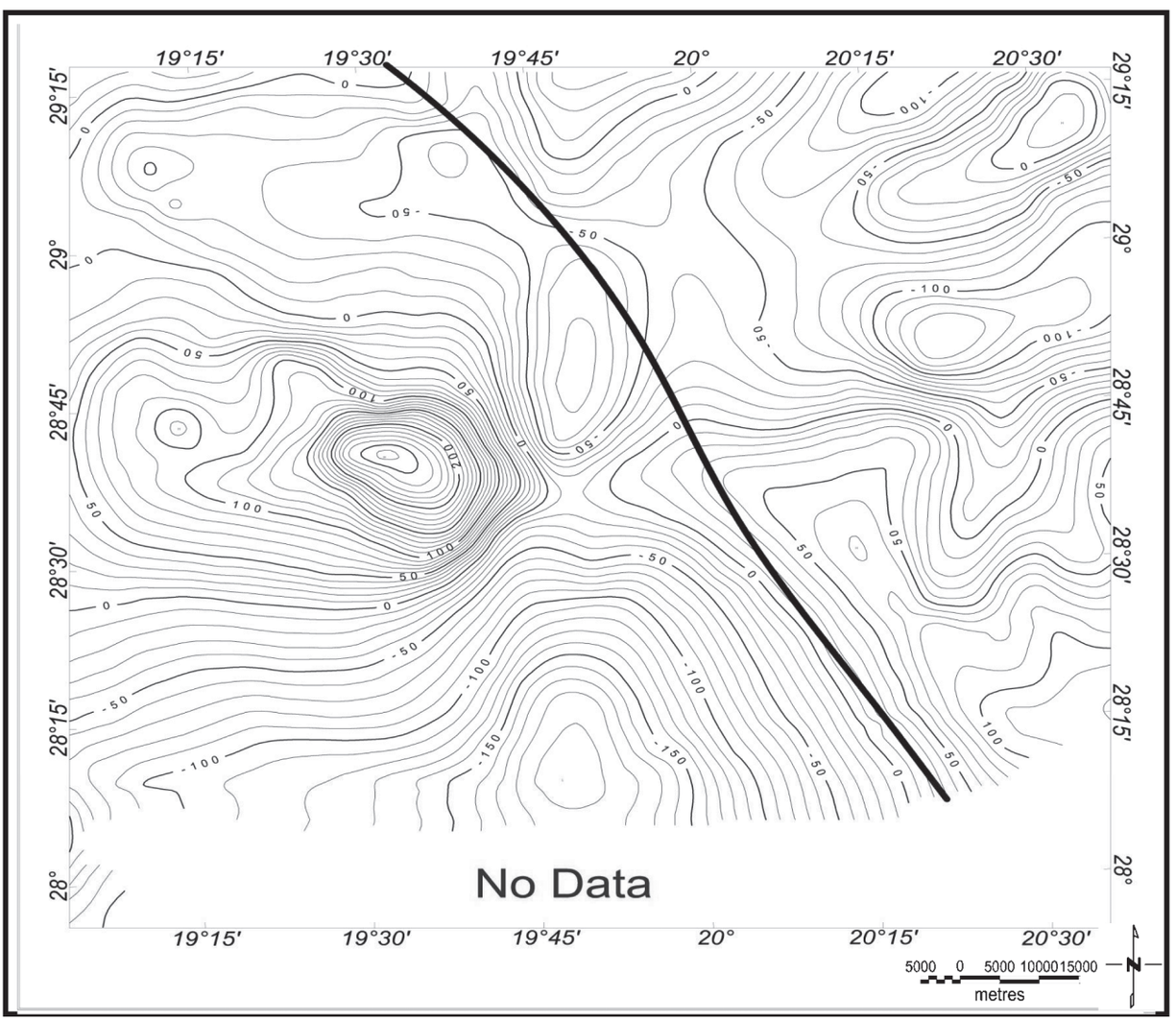


Fig. 13. Total magnetic intensity map of the study area with contours.

The identified major fault zone located between the Zaltan Platform and Al Hagfa Trough was formed by a system of large normal faults, interpreted to be mostly planar, basement – involved fault segments linked together by transfer zones. It is about 150 km long, composed of three 45 – 50 km long normal fault segments trending N - S and NE - SW direction and dipping towards the west direction. The master fault appears in the total horizontal gradient map with different arrays. It is trending NW – SE at the northern portion of the study area with evidence of splays or horizontal displacement along transfer zone, and N – S trend formed at the southern portion due to segment tilting.

As observed from the seismic data and the gravity models, the fault segments separate pre-rift lithologies in the foot-wall from the syn-rift sequences in the hanging- wall. The segments are tipping out along strike with evidence of linkage along the immediate hanging-wall of the fault block at probably breached relay zones.

A series of intra-basin structures can be observed that have axes mainly parallel to the fault zone (transverse folds, anticlines….etc) which probably formed during fault growth process.

Structures Evolution

The material movement along the strike of the hanging-wall is supported by the thickness of the syn-rift contraction sedimentary sequence (McClay, and Scott., 1991, Yamada and McClay, 2002). It is considered that the lower part of Al Hagfa Trough is associated with Cretaceous – Palaeocene syn-tectonic sequences subsequently buried by post-rift sediments. The syn-rift sequences in the wedge forming fault block can be divided into lower and upper sequences with onlap surfaces between them suggesting that there may have been two rift phases. Onlap relationships can sometimes be defined from seismic data, particularly at the base of the lower syn-rift sequences.

From the gravity models and the seismic sections, it has been considered that Pre-Upper Cretaceous section (Nubian) is probably truncated with basement as pre-rift sedimentary section. This needs more future work using high resolution data, because the master fault seems to be segmented below the seismic resolution.

CONCLUSIONS

- The Gravity maps indicates that the study area is marked with elongated gravity maxima and minima trending NW-SE showing a strong correlation with the structural highs (associated with platforms) and the structural lows (associated with sedimentary filled troughs) known from drilling. The maps also shows that Al Hagfa Trough is marked by a long wavelength negative gravity anomaly and very steep gravity gradients which delineate faults along the edges. The horizontal derivative enhances many of the more subtle trends that are masked in the anomaly maps.
- The study area reflects high frequency anomalies consistent with the horst-graben systems and relatively shallow to deep basement depths.
- We investigated structural and stratigraphic signatures related to rifting. Such investigations considered fault initiation during the development of the study area.
- Syn and post tectonic sequences can be resolved from scarce seismic sections within the study area. For example the 2D seismic sections show that truncation of pre-rift strata together with thinning and onlapping syn depositional strata onto fault scarp suggest that the area has experienced a series of rifting episodes during basin evolution.
- Nature of faulting and later subsidence might have had an effect on charge pattern (fetch areas vs. charge volumes, as well as bypassed areas).
- Intra basin transversal structures either related with accommodation zones or further block movement can be interesting for intra-trough hydrocarbon entrapment.
- Transfer and accommodation zones on the platform areas might have affected migration pattern along with interesting main margin faults.
- Enhancement of existing magnetic data will shed more light on basement and anorogenic magmatic rocks configuration which will enrich our understanding of the geology of Sirt Basin.

ACKNOWLEDGEMENTS

We thank LPI management for permission to publish the compiled gravity data used for this study.

REFERENCES

Ahlbrandt, T.S., 2001. *The Sirte Basin Province of Libya—Sirte-Zaltan Total Petroleum System*. U.S. Geological Survey Bulletin 2202–F.

Andrew, G.S., 1994. A structural model of a graben boundary fault system, Sirte Basin, Libya: Compaction structures and transfers zones. *Can. J. Explo. Geophysics*. **30,** No 2, 84 – 92.

Busrewil, M.T., Oun, K.M., and Haman, M., 2008, Neoproterozoic – Lower Cretaceous Tectono-Sedimentary Evolution of the Sirte Basin, Libya. In: Geology of *East Libya*, **IV.** Earthscience Soc. Libya.

Hallett, D. and El Ghoul, A., 1996. Oil and gas potential of the deep trough areas in the Sirt Basin, Libya. *First Symposium on the Sedimentary Basins of Libya, Geology of the Sirt Basin.* **2.** Elseviere Amsterdam.

Libyan Gravity Compilation Project, 2002. Libyan Petroleum Institute

Meer, F.V.D., and Cloetingh, S., 1993, Intraplate stresses and the subsidence history of the Sirte Basin (Libya). *Tectonophysics,* **226**, 37-58.

McClay, K.R., Scott, A.D., 1991. Experimental models of hangingwall deformation in ramp-flat listric extensional fault systems. *Tectonophysics* **188,** 85-96.

Yamada, Y., and McClay, K., 2002. Application of geometric models to inverted listric fault systems in sandbox experiments. Paper 2: insights for possible along strike migration of material during 3D hanging wall deformation, *J. Struc. Geol.* **25**, 1331 – 1336.